TECHNISCHE UNIVERSITÄT DRESDEN

Implementation and phenomenology of polarized cross sections in the simulation of vector boson production with the SHERPA event generator

Master-Arbeit
zur Erlangung des Hochschulgrades
Master of Science
im Master-Studiengang Physik

CERN-THESIS-2023-182
12/04/2023

vorgelegt von

Mareen Hoppe
geboren am 15.07.1997 in Dresden

Institut für Kern- und Teilchenphysik
Fakultät Physik
Bereich Mathematik und Naturwissenschaften
Technische Universität Dresden
2023

Eingereicht am 12. April 2023

1. Gutachter: Dr. Frank Siegert
2. Gutachter: Dr. Marek Schönherr

Abstract

Measurements of vector boson polarization in vector boson production processes offer the possibility to probe the concrete mechanism of electroweak symmetry breaking and the innermost gauge symmetry structure of the Standard Model. In addition, they are sensitive to effects of new physics beyond the Standard Model. Since massive vector bosons can only be observed as intermediate particles, polarized cross section templates from simulation are necessary to extract their polarization from measurable unpolarized distributions. The Monte-Carlo event generator SHERPA is not yet capable of simulating polarized cross sections.

In this work, a new implementation allowing the simulation of polarized cross sections for vector boson production processes is presented and validated by comparison with literature data at fixed leading order. It will be released in SHERPA version 3.0.0. With this implementation, polarized cross sections of all possible polarization combinations for an arbitrary number of intermediate vector bosons can be simulated in a single simulation run by applying a spin-correlated narrow-width approximation. In addition, it is possible to directly predict the interference between different polarizations, and various polarization definitions can be studied. NLO QCD corrections on polarized cross sections of vector boson production processes can be approximately calculated, neglecting influences of virtual corrections on polarization fractions. First applications of the implementation demonstrate that differences of this approximation to full NLO QCD predictions are small. Merged calculations are another possibility to obtain NLO QCD polarization corrections which is also tested within this thesis. Furthermore, the influence of different polarization definitions on polarization fractions and polarized distributions of vector boson scattering processes at fixed leading order is studied.

Kurzdarstellung

Messungen von Vektorboson-Polarisation in Vektorbosonproduktionsprozessen bieten die Möglichkeit, den elektroschwachen Symmetriebrechungsmechanismus und die innere Eichstruktur des Standardmodells zu untersuchen. Zudem sind sie sensitiv auf Effekte neuer Physik jenseits des Standardmodells. Da massive Vektorbosonen nur als intermediäre Teilchen beobachtet werden können, ist die Simulation polarisierter Wirkungsquerschnitte nötig, deren Ergebnisse als Templates genutzt werden, um die Polarisation der Vektorbosonen aus den messbaren, unpolarisierten Verteilungen zu erhalten. Der Monte-Carlo-Eventgenerator SHERPA ist bislang nicht in der Lage, polarisierte Wirkungsquerschnitte zu simulieren.

In dieser Arbeit wird eine neue Implementation, welche die Simulation polarisierter Wirkungsquerschnitte für Vektorbosonproduktionsprozesse ermöglicht, vorgestellt und durch Vergleich mit Literaturdaten auf fester, führender Ordnung validiert. Sie wird mit der nächsten SHERPA-Version 3.0.0 veröffentlicht. Polarisierte Wirkungsquerschnitte aller möglichen Polarizationskombinationen einer beliebigen Anzahl von intermediären Vektorbosonen können damit innerhalb einer Simulation unter Verwendung einer spin-korrelierten Narrow-Width-Approximation (sinngemäß: Näherung der schmalen Breiten) simuliert werden. Überdies ist die direkte Vorhersage der Interferenz zwischen verschiedenen Polarisationen möglich. Verschiedene Polarisationsdefinitionen können untersucht werden. NLO QCD Korrekturen auf polarisierte Wirkungsquerschnitte von Vektorbosonproduktionsprozessen können näherungsweise unter Vernachlässigung von Einflüssen virtueller Korrekturen auf die Polarisationsanteile berechnet werden.

In ersten Anwendungen der Implementation wird gezeigt, dass die Unterschiede dieser Näherung zu vollen NLO QCD Vorhersagen klein sind. Merging-Rechnungen stellen eine andere Möglichkeit dar, polarisierte NLO QCD Korrekturen zu erhalten, was ebenfalls in dieser Arbeit getestet wird. Weiterhin wird der Einfluss verschiedener Polarisationsdefinitionen auf Polarisationsanteile und polarisierte Verteilungen in Vektorbosonstreuprozessen auf fester, führender Ordnung untersucht.

Contents

1 Introduction

Understanding the fundamental constituents of matter and their interactions is the main goal of elementary particle physics. In this research field those objects in the universe are studied which cannot be subdivided further - elementary particles. The Standard Model of Particle Physics (SM) is currently the best model to describe these particles, their properties and especially the interactions between them. To prove its predictions, high energies are necessary as accelerators such as the Large-Hadron-Collider (LHC) at CERN can provide them.
Even though the SM was developed over 50 years ago, its particle content was only completed about 10 years ago in 2012 when the LHC detected a scalar particle having the same properties as the predicted Higgs boson [1, 2]. Its observation confirms the existence of the Higgs field and the mechanism of electroweak spontaneous symmetry breaking (EWSB) which solve one big SM problem - the explanation of the vector boson (VB) masses. However, until now, the concrete mechanism of EWSB is still under investigation. Since the longitudinal polarization of massive VBs is a direct consequence of this mechanism, polarized VB production is a very promising group of processes to study for this purpose.
Without the Higgs boson, the scattering of longitudinal VBs would break unitarity since its cross section would rise with the center-of-mass energy (CME) squared [3] which illustrates the sensitivity of VB polarization to the EWSB mechanism. Furthermore, since triple and quartic gauge coupling vertices appear in diagrams of many VB production processes they can also be a probe for the SM innermost gauge symmetry structure. Moreover, even though no significant deviations from the SM have been found so far, it is not exhaustive. For example, it does not provide explanations for dark matter [4], the hierarchy problem [5] or the matter-antimatter asymmetry in the universe [6]. Therefore, several theories on physics beyond the SM (BSM) have been developed. Measurements of VB polarization could give insights into BSM physics because in models of new physics modifications in the VB scattering (VBS) cross sections of longitudinal polarized $W^{\pm}$ and Z bosons arise due to different Higgs boson couplings to gauge bosons or the presence of new resonances [7, 8]. Some BSM physics models even predict differences in the VBS cross sections of transverse polarized $W^{\pm}$ and Z bosons [9].
First VB polarization measurements at the LHC are conducted with data from collisions at 7 and 8 TeV CME for $W^{\pm}$ boson production in association with jets [10, 11], in top quark decays [12–14] and in inclusive Z boson production [15]. Data taken from the recently finished Run 2 of the LHC at 13 TeV CME is currently being analyzed. First measurements are presented

for $W^{\pm}Z$ production [16, 17] and $W^{\pm}W^{\pm}$-scattering [18]. The expected high luminosity in the forthcoming LHC-runs will provide higher sensitivity to VB polarization and will also enable polarization measurements of very rare processes such as VBS processes [19, 20].

To design analyses for VB polarization measurements, polarized cross section templates provided by Monte-Carlo (MC) event generators are required. They allow to predict the expected distributions of kinematic observables interesting for these processes and to extract polarization information from the unpolarized data. Currently, only a few generators are able to provide polarization information, namely Madgraph [21, 22] and PHANTOM [23]. The general-purpose MC event generator SHERPA [24] is not yet capable of simulating polarized cross sections. Since SHERPA provides a more accurate process description by simulating higher orders of the strong coupling constant α_S, adding this capability would be highly desirable. In addition, this would extend the ability to compare predictions between different generators. Due to its complexity, the simulation of interaction processes always relies on approximations that may differ between MC-generators, so comparing simulations from different generators is essential for a robust prediction.

The aim of this work is to close that gap by adding new functionality to SHERPA to enable the simulation of polarized cross sections for unstable VBs. The framework introduced in this thesis allows the calculation of polarized cross sections of all possible helicity combinations in one simulation run and treats them as additional event weights in SHERPA. Furthermore, the interference between different polarizations can be calculated directly without subtraction and several polarization definitions are provided. Even though the main goal was to describe VB polarization at leading order (LO), it is shown that the new framework can further be utilized to simulate the main behavior of VB polarization at next-to-leading order (NLO) QCD with SHERPA if the influence of virtual corrections on polarization fractions is negligible.

The thesis is organized as follows. In Chap. 2, theoretical concepts important for the description of VB polarization are introduced, including the definition of spin in relativistic theories based on group theory and the quantum field theory of free and interacting massive VBs. Basic aspects about the simulation of hadronic processes, an introduction to the investigated VB production processes as well as the definition of polarization for intermediate VBs and the difficulties associated with that are explained in Chap. 3. The actual implementation of polarized cross sections for VB production in SHERPA is presented in Chap. 4. This covers both the general description of how polarized cross sections are obtained with the SHERPA framework and how the simulation of VB polarization aspects at NLO QCD becomes possible. Chap. 5 validates the implementation against literature data at fixed LO for several processes. First applications of the new framework in phenomenological analyses investigating NLO QCD corrections to polarized cross sections and the influence of different polarization definitions on VBS processes at fixed LO are discussed in Chap. 6. Chap. 7 gives a summary of this work and an outlook into future extensions of the new framework and planned applications.

2 Theoretical foundation

In this chapter, theoretical concepts required to calculate polarized cross sections for massive VBs are displayed[1]. This first includes the definition of spin for massive relativistic particles which is directly connected to the particle's polarization. Among known massive elementary particles, the massive VBs are of special interest for this thesis. Their description in quantum field theory (QFT) is discussed afterwards starting with the corresponding free field theory and followed by the electroweak theory where they appear as mediator particles.
The electroweak theory is part of the Standard Model that is currently the best model to describe the known elementary particles and their interactions with each other. It is formulated as a gauge theory being symmetric under local gauge transformations of the non-Abelian symmetry group product $SU(2)_L \otimes U(1)_Y \otimes SU(3)_C$. Beside the electroweak interaction described by the $SU(2)_L \otimes U(1)_Y$ gauge group, the SM also includes the strong interaction, the corresponding QFT is called quantum chromodynamics (QCD). Details about the parts of the SM not covered by this thesis including QCD, the particle content or certain particle properties can be found in textbooks such as [25–27].

2.1 Group theory and spin for massive particles in relativistic theories

Particle physics investigates particles at very high energies. Therefore, theories describing elementary particles and their interactions are relativistic theories. Particles are characterized by their properties including mass, spin and charges. Particle polarization is defined as the alignment of the particle's spin in a certain direction, usually the particle's momentum.
Relativistic spin can be defined based on group theory. Therefore, this section first introduces important properties of the Poincaré and the Lorentz group and demonstrates different Lorentz group representations necessary to understand the calculation of polarization vectors in SHERPA. Based on this introduction, the definition of spin of massive particles in relativistic theories is discussed. Further details on the aspects mentioned here can be found in

[1]Throughout this chapter, natural units are assumed, i.e. light velocity c and the reduced Planck constant $\hbar$ are set to one. Furthermore, if not stated otherwise, Einstein's summation convention is applied during the whole thesis where repeated three-vector indices (Latin letters) or two-times appearing polarization indices (denoted by λ) as well as pairwise identical contravariant (upper Greek letters) and covariant (lower greek letters) four-vector indices are summed over.

Ref. [26, 28–37] which were consulted for this section.

2.1.1 The Poincaré group $\mathcal{P}$

The Poincaré group (or inhomogeneous Lorentz group) $ISO(3,1)$ is a ten-dimensional Lie group and consists of all linear transformations:

$$x'^{\mu}(x) = \Lambda^{\mu}{}_{\nu} x^{\nu} + a^{\mu}\,, \tag{2.1}$$

which leave the line element $(\mathrm{d}x)^2 = g_{\mu\nu}\mathrm{d}x^{\mu}\mathrm{d}x^{\nu} = (\mathrm{d}t)^2 - (\mathrm{d}\vec{x})$ with the metric tensor $g_{\mu\nu} = \mathrm{diag}(1,-1,-1,-1)$ invariant. These are Lorentz transformations Λ and global translations of space-time a. A generic element of $\mathcal{P}$ has the form:

$$(\Lambda, a) = e^{-\frac{i}{2}\omega_{\mu\nu}M^{\mu\nu}} e^{-ia_{\mu}P^{\mu}} \tag{2.2}$$

and is described by the ten group generators derived by looking at group elements infinitesimally close to the identity. They form the Lie algebra associated with the Poincaré group. It is defined by the commutator relations:

$$\begin{aligned} [M^{\mu\nu}, M^{\rho\sigma}] &= i(g^{\mu\sigma}M^{\nu\rho} + g^{\nu\rho}M^{\mu\sigma} - g^{\mu\rho}M^{\nu\sigma} - g^{\nu\sigma}M^{\mu\rho})\,, \\ [P^{\mu}, M^{\rho\sigma}] &= i(g^{\mu\rho}P^{\sigma} - g^{\mu\sigma}P^{\rho}) \quad \text{and} \quad [P^{\mu}, P^{\nu}] = 0\,. \end{aligned} \tag{2.3}$$

The six generators in $\hat{M}^{\mu\nu}$ are responsible for the generation of homogeneous Lorentz transformations, which themselves form a subgroup of $\mathcal{P}$, the Lorentz group. The remaining four P^{μ} are the components of the momentum operator and generate space-time translations. a_{μ} and $\omega_{\mu\nu}$ contain the transformation parameters. $\omega_{\mu\nu}$ is an antisymmetric tensor describing therefore six of the ten parameters. The specific form of the generators depends on the chosen representation. In the four-vector representation, $M^{\mu\nu}$ takes the form:

$$(M^{\mu\nu})^{\rho}{}_{\sigma} = i(g^{\mu\rho}\delta^{\nu}{}_{\sigma} - g^{\nu\rho}\delta^{\mu}{}_{\sigma})\,. \tag{2.4}$$

2.1.2 Lorentz group $\mathcal{L}$

The Lorentz group $O(3,1)$ contains all transformations which satisfy:

$$g_{\mu\nu}\Lambda^{\mu}{}_{\alpha}\Lambda^{\nu}{}_{\beta} = g_{\alpha\beta}\,. \tag{2.5}$$

It can be split into four disconnected sectors according to properties of Λ, $\det\lambda = \pm 1$ and $\lambda^{0}{}_{0} \geq 1$ or ≤ -1, as shown in Tab. 2.1. The component $\mathcal{L}^{\uparrow}_{+}$ is the only sector which forms a subgroup of the Lorentz group, $SO^{+}(3,1)$, containing proper orthochronous Lorentz transformations. It consists of Lorentz boosts and space rotations; each element of $\mathcal{L}_+^\uparrow$ can be written as a pure Lorentz boost L times a pure rotation R. The associated Lie algebra is defined by the commutators of their generators $M_{\mu\nu}$ already given in Eq. 2.3. The generators $M_{\mu\nu}$ consists of the generators of $SO(3)$ rotations $J^i = \frac{1}{2}\epsilon^{ijk}J^{jk}$ and of boosts $K^i = M^{i0}$ which fulfill the commutator relations:

$$[J^i, J^j] = i\epsilon^{ijk}J^k\,, \qquad [J^i, K^j] = i\epsilon^{ijk}K^k\,, \qquad [K^i, K^j] = -i\epsilon^{ijk}J^k\,. \tag{2.6}$$

ϵ_{ijk} denotes the Levi-Civita tensor. An arbitrary finite element of $\mathcal{L}_+^\uparrow$ can be written according to:

$$\Lambda = e^{-i\vec{\theta}\cdot\vec{J}+i\vec{\eta}\cdot\vec{K}} = R\cdot L\,, \tag{2.7}$$

when $\vec{\theta}$ with $\theta^i = (1/2)\epsilon^{ijk}\omega^{jk}$ is the vector of the rotation angles and $\vec{\eta}$ with $\eta^i{=}\omega^{i0}$ describes the boost parameters η. A general rotation specified by the vector of rotation angles $\vec{\theta}$ and a pure Lorentz boost with velocity $\vec{\beta}$, $|\beta| = \tanh|\vec{\eta}|$, $\gamma = \frac{1}{\sqrt{1-\beta^2}}$ can be represented in the four-vector representation of $\mathcal{L}_+^\uparrow$ by the matrices:

$$L(\vec{\beta}) = e^{i\vec{\eta}\cdot\vec{K}} = \begin{pmatrix} \gamma & \beta_j\gamma \\ \beta_i\gamma & \delta^{ij} + \frac{\beta_i\beta_j}{\beta^2}(\gamma-1) \end{pmatrix}, \qquad R(\vec{\theta}) = \begin{pmatrix} 1 & 0 \\ 0 & R_{\vec{\theta}} \end{pmatrix}. \tag{2.8}$$

$R_{\vec{\theta}}$ describes an element of the three-dimensional rotation group $SO(3)$. With these definitions a boost of velocity v applied on a particle at rest would result in a particle moving with velocity v. A rotation by an angle $\theta > 0$ in the (x,y)-plane would rotate the position of a point counterclockwise with respect to a fixed reference frame. [34]

Some of the irreducible representations (IR) of $\mathcal{L}_+^\uparrow$ are important for this work, which is why they will be discussed in more detail here. For this, it is worth to define the following hermitian linear combinations of the generators $\vec{J}$ and $\vec{K}$:

$$\vec{A} = \frac{1}{2}(\vec{J} - i\vec{K})\,, \qquad \vec{B} = \frac{1}{2}(\vec{J} + i\vec{K})\,, \tag{2.9}$$

Table 2.1: The four components of the Lorentz group $\mathcal{L}$.

Component	det Λ	$\Lambda^0{}_0$	characteristic (discrete) representatives
$\mathcal{L}_+^\uparrow$	+1	≥ 1	identity
$\mathcal{L}_-^\uparrow$	-1	≥ 1	parity transformation
$\mathcal{L}_+^\downarrow$	+1	≤ -1	time reversal
$\mathcal{L}_-^\downarrow$	-1	≤ -1	space-time reversal

with the commutator relations:

$$[A^i, A^j] = i\epsilon^{ijk}A^k\,, \qquad [B^i, B^j] = i\epsilon^{ijk}B^k\,, \qquad [A^i, B^j] = 0\,. \tag{2.10}$$

It can be seen that the generators form two commuting subsets, each satisfying the commutator relation of the $SU(2)^2$ algebra. Thus, $\vec{A}$ and $\vec{B}$ are each generators of the $SU(2)$. The IRs of the $SU(2)$ are characterized by an integer or half-integer value j [33], the eigenvalues of the Casimir operators $\vec{A}^2$ or $\vec{B}^2$. This can be used to specify representations of $\mathcal{L}_+^\uparrow$, denoted by D, by two numbers a and b which can independently be zero, positive integral or half-integral. $(2a+1)(2b+1)$ eigenstates correspond to each (a,b) combination which can be taken as the basis of the IR's of $\mathcal{L}_+^\uparrow$ with dimension $(2a+1)(2b+1)$. Generally, tensorial ($a+b$=integer) and spinor representations ($a+b$=half integer) are distinguished. In the following, the non-trivial irreducible representations are introduced that are of interest for this thesis.

Fundamental representations $D(\frac{1}{2},0)$ and $D(0,\frac{1}{2})$

There exist two inequivalent representations of dimension two, $D(\frac{1}{2},0)$ and $D(0,\frac{1}{2})$. Due to their behavior under parity transformation, they are often called left- and right-handed spinor representation. In the former, the generators $\vec{A}$ and $\vec{B}$ become $\vec{A}=\frac{\vec{\sigma}}{2}$ and $\vec{B}=0$, in the latter $\vec{A}=0$ and $\vec{B}=\frac{\vec{\sigma}}{2}$ with $\vec{\sigma}=(\sigma_1,\sigma_2,\sigma_3)$ being the vector of the Pauli matrices:

$$\sigma_1 = \begin{pmatrix} 0 & 1 \\ 1 & 0 \end{pmatrix}, \qquad \sigma_2 = \begin{pmatrix} 0 & -i \\ i & 0 \end{pmatrix}, \qquad \sigma_3 = \begin{pmatrix} 1 & 0 \\ 0 & -1 \end{pmatrix}. \tag{2.11}$$

The boost and rotation generators then take the form:

$$\left(\frac{1}{2},0\right): \; \vec{J}=\frac{\vec{\sigma}}{2} \qquad \vec{K}=i\frac{\vec{\sigma}}{2}\,, \qquad \left(0,\frac{1}{2}\right): \; \vec{J}=\frac{\vec{\sigma}}{2} \qquad \vec{K}=-i\frac{\vec{\sigma}}{2}\,. \tag{2.12}$$

B.L. van der Waerden [38] introduces a dot notation for spinors transforming according to these representations. The notation presented here follows Ref. [35]. Spinors transforming according to the $D(\frac{1}{2},0)$-representation stay without a dot ψ_A whereas spinors transforming according to the $D(0,\frac{1}{2})$-representation get a dot $\psi^{\dot{A}}$. Dotting and undotting indices correspond to complex conjugation: $\psi_{\dot{A}}=(\psi_A)^*$, $\psi^A=(\psi^{\dot{A}})^*$. A summation is implicit if the same index is once an upper and once a lower index. Both representations are connected to each other by:

$$\psi^A=\epsilon^{AB}\psi_B,\; \psi^{\dot{A}}=\epsilon^{\dot{A}\dot{B}}\psi_{\dot{B}} \quad \text{with} \quad \epsilon^{AB}=\epsilon^{\dot{A}\dot{B}}=\epsilon_{AB}=\epsilon_{\dot{A}\dot{B}}=i\sigma^2=\begin{pmatrix} 0 & 1 \\ -1 & 0 \end{pmatrix}. \tag{2.13}$$

[2] $SU(2)$ denotes the special unitary group of degree two, the linear group of unitary (2x2) matrices with determinant 1.

A Lorentz invariant spinor product is defined by:

$$\langle\phi\psi\rangle = \phi_A\psi^A = \phi_1\psi_2 - \phi_2\psi_1 \qquad \text{and} \qquad \langle\phi\psi\rangle^* = \phi_{\dot{A}}\psi^{\dot{A}} = (\phi_1\psi_2 - \phi_2\psi_1)^* . \quad (2.14)$$

Vectorial representation $D(\frac{1}{2},\frac{1}{2})$

The $D(\frac{1}{2},\frac{1}{2})$-representation is four-dimensional. The former two representations are called fundamental as they are the building blocks for all higher-dimensional representations of the Lorentz group. In this case $D(\frac{1}{2},\frac{1}{2}) = D(\frac{1}{2},0)\otimes D(0,\frac{1}{2})$ applies, so the objects transforming in this representation have two indices $K_{\dot{A}B}$. The standard form of the $D(\frac{1}{2},\frac{1}{2})$-representation would be complex (2x2) matrices but it can be shown that they transform like four-vectors, i.e. this representation is equivalent to the four-vector representation of the Lorentz group $SO^+(3,1)$. Thus, the form of the generators in this representation is already given in Eq. 2.4. The transition between the representation $K_{\dot{A}B}$, also called spinor representation, and a usual four-vector $k^\mu = (k^0,\vec{k})$ is possible with the help of the matrices $\sigma^{\mu,\dot{A}B} = (\sigma^0,\vec{\sigma})$ and $\sigma^\mu_{A\dot{B}} = (\sigma^0,-\vec{\sigma})$ with σ^0 being the two-dimensional unit matrix:

$$K_{\dot{A}B} = k^\mu\sigma_{\mu,\dot{A}B} = \begin{pmatrix} k^0+k^3 & k^1+ik^2 \\ k^1-ik^2 & k^0-k^3 \end{pmatrix}, \qquad k^\mu = \frac{1}{2}\sigma^{\mu,\dot{A}B}K_{\dot{A}B} . \quad (2.15)$$

Furthermore, $K_{\dot{A}B}$ can also be expressed in terms of products of $D(\frac{1}{2},0)$- and $D(0,\frac{1}{2})$ spinors. This is used in matrix element calculations to simplify their structure by describing all occurring mathematical objects with those spinors (Weyl-van-der-Waerden technique [35]). There is no unique spinor product decomposition for $K_{\dot{A}B}$. One possibility is represented by the eigenvector decomposition which is possible if k^μ is real and therefore $K_{\dot{A}B}$ a Hermitian matrix (cf. Ref. [35]). Other decompositions exploit the fact that light-like vectors $k^\mu = |\vec{k}|(1,\cos\phi\sin\theta,\sin\phi\sin\theta,\cos\theta)$ can be described by a single spinor product:

$$K_{\dot{A}B} = k_{\dot{A}}k_B \qquad \text{with} \qquad k_A = \sqrt{2k^0}\begin{pmatrix} e^{-i\phi}\cos\frac{\theta}{2} \\ \sin\frac{\theta}{2} \end{pmatrix} . \quad (2.16)$$

The k_A given in Eq. 2.16 is only one possible choice, any arbitrary phase can be added to them without changing the physics. Four-vectors k^μ with $k^2 \neq 0$ can be written as sum of two light-like vectors a^μ, b^μ, if $a\cdot k \neq 0$, where a^μ is arbitrarily chosen:

$$k^\mu = \alpha a^\mu + b^\mu \qquad \text{with} \quad \alpha = \frac{k^2}{2a\cdot k}, \qquad b^\mu = k^\mu - \alpha a^\mu . \quad (2.17)$$

By the help of Eq. 2.16, a^μ can be reformulated as spinor product. The resulting spinors then define another possible decomposition of $K_{\dot{A}B}$ into spinor products, if $K_{\dot{C}D}a^{\dot{C}}a^D \neq 0$:

$$K_{\dot{A}B} = \alpha a_{\dot{A}} a_B + b_{\dot{A}} b_{\dot{B}} \qquad \text{with} \qquad b_A = -\frac{K_{\dot{B}A} a^{\dot{B}}}{\sqrt{K_{\dot{C}D} a^{\dot{C}} a^D}}\,, \qquad \alpha = \frac{k^2}{K_{\dot{C}D} a^{\dot{C}} a^D}\,. \quad (2.18)$$

2.1.3 From group theory to particle properties - the definition of spin in relativistic theories

In the previous sections, the Poincaré group and its subgroup, the Lorentz group, are introduced describing two fundamental symmetries of the universe. Each physical theory must be invariant under their transformations. States of particles are transformed by them. But since there are particle properties that do not change under Poincaré transformations, like the rest mass, associated particle states should only mix among themselves. This is naturally given by the basis of irreducible group representations. Hence, one-particle state vectors in a Hilbert space can be interpreted as the basis of irreducible (unitary[3]) representations of the Poincaré group [25]. They (and with that the states) can be characterized by the eigenvalues of the associated two Casimir operators. The first one is $P^2 = P_\mu P^\mu$. Its eigenvalue when acting on one-particle states is called m^2 where m can be identified as the rest mass of a particle. The second Casimir operator is $W^\mu W_\mu$ where W_μ is the Pauli-Lubanski operator:

$$W^\mu = -\frac{1}{2}\epsilon^{\mu\nu\rho\sigma} M_{\nu\rho} P_\sigma\,. \quad (2.19)$$

It obeys the following relations:

$$[W^\mu, P^\nu] = 0\,, \quad [W^\mu, M^{\rho\sigma}] = i(g^{\mu\sigma}W^\rho - g^{\mu\rho}W^\sigma)\,, \quad [W^\mu, W^\nu] = i\epsilon^{\mu\nu\rho\sigma} W_\rho P_\sigma\,, \quad W_\mu P^\mu = 0\,. \quad (2.20)$$

$\epsilon_{\mu\nu\rho\sigma}$ is the relativistic extension of the three-dimensional Levi-Civitâ symbol i.e. it is a four-dimensional, totally anti-symmetric tensor with $\epsilon_{0123} = 1$, being antisymmetric versus the exchange of two indices. In order to find the physical interpretation of W^μ, it is convenient to go to the particle's rest frame, if $m > 0$ [4]. Then W^μ becomes $W^\mu = -\frac{1}{2}\epsilon^{\mu\nu\rho 0} M_{\nu\rho} m$ when acting on rest-frame states $|\tilde{p}^\mu, m\rangle$ with four-momentum $\tilde{p}^\mu = (m, 0, 0, 0)$. Thus, $W_0 = 0$ and

$$W^i = \frac{m}{2}\epsilon^{0ijk} M^{jk} = \frac{m}{2}\epsilon^{ijk} M^{jk}\,. \quad (2.21)$$

[3]Representations of the Poincaré group connected to one-particle state-vectors need to be unitary to ensure Poincaré invariance of the matrix elements [25]. The finite-dimensional Lorentz group representations discussed in the previous section are not unitary and thus can not be used to describe particles, in fact there are no finite irreducible unitary representations of the Poincaré group.

[4]Massless particles need to be treated differently which is not covered by this thesis.

The W^μ,W^μ commutator in Eq. 2.20 then takes the form:

$$[W_i, W_j] = i\epsilon_{ijk}W_k \,. \tag{2.22}$$

From the previous section, it is known, that $\frac{1}{2}\epsilon^{ijk}M^{jk} = J^i$ are the generators of the $SO(3)$- and $SU(2)$ algebra with Eq. 2.22 being its defining commutator relation. Unitary representations of these groups describe spin in non-relativistic quantum mechanics. Thus, in the rest frame of the particle, the Pauli-Lubanski operator can be interpreted as the spin angular momentum operator and all the rotational properties known from non-relativistic quantum mechanical spins can also be applied to relativistic particles at rest. Therefore, the eigenvalues of $W^\mu W_\mu$ have the form $-m^2s(s+1)$ with s being positive integer or half integer. The quantity s defines the spin of massive particles [36]. Since $W^\mu W_\mu$ is a Casimir operator, its eigenvalues and hence s are Lorentz invariant. Furthermore, analogous to the non-relativistic case, massive relativistic particles can obey $(2s+1)$ independent particle states corresponding to $(2s+1)$ polarization degrees of freedom. These states are distinguished by the spin's projection onto an arbitrary axis $s^\mu = (0, \vec{n})$ in the current rest frame of the particle, denoted by s_n. The four-vector s^μ is often called spin vector and $\vec{n}$ is typically chosen along the z-direction of the considered rest frame. The projection values are defined as the eigenvalues of $-\frac{1}{m}s^iW^i$, which can take the values $s_n = -s, -s+1, ..., s$. In contrast to s, s_n is not Lorentz invariant. All in all, states of massive, relativistic particles at rest can thus be characterized by: m, p^μ, s, s_n.

The described characterization of particles and their states is only possible for particles at rest where $W^i = mJ^i$. States of moving particles can be obtained from the states defined in the rest frame by Lorentz transformations but there are infinitely many transition choices: there are infinitely many systems from which an observer would see the particle as moving with momentum $\vec{p}$. They differ by rotations around $\vec{p}$ so they would each report a different spin state for the same particle. Thus, to unambiguously define spin states and operators for moving particles, their momenta in the transformed frame and the Lorentz transformation(s) performed to reach it from the spin-defining rest frame need to be specified. In the literature, the canonical spin, the light-cone spin and the helicity definition are frequently used [36, 37]. The polarization of VBs is usually measured in the helicity basis. The helicity λ, with $\lambda \in -s, ..., s$, denotes the projection of the spin $\vec{J}$ onto the direction of the particle's momentum. Particle states in this basis are eigenvectors of the helicity operator:

$$\frac{\vec{J}\cdot\vec{p}}{|\vec{p}|}\,|\vec{p}, m, s, \lambda\rangle = \lambda\,|\vec{p}, m, s, \lambda\rangle \,. \tag{2.23}$$

They can be obtained from the particle states defined in the rest frame $|\tilde{p}^\mu, m, s, s_z = \lambda\rangle$ with λ being the z-component of the spin by first boosting it in z-direction yielding
$|p'^\mu, m, s, s_z = \lambda\rangle = U(L(p'))\,|\tilde{p}^\mu, m, s, \lambda\rangle$ with $p'^\mu = (E, 0, 0, p) = L^\mu{}_\nu(p)\tilde{p}^\nu$. $U(L(p'))$ is the

unitary IR of the Poincaré group on the vector space of one-particle states. A subsequent rotation brings the three-momentum in the desired $\vec{p}$ direction[5]:

$$|p^\mu, m, s, \lambda\rangle = U(R_{pp'})\,|p'^\mu, m, s, \lambda\rangle = U(R_{pp'})U(L(p'))\,|\tilde{p}^\mu, m, s, \lambda\rangle\,. \tag{2.24}$$

The connection between irreducible (unitary) representations and particle properties briefly discussed here for massive particles in respect of spin was elaborated by E. Wigner [39]. He also explained with group theory arguments why massless particles only have one spin degree of freedom (if parity invariance holds two, like the photon) regardless of their spin. A more detailed discussion about Wigner's classification of one-particle states can be found e.g. in Ref. [26, 32, 39, 40].

2.2 Quantum field theory of massive spin-1 particles

At the end of the previous section, some properties of massive one-particle states are discussed to introduce spin as a particle property. However, in contrast to non-relativistic quantum mechanics it is not possible to construct a consistent relativistic theory in terms of single particles inter alia due to causality and the existence of particle creation/annihilation. Instead, theories of elementary particles are field theories. In this section, the theory of free massive spin-1 fields, also called massive VBs, is discussed in order to introduce the description of VB polarization in QFTs. The only massive elementary particles with spin-1 currently known are the $W^\pm$- and Z-bosons which appear as mediators for the weak interaction. At large energies, the weak and the electromagnetic interaction unify and are described as one non-abelian gauge theory with the gauge group $SU(2)_L \otimes U(1)_Y$. This theory is introduced in the second part of this section. Both parts of this section are founded on Ref. [26, 27, 41–43]. The discussion also covers Feynman rules which can be derived from Lagrangians and form the basic building blocks for matrix element calculation. Matrix elements are a major part of the cross section of a process, which in turn is a measure of the probability that the particular process will occur (for more details see Sec. 3.1).

[5] An equivalent sequence of transformations leading to the same particle states in the helicity basis would be to first rotate the state such that the spin quantization axis points in the $\vec{p}$ direction, and then to boost the state along the $\vec{p}$ direction such that the previously stationary particle moves with momentum $\vec{p}$.

2.2.1 Massive spin-1 fields

Free real fields for massive spin-1 particles V^μ [6] are described by the Lagrangian density[7]:

$$\mathcal{L} = -\frac{1}{4}F^{\mu\nu}F_{\mu\nu} + \frac{1}{2}m^2 V^\mu V_\mu\,, \quad \text{with field-strength tensor } F^{\mu\nu} = \partial^\mu V^\nu - \partial^\nu V^\mu\,. \tag{2.25}$$

The associated equation of motion, which can be derived from Eq. 2.25 by the Euler-Lagrange equations, is the Proca equation:

$$(\Box + m^2)V^\mu - \partial^\mu(\partial_\nu V^\nu) = 0\,. \tag{2.26}$$

Taking the divergence of the Proca equation gives the Lorenz condition:

$$\partial_\mu V^\mu = 0\,, \tag{2.27}$$

which also simplifies Eq. 2.26. It reduces the theory's degrees of freedom by one so that massive spin-1 particles with three degrees of freedom can be described by the four-component field V^μ without imposing any additional gauge conditions. The simplified Proca equation:

$$(\Box + m^2)V^\mu = 0\,, \tag{2.28}$$

is essentially a vectorial Klein-Gordon equation (KGE). Identically to the latter, Eq. 2.28 can be solved by expanding V^μ in a complete set of plane waves:

$$V^\mu(x) = \int \frac{d^3\vec{p}}{(2\pi)^2 2E_{\vec{p}}} \sum_{\lambda=1}^{3} [\varepsilon^\mu_\lambda(p)a(p,\lambda)e^{-ip\cdot x} + \varepsilon^{*\mu}_\lambda(p)a^\dagger(p,\lambda)e^{ip\cdot x}]\,, \tag{2.29}$$

with energy of the VB $E_{\vec{p}} = \sqrt{\vec{p}^{\,2} + m^2}$, creation $a(\vec{p},\lambda)$ and annihilation $a^\dagger(\vec{p},\lambda)$ operators. Unlike the KGE solution, additional four-vectors $\varepsilon^\mu_\lambda(p)$ with $\lambda = 0, \pm1$ must be introduced, called polarization vectors, to account for the spin degrees of freedom of a massive spin-1 field. These four-vectors describe the polarization of VBs. They form a complete set of orthonormal four-vectors normalized according to:

$$\varepsilon^\mu_\lambda(p)\varepsilon^*_{\mu,\lambda'}(p) = -\delta_{\lambda\lambda'} \tag{2.30}$$

[6] All fields in the rest of this chapter have an argument x which is omitted for simplicity.
[7] For simplicity only the case of a neutral VB is shown explicitly here, massive charged spin-1 particles can be described by either introducing two real fields $V^{(1)\mu}$, $V^{(2)\mu}$ or by defining two complex fields $W^{\mu\pm} = (V^{(1)\mu} \mp iV^{(2)\mu})$, the corresponding Lagrangian for the complex fields then has the form $\mathcal{L}_{\text{charged}} = -\frac{1}{2}W^+_{\mu\nu}W^{-\mu\nu} + m^2_W W^+_\mu W^{-\mu}$.

and the Lorenz condition Eq. 2.27 leads to:

$$p^\mu \varepsilon_{\mu,\lambda}(p) = 0\,. \tag{2.31}$$

Following the approach used in the previous section to derive one-particle states for a particle with momentum p^μ in the helicity basis, polarization vectors first need to be determined in the VB's rest frame. There, they are eigenstates of the angular momentum operator J_3 in spin-1 representation $(J_3)_{jk} = -i\epsilon_{3jk}$, $(J_3)_{0\rho} = (J_3)_{\rho 0} = 0$ with eigenvalues λ. One possible choice of eigenstates, normalized according to Eq. 2.30, is:

$$\varepsilon^\mu_+ = \frac{1}{\sqrt{2}}(0,-1,-i,0)\,, \qquad \varepsilon^\mu_- = \frac{1}{\sqrt{2}}(0,-1,i,0)\,, \qquad \varepsilon^\mu_0 = (0,0,0,1)\,, \tag{2.32}$$

where ε_+ and ε_- are circular polarization states. After boosting along the z-direction such that $p'^\mu = (E_{\vec{p}}, 0, 0, |\vec{p}|)$ and subsequent rotation R with $\hat{\vec{p}} = \vec{p}/|\vec{p}| = R\hat{\vec{z}} = (\cos\phi\sin\theta, \sin\phi\sin\theta, \cos\theta)$, polarization vectors in the helicity basis are obtained (for details cf. Ref. [43]):

$$\begin{aligned}
\varepsilon^\mu_\pm(p) &= \frac{e^{\pm i\phi}}{\sqrt{2}}(0. - \cos\theta\cos\phi \pm i\sin\phi, -\cos\theta\sin\phi \mp i\cos\phi, \sin\theta)\,,\\
\varepsilon^\mu_0(p) &= \frac{p^0}{m}\Big(\frac{|\vec{p}|}{p^0}, \cos\phi\sin\theta, \sin\phi\sin\theta, \cos\theta\Big)\,.
\end{aligned} \tag{2.33}$$

Vector bosons with helicity + or - are called transverse polarized or right-handed (plus) and left-handed (minus), respectively, those with helicity 0 are called longitudinal polarized.
The polarization vectors fulfill the completeness relation:

$$\sum_{\lambda=1}^{3} \varepsilon^\mu_\lambda(p)\varepsilon^{*\nu}_\lambda(p) = -g^{\mu\nu} + \frac{p^\mu p^\nu}{m^2}\,, \tag{2.34}$$

as can be shown by using their explicit representation in the helicity basis Eq. 2.33. From the Proca equation with an additional classical source j_c added:

$$j^\mu_c(x) = [g^{\mu\nu}(\Box + m^2) - \partial^\mu\partial^\nu]V_\nu(x) \equiv K^{\mu\nu}(x)V_\nu(x)\,, \tag{2.35}$$

the (Feynman-)propagator $\Delta_F(x-y)$ for massive spin-1 particles can be derived. It is directly connected to the Green function $G_{\nu\kappa}(x-y)$ of the kernel $K^{\mu\nu}(x)$ [26]:

$$\Delta_F(x-y) \equiv iG_{\nu\kappa}(x-y) = i\int \frac{d^4p}{(2\pi)^4} e^{ip(x-y)} \frac{(-g_{\nu\kappa} + \frac{p_\nu p_\kappa}{m^2})}{p^2 - m^2 + i\epsilon}\,, \tag{2.36}$$

from which the propagator in momentum space can be read of:

$$\frac{i(-g_{\mu\nu} + \frac{p_\mu p_\nu}{m^2})}{p^2 - m^2 + i\epsilon}\,. \tag{2.37}$$

This will be the Feynman rule for internal lines of massive spin-1 particles in the electroweak theory (in unitary gauge). The polarization vectors then appear in the Feynman rule for external lines:

 $\varepsilon_\lambda(\vec{p})$  $\varepsilon^*_\lambda(\vec{p})$.

2.2.2 Electroweak theory

The electroweak interaction can be formulated as a non-abelian gauge theory with the gauge group $SU(2)_L \otimes U(1)_Y$ which was first done by S.L. Glashow [44] in 1961 for the lepton sector. In the previous section, only bosonic elementary particles with spin-1 are discussed which are described by polarization vectors. Matter in the universe, however, is composed of spin-1/2 fermions, which are expressed by Dirac spinors satisfying the Dirac equation. $SU(2)_L \otimes U(1)_Y$ gauge transformations operate differently on the left(L)- and right(R)-handed components of Dirac fermion field spinors $\psi = \psi_L + \psi_R$:

$$\Psi_L \to e^{i\alpha_a(x)T^a} e^{i\beta(x)Y} \Psi_L\,, \qquad \psi_R \to \mathbb{1} \cdot e^{i\beta(x)Y} \psi_R\,. \tag{2.38}$$

$\alpha_a(x)$ and $\beta(x)$ denote the space-time dependent gauge parameters. The weak hypercharge Y and $T^a = \frac{1}{2}\sigma^a$ are the generators of the $U(1)_Y$ and $SU(2)_L$ group, respectively. The weak hypercharge Y is $-\frac{1}{2}$ for left-handed leptons, -1 for right-handed charged leptons, 0 for right-handed neutrinos, $\frac{1}{6}$ for left-handed quarks, $\frac{2}{3}$ for up-type and $-\frac{1}{3}$ for down-type, right-handed quarks. Left-handed fermions $\psi_L = \frac{1}{2}(1-\gamma_5)\psi(x)$ appear as $SU(2)_L$ doublets Ψ_L while right-handed fermion spinors $\psi_R = \frac{1}{2}(1+\gamma_5)\psi(x)$ form singlets under the $SU(2)_L$ transformations. The matrix γ^5 is defined as:

$$\gamma^5 = i\gamma^0\gamma^1\gamma^2\gamma^3 = \begin{pmatrix} 0 & \mathbb{1}_{(2\times 2)} \\ \mathbb{1}_{(2\times 2)} & 0 \end{pmatrix}\,, \quad \gamma^0 = \begin{pmatrix} \mathbb{1}_{(2\times 2)} & 0 \\ 0 & -\mathbb{1}_{(2\times 2)} \end{pmatrix}\,, \quad \gamma^i = \begin{pmatrix} 0 & \sigma_i \\ \sigma_i & 0 \end{pmatrix}\,. \tag{2.39}$$

The fermion Lagrangian density is:

$$\mathcal{L}_{\text{fermion}} = \sum_f \bar{\Psi}_{f,L} i\gamma^\mu D_\mu \Psi_{f,L} + \bar{\psi}_{f,R} i\gamma^\mu D_\mu \psi_{f,R}\,, \tag{2.40}$$

with the adjoint spinor $\bar{\psi} = \psi^\dagger\gamma^0$. The sum runs over all fermions f. Since the free fermion Lagrangian with $D_\mu = \partial_\mu$ would not be invariant under the gauge transformations in Eq. 2.38, four gauge fields, three W^a_μ (a=1,2,3), generated by the $SU(2)_L$ and one, B^μ, by the $U(1)_Y$, are introduced by minimal coupling with the associated couplings g_W and g_Y:

$$D_\mu \Psi_{f,L} = \Big[\partial_\mu + ig_W T^a W^a_\mu + ig_Y Y B_\mu\Big]\Psi_{f,L}\,, \qquad D_\mu \psi_{f,R} = \Big[\partial_\mu + ig_Y Y B_\mu\Big]\psi_{f,R}\,. \tag{2.41}$$

The couplings g_W and g_Y are free parameters of the theory and need to be determined by experiments. In order to retain local gauge invariance, the gauge fields for small $\alpha^a(x)$, $\beta(x)$ have to satisfy the following infinitesimal transformation rules :

$$W_\mu^a \to W_\mu^a - \frac{1}{g_W}\partial_\mu \alpha^a(x) - \epsilon^{abc}\alpha^b(x)W_\mu^c\,, \qquad B_\mu \to B_\mu - \frac{1}{g_Y}\partial_\mu \beta(x)\,, \tag{2.42}$$

where ϵ^{abc} are the $SU(2)_L$ group structure constants.
Thus, the Lagrangian density $\mathcal{L}$ describes free fermions and their interaction with the electroweak gauge fields (Fig. 2.1 for charged leptons) [8]. The emergence of the latter also requires

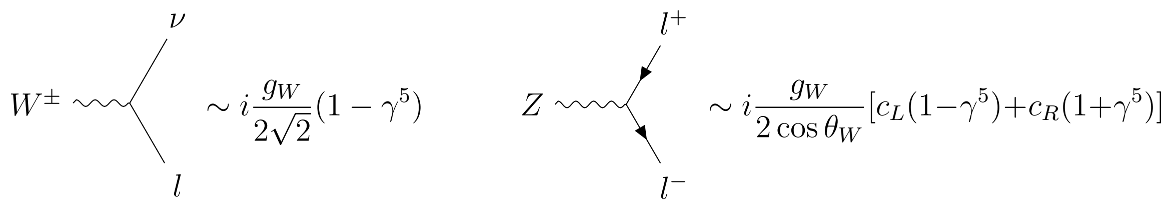

Figure 2.1: Vertices of lepton interactions with massive gauge bosons; coefficients are $c_L = I^W_{3,l^-} - Q_{l^-}\sin^2\theta_W = -\frac{1}{2} + \sin^2\theta_W$ and $c_R = -Q_{l^-}\sin^2\theta_W = \sin^2\theta_W$

the introduction of terms which describe the dynamics of the gauge fields if no fermions are present:

$$\mathcal{L}_{\text{gauge}} = -\frac{1}{4}W^a_{\mu\nu}W^{a\mu\nu} - \frac{1}{4}B_{\mu\nu}B^{\mu\nu}\,, \tag{2.43}$$

containing the field strength tensors:

$$B_{\mu\nu} = \partial_\mu B_\nu - \partial_v B_\mu\,, \qquad W^a_{\mu\nu} = \partial_\mu W^a_\nu - \partial_\nu W^a_\mu + g_W\epsilon^{abc}W_{b,\mu}W_{c,\nu}\,. \tag{2.44}$$

Compared to the field strength tensor in the free field theory (Eq. 2.25), $W^a_{\mu\nu}$ has an additional term which leads to cubic and quartic gauge-field self-interaction terms in Eq. 2.43. It emerges to preserve the invariance of the Lagrangian in Eq. 2.43 under the transformations in Eq. 2.42 and is a consequence of the non-abelian structure of the gauge-group $SU(2)_L$.
So far, the Lagrangian $\mathcal{L} = \mathcal{L}_{\text{fermion}} + \mathcal{L}_{\text{gauge}}$ does not contain mass terms although experimental evince for massive fermions and VBs clearly exists. Introducing mass terms for massive VBs $\frac{1}{2}m_W^2 W^a_\mu W^{a\mu} + \frac{1}{2}m_B^2 B_\mu B^\mu$ and massive fermions $m_f\psi\bar{\psi}$ would violate $SU(2)_L \otimes U(1)_Y$ gauge invariance which can be seen by applying the transformations of Eq. 2.42 onto the new mass terms. This problem was solved by A. Salam and S. Weinberg [45, 46]. They used the Brout-Englert-Higgs mechanism, proposed in 1964 independently by several parties [47–49], to generate gauge invariant mass terms. In order to achieve this, two complex scalar fields are

[8]Fields $W^{\pm\mu}$, Z^μ in Fig. 2.1 are not the gauge fields W^μ_a, B^μ, they mix to build the physical fields $W^{\pm\mu}$, Z^μ, γ which are given later in Eq. 2.50.

introduced that together form a $SU(2)_L$-doublet with $U(1)_Y$ hypercharge $Y = \frac{1}{2}$:

$$\Phi = \begin{pmatrix} \phi^+ \\ \phi^0 \end{pmatrix} = \frac{1}{\sqrt{2}} \begin{pmatrix} \phi_1 + i\phi_2 \\ \phi_3 + i\phi_4 \end{pmatrix} . \tag{2.45}$$

One component of the doublet must be charged, one neutral to generate longitudinal degrees of freedom for the $\mathrm{W}^{\pm}$ as well as the Z boson. The corresponding Lagrangian is:

$$\mathcal{L}_{\text{scalar}} = (D^\mu\Phi)^\dagger(D_\mu\Phi) - V(\Phi) = (D^\mu\Phi)^\dagger(D_\mu\Phi) - \mu^2\Phi^\dagger\Phi - \lambda(\Phi^\dagger\Phi)^2 , \tag{2.46}$$

with parameters μ and λ not predicted by the theory. For $\mu^2 < 0$ and $\lambda > 0$, the gauge-invariant potential $V(\phi)$ has an infinite set of degenerate non-vanishing minima, thus the vacuum ground state is non-symmetric. Since the Lagrangian remains fully $SU(2)_L \otimes U(1)_Y$ gauge invariant the electroweak gauge symmetry is spontaneously broken by choosing a certain ground state. Without loss of generality, the following ground state can be chosen [26]:

$$\Phi_0 = \begin{pmatrix} 0 \\ \frac{v}{\sqrt{2}} \end{pmatrix} \qquad \text{with vacuum expectation value} \quad v = \sqrt{\frac{-\mu^2}{\lambda}} = 246\,\text{GeV} . \tag{2.47}$$

The upper doublet component is zero to ensure that the electromagnetic gauge group $U(1)_{\text{QED}}$ remains unbroken. Otherwise, also the photon would acquire a mass. In order to investigate the consequences of the EWSB, the doublet Φ is expanded around the potential minimum $\Phi = \Phi_0 + \tilde{\Phi}$ with $\phi_3 = v + \tilde{\phi}_3$, $\phi_{1,2,4} = \tilde{\phi}_{1,2,4}$. The goal of the EWSB mechanism is to generate masses of the massive VBs. This would introduce new degrees of freedom into the theory in addition to the already existing four of the scalar fields ϕ_i. These are the longitudinal modes of the massive VBs, which were not apparent before the symmetry breaking. Within the unitary gauge, the three massless would-be Nambu-Goldstone bosons $\phi_{1,2,4}$ are eliminated, i.e. the Goldstone bosons are replaced by the longitudinal polarization mode of the gauge fields becoming massive. The Goldstone bosons are therefore unphysical so that the number of physical degrees of freedom is restored. In other gauges, e.g. 't Hooft-Feynman gauge, they remain in the theory and are then called ghosts. Applying the unitary gauge, corresponds to assuming:

$$\Phi = \begin{pmatrix} 0 \\ \frac{v}{\sqrt{2}} + h(x) \end{pmatrix} = \Phi_0 + \tilde{\Phi} \tag{2.48}$$

for the Higgs doublet expanded around the minimum if all other fields are already expressed in the unitary gauge. Its insertion into Eq. 2.46 leads to the findings discussed below.

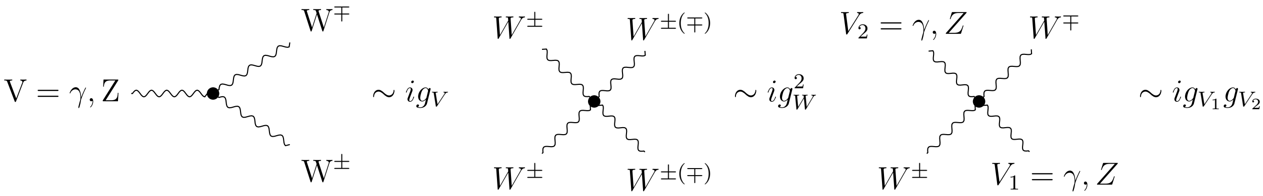

Figure 2.2: Triple (left) and quartic (middle, right) self interactions of electroweak gauge bosons with $g_\gamma = e$, $g_Z = g_W \cos\theta_W$.

Vector boson masses and physical fields

After inserting the expanded fields into the kinetic terms of Eq. 2.46, the term only depending on Φ_0 reads:

$$(D_\mu\Phi_0)^\dagger(D^\mu\Phi_0) = \frac{1}{2}W^a_\mu W^{a\mu}\big(\frac{g_W^2 v^2}{4}\big) + W^3_\mu B^\mu\big(\frac{-g_W g_Y v^2}{4}\big) + B_\mu B^\mu\big(\frac{g_Y^2 v^2}{8}\big)\,. \tag{2.49}$$

The gauge fields W^a_μ and B_μ that appear in the Lagrangian are not the physical fields. In order to obtain the experimentally confirmed electroweak currents, the physical photon, Z- and W$^\pm$-boson fields A^μ, Z^μ and $W^\pm_\mu$ depend on the gauge fields in $\mathcal{L}$ as follows:

$$W^\pm_\mu = \frac{W^1_\mu \mp iW^2_\mu}{\sqrt{2}}\,, \qquad Z_\mu = -\sin\theta_W B_\mu + \cos\theta_W W^3_\mu\,, \qquad A_\mu = \cos\theta_W B_\mu + \sin\theta_W W^3_\mu\,. \tag{2.50}$$

With that, the masses of the bosons can be read off Eq. 2.49:

$$m_W = \frac{g_W v}{2}\,, \qquad m_A = 0\,, \qquad m_Z = \frac{1}{2}v\sqrt{g_W^2 + g_Y^2} = \frac{1}{2}v g_Z = \frac{1}{2}\frac{g_W}{\cos\theta_W}v\,. \tag{2.51}$$

θ_W denotes the weak mixing angle defined by tan $\theta_W = \frac{g_Y}{g_W}$. Thus, the mechanism of EWSB indeed generates mass terms for the massive VBs by simultaneously leaving the photon mass unchanged. The strength of the electric charge e is connected to the gauge couplings g_W, g_Y via $g_W \sin\theta_W = g_Y \cos\theta_W = e$. The generators of the unbroken $U(1)_{\mathrm{QED}}$ gauge group, giving the electric charges, then take the form $Q = I_3^W + Y$, with I_3^W being the third component of the weak isospin.

After defining the physical fields and generating mass terms, the Lagrangian of the gauge fields reads:

$$\mathcal{L}^{\mathrm{EWSB}}_{\mathrm{gauge}} = \mathcal{L}_{\mathrm{B}} + \mathcal{L}_{\mathrm{BB}} = -\frac{1}{4}F_{\mu\nu}F^{\mu\nu} - \frac{1}{2}W^+_{\mu\nu}W^{-\mu\nu} + m_W^2 W^+_\mu W^{-\mu} - \frac{1}{4}Z_{\mu\nu}Z^{\mu\nu} + \frac{1}{2}m_Z^2 Z_\mu Z^\mu + \mathcal{L}_{\mathrm{BB}}\,. \tag{2.52}$$

The field strength tensors $F^{\mu\nu}$, $Z^{\mu\nu}$ and $W^{\pm\mu\nu}$ of photon, Z and W$^{\pm}$ boson respectively in the free boson Lagrangian $\mathcal{L}_{\mathrm{B}}$ have the same form as $F^{\mu\nu}$ in Eq. 2.25, i.e. the free Lagrangian for massive spin-1 particles in Eq. 2.25 is retained. The propagator derived there also follows from the EW theory but its form in Eq. 2.37 is only received in the unitary gauge. The additional term in the field strength tensor of the gauge fields $W^a_{\mu\nu}$ in Eq. 2.44 leads to triple (Fig. 2.2 (a)) and quartic (Fig. 2.2 (b),(c)) self-interactions of the gauge bosons ($\mathcal{L}_{BB}$) after converting corresponding terms in the Lagrangian in Eq. 2.43 to the physical fields.

Higgs boson

The scalar potential and the remaining kinetic terms take the form:

$$\begin{aligned}\mathcal{L}_{\mathrm{BHiggs}} + \mathcal{L}_{\mathrm{Higgs}} &= [(D_\mu\tilde{\Phi})^\dagger(D^\mu\Phi_0) + h.c.] + (D_\mu\tilde{\Phi})^\dagger(D^\mu\tilde{\Phi}) + V(\Phi) \\ &= \underbrace{m_W^2(2\frac{h}{v} + \frac{h^2}{v^2})W_\mu^+W^{\mu-} + \frac{1}{2}m_Z^2(2\frac{h}{v} + \frac{h^2}{v^2})Z_\mu Z^\mu}_{\text{W,Z-Higgs interactions } \mathcal{L}_{\mathrm{BHiggs}}} + \underbrace{\frac{1}{2}(\partial_\mu h)^2 - \lambda v^2 h^2}_{\text{free Higgs-Lagrangian}} - \underbrace{\frac{\lambda}{4}(h^4 + 4vh^3)}_{\text{Higgs-self interaction}}\ .\end{aligned} \tag{2.53}$$

A new massive boson with mass $m_H = \sqrt{2\lambda}v$ arises which can be identified with the physical Higgs boson. Beside the Higgs-Lagrangian, the terms in Eq. 2.53 give rise to Higgs-self couplings and interactions of Higgs bosons with massive gauge bosons. The latter are shown in Fig. 2.3.

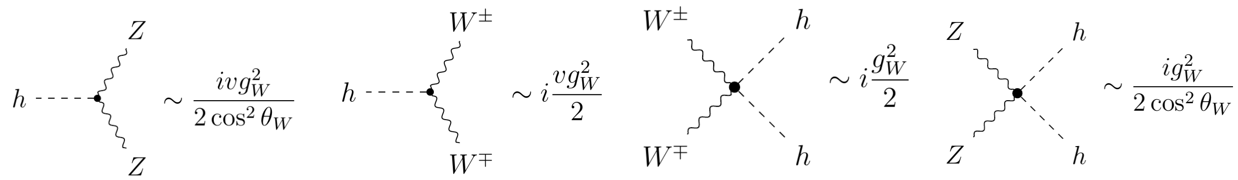

Figure 2.3: Higgs boson interactions with massive gauge bosons.

Fermion masses

Additionally, with the help of the Higgs doublet, it is possible to construct operators that combine left-handed and right-handed spinors while preserving the $SU(2)_L \otimes U(1)_Y$ gauge symmetry. They can be utilized to form gauge-invariant fermion mass terms in the Lagrangian:

$$\mathcal{L}_{\mathrm{Yukawa}} = -y_1^f \bar{\Psi}_L^f \Phi \psi_R^f - y_2^f \bar{\Psi}_L^f \Phi_c \psi_R^f + h.c.\,. \tag{2.54}$$

Since only the lower component of the Higgs doublet has a non-zero vacuum expectation value, the first term in $\mathcal{L}_{\mathrm{Yukawa}}$ can only generate masses for the fermions in the lower component of a $SU(2)_L$ doublet. This includes charged leptons and down-type quarks. In order to account for masses of up-type quarks, the second term in Eq. 2.54 including the conjugate doublet

$\Phi_c = i\sigma_2\Phi^*$ is added to the Lagrangian. Neutrino masses are not part of the SM. y_1^f and y_2^f are the Yukawa couplings whose values are not predicted by the SM. Inserting the expanded scalar field of Eq. 2.48 in Eq. 2.54 will give the fermion masses:

$$m_f = v\frac{y_{1,2}^f}{\sqrt{2}} \tag{2.55}$$

through coupling of the fermions to the Higgs-field. Furthermore, the coupling of the fermions to the Higgs boson itself is obtained.

In summary, the Lagrangian of the electroweak theory after EWSB in unitary gauge is:

$$\mathcal{L}_{\mathrm{EW}} = \mathcal{L}_{\mathrm{gauge}}^{\mathrm{EWSB}} + \mathcal{L}_{\mathrm{fermion}} + \mathcal{L}_{\mathrm{Higgs}} + \mathcal{L}_{\mathrm{BHiggs}} + \mathcal{L}_{\mathrm{Yukawa}}. \tag{2.56}$$

with $\mathcal{L}_{\mathrm{gauge}}^{\mathrm{EWSB}}$, $\mathcal{L}_{\mathrm{fermion}}$, $\mathcal{L}_{\mathrm{Higgs}}$, $\mathcal{L}_{\mathrm{BHiggs}}$ and $\mathcal{L}_{\mathrm{Yukawa}}$ being introduced in Eq.s 2.52, 2.40, 2.53, 2.53 and 2.54, respectively.

3 Simulation of vector boson production

Experiments at particle collider facilities are an important handle to explore the SM and its limits at high energies. The most powerful current collider is the LHC. It collides protons as they are easier to accelerate to sufficiently high energies than lighter particles, such as electrons, due to lower bremsstrahlung losses in circular facilities. However, making theoretical predictions of the collisions is very challenging because of the non-abelian nature of Quantum Chromodynamics (QCD) leading to color confinement at long distances and the high-dimensional phase space covered by the LHC. In most cases, these aspects can no longer be handled by analytical calculations, but MC event generators are able to deal with these problems to a good approximation. Some popular general-purpose event generators are PYTHIA8 [50], HERWIG [51, 52] and SHERPA [24]. These tools can also be used to make predictions for VB production processes. This thesis focuses on SHERPA. In the first part of this chapter, some basic concepts of MC simulations relevant for this work are discussed. The discussion is based on Ref. [53–57] where future details of this wide field can be found. After that, the VB production processes investigated in this thesis are introduced. For this work, the polarization of the VBs in these processes is of particular interest. Since they only appear as intermediate particles in measurable processes, the definition of their polarization poses some difficulties, which are discussed in the last part of this section, based on Ref. [58, 59].

3.1 Simulation of hadronic collisions

Processes that occur in proton-proton (pp) collisions are usually very complex such that analytical calculations are unfeasible in the most cases, and simulations of collisions based on MC methods are used to provide predictions for such processes. The main part of pp collisions is described by QCD, the theory of strong interactions. It behaves different on various energy scales which allows to factorize the simulation of particle collisions into several phases operating in distinct energy ranges. All typical steps of a MC event generation are illustrated in Fig. 3.1 where two protons coming from left and right, collide and initially produce a Higgs boson and two top quarks which subsequently decay. This is an example of the inner core of the event simulation, the hard process (or hard-interaction), which occurs at the highest energies of the entire event and represents the process of interest. Since such processes are usually very rare, the simulation of collision events starts by computing this process instead of generating typical

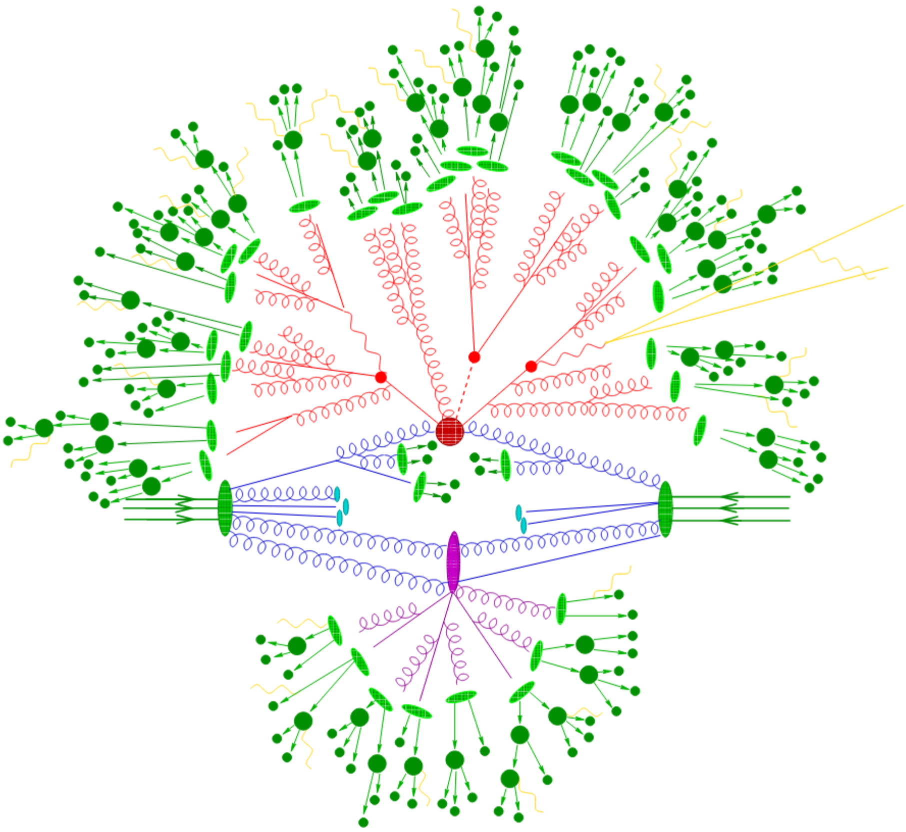

Figure 3.1: Illustration of the different steps in a Monte-Carlo event generator exemplary for the production of a Higgs boson associated with two top quarks; the parts of the event generation are the hard interaction (big red circle) followed by the decay of the top quarks and the Higgs boson (small red circles), the initial (blue) and final state (red) parton shower, the hadronisation (light green ellipses), the hadron decays (dark green circles), photon radiation (yellow) and secondary interactions (underlying event, purple); figure taken from Ref. [60].

pp collision events. Due to the high energies of the hard process, the strong coupling constant α_S is small and thus, perturbation theory can be used to describe it. This step determines the cross section of an event sample since contributions from other phases integrate to one[1]. The calculation of polarized cross sections, the purpose of this thesis, corresponds to this event generation phase which is why it is treated in more detail in the subsequent section. If only fixed-order calculations are performed as in most cases in this thesis, the event generation stops at this step. However, this does not lead to an experimentally realistic event.
At the energy scales of the hard-scattering, the partons (quarks, gluons), that build up the colliding protons, are basically free. Before some of them collide to perform the hard process, they can irradiate gluons which themselves can generate further ones or quark-antiquark pairs leading to the so called initial state parton shower. Furthermore, many hard interactions of interest result in QCD partons in the final state which also build a parton shower (PS)

[1]This is not fully true if selection requirements on the final state after the full event simulation are applied.

after the hard scattering. In order to describe these showers, parton shower algorithms are used. They are formulated as the downwards evolution in a momentum-transfer-like variable starting at the scale of the hard process forwards for the outgoing and backwards for the incoming hard-scattered partons [55]. During this evolution, the mean momentum transfer decreases. At energies of about 1 GeV the strong coupling constant is of $\mathcal{O}(1)$ implying that perturbation theory breaks down. Formerly asymptotically free colored partons now become confined in colorless hadrons. This process of hadronization is described by non-perturbative, phenomenological models whose free parameters are tuned by comparing with experimental data. Resulting hadrons are decayed until only longer living or stable particles remain which are able to escape the detector. Usually, charged particles participate in all steps of the MC-simulation, leading to QED radiation. Since the incoming protons are complex bound-states of several partons, more than one pair of partons can interact with each other within one pp collision event. These secondary interactions are called underlying event.

3.1.1 Cross sections of proton-proton collisions and the hard subprocess

The hard subprocess is typically the process with the largest scales involving mostly large momentum transfers or the creation of heavy particles. It is the actual one which shall be analyzed by the collider experiment. To calculate the cross section for a scattering process $pp \to n$ producing a parton-level n-particles final state from the collision of two protons, the factorization ansatz of the QCD is applied. Accordingly, the probability of finding a certain parton with momentum fraction x in a proton is decoupled from the hard interaction $ab \to n$ of the single high-energetic partons a, b:

$$\sigma_{pp\to n} = \sum_{a,b\in\{\mathrm{q,g}\}} \int_0^1 \int_0^1 \mathrm{d}x_a \mathrm{d}x_b f_a^{h_1}(x_a, \mu_F) f_b^{h_2}(x_b, \mu_F) \hat{\sigma}_{a,b\to n}(\mu_F, \mu_R)\,. \tag{3.1}$$

$f_a^{h_1}$ and $f_b^{h_2}$ denote parton distribution functions which at leading order describe the probability to find a parton of type a/b with momentum fraction x_a/x_b (Bjorken variable) in a hadron h_1/h_2 at scale μ_F. They cannot be computed by perturbation theory, and are instead based on measurements that examine the proton content at a given scale. With the help of the DGLAP equations, their evolution to other scales can be determined. The scale μ_F, at which the PDFs are evaluated, is called factorization scale and separates hard emissions described by the partonic cross section and soft emissions below μ_F absorbed in the PDFs.

$\hat{\sigma}_{a,b\to n}(\mu_F, \mu_R)$ is the cross section of the actual hard scattering of two partons a,b resulting in n final state particles. It can be calculated utilizing perturbation theory where the cross section is expanded in the (small) coupling constant of the interaction and can be formulated as the integral of squared matrix elements $|\mathcal{M}_{a\to b}(\Phi_n; \mu_F, \mu_R)|^2$ over the available phase space of the n final state particles Φ_n:

$$\begin{aligned}\hat{\sigma}_{a,b\to n}(\mu_F,\mu_R) &= \int \mathrm{d}\Phi_n \mathcal{F}|\mathcal{M}_{a\to b}(\Phi_n;\mu_F,\mu_R)|^2 \quad \text{with} \\ \mathrm{d}\Phi_n &= \frac{d^3p_i}{(2\pi)^3 2E_i}\cdot(2\pi)^4\delta^{(4)}(p_a+p_b-\sum_{i=1}^{n}p_i)\,.\end{aligned} \tag{3.2}$$

Within the differential phase space element $\mathrm{d}\Phi_n$, the p_i represent the final state particles' and the $p_{a,b}$ are the initial state particles' momenta. For hadronic collisions, $p_{a,b} = x_{a,b}P_{a,b}$ holds with $P_{a,b}$ being the fixed hadron momenta. The delta function implements the overall energy- and momentum conservation. The energy of the incoming partons is taken into account by the flux factor $\mathcal{F}$. For massless partons, $\mathcal{F} = \frac{1}{2\hat{s}} = \frac{1}{2x_a x_b s}$ applies, where $\hat{s}$ and s are the partonic and hadronic center-of-mass energy squared, respectively. μ_R is another unphysical scale, the renormalization scale, which is explained later.
The matrix elements $\mathcal{M}_{a\to b}(\Phi_n;\mu_F,\mu_R)$ can be formulated as a sum over Feynman diagrams. These are pictorial representations of all possible quantum mechanical transition amplitudes contributing to the required process. Using Feynman rules, they can be translated one-to-one into the mathematical term in the perturbative expansion of $\hat{\sigma}_{a,b\to n}(\mu_F,\mu_R)$ they correspond to. The absolute squared matrix elements also include an average over initial state as well as a summation over final state colors and helicities which can be moved outside the square.
Eq. 3.1 is valid for all orders of the perturbative expansion of $\hat{\sigma}_{a,b\to n}(\mu_F,\mu_R)$. In practice, the hard subprocess' cross section $\hat{\sigma}_{a,b\to n}(\mu_F,\mu_R)$ can be calculated accurately for a few orders only. When going beyond leading order (=lowest order in perturbation series) calculations, some complications arise due to the emergence of divergencies. At NLO QCD, the partonic cross section for a $2\to n$ process:

$$\begin{aligned}\hat{\sigma}^{\text{NLO}}_{ab\to n} &= \int \mathrm{d}\Phi_n\Big[\mathcal{B}_n(\Phi_n;\mu_F,\mu_R)+\mathcal{V}_n(\Phi_n;\mu_F,\mu_R)\Big] + \int \mathrm{d}\Phi_{n+1}\mathcal{R}_n(\Phi_{n+1};\mu_F,\mu_R) \\ &= \frac{1}{2\hat{s}_{a,b}}\int \mathrm{d}\Phi_n\Big[|\mathcal{M}_{\text{LO}}(\Phi_n;\mu_F,\mu_R)|^2 + 2\,\mathfrak{Re}\{\mathcal{M}_{\text{LO}}(\Phi_n;\mu_F,\mu_R)\mathcal{M}^*_{\text{NLO,V}}(\Phi_n;\mu_F,\mu_R)\}\Big] \\ &+ \frac{1}{2\hat{s}_{a',b'}}\int \mathrm{d}\Phi_{n+1}|\mathcal{M}_{\text{NLO,R}}(\Phi_{n+1};\mu_F,\mu_R)|^2\end{aligned} \tag{3.3}$$

consists of three parts:

- **Born term** $\mathcal{B}_n$: describing the leading-order contribution;
- **Real correction term** $\mathcal{R}_n$: containing an additional final state emission compared to the leading-order contribution, the corresponding phase space Φ_{n+1} is the phase space of $(n+1)$ final state particles; furthermore, the type of the initial partons a', b' may change with respect to the Born contribution with partons of type a and b which also affects the

PDFs contributing to Eq. 3.1;

- **Virtual correction term** $\mathcal{V}_n$: obtained by multiplying Born-level matrix elements with virtual matrix elements, the latter can be obtained from the former by adding a closed loop; the external particles of both matrix elements are the same, wherefore they have the same phase space.

Fig. 3.2 displays example diagrams for the $W^{\pm}Z$-production process ($\mathcal{O}(\alpha_{EW}^2)$ at LO) each contributing to one of the three matrix elements. Real and virtual terms are by themselves

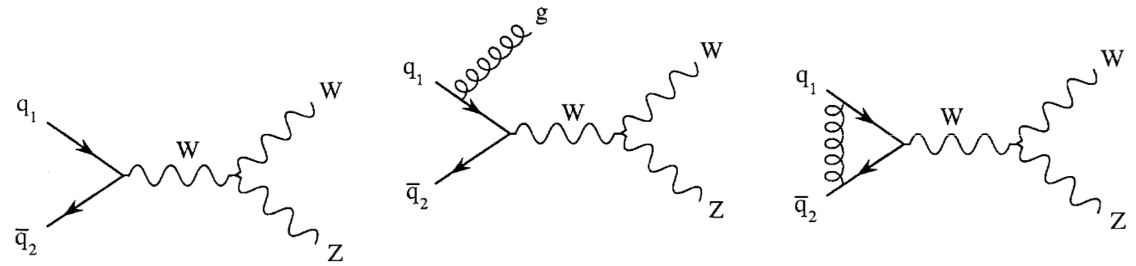

(a) Born diagram **(b)** Real correction diagram **(c)** Virtual correction diagram

Figure 3.2: Example diagrams for the different matrix element types contributing to a NLO QCD calculation of inclusive $W^{\pm}Z$-production (diagrams taken from [61]).

divergent. The loop in $\mathcal{M}_{\mathrm{NLO,V}}(\Phi_n; \mu_F, \mu_R)$ introduces an additional degree of freedom, the loop momentum, that is integrated over. It can take any value allowed by four-momentum conservation at the interaction vertices. In particular, it can get infinitely large resulting in ultraviolet (UV) divergences of the amplitude. They can be handled by first regularizating the UV-divergencies by e.g. dimensional regularization and then absorbing them via the redefinition of all couplings and masses based on the idea that all parameters appearing in the Lagrangian are non-observable, "bare" quantities (=renormalization). This introduces another scale, the renormalization scale μ_R, which separates UV-effects from effects described in the matrix element.

Additionally, IR divergences emerge in real and virtual corrections. According to the Bloch-Nordsieck [62] and Kinoshita-Lee-Naunberg theorems [63, 64], these need to cancel each other for physically meaningful (IR-safe) observables [56]. This cancellation is not straightforward to model since the two terms to cancel correspond to different phase spaces. Methods solving this problem are phase space slicing or subtraction methods. Nowadays, the latter group of methods is more common. Subtraction methods are based on the observation that soft and collinear divergencies in real correction terms have a universal structure which can be described by a convolution $\mathcal{D}_n^{\mathcal{S}} = \mathcal{B}_n \otimes \mathcal{K}_n$ of (finite) Born matrix elements $\mathcal{B}_n$ with suitably defined operators $\mathcal{K}_n$ [55]. The integrand $\mathcal{R}_n - \mathcal{D}_n^{\mathcal{S}}$ is IR-finite which means that the integration over the full real correction phase space Φ_{n+1} becomes feasible. The same holds for the virtual corrections, if the subtraction term $\mathcal{D}_n^{\mathcal{S}}$ integrated over the radiative phase space Φ_1, $\mathcal{I}_n^{\mathcal{S}} = \int \mathrm{d}\Phi_1 \mathcal{D}_n^{\mathcal{S}}$, is added to them. The partonic cross section for a $2 \to n$ process at NLO QCD accuracy then takes the form:

$$\begin{aligned}\hat{\sigma}^{\text{NLO}}_{ab\to n} = &\int \mathrm{d}\Phi_n \Big[\mathcal{B}_n(\Phi_n;\mu_F,\mu_R) + \tilde{\mathcal{V}}_n(\Phi_n;\mu_F,\mu_R) + \mathcal{I}^{\mathcal{S}}_n(\Phi_n;\mu_F,\mu_R)\Big] \\ &+ \int \mathrm{d}\Phi_{n+1}\Big[\mathcal{R}_n(\Phi_{n+1};\mu_F,\mu_R) - \mathcal{D}^{\mathcal{S}}_n(\Phi_n;\mu_F,\mu_R)\Big]\,,\end{aligned} \tag{3.4}$$

where $\tilde{V}_n$ already contains collinear counter terms. The definition of the subtraction kernels $\mathcal{D}^{\mathcal{S}}_n$ is not unambiguous. One very prominent method to define them, which is also employed in SHERPA, was introduced by S. Catani and M.H. Seymour [65, 66].

The calculation of tree-level (Born term, real correction) and one-loop matrix elements is usually done by different tools. Specialized tools e.g. OpenLoops [67] deliver one-loop matrix elements, whereas generic tree-level matrix element generators provide the other matrix elements and perform the phase space integration. There exist many tree-level matrix element generators such as AMEGIC++ [68], COMIX [69], MadGraph [21] or O'Mega [70] from which the former two are used in this thesis. Even the calculation of tree-level matrix elements can be very challenging when multi-particle final states come into play since the number of contributing Feynman diagrams increases roughly factorial with the number of final state particles [55]. Textbooks method of squaring matrix elements and summing over unobserved helicities and colors based on completeness relation and Dirac trace techniques become too complex. Instead, amplitudes are directly evaluated before summing and squaring them. In order to achieve an efficiently calculable representation of them, all parts of the amplitude are expressed in terms of spinor products in the manner introduced for four-vectors in Sec. 2.1.2. For the generation of the amplitudes, Feynman diagram based methods (e.g. in MadGraph, AMEGIC) or recursive techniques such as the Berends-Giele recursion algorithm [71] (e.g. in COMIX) are applied.

After constructing the matrix elements for the process of interest, the related integral over the phase space of the initial and final state particles need to be performed. Phase space integrations rely on dedicated MC sampling methods, e.g. multi-channel sampling. They enable the integration of integrands with difficult structures due to pronounced peaks, which could affect the convergence of the integration over the usually large $(3n-4)+2$ dimensional phase space.

When using matrix elements of NLO QCD accuracy for the cross section of the hard scattering process in the full event simulation, the fixed-order calculation needs to be matched to the parton shower. This is briefly discussed in the following section.

3.1.2 Matching and Merging

Matching In the previous section, the hard process is discussed as the first part of the event generation. If the hard process is generated, the parton shower takes over which is not introduced here (see e.g. Ref. [53–56]). Matching the fixed-order hard matrix elements to the parton shower is only trivial at LO, where the showering can simply begin on top of the hard process. At higher orders, double counting can emerge. To deal with this, basically two approaches are used, the POWHEG [72] and the MC@NLO [73] methods. In this thesis, the latter is applied as already implemented in SHERPA. At this point, some ideas of MC@NLO, that are relevant for later parts of this thesis, are briefly summarized. The MC@NLO method follows the idea of eliminating double counting by subtracting the shower contribution at fixed order from the higher-order hard process calculation [53]. For this, the real correction term is split into two parts $R_n = D_n^{\mathcal{A}} + H_n^{\mathcal{A}}$, an IR-singular $D_n^{\mathcal{A}}$ and an IR-regular (hard) part $H_n^{\mathcal{A}}$. Thus, the total hadronic NLO QCD cross section, obtained from combining Eq.s 3.1 and 3.3, can be rewritten as:

$$\sigma^{\mathrm{NLO}} = \int \mathrm{d}\tilde{\Phi}_n \bar{B}^{\mathcal{A}}(\tilde{\Phi}_n) + \int \mathrm{d}\tilde{\Phi}_{n+1} H^{\mathcal{A}}(\tilde{\Phi}_{n+1}) \,, \tag{3.5}$$

with $\bar{B}^{\mathcal{A}}$ being the NLO-weighted Born-level cross section:

$$\bar{B}^{\mathcal{A}}(\tilde{\Phi}_n) = B_n(\tilde{\Phi}_n) + \tilde{V}_n(\tilde{\Phi}_n) + I_n^{\mathcal{S}}(\tilde{\Phi}_n) + \int \mathrm{d}\tilde{\Phi}_1 \Big[D_n^{\mathcal{A}}(\tilde{\Phi}_{n+1}) - D_n^{\mathcal{S}}(\tilde{\Phi}_{n+1}) \Big] \,. \tag{3.6}$$

The differential phase space element $\mathrm{d}\tilde{\Phi}$ additionally contains the incoming partonic flux and the integrals over the Bjorken variables compared to $\mathrm{d}\Phi$; $B, R, V, I, D^{\mathcal{S}}$ include the PDFs and the summation over the flavors compared to their correspondences in Eq. 3.3. The matched NLO cross section up to the first emission[2] is then given by [57]:

$$\sigma^{\mathrm{NLO}}_{\mathrm{MC@NLO}} = \underbrace{\int \mathrm{d}\tilde{\Phi}_n \bar{B}_n^{\mathcal{A}}(\tilde{\Phi}_n) \Big[\bar{\Delta}^{\mathcal{A}}(t_0) + \int_{t_0} \mathrm{d}\tilde{\Phi}_1 \frac{D_n^{\mathcal{A}}(\tilde{\Phi}_{n+1})}{B_n(\tilde{\Phi}_n)} \bar{\Delta}^{\mathcal{A}}(t) \Big]}_{=:\sigma_{\mathbb{S}}} + \underbrace{\int \mathrm{d}\tilde{\Phi}_{n+1} H_n^{\mathcal{A}}(\tilde{\Phi}_{n+1})}_{=:\sigma_{\mathbb{H}}} \,, \tag{3.7}$$

with a modified Sudakov form factor of $\bar{\Delta}^{\mathcal{A}}(t, t') = \exp\Big\{ - \int_t^{t'} \mathrm{d}\Phi_1 \frac{D_n^{\mathcal{A}}(\tilde{\Phi}_{n+1})}{B_n(\tilde{\Phi}_n)} \Big\}$ and t being the order parameter of the shower emissions. Sudakov form factors describe the non-branching probability between the two scales t and t' in a parton shower.

For event generation, $\sigma_{\mathbb{S}}$ and $\sigma_{\mathbb{H}}$ are identified with two different types of events, named $\mathbb{S}$- and $\mathbb{H}$-events. The latter has real kinematics. The parton shower is added after the first emission is produced according to the (hard process) matrix elements. The hard process matrix element in the $\mathbb{S}$-event, on the other hand, has Born-like kinematics. The first emission is generated, if occurs at all, by the parton shower as represented by the term in square brackets in Eq. 3.7.

Merging Parton showers can account for higher-order effects but fail to describe additional hard emissions [54]. In order to provide a more accurate prediction for processes with multiple

[2]First emission means the first emission additionally to the LO hard process.

jets in the final state, separate tree-level matrix elements are calculated for each desired parton multiplicity. The combination of all these separate calculations with the parton shower is done by merging algorithms. These rely on an additional merging scale, above which every QCD-emission up to a chosen maximum parton multiplicity is described by the appropriate tree-level matrix elements. Parton emissions softer than the merging scale are instead produced by the parton shower. The first merging algorithm proposed was the CKKW approach [74], which was adapted and extended several times since then, as done for the merging algorithm implemented in SHERPA [75]. Merging algorithms can be extended to also merge NLO calculations to parton showers. This is beyond the scope of this thesis.

3.2 Vector boson production processes

In the previous section, the setup and relevant phases of a MC event generator are introduced. Within this thesis, the existing MC event generator SHERPA is extended to enable the simulation of polarized cross sections for massive VB production. The motivation for studying VB polarization is already discussed in the introductory part of this thesis. This section gives an overview of the VB production processes studied in this work with the aim to test the newly implemented features and outline first phenomenological applications thereof. In terms of MC event generation, the processes presented in this section are hard processes. VBs have a very short lifetime, making their direct observation impossible. Merely, their decay products can be measured, which can either be quarks or leptons. In this work, exclusively leptonic VB decay channels are considered wherefore only contributing diagrams of processes associated with these VB decays are displayed in this section at LO. Perturbative orders specified in the subsequent parts of this work refer to the coupling structure of the squared matrix elements.

3.2.1 Single W^++Jet production

The production of a single VB in association with one jet is one of the simplest VB production processes corresponding to a coupling order of $\mathcal{O}(\alpha_S \alpha_{EW}^2)$ at LO. It has one of the highest cross sections for electroweak boson production and therefore represents an important background in measurements of many other SM processes at the LHC. At lowest order, only diagrams are contributing that take the form given in Fig. 3.3 for the W^+j production.

3.2.2 Vector boson pair production at $\mathcal{O}(\alpha_{EW}^4)$

Vector boson pair production at order $\mathcal{O}(\alpha_{EW}^4)$ is possible for WZ, ZZ and W^+W^- VB pairs. In this thesis, only the W^+Z process is investigated. Diagrams, contributing to this process at LO, can be subdivided into diagrams where both (double-resonant, (a) and (b) in Fig. 3.4) and only one (single-resonant, (c) in Fig. 3.4) pair of final state leptons are produced by

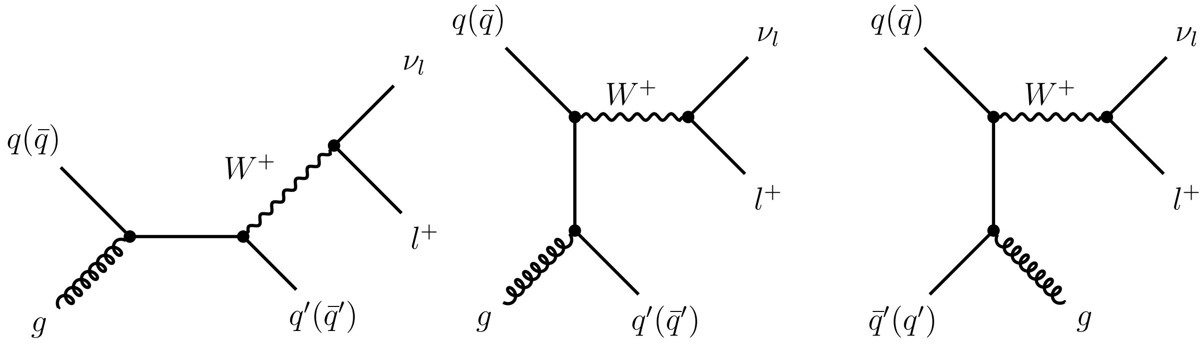

Figure 3.3: Leading-order Feynman diagrams of the hadronic $\mathrm{pp} \to \mathrm{l}^+\nu_\mathrm{l}\,\mathrm{j}$ process.

resonant VBs. The first group also includes diagrams with VB triple gauge coupling interaction (diagram (a)), emphasizing interest in this process for testing the SM gauge symmetry structure and searching for deviations from that due to possible new physics. It is important to note that some diagrams may also contain photons instead of Z bosons. Their contribution is reduced by phase space restrictions that force the invariant mass of the lepton-anti-lepton pair to values close to the Z mass. This also avoids the divergence of the cross section when $m_{\mathrm{l}^+\mathrm{l}^-} \to 0$. Radiative corrections to this process considered in this thesis are of order $\mathcal{O}(\alpha_S \alpha_{EW}^4)$. The general form of NLO QCD corrections is discussed in the previous section.

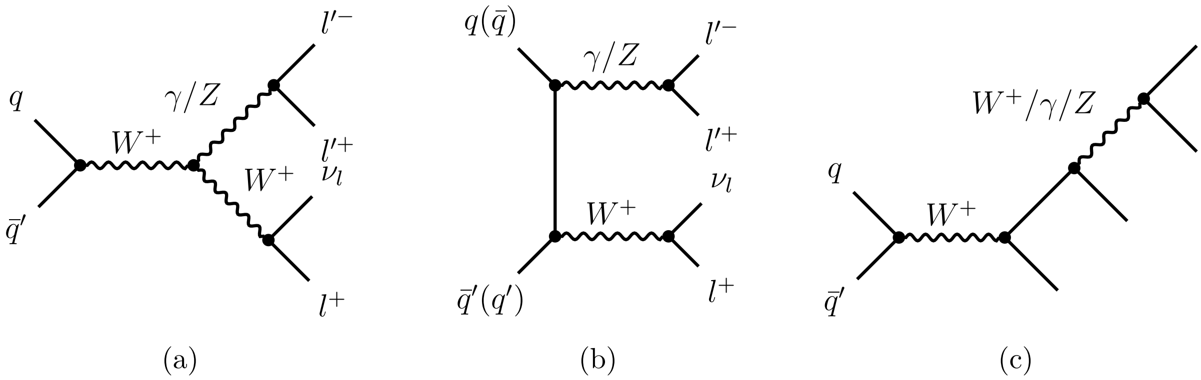

Figure 3.4: Leading-order Feynman diagrams of the hadronic $\mathrm{pp} \to \mathrm{l}^+\,\nu_\mathrm{l}\,\mathrm{l}'^+\,\mathrm{l}'^-$ process; diagram (c) summarizes several Feynman diagrams of the same form, which is why no concrete final states are given.

3.2.3 Vector boson pair production in association with two jets at $\mathcal{O}(\alpha_{EW}^6)$

The most interesting contributions to the VB pair production in association with two jets at order $\mathcal{O}(\alpha_{EW}^6)$ are diagrams which include the scattering of two VBs VV $\to$ VV (see Fig. 3.6 (a)) with V = Z,W$^\pm$ and γ (not all combinations of them are allowed). They are special due to the delicate cancellation of large unitarity-violating contributions from pure gauge and Higgs diagrams for the scattering of longitudinal VBs in the SM [76]. BSM effects could influence this cancellation, resulting in potentially large enhancements of the VBS rate [58]. The dashed circle in Fig 3.6 (a) refers to the interactions given in Fig. 3.5, namely the quartic self-interaction vertex, s- and t/u channel triple gauge boson interactions as well as interactions of the Higgs boson with the massive electroweak gauge bosons. The VBS contribution has a characteristic signature: since the initial state quarks in Fig. 3.6 (a) undergo an electroweak interaction only, they are only deflected slightly from the beam axis resulting in a high invariant mass of and a significant rapidity difference between the two jets. Appropriate selection criteria on these observables can enhance the VBS contribution with respect to the overall VB pair production process since many other diagrams featuring no VBS configuration contribute to these processes. For the purpose of this work, it is useful also for this group of VB pair production processes to

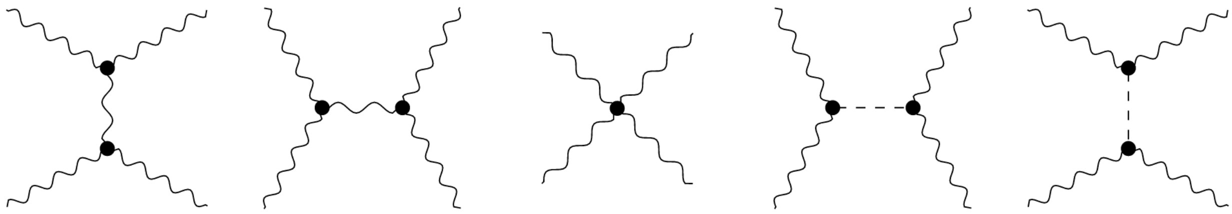

Figure 3.5: Leading order Feynman diagrams contributing to the scattering of two massive vector bosons VV $\rightarrow$ VV [3].

categorize contributing diagrams according to the number of resonant (leptonically decaying) VBs occurring, i.e. into double-, single- and non-resonant diagrams. Fig. 3.6 and 3.7[3] display example diagrams for each of these groups indicating that contributing diagrams obey very different structures including diagrams with three resonant VBs (diagrams (d)-(f) in Fig. 3.6) or further diagrams involving triple gauge couplings (diagrams (b), (d), (e) in Fig. 3.6, diagram (c) in Fig. 3.7).

For simplicity, to distinguish $\mathcal{O}(\alpha_{EW}^6)$ from $\mathcal{O}(\alpha_{EW}^4)$ VB production processes at LO subsequently in this work, the first are also called VBS processes (even though also non-VBS-configurations are included) or VVjj processes, while the latter are denoted as inclusive VV-production. The notations LO and NLO QCD refer to the coupling orders which are discussed in this section.
Similarly to the inclusive W^+Z-production discussed in the previous section, $W^\pm Zjj$- and ZZjj processes include contributions from diagrams where Z bosons are replaced by photons. Their contribution can again be reduced by restricting the Z-decay-products' invariant mass to values near the Z-mass. $W^\pm Zjj$ and W^+W^-jj processes contain large contributions from resonant tops/anti-tops. They emerge e.g. from diagram (c) in Fig. 3.6, if the intermediate quark radiating a boson is a (resonant) (anti-)top quark. By only considering final states without bottom quarks, this contribution can be suppressed.

[3]Clearly, dependent on the chosen final state, not all of these diagrams contribute.

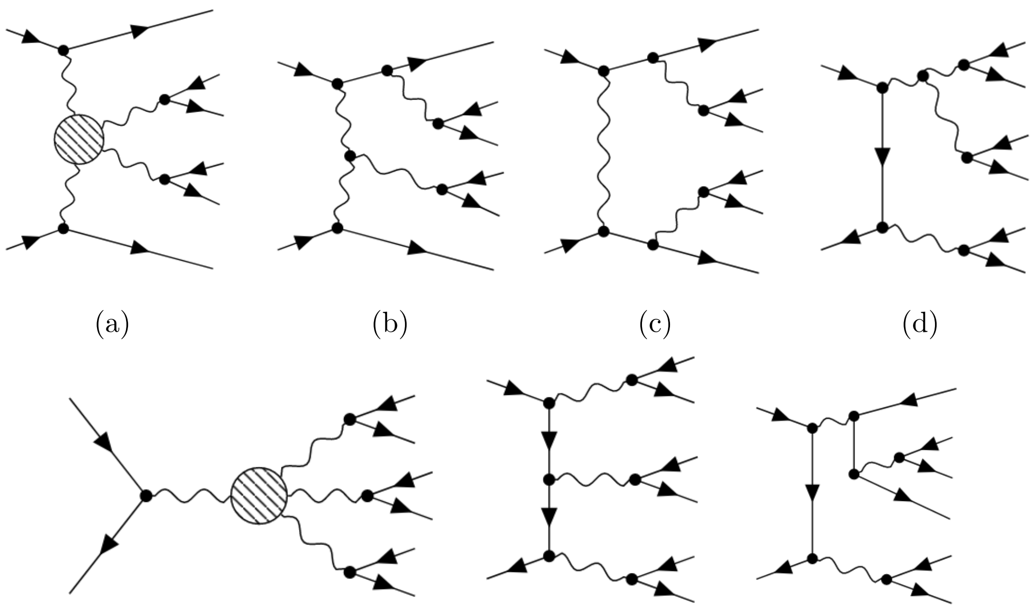

(a) (b) (c) (d) (e) (f) (g)

Figure 3.6: Double-resonant Feynman diagrams contributing to pure electroweak vector boson production processes in association with two jets at LO, the dashed circle is a placeholder for the diagrams from Fig. 3.5 (diagrams taken from Ref. [3]).

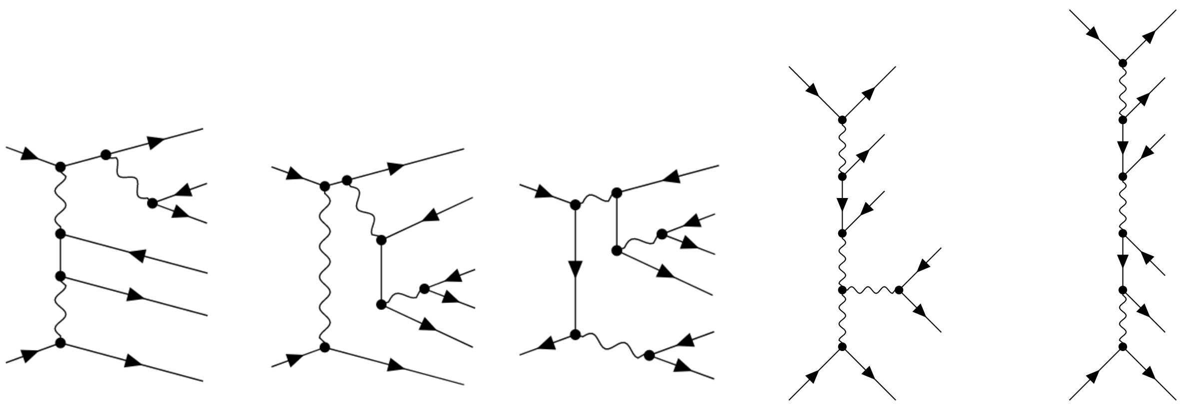

(a) (b) (c) (d) (e)

Figure 3.7: Single ((a)-(d))- and non-resonant ((e)) Feynman diagrams contributing to pure electroweak vector boson production processes in association with two jets at LO (diagrams (a)-(c) taken from Ref. [3]).

3.3 Definition of polarization for intermediate vector bosons

In the previous chapter, some electroweak Feynman rules are displayed. They illustrate that the polarization of external VBs is easily accessible because they are directly represented by their polarization vectors in matrix elements. But with massive VBs being very short-living, they can only be measured as intermediate particles described by propagator terms:

$$D_{\mu\nu} = \frac{i(-g^{\mu\nu} + \frac{q^\mu q^\nu}{m_V^2})}{q^2 - m_V^2 + i\Gamma_V m_V}\,, \tag{3.8}$$

with q being the VB momentum[4]. With that, the production of a single VB and its decay into a final state lepton pair is described, in unitary gauge, by the matrix element:

$$\mathcal{M} = \mathcal{M}_\mu^{\text{prod}} \left(\frac{i(-g_W^{\mu\nu} + \frac{q^\mu q^\nu}{m_V^2})}{q^2 - m_V^2 + i\Gamma_V m_V} \right) \Big[-ig\bar{\psi}_f \gamma_\nu \Big(c_L \frac{1-\gamma^5}{2} + c_R \frac{1+\gamma^5}{2} \Big) \psi_{f'} \Big]\,, \tag{3.9}$$

with $\bar{\psi}_f$, $\psi_{f'}$ being the spinors of the final state leptons. Coefficients c_L and c_R represent the left- and right-handed fermion couplings to the VB[5] and $\mathcal{M}_\mu^{\text{prod}}$ denotes the matrix element of the VB production. Since the propagator does not contain any polarization vectors, the completeness relation[6]:

$$\left(-g^{\mu\nu} + \frac{q^\mu q^\nu}{m_V^2} \right) = \sum_{\lambda=1}^{4} \varepsilon_\lambda^\mu(q) \varepsilon_\lambda^{*\nu}(q) \tag{3.10}$$

can be used to reintroduce a polarization dependency by replacing the numerator with a sum over polarization vectors. This sum contains a fourth unphysical polarization which automatically vanishes for on-shell particles or in the special case of massless leptons [58]. With at least the latter requirement, the angular distribution of the $W^\pm/Z$ decay products takes the following form if the VB polarization is defined in the helicity basis, no lepton selection criteria are applied and the integration over the full range of the decay product's azimuthal angle is performed [58, 59]:

$$\begin{aligned} \frac{1}{\frac{d\sigma(X)}{dX}} \frac{d\sigma(\theta^*, X)}{d\cos\theta^* dX} &= \frac{3}{8} f_L(X) \Big(1 + \cos^2\theta^* \mp \frac{2(c_L^2 - c_R^2)}{(c_L^2 + c_R^2)} \cos\theta^* \Big) \\ &+ \frac{3}{8} f_R(X) \Big(1 + \cos^2\theta^* \pm \frac{2(c_L^2 - c_R^2)}{(c_L^2 + c_R^2)} \cos\theta^* \Big) + \frac{3}{4} f_0(X) \sin^2\theta^*, \end{aligned} \tag{3.11}$$

with the variables:

[4] This propagator differs from the one derived in the previous chapter given in Eq. 2.37 by the last term in the denominator. It accounts for the finite width of the unstable VBs.

[5] Coefficients appearing in Eq. 3.9 denote $c_{L,W} = 1/\sqrt{2}$, $c_{R,W} = 0$, $c_{L,Z} = (I_{3,f}^W - s^2 Q_f)/c$ and $c_{R,Z} = -s^2 Q_f/c$ with $c = m_W/m_Z$, $s = \sin\theta_W$.

[6] The connection of Eq. 3.10 to the on-shell completeness relation in Eq. 2.34 is discussed in Appendix B.1.

- θ^*: (lepton) decay angle, it is defined as the angle between the charged leptons momentum in the VB rest frame and the VB's flight direction in the reference frame used for polarization definition (motivated in Sec. 4.2), the VB rest frame is reached by boosting the charged leptons momentum from the reference frame, for Z the anti-fermion is used (in the rest of this thesis, it is also referred to as decay angle of the VB);
- X: other phase space variables the cross section depends on beside θ^*;
- $\frac{d\sigma(X)}{dX} = \int d\cos\theta^* \frac{d\sigma(X,\theta^*)}{d\cos\theta^* dX}$;
- f_i: normalized polarization fractions - $f_L + f_R + f_0 = 1$.

The upper sign holds for W^+ and Z bosons, the lower sign for W^- bosons. By projecting the angular distribution on the first Legendre polynomials α_i ($i = 0-2$), the polarization fractions can be determined [58]. However, in realistic setups, lepton selection criteria need to be applied, which spoil the factorization of the angular dependence of the decay and the other kinematic variables X, since lepton acceptance criteria (like on the lepton's transverse momentum) depend on both of them. Hence, to measure polarization fractions in realistic setups, polarized cross sections need to be simulated.
The fact that VBs only emerge as intermediate particles in observable processes leads to two difficulties in the definition of polarized cross sections which would not arise for external VBs. The first one can already be observed for the single VB production process. By inserting Eq. 3.10 into Eq. 3.9, the matrix element can be factorized into VB production and decay:

$$\begin{aligned} \mathcal{M} &= \frac{i}{q^2 - m_V^2 + i\Gamma_V m_V} \sum_\lambda \mathcal{M}_\mu^{\text{prod}} \varepsilon_\lambda^{*\mu} \varepsilon_\lambda^\nu \Big[-ig\bar{\psi}_f \gamma_\nu \Big(c_L \frac{1-\gamma^5}{2} + c_R \frac{1+\gamma^5}{2} \Big) \psi_{f'} \Big] \\ &= \frac{i}{q^2 - m_V^2 + i\Gamma_V m_V} \sum_\lambda \mathcal{M}_\lambda^{\mathcal{P}} \mathcal{M}_\lambda^{\mathcal{D}} =: \sum_\lambda \mathcal{M}_\lambda^{\mathcal{F}}, \end{aligned} \tag{3.12}$$

with $\mathcal{M}_\lambda^{\mathcal{F}}$ being the full polarized amplitude for a single VB with polarization λ, $\mathcal{M}_\lambda^{\mathcal{P}}$ and $\mathcal{M}_\lambda^{\mathcal{D}}$ the ones for VB production and decay. If this amplitude is squared:

$$\underbrace{|\mathcal{M}|^2}_{\text{coherent sum}} = \underbrace{\sum_\lambda |\mathcal{M}_\lambda^{\mathcal{F}}|^2}_{\text{polarized contributions, incoherent sum}} + \underbrace{\sum_{\lambda\neq\lambda'} \mathcal{M}_\lambda^{\mathcal{F}} \mathcal{M}_{\lambda'}^{*\mathcal{F}}}_{\text{interference}}, \tag{3.13}$$

interference terms between different polarizations emerge. They only sum up to zero in the absence of lepton selection criteria [58]. Apart from that, they need to be considered as additional part of the polarization measurement if the phase space is not chosen such that their contribution is small. Unless stated otherwise, interference is always referred to interference between different polarizations further on in this thesis. Likewise, polarized contributions refer to summands of the incoherent sum, where all intermediate VBs have a definite polarization.
The second difficulty arises if more complicated processes are considered involving at least

two intermediate VBs. According to Sec. 3.2, not all diagrams participating in VB pair production processes exclusively contain final state leptonic lines connected to a single VB each (double-resonant diagrams). For diagrams of the non- and single-resonant type, the definition of polarization for two VBs is unfeasible, since they cannot be interpreted as the production and decay of two VBs. Simply ignoring these diagrams would break electroweak gauge invariance. Thus, suitable approximations are necessary which allow to omit these diagrams while retaining gauge invariance at the same time. The two common approximations which fulfill these requirements are described below.

- **Narrow-Width Approximation (NWA)** is the approximation utilized by SHERPA. It mainly replaces the denominator of the propagator by a delta function such that only on-shell contributions remain:

$$\frac{1}{q^2 - m_V^2 + i\Gamma_V m_V} \to \frac{\pi}{M_V \Gamma_V}\delta(q^2 - M_V^2)\,. \tag{3.14}$$

- **(Double[7]-)Pole Approximation (DPA)** is used by several MC event generators such as PHANTOM [23]. It partially considers off-shell effects by only projecting the numerator of the propagator to on-shell momenta while leaving the denominator unchanged. This projection is not unique since sending the boson to mass-shell requires at least the adjustment of the VB decay products' momenta. Further details about this approximation can be found e.g. in Ref. [58]. In the literature, the DPA is often also referred to as On-Shell projection technique (OSP).

The accuracy of both approximations is of order $\mathcal{O}(\Gamma_V/M_V)$ [59, 77]. Amplitudes resulting from inserting the completeness relation into the VB propagators and applying one of the approximations above are the product of complete, ordinary production and decay matrix elements of external, on-shell VBs $\mathcal{M}^{\mathcal{P}}_{\lambda_1,\dots,\lambda_n}$ and $\mathcal{M}^{\mathcal{D}}_{\lambda_n}$:

$$\mathcal{M}_{\text{approx}} \propto \sum_{\lambda_1\dots\lambda_n} \mathcal{M}^{\text{prod}}_{\mu_1\dots\mu_n} \varepsilon^{*\mu_1}_{\lambda_1} \cdots \varepsilon^{*\mu_n}_{\lambda_n} \varepsilon^{\nu_1}_{\lambda_1} \cdots \varepsilon^{\nu_n}_{\lambda_n} \mathcal{M}^{\text{decay}}_{\nu_1} \cdots \mathcal{M}^{\text{decay}}_{\nu_n} = \sum_{\lambda_1\dots\lambda_n} \mathcal{M}^{\mathcal{P}}_{\lambda_1\dots\lambda_n} \mathcal{M}^{\mathcal{D}}_{\lambda_1} \cdots \mathcal{M}^{\mathcal{D}}_{\lambda_n}\,. \tag{3.15}$$

If both factors are gauge invariant, this also holds for the overall approximated matrix element. Since the VBs are on-shell in the polarization dependent part of the matrix element in both approximations, the unphysical auxiliary polarization does not contribute so that each term of the polarization sum in Eq. 3.15 provides a physical polarization contribution to the process.

[7]The pole approximation is also called double-pole approximation for the case of VB pair production processes.

4 Implementation of polarized cross sections for vector boson production in SHERPA

This chapter explains the new implementation developed to enable the simulation of polarized cross sections for an arbitrary number of unstable, resonant VBs within SHERPA. As already discussed in Sec. 3.3, approximations are necessary to perform such calculations. It turned out that they lead to factorized matrix elements of the form:

$$|\mathcal{M}_{\text{approx}}|^2 \propto \sum_{\lambda_1 \dots \lambda_n; \lambda'_1 \dots \lambda'_n} \mathcal{M}^{\mathcal{P}}_{\lambda_1 \dots \lambda_n} \mathcal{M}^{*\mathcal{P}}_{\lambda'_1 \dots \lambda'_n} \mathcal{M}^{\mathcal{D}}_{\lambda_1 \dots \lambda_n} \mathcal{M}^{*\mathcal{D}}_{\lambda'_1 \dots \lambda'_n} \,, \tag{4.1}$$

consisting of matrix elements for the production $\mathcal{M}^{\mathcal{P}}_{\lambda_1 \dots \lambda_n}$ and the decay $\mathcal{M}^{\mathcal{D}}_{\lambda_1 \dots \lambda_n}$ of n on-shell VBs[1].

The current SHERPA release [78] is already able to simulate such factorized matrix elements of processes with unstable, intermediate (resonant) particles in an extended narrow-width approximation. Spin-correlations between production and decay matrix elements are thereby preserved. Details about this prerequisite for the actual polarization simulation are described in the first section of this chapter. It fixes the approximation necessary to define polarized amplitudes. After that, SHERPA's description of polarization vectors is introduced. In the subsequent sections, the new implementation is explained which allows to extract polarized cross sections from the already existing framework. Furthermore, its application for the calculation of NLO QCD polarization contributions is discussed. The focus of that section is to explain the ideas and concepts behind the implementation. The introduced syntax and the application of the implementation for concrete simulations can be found in the corresponding section in the SHERPA manual, see Appendix A.
The new implementation is based on the current development version of SHERPA, which will be released as version 3.0.0 in the future [79].

[1]In NWA, the proportionality constant in Eq. 4.1 stands for the factors $\frac{\pi}{M_V \Gamma_V}$, one for each VB propagator for which the NWA is applied.

4.1 Calculation of factorized matrix elements in SHERPA

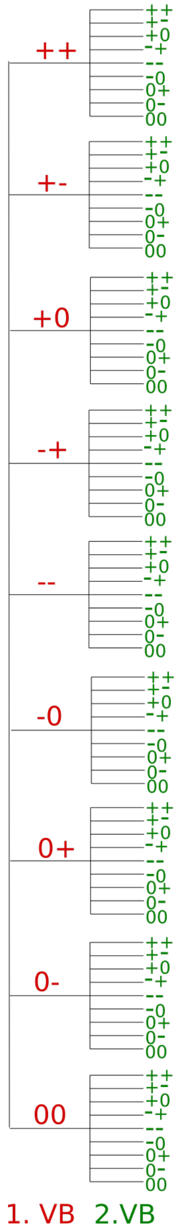

Figure 4.1: Sketch of the production amplitude tensor structure for a process with two intermediate vector bosons (VB), second index accounts for the matrix element, the first for its complex conjugate.

The current SHERPA release is already able to sample events according to factorized matrix elements of the form Eq. 4.1 for processes with intermediate, unstable particles such as VB production processes in a spin-correlated narrow-width approximation [80]. For that, the VB production subprocess (called hard process) and the VB decays (called hard decays) are considered separately. Naive separate generation of these subprocesses would produce:

$$|\mathcal{M}|^2 = \frac{1}{N}\left(\sum_{\lambda_1\ldots\lambda_n} \mathcal{M}^{\mathcal{P}}_{\lambda_1\ldots\lambda_n}\mathcal{M}^{*\mathcal{P}}_{\lambda_1\ldots\lambda_n}\right)\cdot\left(\sum_{\lambda'_1,\ldots,\lambda'_n} \mathcal{M}^{\mathcal{D}}_{\lambda'_1\ldots\lambda'_n}\mathcal{M}^{*\mathcal{D}}_{\lambda'_1\ldots\lambda'_n}\right), \tag{4.2}$$

with N consisting of the product of all helicities of the decaying VBs, ignoring spin-correlations between VB production and decays. This would lead to wrong cross sections and wrong dynamics. Therefore, the spin-correlation algorithm of Peter Richardson [81] is implemented to preserve spin-correlations. After calculating the production subprocess, it generates the whole decay chain of the intermediate particles. For VBs decaying into stable particles, the algorithm is sketched in Fig. 4.2 since only such processes are investigated in this thesis. Its implementation can be found in the `Decay_Handler_Base` class of SHERPA.

During algorithm execution, a decay matrix is calculated for each particle. The product of the decay matrices of all intermediate VBs equals to the decay matrix elements $\mathcal{M}^{\mathcal{D}}_{\lambda_1\ldots\lambda_n}\mathcal{M}^{*\mathcal{D}}_{\lambda'_1\ldots\lambda'_n}$ up to a normalization constant (cf. Eq. 4.6).

The generation of the VB decay products does not affect the integration and the computation of the hard process (VB production). The initial and final state particles of the production subprocess are generated first according to the (unpolarized) production amplitude. Then, the production amplitude tensor $\mathcal{M}^{\mathcal{P}}_{\lambda_1\ldots\lambda_n}\mathcal{M}^{*\mathcal{P}}_{\lambda'_1\ldots\lambda'_n}$ is recalculated to get the spin-dependent matrix elements serving as input for the spin-correlation algorithm which subsequently computes the VB decays.

The calculation of the spin-dependent production amplitude tensor (abbreviated to production tensor in the following) and the decay

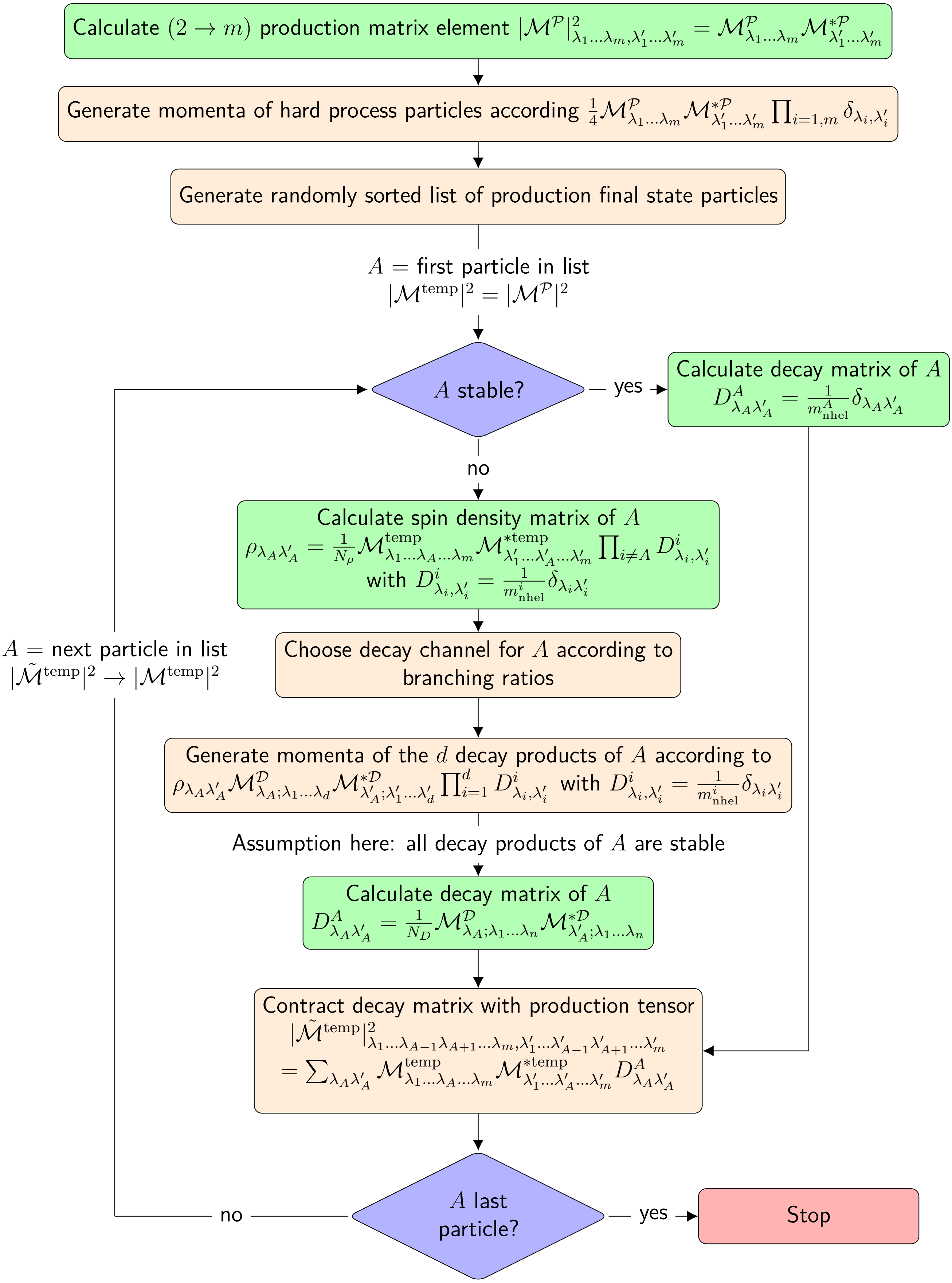

Figure 4.2: Sketch of the spin-correlation algorithm of P. Richardson [81] for the special case of unpolarized initial state particles and unstable particles decaying directly into stable decay products; λ_i=polarization of particle i, N_ρ, N_D=normalization constants such that ρ, D has a trace of one, m^i_{nhel} =number of spin degrees of freedom of the ith particle.

matrices is done by the matrix element generator COMIX [69]. The VBs in both the final state of the production and the initial state of the decay subprocesses are all generated on their mass shells. In order to at least partly recover the off-shell kinematics of the total process, a smearing of the unstable particle's invariant mass according to the Breit-Wigner distribution is performed after their generation, affecting only the kinematics of the final state particles. The matrix elements remain unchanged i.e. calculated in NWA with on-shell VBs.

The absolute squared polarized production matrix elements $|\mathcal{M}^{\mathcal{P}}_{\lambda_1 \ldots \lambda_n, \lambda'_1 \ldots \lambda'_n}|^2$ are stored in a tree-like structure to account for an arbitrary number of unstable particles. Deviating from the original spin-correlation algorithm shown in Fig. 4.2, all stable hard process final state particles are contracted before the production tensor enters the spin-correlation algorithm, i.e. for VB production processes it only depends on the polarization of the VBs. Fig. 4.1 sketches the structure of the production tensor for a process involving two intermediate VBs. It also indicates the polarization ordering in this tensor. Each level corresponds to one particle. At each level, $m_{\text{nhel}} \cdot m_{\text{nhel}}$ branches are starting where m_{nhel} denotes the particle's spin degrees of freedom. Each starting branch stands for one possible polarization combination of the current particle in the matrix elements and their complex conjugates. At the end of each path corresponding to a particular polarization combination of the intermediate particles, the associated absolute squared matrix element is stored.

4.2 Polarization vectors and polarization definition in COMIX

Since factorized matrix elements are always calculated by COMIX the handling of polarization vectors in this matrix element generator is described here. Polarization vectors in COMIX are implemented similar to Ref. [35]. They are calculated utilizing Weyl-van-der-Waerden spinors introduced in Sec. 2.1.2, starting from the particle momentum p^μ and an arbitrary light-like four-vector a^μ and can be obtained by performing the following steps:

1. Decompose p^μ into two light-like vectors a^μ and b^μ by calculating b^μ according to Eq. 2.17
2. Calculate the spinors $a_{\dot{A}}$ and a_A as well as $b_{\dot{A}}$ and b_A with Eq. 2.16 whose products yield the spinor representations $A_{\dot{A}B}$ and $B_{\dot{A}B}$ of a^μ and b^μ, respectively
3. Determine the polarization vectors in spinor representation:

$$\varepsilon_{+,\dot{A}B}(p) = \frac{\sqrt{2} a_{\dot{A}} b_B}{\langle ab \rangle^*} \qquad \varepsilon_{-,\dot{A}B}(p) = \frac{\sqrt{2} b_{\dot{A}} a_B}{\langle ab \rangle} \qquad \varepsilon_{0,\dot{A}B}(p) = \frac{1}{m}\big(b_{\dot{A}} b_B - \alpha a_{\dot{A}} a_B\big) \quad (4.3)$$

4. Transform the polarization vectors back to the four-vector representation using Eq. 2.15 (right)

Resulting polarization vectors are those of incoming particles. In order to completely define the VB polarization, the following two choices are necessary:

- **Reference system:** Polarization vectors constructed as described above are not Lorentz covariant, $\Lambda^\mu{}_\nu \varepsilon^\nu(p,\lambda) \neq \varepsilon^\mu(\Lambda p, \lambda)$, as e.g. can be seen from their representation in the helicity basis in Eq. 2.33. This means that the polarization of a particle depends on the frame in which its polarization vectors are calculated. Thus, two different frames can be distinguished in polarization measurements - the measurement system and the reference system for polarization definition. The measurement system denotes the frame, where the matrix elements are evaluated and the particles' momenta are measured. The polarization vectors, however, can first be computed in another frame, the reference system, before they are transformed to the measurement frame. Resulting polarization vectors differ from those that would be obtained if they were calculated directly in the measurement system.

  The measurement frame in SHERPA is the laboratory frame and can not be changed. Distinct reference systems change the contributions of the single polarizations to the unpolarized cross section of the whole process, i.e. longitudinal and transverse contributions are mixed. This fact is used in experimental analyses [16, 18] to maximize the contribution of the interesting polarization (usually the longitudinal polarization). The default reference system in SHERPA is the laboratory frame.

- **Spin basis:** For massive particles, the light-like vector a^μ, arbitrarily chosen in the splitting of the massive four-momentum into two massless ones, has a physical meaning since the spin vector introduced in Sec. 2.1.3 takes the form [82]:

  $$s^\mu = \frac{1}{m}(p^\mu - 2\alpha a^\mu)\,. \tag{4.4}$$

  Consequently, a^μ taken in the desired reference frame determines the axis along which the spin is measured. To receive the helicity basis, which is typically used to define VB polarization, a^μ must be set (proportional) to $(1, -\vec{p}/|\vec{p}|)$ resulting in the spin vector pointing in the direction of $\vec{p}$:

  $$s^\mu_{\text{hel}} = \frac{1}{m}\left(|\vec{p}|, p^0 \frac{\vec{p}}{|\vec{p}|}\right)\,. \tag{4.5}$$

  Then, polarization vectors calculated in SHERPA according to the four steps above have the form of Eq. 2.33.

  For matrix element calculations, SHERPA uses a chirality basis defined by a constant a^μ. In dependency of the chosen gauge for the Weyl spinors, COMIX utilizes different a^μs. To get polarization vectors as described by the four steps above, a special gauge need to be applied (cf. manual in Appendix A) which leads to $a^\mu = (1, 0, 1, 0)$.

In the following discussions, the reference vector a^μ and the reference system used for matrix element calculation is referred to as the default reference vector and default reference system, respectively, which together define the default polarization definition/basis.
It is worth noting that the unpolarized result (coherent sum in Eq. 3.13) is Lorentz invariant and therefore unaffected by the choice of the polarization definition.

This section has introduced the principles of VB polarization definition in SHERPA. At the moment, there is an unresolved issue in the actual implementation of the polarization vectors that leads to ε^+ and ε^- being interchanged compared to their definition in Eq. 4.3 which was detected during the validation. Until the issue is resolved, it gets mitigated by switching the left- and right-handed labels of the final polarized cross sections within the simulation.

4.3 Calculation of polarized cross sections

The framework described in Sec. 4.1 can already provide production and decay matrix elements where the summation over the VB polarizations is not yet performed and which are computed in an approximation appropriate for polarized cross section calculations. Therefore, it can be kept unchanged and only copies of the production tensor and each decay matrix must get stored before they are contracted with each other. Thus, the whole event is generated unpolarized and only polarization fractions are computed describing the fraction of the polarized cross section of a certain VB polarization combination on the entire event. After their calculation, the polarization fractions are multiplied with the unpolarized event cross section. Resulting polarized cross sections are output as additional event weights.
The following steps are done to obtain the polarized cross sections from the copies of the production and decay amplitudes:

1. **Transformation** of polarized production tensor and decay matrices to get the matrix elements with VB polarization defined in the polarization basis of interest (if not identical to the default polarization basis)

2. **Multiplication** of production tensor $P_{\lambda_1 \dots \lambda_n, \lambda'_1 \dots \lambda'_n}$ and decay matrices $D_{\lambda_i \lambda'_i}$ to receive the amplitude tensor of the whole VB production and decay process according to (no summation convention here!):

$$
\begin{aligned}
|\mathcal{M}_{\text{pol}}|^2_{\lambda_1 \dots \lambda_n, \lambda'_1 \dots \lambda'_n} &= \mathcal{M}^{\mathcal{P}}_{\lambda_1 \dots \lambda_n} \mathcal{M}^{*\mathcal{P}}_{\lambda'_1 \dots \lambda'_n} \mathcal{M}^{\mathcal{D}}_{\lambda_1 \dots \lambda_n} \mathcal{M}^{*\mathcal{D}}_{\lambda'_1 \dots \lambda'_n} \\
&= N \cdot P_{\lambda_1 \dots \lambda_n, \lambda'_1 \dots \lambda'_n} \prod_{\lambda_i, \lambda'_i = 1}^{n} D_{\lambda_i \lambda'_i} \,.
\end{aligned} \tag{4.6}
$$

   N contains the normalization constants of the decay matrices and can be ignored since it cancels in step three when polarization fractions are calculated. Fig. 4.3 illustrates how this multiplication is performed considering the different form of the production tensor and the decay matrices.

3. **Labeling & Output** of the polarization contributions, calculation of user-defined polarized cross sections, if desired

Details about the more comprehensive steps one and three are given in the following sections.

This approach allows to simulate all polarized cross sections for all VB polarization combinations simultaneously within a single simulation run. Furthermore, the interference between different polarizations can be computed event-wise since the production tensor and the decay matrices contain all interference terms as off-diagonal entries. Thus, an interference template can be directly provided for polarization analyses. This can be included as an additional background in the polarization measurement without relying on subtraction methods that can lead to large MC-uncertainties. Moreover, predictions for more than one reference system can be obtained with one simulation run by repeating above steps for each desired polarization definition.

4.3.1 Change of polarization definition

The definition of polarization for VBs is not unambiguous as discussed in Sec. 2.1.3 and 4.2. In order to calculate production and decay matrix elements, COMIX uses the formalism described in Sec. 4.2 to define VB polarizations. A chirality basis is chosen as spin basis and the reference system is the laboratory frame. As mentioned earlier, a more physical basis for polarization definition is the helicity basis. Furthermore, other reference systems than the laboratory frame may be interesting to e.g. maximize the longitudinal contribution of VBs in VB production processes. To change the definition of polarization, two approaches are conceivable, an a priori way changing the polarization definition directly during the matrix element calculation or an a posteriori way adjusting it by performing a transformation of the matrix elements after their calculation. Due to its generator independence, the second approach is chosen.
The a posteriori change of the polarization definition is based on the fact that polarization objects (spinors, polarization vectors) defined in one basis can be expressed as a linear combination of polarization objects obtained in another basis. By replacing the polarization objects defined in the desired polarization definition in the corresponding matrix elements by the linear combination of the polarization objects used in the matrix element calculation, the following transformation is obtained (cf. Appendix B.2):

$$|\mathcal{M}^{\text{new}}|^2_{\lambda_1\ldots\lambda_n,\lambda'_1\ldots\lambda'_n} = \sum_{\kappa_1\ldots\kappa_n,\kappa'_1\ldots\kappa'_n} a^{\text{part1}}_{\lambda_1,\kappa_1} a^{*\text{part1}}_{\lambda'_1,\kappa'_1} \cdots a^{\text{partn}}_{\lambda_n,\kappa_n} a^{*\text{partn}}_{\lambda'_n,\kappa'_n} |\mathcal{M}^{\text{old}}|^2_{\kappa_1\ldots\kappa_n,\kappa'_1\ldots\kappa'_n}\,, \tag{4.7}$$

with λ_i and κ_i describing the polarizations of the ith particle in the desired (new) and the default (old) polarization definition. The absolute squared matrix elements $|\mathcal{M}^{\text{old}}|^2_{\kappa_1\ldots\kappa_n,\kappa'_1\ldots\kappa'_n}$ are the

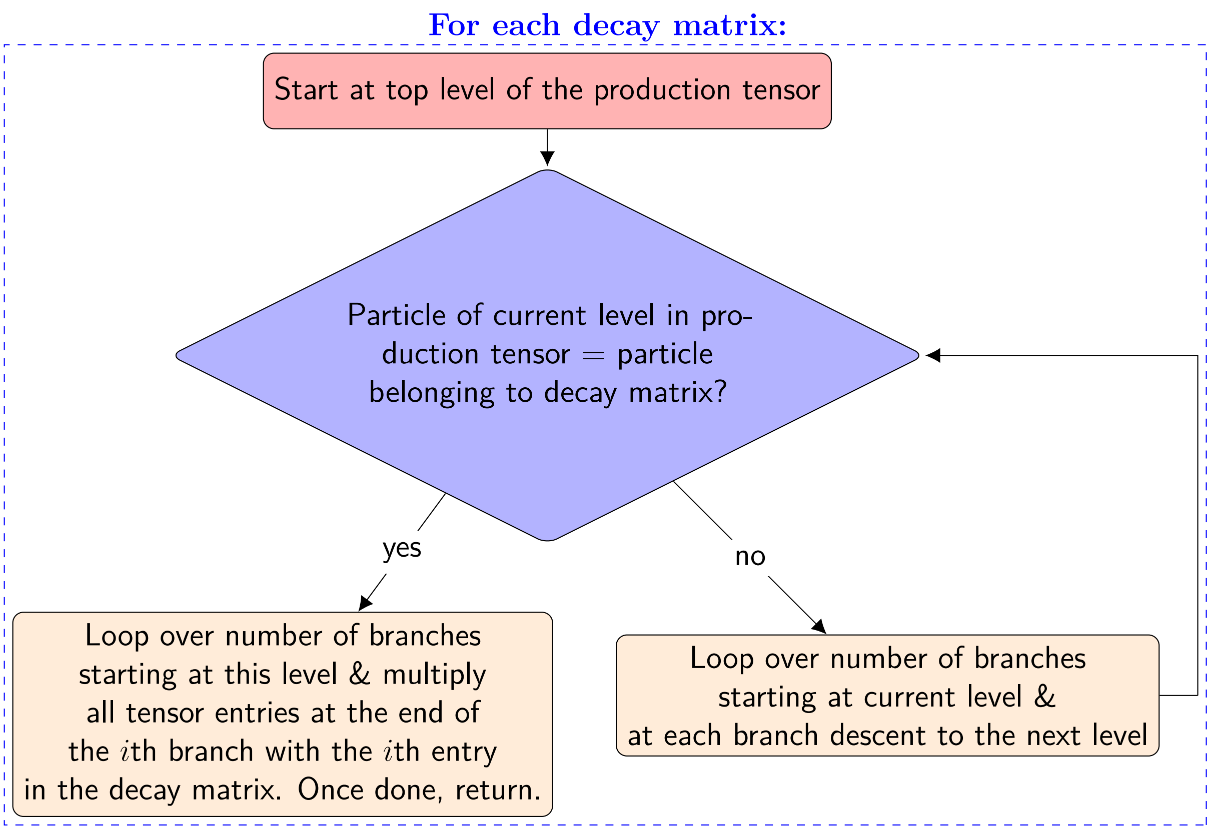

Figure 4.3: Flow chart for the calculation of the polarized matrix elements from the production tensor and the decay matrices.

ones calculated with SHERPA's default polarization basis; $|\mathcal{M}^{\text{new}}|^2_{\lambda_1...\lambda_n,\lambda'_1...\lambda'_n}$ are computed in the desired polarization basis. The transformation coefficient $a^{\text{parti}}_{\lambda_i,\kappa_i}$ is the linear combination coefficient which corresponds to the polarization object with polarization κ_i in the linear combination of the κ_is describing the polarization object with polarization λ_i. They correspond to the polarization objects in the matrix elements, $a^{*\text{parti}}_{\lambda'_i,\kappa'_i}$ to the polarizations in the complex conjugate one. $\mathcal{M}$ denotes either the production tensor or a decay matrix. The following steps are necessary to perform the transformation:

1. **Calculation of the polarization objects with default and desired polarization definition for each intermediate particle**
   The handling of polarization vectors in COMIX is introduced in Sec. 4.2. For each intermediate VB, two sets of polarization vectors are calculated, one assuming the polarization definition applied during matrix element calculation and one using the desired definition. The VB momentum necessary to calculate the polarization vectors must be taken in the default and desired reference system, respectively. Currently, the laboratory frame (Lab, default), the center-of-mass frame of all intermediate particles (COM), the parton-parton frame (PPFr) and all center-of-mass frames defined by any combination of initial or final state particles of the VB production process are supported. Since SHERPA always calculates matrix elements in the Lab, polarization vectors obtained

in a different reference frame must be transformed back to the Lab. This can be done by the inverse of the Lorentz boost necessary to transform the VB momentum in the desired reference system. The former is given in Eq. 2.8. Its inverse can be obtained from that by changing the sign of each β.
Per default, SHERPA calculates polarized cross sections with polarization defined in the helicity basis assuming the Lab as reference system. In principle, there is also the possibility to choose a spin basis other than the helicity basis, but the possibilities implemented so far are limited to rather non-physical spin bases (cf. Manual Appendix A) which are not connected to particle properties like the particle's momentum.

2. **Determination of the linear combination coefficients**
In order to facilitate the transformation of the matrix elements, the transformations coefficients in Eq. 4.7 need to be determined. This is done separately for each intermediate particle. All m_{nhel} linear combinations of one particle can be combined to a system of inhomogeneous equations. Its solution supplies the linear combination coefficients a_{ij} for the corresponding particle.
For massive spin-1 particles, only three of four polarization vector components are linear independent (cf. Eq. 2.31), thus the original (4x3) system can be reduced to a quadratic (3x3) one:

$$\begin{pmatrix} \tilde{\varepsilon}^1_+ & \tilde{\varepsilon}^1_- & \tilde{\varepsilon}^1_0 \\ \tilde{\varepsilon}^2_+ & \tilde{\varepsilon}^2_- & \tilde{\varepsilon}^2_0 \\ \tilde{\varepsilon}^3_+ & \tilde{\varepsilon}^3_- & \tilde{\varepsilon}^3_0 \end{pmatrix} = \begin{pmatrix} \varepsilon^1_+ & \varepsilon^1_- & \varepsilon^1_0 \\ \varepsilon^2_+ & \varepsilon^2_- & \varepsilon^2_0 \\ \varepsilon^3_+ & \varepsilon^3_- & \varepsilon^3_0 \end{pmatrix} \begin{pmatrix} a_{++} & a_{+-} & a_{+0} \\ a_{-+} & a_{--} & a_{-0} \\ a_{0+} & a_{0-} & a_{00} \end{pmatrix}, \tag{4.8}$$

with $\tilde{\varepsilon}$ naming the polarization vectors in the desired polarization definition. This system of equations can be solved by determining the inverse of the matrix containing the default polarization vectors ε. For that, the analytical solution for inverses of (3x3) invertible ($\det A \neq 0$) matrices A=$\left(\begin{smallmatrix} a & b & c \\ d & e & f \\ g & h & i \end{smallmatrix}\right)$ is utilized:

$$A^{-1} = \frac{1}{\det A} \begin{pmatrix} ei - fh & ch - bi & bf - ce \\ fg - di & ai - cg & cd - af \\ dh - eg & bg - ah & ae - bd \end{pmatrix}. \tag{4.9}$$

Since the polarization vectors in step one are calculated only for incoming VBs whereas outgoing VBs are described by their complex conjugate, all obtained transformations coefficients are complex conjugated, if outgoing VBs are considered. Antiparticles are handled identical to particles in SHERPA.

3. **Execution of the transformation of the production tensor and the decay matrices according to Eq. 4.7**

   The transformation execution for decay matrices is straightforward: Eq. 4.7 simplifies to a matrix multiplication since the decay matrix only depends on one particle's polarization. The production tensor, on the other hand, can have any order, depending on the number of intermediate particles involved. The tree structure, that holds the tensor entries, allows for a recursive calculation of Eq. 4.7 steered by a level variable numerating the levels in the amplitude tensor. It operates directly on the production tensor and uses the transformation coefficients determined in step two and *level*=0 as input. Depending on the value of the variable *level* the following is done:

   a) ***level* = 0: Saving the untransformed amplitude tensor**

      During the first call of the transformation method (*level*=0), the - yet untransformed - amplitude tensor is copied and set aside, because the original tensor will be modified along the way. The untransformed tensor copy will then be passed as additional parameter to all recursive transformation method calls until it is eventually used.

   b) ***level* < number of particles: Selecting coefficients according to polarizations in the transformed amplitude tensor**

      A loop over all branches starting at level *level* of the tensor is performed and for each iteration only those transformation coefficients are retained which describe the transformation to the polarization component of the particle at level *level* the current branch stands for. This is simultaneously done for the transformation coefficients of the polarization objects and of their complex conjugates. The remaining transformation coefficients are then passed to the subsequent recursion of the transformation method with $level + 1$.

   c) ***level* = number of particles: Calculating the tensor entries in the new polarization basis according to Eq. 4.7**

      The end of one tensor path is reached. All remaining transformation coefficients belong to the linear combinations that express the polarization objects describing the current tensor entry in the new polarization definition in terms of the default ones. Now, the calculation of the current tensor entry in the new polarization basis according to Eq. 4.7 is performed by calling the transformation method with $level + 1$ on the untransformed tensor copied at the top level of the recursion. The result contains all the summands in the polarization sum in Eq. 4.7 so the current tensor entry is obtained by summing over all the entries of that tensor.

d) **number of particles $<$ *level* $<$ 2 x number of particles+1: Selecting coefficients according to polarizations in the default amplitude tensor**
A loop over all branches starting at level *level* of the untransformed tensor is performed. For each branch only those transformation coefficients are retained that belong to the current particle's polarization object used to calculate the matrix element at the end of that branch. This is simultaneously done for the transformation coefficients of the polarization objects and of their complex conjugates. The remaining transformation coefficients are then passed to the subsequent recursion of the transformation method with $level + 1$.

e) ***level* $=$ 2 x number of particles+1: Calculating the summands in Eq. 4.7**
The end of one tensor path in the untransformed tensor is reached. The vectors holding the transformation coefficients for the matrix elements and their complex conjugates now only contain one value for each particle, respectively. The summand of Eq. 4.7 corresponding to the polarization combination described by the current path is calculated by multiplying all remaining coefficients with the current tensor entry. The result of this multiplication replaces the untransformed tensor entry.

Currently, this transformation is only implemented for massive spin-1 particles but it can be extended easily to e.g. unstable spin-1/2 particles (cf. Sec. 4.4.1). The execution of the transformation (step three) work already independent of the spin of the intermediate particles of interest. It only relies on the transformation coefficients $a^{(*)\mathrm{parti}}_{\lambda_i,\kappa_i}$ in Eq. 4.7 as input parameters. The transformation is not allowed to change the unpolarized result because it is independent of the specific choice of the basis for the polarization objects. This is checked for each event by comparing the unpolarized cross section before and after the transformation.

4.3.2 Labeling and Output of polarized cross sections

The multiplication of production tensor and decay matrices results in an amplitude tensor containing the squared matrix elements of all possible polarization combinations of the intermediate particles. They will be treated as additional weights for each event. For that, all tensor entries need to be named according to the polarization combination they describe. This is done in the constructor of a new class called `PolWeights_Map`. It inherits from a standard C++ map class and will contain all named polarization weights as spin label(key)-value pairs. By recursively traversing the amplitude tensor in a manner analogous to the transformation process described before, a spin label of the form `particle1.polarization1_particle2.polarization2`... (for concrete examples see Appendix A) is generated stepwise for each tensor path which describes a polarized matrix element contributing to the incoherent sum in Eq. 3.13. Concretely, these are the diagonal terms of the amplitude tensor. All other entries (=off-diagonal terms of the amplitude tensor) are totaled to an overall interference contribution. This procedure is

illustrated in Fig. 4.4. The values added to the map are polarization fractions obtained from dividing each polarized matrix element by the unpolarized result (=sum over all entries in the amplitude tensor).
Based on these base polarization weights, combined polarization fractions can be calculated. For massive VBs, additional weights are calculated where the transverse (plus and minus) polarization fractions are added. In order to obtain all polarization combinations of transverse polarized VBs with differently polarized particles, the weights to add are selected by iterating over the newly generated spin labels. The precise procedure is shown in Fig. 4.5.
Furthermore, the following additional weights are provided if specified in the run card:

partially unpolarized weights Intermediate particles, that shall get considered as non-polarized, can be specified by a comma-separated list of their particle numbers according to SHERPA's internal particle numbering in the run card. The associated weights are obtained by contracting the polarization indices of each future unpolarized particle (with m_{nhel} spin degrees of freedom) with a ($m_{\text{nhel}} \times m_{\text{nhel}}$)-matrix filled with ones. The algorithm described in Fig. 4.4 is subsequently applied on the resulting reduced amplitude tensor to label the remaining entries and calculate the associated interference contribution. It is smaller than the interference corresponding to the base weights, since the polarization weights in which the remaining polarized intermediate particles have a definite polarization also contain interference terms from the unpolarized particle. For example, if a process with two VBs is considered and the VB with the polarization indices λ_1, λ_1' in Eq. 4.6 remains unpolarized then the following entries of the amplitude tensor would contribute to the resulting single-polarized (=one of two intermediate VBs is in a definite polarization state) longitudinal weight with the interference terms in square brackets:
$|\mathcal{M}_{\text{singlepol}}|^2_{00} = |\mathcal{M}|^2_{+0+0} + |\mathcal{M}|^2_{-0-0} + |\mathcal{M}|^2_{0000} + \Big[|\mathcal{M}|^2_{+0-0} + |\mathcal{M}|^2_{+000} + |\mathcal{M}|^2_{-0+0} + |\mathcal{M}|^2_{-000} + |\mathcal{M}|^2_{00+0} + |\mathcal{M}|^2_{00-0}\Big]$.

sum of specified weights All base weights, which are specified as comma separated list of their weight names (spin label) in the run card are totaled. The calculation of these weights is straightforward by simply searching the respective weight names in the already generated `PolWeights_Map`.

Finally, the populated `PolWeights_Map` is added to the overall `Weights_Map`. It contains all event weights which will be output once the calculation of the current event is finished. All its entries are multiplied with the unpolarized event cross section in NWA to retrieve cross sections from the stored fractions.

The algorithm displayed in Fig. 4.4 strictly separates polarization contributions from interferences between different polarizations. Consequently, transverse weights calculated based

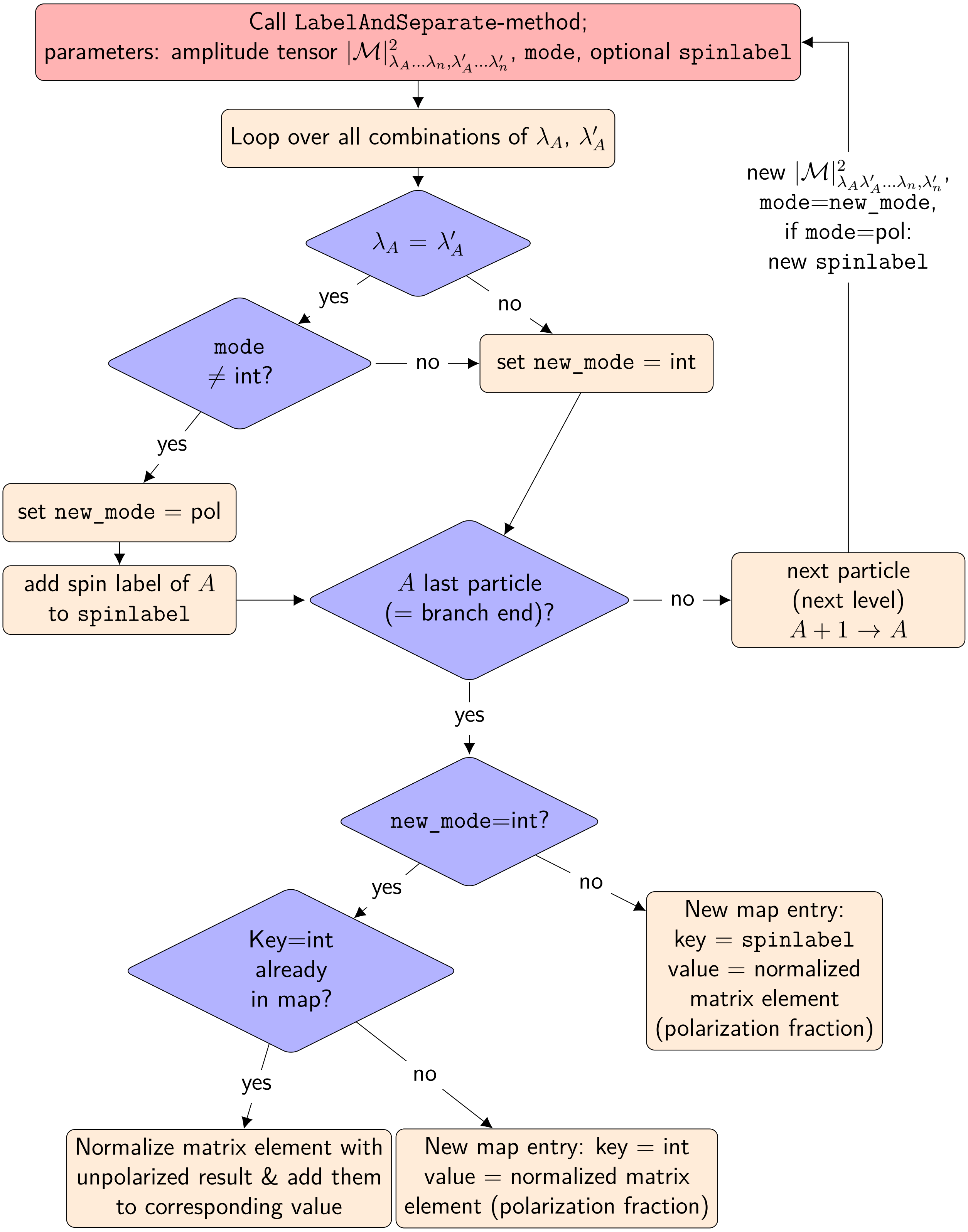

Figure 4.4: Flow chart for the labeling of the calculated polarized matrix elements and the separation of amplitude tensor entries where all intermediate particles are in a definite polarization state (diagonal terms, `mode`=pol) from the interference terms (off-diagonal terms, `mode`=int); spin labels have the form `particle1.polarization1_particle2.polarization2...`; besides `mode`={int, pol} there is also a third mode but it is not important for labeling and separation of polarized matrix elements and interferences; the unpolarized result necessary to get polarization fractions is given by the sum over all amplitude tensor entries.

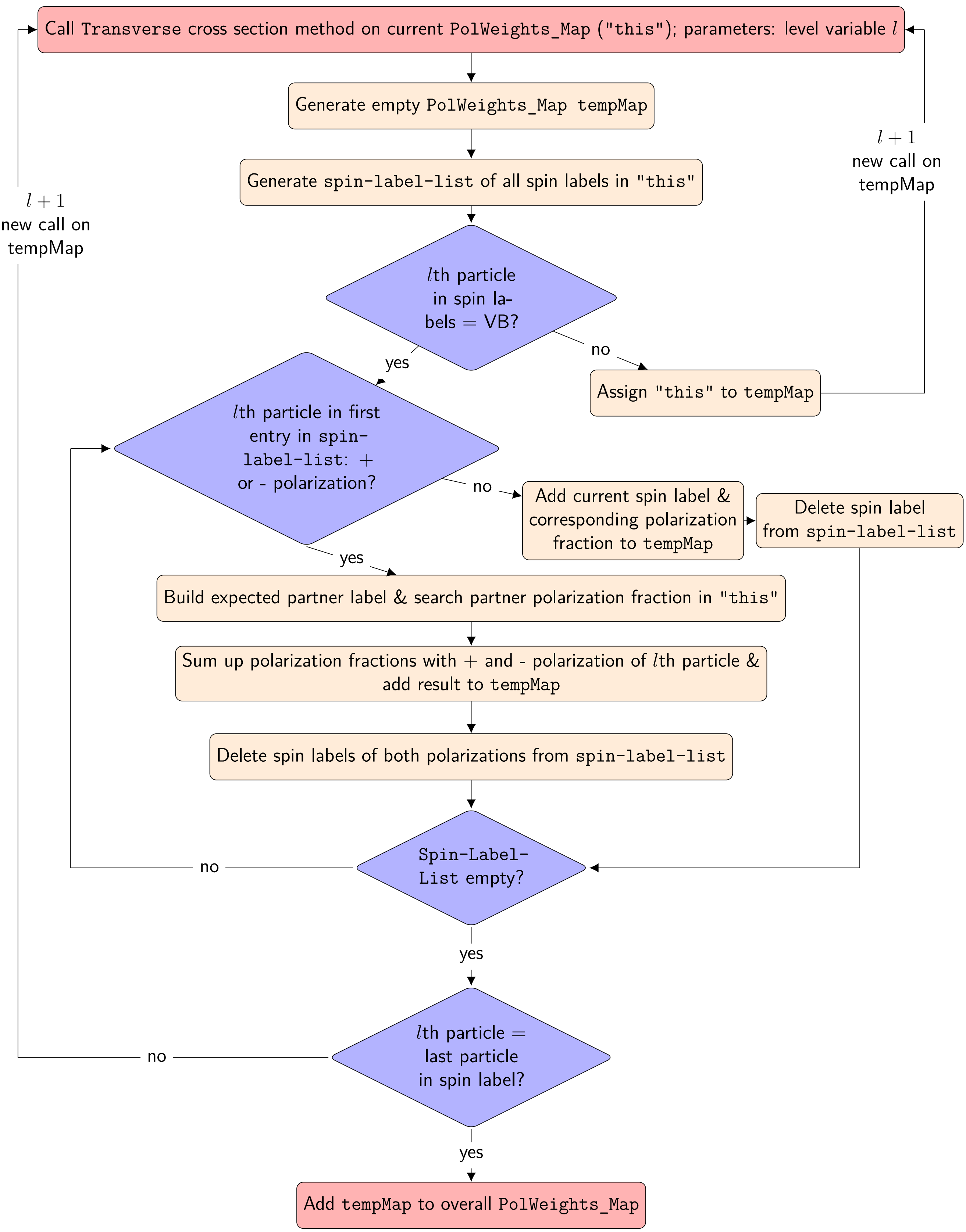

Figure 4.5: Flow chart for the calculation of transverse weights for massive vector bosons (VB), spin labels in `PolWeightMap` have the form `particle1.polarization1_particle2.polarization2...`, particles in the label are in the same order as in the `Amplitude2_Tensor`, level variable l numbers the particles in the spin label.

on the resulting labeled base weights can only contain polarized contributions from the incoherent sum in Eq. 3.13 (incoherent definition) where the matrix elements and their complex conjugates have the same polarization index. In the literature, it is more common [83] to add left-right interference terms to the definition of transverse polarized signals (coherent definition). For the single VB-production processes the following terms would e.g. be included: $|\mathcal{M}|^2_T = |\mathcal{M}|^2_{++} + |\mathcal{M}|^2_{--} + \left[|\mathcal{M}|^2_{+-} + |\mathcal{M}|^2_{-+}\right]$
The terms is square brackets denote the interference terms which are lacking in the incoherent transverse signal definition with respect to the coherent one. The coherent definition of the transverse signal can be useful when only the longitudinal polarization component is to be studied. By including a large part of the interference terms in the transverse signal, the need for an additional interference sample could be eliminated. The ability to calculate such weights with SHERPA is currently being added to the polarization framework. It is not yet tested and therefore not discussed in this thesis.

4.4 Implementation structure

In order to realize the described calculation steps, two new classes are introduced to SHERPA. If the calculation of polarized cross sections is enabled for a simulation run, a single instance of the `Polarized_CrossSections_Handler` class is initialized during the initialization of the `Hard_Decay_Handler`. It contains all polarization settings as members (`InitPolSettings()`). These are the spin basis, the reference systems of interest and optional custom weights. Furthermore, the default and the desired reference vector are set during the `Polarized_CrossSections_Handler` object construction if they are the same for each particle in each event (`InitRefMoms()`). This is the case for the default reference vector used for matrix element generation with COMIX.
Unless indicated otherwise, all methods mentioned in that section are methods of the `Polarized_CrossSections_Handler` class.
The actual calculation of polarized cross sections is steered by the `Treat()` method. It is called in `Hard_Decays::Treat()` after the simulation of all hard decays taking place in one event[2] so that the decay matrices of all unstable particles are available. The production tensor is read from the database of the signal vertex (signal blob) where it is stored after its construction from COMIX spin amplitudes in `Signal_Process::Fill_Blob()`.
For each desired reference frame, the `Treat()` method executes the `Calculation()` method which calculates the polarization fractions for the current polarization definition by calling all methods necessary to perform the steps described in the previous section. It determines the currently used and the desired polarization objects for each particle. The `Beta()` method

[2] The decays of the intermediate particles are generated in `Decay_Handler_Base::TreatInitialBlob()` which is also called by the `Hard_Decays::Treat()` method before the calculation of polarized cross sections starts.

provides the $\vec{\beta}$-vectors for the Lorentz transformation of the particle momenta to the desired reference system. The subsequent computation of the transformation coefficients is done in the classes of the polarization objects. The actual transformation of the matrix elements is a method of the `Amplitude2_Tensor` and `Amplitude2_Matrix` classes whose objects store the matrix elements of the production and decay subprocess, respectively.
Once the transformations of the production tensor and the decay matrices to the desired polarization basis are finished and their multiplication was performed, an instance of the second class `PolWeights_Map` is constructed as described in the previous section. For each reference system, a separate `PolWeights_Map` is computed which are finally all appended to the overall `Weights_Map` of the current event.

4.4.1 How to extend the current framework

Currently, the determination of the transformation coefficients is only implemented for massive spin-1 particles. However, the framework can easily be extended to particles with other spins. A new code block would need to be implemented in the `Calculation()` method to calculate the different polarization objects and their transformation coefficients. For that, the representation of the Lorentz transformation belonging to the new polarization objects as well as the solution of the system of equation resulting from the linear combinations connecting differently defined polarization objects would need to be added to SHERPA.
New spin bases can be implemented by adding a new keyword and the corresponding reference vector to the `InitRefMoms()` method. For additional reference systems, a new keyword and the associated $\vec{\beta}$-vector for the Lorentz transformation from the laboratory frame in the desired frame need to be appended to the `Beta()` method. This approach does not apply to $\vec{\beta}$- and reference vectors that differ for various particles. Such vectors must be implemented directly in the `Calculation()` method.

4.5 Calculation of polarized cross sections at NLO QCD with SHERPA

As described in the first part of this section, the new polarization feature is based on SHERPA's framework for computing factorized matrix elements of the production and decay of unstable, intermediate particles. This is not limited to LO, the production tensor can also include NLO contributions. This can in turn be used for the polarization calculation enabling the simulation of NLO polarization effects. Since NLO matrix elements can not be taken into account for the decay part of the process in SHERPA yet, only NLO QCD polarization effects can be investigated for VB production processes so far. This is due to the fact that NLO QCD corrections are only involved in the VB production (if only leptonic VB decays are considered) whereas NLO EW contributions would also affect the decay subprocess.

Moreover, the calculation of the production tensor relies on some approximations depending on the event type. Currently, polarization fractions beyond LO can only be calculated for event generation at particle-level where the matching of the NLO QCD fixed-order calculation to the parton shower is performed by the MC@NLO method. It leads to $\mathbb{S}$- and $\mathbb{H}$- events (see Sec. 3.1.2). For $\mathbb{S}$-events, the production tensor is calculated relying on real correction or Born matrix elements, depending on whether the first emission occurs or not. This leads to tree-level spin-correlations between the VB production and decay subprocesses with real or Born kinematics. For $\mathbb{H}$-events, the production tensor is exact, using real correction matrix elements for its computation. This results in tree-level spin-correlations with real kinematics. With this approach, effects of virtual corrections on the polarization fractions calculated from the amplitude tensor remain unconsidered. Therefore, the SHERPA setups for computing polarized cross sections beyond LO is referred as nLO setups in the following. The unpolarized result, however, includes the full NLO QCD corrections since the production tensor is only calculated on top of the generation of the unpolarized VB production event.

5 Validation of the implementation at fixed leading order

In this chapter, polarized integrated cross sections and differential distributions obtained with the new polarization framework are compared with literature data to validate the new implementation. More specific, integrated cross sections for the pure electroweak W^+W^+-, W^+W^--, ZZ- and W^+Z-production processes in association with two jets as well as differential distributions of all of them except for the W^+Zjj process are investigated at fixed LO ($\mathcal{O}(\alpha_{EW}^6)$). Additional validation was done for the pure electroweak W^+Zjj and inclusive W^+Z processes at fixed LO by two bachelor theses running parallel to this work [84, 85]. Both suggest a good agreement between literature results [59, 86] and the new implementation in SHERPA.
All considered literature data were obtained with PHANTOM [23] which, for the most processes, relies on the On-Shell-Projection technique [58] to omit single- and non-resonant diagrams. The only exception from that is the study of the ZZjj process in Ref. [59] where all double-resonant diagrams with full off-shell kinematics were taken into account. As described in the previous section, SHERPA uses a different approximation, so literature and SHERPA predictions may differ on the order of $\mathcal{O}(\Gamma_V/m_V)$ due to the deviating approaches used.
Before introducing the concrete simulation setups applied for the validation, some general remarks are made that apply to all simulations done throughout this thesis. After describing the studied processes and the simulation setups used, the SHERPA simulation results obtained with them are compared with literature predictions. At the end of this chapter, a short study of the W^+j process is performed to investigate the influence of the deviating transverse polarization definition used in the literature and in SHERPA (cf. Sec. 4.3.2) on the polarized predictions.

5.1 General remarks on SHERPA simulations in this thesis

All predictions within this work are computed for a LHC beam setup with 13 TeV proton-proton center of mass energy assuming Standard Model (SM) dynamics. Only fully leptonic, mixed flavor (for two VB production processes) VB decay channels are studied. All leptons are considered as massless. The same holds for the quarks except the top quark, if not stated otherwise. Masses and widths of the massive particles remain unchanged compared to the

SHERPA default if not given differently. The polarization is always defined in the helicity basis. For each investigated process, two simulation runs are done:

- **Full calculation (short: full):** No approximation is applied so that all effects from the actual offshellness of the intermediate VBs as well as all from not-fully-resonant contributions (short: non-resonant contributions for simplicity) are retained. If comparisons with literature data are performed, a comparison of the full integrated cross sections between SHERPA and literature ensures that identical simulation parameters are used.

- **Polarized calculation:** uses SHERPA's spin-correlated narrow-width approximation as introduced in Sec. 4.1 to compute polarized cross sections and distributions. Furthermore, the unpolarized cross section in NWA (short: unpol) is obtained from this calculation. It represents the sum of all polarization contributions (short: polsum) and the interferences, i.e. the coherent sum of all polarized matrix elements. The unpol differs from the full result by the missing non-resonant contributions and not-completely covered off-shell effects. However, since experiments allow measuring the full result only, these differences should be small in considered phase spaces.

Errors given to the simulation results within this thesis consists only of statistical MC-errors caused by the limited number of events simulated. There are also systematical errors due to scale and PDF choice, which could be estimated by scale- and PDF-variations. In SHERPA, these variations would not have any influence on the polarization fractions; the same fractions would only be multiplied by another unpolarized cross section for each variation. Therefore, they are not shown in the following.
The data generated with SHERPA is analyzed via the analysis-framework RIVET (version 3) [87]. It is used to compute and plot differential distributions. For the calculation of $W^{\pm}$ boson observables, a perfect neutrino reconstruction is assumed. Within the event generation, only selection criteria on final state particles of the hard scattering process (= VB production subprocess) can be applied. All remaining selection criteria are then implemented in the subsequent RIVET-analysis.

5.2 Simulation setup

This section compiles all simulation parameters and phase space definitions, that are employed for the validation. They are chosen identical to the literature. Example run cards which define the applied SHERPA setups for the full as well as the polarization simulation can be found in Appendix C.
Tab. 5.1 shows all investigated processes together with the corresponding literature reference, the used reference frame for polarization definition, and whether only integrated cross sections

are provided in the associated paper. PDF set, factorization scale, coupling constants as well as VB masses and decay widths are set to:

- PDF-Set: NNPDF30_lo_as_0130 from LHAPDF6 [88]
- Electroweak scheme: G_μ scheme with $G_\mu = 1.16637 \cdot 10^{-5}$ GeV^{-2} and

$$\alpha_{\mathrm{EW}} = \frac{\sqrt{2} G_\mu M_{\mathrm{W}}^2}{\pi} \left(1 - \left(\frac{M_{\mathrm{W}}}{M_{\mathrm{Z}}}\right)^2\right) \tag{5.1}$$

  For the full calculation, the complex mass scheme is assumed, for polarized calculations real EW parameters are applied to retain gauge invariance (see Ref. [58] for details)
- Strong coupling: consistent with PDF set $\alpha_S(M_{\mathrm{Z}}^2) = 0.130$
- Factorization scale: $\mu_F = M_{4\mathrm{l}}/\sqrt{2}$ (ZZjj, $\mathrm{W}^+\mathrm{W}^-$jj), $\mu_F = \sqrt{p_{\perp,\mathrm{j}_1} p_{\perp,\mathrm{j}_2}}$ (all results from Ref. [76])
- VB pol masses: $M_{\mathrm{W}} = 80.358$ GeV, $M_{\mathrm{Z}} = 91.153$ GeV
- VB pol widths: zero for all VB in polarization calculations [1], $\Gamma_{\mathrm{W}} = 2.084$ GeV, $\Gamma_{\mathrm{Z}} = 2.494$ GeV otherwise.

Usually, two different phase spaces were investigated in the literature which are called inclusive and fiducial phase space. The former is only described by acceptance criteria on jets and the VB masses whereas the latter also includes selection criteria on leptons. Differential distributions are usually only given for the fiducial phase space in the literature. For all studied VBS-processes, the applied phase space definition is very similar:

- inclusive phase space
  - maximum jet pseudorapidity $|\eta_{\mathrm{j}}| < 5$
  - minimum jet transverse momentum $p_{\perp,\mathrm{j}} > 20$ GeV
  - minimum jet-jet invariant mass $M_{\mathrm{jj}} > 500$ GeV
  - minimum jet-jet pseudorapidity separation $|\Delta\eta_{\mathrm{jj}}| > 2.5$
- additional selection criteria for the fiducial phase space definition
  - maximum lepton pseudorapidity $|\eta_{\mathrm{l}}| < 2.5$
  - minimum lepton transverse momentum $p_{\perp,\mathrm{l}} > 20$ GeV
  - if neutrino(s) are contributing: minimum missing transverse momentum $p_{\perp,\mathrm{miss}} > 40$ GeV.

[1] Regardless of whether all VB types occur as intermediate particles in a process, all VB widths must be set to zero if this is done for one VB type. Otherwise, the $SU(2)$-Ward identities are violated [83].

If additional or deviating selection criteria are applied, they are stated in Tab. 5.1. A b-veto is understood as a perfect b-veto on initial and final states.
RIVET-analyses used for analyzing the simulation data are based on a suitable RIVET standard analysis (ATLAS_2017_I1625109 for ZZjj), on a RIVET-Analysis of Carsten Bittrich & Maren Buhring [89] (W^+W^+jj) or are completely self written (W^+Zjj, W^+W^-jj).
For all processes, observables are investigated, that can only be defined for the mixed lepton flavor decay channel of the VB pair, if the VBs are identical. Same flavor lepton decay channels which can not be excluded by SHERPA during the simulation of several identical VBs (ZZjj, W^+W^+jj process), get then vetoed during the Rivet-analyses for all observables. Therefore, no ambiguity for the reconstruction of the VBs from their decay products exist. Corresponding single-polarized cross sections are calculated by an additional method in the `PolWeights_Map` class, that adds up all helicities, leaving only the VB decaying in a specified decay channel polarized. The resulting weights are zero for same flavor decay channels and if the specified decay channel does not occur in the current event (syntax cf. Appendix C).
Typically, the considered observables are directly related to the momenta of the final state particles. The lepton decay angle forms an exception and is defined in Sec. 3.3.

Table 5.1: Some details about the literature studies used to validate the new SHERPA implementation for simulating polarized cross sections for vector boson (VB) production; abbreviations: M=invariant mass, η=pseudorapidity, XS=cross section, Lab=laboratory frame, COM=center-of-mass frame of the VB pair; listed additional selection criteria are applied for both the inclusive and fiducial phase space.

Process $\mathcal{O}(\alpha^6_{\mathbf{EW}})$	**Reference**	**additional selection criteria**	**Reference system**	**Only XS**
W^+W^+jj: $pp \to e^+\ \nu_e\ \mu^+\nu_\mu jj$	[76]	$M_{4l} > 161$ GeV [2]	Lab, COM	
W^+W^-jj: $pp \to e^+\ \nu_e\ \mu^-\ \bar{\nu}_\mu jj$	[76]	b-veto, $M_{4l} > 2M_W$	Lab, COM	×
W^+W^-jj: $pp \to \mu^+\ \nu_\mu\ e^-\ \bar{\nu}_e jj$	[58]	b-veto, $M_{WW} > 300$ GeV $M_{jj} > 600$ GeV, $\lvert\Delta\eta_{jj}\rvert > 3.6$, $\eta_{j_1} \cdot \eta_{j_2} < 0$ lepton selection criteria only on e^-	Lab	
W^+Zjj: $pp \to e^+\ \nu_e\ \mu^+\mu^- jj$	[76]	b-veto, $M_{4l} > 200$ GeV $\lvert M_{e^+e^-} - M_Z\rvert < 10$ GeV	Lab, COM	×
$ZZjj$: $pp \to e^+\ e^-\ \mu^+\mu^- jj$	[76]	b-veto, $M_{4l} > 200$ GeV $\lvert M_{l^+l^-} - M_Z\rvert < 10$ GeV	Lab, COM	×
	[59]	b-veto, $M_{4l} > 200$ GeV $\lvert M_{l^+l^-} - M_Z\rvert < 15$ GeV	Lab	

[2]The M_{4l} selection requirement for the W^+W^+jj process is only applied during the polarization calculation.

5.3 Integrated polarized cross sections and polarization fractions

Inclusive phase space

A first validation of the new implementation is done against data supplied by Ref. [76]. There, integrated polarized cross sections with VB polarization defined in both laboratory (Lab) and VB-pair center-of-mass frames (COM) are published for four VBS-processes in the inclusive phase spaces defined in the previous section. In particular, the implemented matrix element transformation can be verified by comparing the results obtained for the COM with the literature data.
The general behavior, expected from the literature predictions, is that pure longitudinal contribution and pure transverse polarization have the smallest and largest cross section, respectively. For the double-polarized signals (=short for both VBs are in a definite polarization state) discussed here, the definition of polarization in the COM typically shows an increased longitudinal contribution compared to the Lab definition. The behavior of the other polarization contributions depends on the concrete process under consideration [76] (see also Sec. 6.1).
Tab.s 5.2-5.5 compare literature and SHERPA results for the four processes. The unpolarized cross sections obtained with SHERPA agree with the full calculation within the MC errors (W^+W^+jj, W^+Zjj) or within the sub-percent level (ZZjj, W^+W^-jj). This indicates that the approximation used by SHERPA provides a good description of the full result for the investigated phase space region.
The delta between the unpolarized results from the literature and SHERPA ranges in the sub-percent area for all processes except ZZjj. This deviation is much smaller than the accuracy of $\mathcal{O}(\Gamma/M)$ ($\sim$ 2.5%) expected due to the different approximations used. For the ZZjj process, the relative difference between the unpolarized cross sections provided by SHERPA and PHANTOM is about twice as large as for the other processes (∼1.3%[3]), but still within the expected accuracy.
Polarized predictions made by the new implementation show similar deviations as the corresponding unpolarized cross sections compared to the literature results, independent of the chosen reference frame. Consequently, the polarization fractions calculated relative to the unpolarized results mostly agree within the MC-errors. The few exceptions such as $W^+_L W^-_L jj$ (COM), $W^+_L W^+_L jj$ (Lab) and $W^+_L Z_T jj$ (COM) have deviations of less than 0.6%. The simulated interference contribution is compatible to zero within the MC-errors, as expected when no lepton acceptance criteria are applied.
Generally, the cross sections obtained with SHERPA are slightly larger than the PHANTOM predictions. Since this tendency is already present in the unpolarized result and thus unaffected

[3]Deviations between the literature and SHERPA cross sections/fractions are quantified in this chapter by reporting relative differences, if not stated otherwise.

Table 5.2: Integrated double-polarized cross sections for the W^+W^+jj process at fixed LO obtained with PHANTOM in Ref. [76] and SHERPA in the inclusive phase space defined in Sec. 5.2; the polarization is defined in the laboratory and the W^+W^+-center-of-mass frame; polarization fractions are calculated relative to the unpolarized result.

W^+W^+	σ_{Phantom} [fb]	fraction [%]	σ_{Sherpa} [fb]	fraction [%]
full	3.185(3)		3.1814(13)	
unpol	3.167(2)	100	3.1839(10)	100
Laboratory frame				
polsum	3.1631(16)	99.88(8)	3.1827(22)	99.96(8)
int			0.0012(19)	
L-L	0.2573(3)	8.124(11)	0.25722(28)	8.079(9)
T-L+L-T	1.2398(12)	39.15(5)	1.2485(10)	39.212(34)
T-T	1.666(1)	52.60(5)	1.6770(13)	52.67(4)
W^+W^+-center-of-mass frame				
polsum	3.1637(15)	99.90(8)	3.1819(21)	99.94(7)
int			0.0019(18)	
L-L	0.3275(4)	10.341(14)	0.32986(31)	10.360(10)
T-L+L-T	1.0162(10)	32.087(38)	1.0239(8)	32.160(27)
T-T	1.820(1)	57.47(5)	1.8281(14)	57.42(5)

Table 5.3: Integrated double-polarized cross sections for the W^+W^-jj process at fixed LO obtained with PHANTOM in Ref. [76] and SHERPA in the inclusive phase space defined in Sec. 5.2; the polarization is defined in the laboratory and the W^+W^--center-of-mass frame; polarization fractions are calculated relative to the unpolarized result.

W^+W^-	σ_{Phantom} [fb]	fraction [%]	σ_{Sherpa} [fb]	fraction [%]
full	4.651(2)		4.631(22)	
unpol	4.641(2)	100	4.6707(22)	100
Laboratory frame				
polsum	4.6401(12)	99.98(5)	4.673(4)	100.05(10)
int			-0.003(5)	
L-L	0.3314(2)	7.141(5)	0.3338(6)	7.147(14)
L-T	0.8545(4)	18.412(12)	0.8616(12)	18.448(28)
T-L	0.8912(4)	19.203(12)	0.8974(11)	19.213(25)
T-T	2.563(1)	55.225(32)	2.5802(24)	55.24(6)
W^+W^--center-of-mass frame				
polsum	4.6404(12)	99.98(5)	4.675(4)	100.09(10)
int			-0.0041(34)	
L-L	0.3786(3)	8.158(7)	0.3826(8)	8.192(17)
L-T	0.7669(3)	16.524(10)	0.7736(12)	16.562(28)
T-L	0.8119(4)	17.500(11)	0.8176(13)	17.506(29)
T-T	2.683(1)	57.811(33)	2.7009(24)	57.83(6)

Table 5.4: Integrated double-polarized cross sections for the W^+Zjj process at fixed LO obtained with PHANTOM in Ref. [76] and SHERPA in the inclusive phase space defined in Sec. 5.2; the polarization is defined in the laboratory and the W^+Z-center-of-mass frame; polarization fractions are calculated relative to the unpolarized result.

W^+Z	σ_{Phantom} [fb]	fraction [%]	σ_{Sherpa} [fb]	fraction [%]
full	0.5253(3)		0.5258(11)	
unpol	0.5210(3)	100	0.52471(27)	100
		Laboratory frame		
polsum	0.52089(24)	99.98(7)	0.52473(40)	100.00(9)
int			-0.000013(296)	
L-L	0.03236(3)	6.211(7)	0.03270(6)	6.232(12)
L-T	0.08923(8)	17.127(18)	0.09002(11)	17.156(23)
T-L	0.1045(1)	20.058(22)	0.10535(12)	20.078(25)
T-T	0.2948(2)	56.60(5)	0.29669(25)	56.54(6)
		W^+Z-center-of-mass frame		
polsum	0.52069(24)	99.94(7)	0.52474(39)	100.00(9)
int			-0.000029(292)	
L-L	0.03993(5)	7.664(11)	0.04031(7)	7.682(14)
L-T	0.08926(8)	17.132(18)	0.09020(11)	17.190(23)
T-L	0.1039(1)	19.942(22)	0.10462(12)	19.939(25)
T-T	0.2876(2)	55.20(5)	0.28962(24)	55.196(5)

Table 5.5: Integrated double-polarized cross sections for the ZZjj process at fixed LO obtained with PHANTOM in Ref. [76] and SHERPA in the inclusive phase space defined in Sec. 5.2; the polarization is defined in the laboratory and the ZZ-center-of-mass frame; polarization fractions are calculated relative to the unpolarized result.

ZZ	σ_{Phantom} [fb]	fraction [%]	σ_{Sherpa} [fb]	fraction [%]
full	0.1270(1)		0.12715(25)	
unpol	0.1264(1)	100	0.12801(10)	100
		Laboratory frame		
polsum	0.12621(5)	99.85(9)	0.12798(14)	99.97(14)
int			0.00003(10)	
L-L	0.00910(1)	7.199(10)	0.009235(22)	7.214(18)
T-L+L-T	0.04842(4)	38.31(4)	0.04903(7)	38.30(6)
T-T	0.06869(3)	54.34(5)	0.06972(9)	54.46(8)
		ZZ-center-of-mass frame		
polsum	0.12621(6)	100	0.12800(14)	99.99(14)
int			0.00002(10)	
L-L	0.01087(2)	8.600(17)	0.010968(24)	8.568(20)
T-L+L-T	0.04044(4)	31.99(4)	0.04103(6)	32.05(5)
T-T	0.07490(4)	59.26(6)	0.07600(10)	59.37(9)

by the new implementation, it is clearly caused by the different approximations.
All in all, perfect agreement is found between the two generators regarding the VBS processes in the studied inclusive phase space indicating that the separation of polarized cross sections from the unpolarized calculation and the transformation to physical polarizations bases works at least at the level of integrated cross sections.

Fiducial phase space

For a more thorough validation, this thesis also compares polarized differential distributions with literature data for the W^+W^+jj, the ZZjj and the W^+W^-jj process. They are computed in the fiducial phase spaces defined in Sec. 5.2. At first, the resulting integrated cross sections are discussed, displayed in Tab.s 5.8-5.7. For all three processes, the unpolarized result reproduces the full cross section at the 1% level, indicating small non-resonant contributions and low off-shell effects not covered by the mass smearing.

Table 5.6: Integrated single-polarized cross sections for the ZZjj process at fixed LO obtained with PHANTOM in Ref. [59] and SHERPA in the fiducial phase space introduced in Sec. 5.2; single-polarized cross sections are given for the Z boson decaying into an electron-positron pair being polarized; the polarization is defined in the laboratory frame; polarization fractions are calculated relative to the unpolarized result.

ZZ	σ_{Phantom} [fb]	fraction [%]	σ_{Sherpa} [fb]	fraction [%]
full	0.06102(4)		0.060987(27)	
unpol	0.06059(4)	100	0.06116(4)	100
polsum	0.05891(2)	97.23(7)	0.059452(29)	97.21(8)
int	0.00168(4) (diff)	2.77(7)	0.001712(24)	2.80(4)
long-unpol	0.01619(1)	26.721(24)	0.016230(15)	26.536(29)
left(-)-unpol	0.02676(2)	44.17(4)	0.027079(21)	44.27(4)
right(+)-unpol	0.01595(1)	26.324(24)	0.016143(14)	26.394(28)

For the ZZjj (Tab. 5.6) and the W^+W^-jj process (Tab. 5.7), the literature only reports single-polarized cross sections with polarization defined in the Lab, where the Z boson decaying into an electron-positron pair or the W^- boson are considered as polarized. Generating a left-handed Z or W^- boson seem to be most probable. For the W^+W^-jj process, it was not possible to achieve a perfect agreement of the full results from SHERPA and PHANTOM. However, since the literature only provides polarization fractions (relative to the full!) for this process, this does not pose a limitation for the comparison.
Polarization and interference fractions obtained with SHERPA are in very good agreement with the literature for both processes showing deviations in the sub-percent range at most.
The polarized cross sections for the ZZjj process differ from the literature about the same as the unpol result (<1.5%), which is perfectly within the expected accuracy. The interference

Table 5.7: Integrated cross sections for the W^+W^-jj process at fixed LO obtained with PHANTOM in Ref. [58] and SHERPA in the fiducial phase space introduced in Sec. 5.2; single-polarized cross sections are given for the W^- boson being polarized; the polarization is defined in the laboratory frame; polarization fractions are calculated relative to the full result.

W^+W^-	σ_{Phantom} [fb]	fraction [%]	σ_{Sherpa} [fb]	fraction [%]
full	1.411(1)	100	1.3537(11)	100
unpol	1.401(1)	99.29(10)	1.3497(5)	99.70(9)
polsum	1.382(1)	97.94(10)	1.3309(9)	98.32(11)
int	0.019(1) (diff)	1.35(7)	0.0188(8)	1.39(6)
unpol-long		21	0.28969(33)	21.400(30)
unpol-left(-)		52	0.7047(5)	52.06(6)
unpol-right(+)		25	0.3365(4)	24.86(4)

prediction for both processes, whose cancellation is spoiled by the lepton selection criteria, agree perfectly between the two generators.

Regarding the W^+W^+jj process, polarized cross sections for single- and double-polarized (Tab. 5.8) signals with polarization defined in the Lab and in the COM are available in the literature. For single-polarized cross sections, the W^+ boson decaying into $e^+\nu_e$ is considered as polarized and is mostly transverse polarized (~75%). Compared to the inclusive phase space, the additional lepton selection criteria applied reduce the cross section by roughly a factor of two. Fiducial polarization fractions differ in absolute terms by at most a few percent from the inclusive fractions (max. 2.7(2)% for TT-Lab(COM)), the differences between the two polarization definitions remain. In contrast to the fiducial cross sections discussed for the other two processes, the different definition of the transverse signals in SHERPA and PHANTOM plays a role here and may be the reason for the 1.5%-4.5% reduction observed for the SHERPA transverse cross sections[4] compared to literature data and for the different sign of the interference. Deviations for the COM are slightly smaller than for the Lab polarization definition. The observations that the longitudinal cross sections show only <1% difference (LL in COM) or even complete agreement (Lab, single-polarized signals), the TT cross sections are most affected (4-4.5% reduction w.r.t. the literature) and the differences between the PHANTOM and SHERPA transverse cross sections are as large as the differences between the interference predictions, fit to the expected behavior when comparing the two different definitions. Therefore, a bug in the new implementation seems unlikely as an alternative cause. As both generators deliver the same results for the unpolarized cross sections, the polarization fractions differ by the same amount as the cross sections. For transverse signals, fractions

[4]A note on the terminology: The terms transverse cross sections/fractions/distributions in the case of double-polarized cross sections include the pure transverse contribution (TT) but also the mixed components (LT, TL) in the rest of the thesis. The TT contribution is then denoted as pure transverse contribution.

relative to the polsum are also given in Tab. 5.8. For those, the influence of the different definitions is reduced, leading to an agreement of closer than 1.5(1)% (double(single)-polarized) with the literature for both polarization definitions, which is within the expected accuracy due to the different approximations used.

Table 5.8: Integrated single- and double-polarized cross sections for the W^+W^+jj process at fixed LO obtained with PHANTOM in Ref. [76] and SHERPA in the fiducial phase space introduced in Sec. 5.2; single-polarized cross sections are given for the W^+ boson decaying into $e^+\nu_e$ being polarized; the polarization is defined in the laboratory and the W^+W^+-center-of-mass frame; polarization fractions are calculated relative to the unpolarized [polsum] result.

W^+W^+	σ_{Phantom} [fb]	fraction [%]	σ_{Sherpa} [fb]	fraction [%]
full	1.593(2)		1.5901(13)	
unpol (double)	1.572(2)	100	1.5744(7)	100
unpol (single)	1.572(2)	100	1.5726(9)	100
		Laboratory frame		
polsum (single)	1.5876(11)	100.99(15)	1.5591(11)	99.14(9)
int (single)	-0.0156(23)	-0.99(15)	0.0136(9)	0.86(6)
T-unpol	1.165(1)	74.11(11) [73.38(8)]	1.1369(10)	72.29(8) [72.92(8)]
L-unpol	0.4226(4)	26.88(4)	0.4222(5)	26.847(35)
polsum (double)	1.5999(10)	98.62(17) [100]	1.5503(17)	98.47(6) [100]
int (double)	-0.0279(22) (diff)	-1.77(14)	0.0241(15)	1.53(10)
L-L	0.1185(1)	7.538(12)	0.11871(18)	7.540(12)
T-L+L-T	0.6124(6)	38.96(6) [38.28(4)]	0.6005(8)	38.14(5) [38.73(6)]
T-T	0.8690(9)	55.28(9) [54.32(7)]	0.8311(10)	52.79(7) [53.61(8)]
		W^+W^+-center-of-mass frame		
polsum (single)	1.5856(21)	100.87(19)	1.5604(11)	99.22(9)
int (single)	-0.0136(29) (diff)	-0.87(18)	0.0122(8)	0.78(5)
T-unpol	1.182(2)	75.19(16) [74.45(14)]	1.1565(10)	73.54(8) [74.18(8)]
L-unpol	0.4036(5)	25.67(5)	0.4039(4)	25.684(29)
polsum (double)	1.5940(10)	101.40(14) [100]	1.5520(15)	98.58(10) [100]
int (double)	-0.0220(22) (diff)	-1.40(14)	0.0224(14)	1.42(9)
L-L	0.1552(2)	9.873(18)	0.15633(20)	9.929(13)
T-L+L-T	0.5038(6)	32.05(6) [31.606(38)]	0.4961(6)	31.51(4) [31.97(5)]
T-T	0.9350(9)	59.48(9) [58.66(6)]	0.8995(10)	57.13(7) [57.96(9)]

5.4 Differential cross sections

As already announced in the previous section, differential distributions for the W^+W^+jj, the ZZjj and the W^+W^-jj process are also compared with literature results for a more thorough validation. In Fig. 5.1-5.3 distributions of two observables for each process are shown. For a better comparison, the literature and the SHERPA distributions are shown side by side. Further studied distributions can be found in Appendix D.1. Polarization definitions and type of signal (single-/double-polarized) are identical to the integrated cross sections in the fiducial phase space.
The shapes of the distributions generated with the new SHERPA implementation are in very good agreement with the literature. Relative contributions of the several polarization modes to the full and the relative differences between examined polarization definitions (if more than one provided) seem to behave very similar. Slight differences in individual bins are well within the accuracy expected when comparing the two different approximations. Except for the W^+W^-jj process (incompletely fitting full result), the normalization of the distributions also fit well.

W^+W^+jj: For the W^+W^+jj process (Fig. 5.1), notable differences between the SHERPA and PHANTOM polarized distributions can be observed above all for the TT contributions ($p_{\perp,\mathrm{WW}} < 180$ GeV, around $\eta_{e^+} = 0$ and $\Delta\phi_{\mathrm{ll}} < 1.5$ (see Appendix D.1)). These regions, too, stand out in the ratio plots for either slightly different shape of the polsum (Lab polsum around $\eta_{e^+} = 0$ and COM polsum for $\Delta\phi_{\mathrm{ll}} < 1.5$) or large interference effects in general ($p_{\perp,\mathrm{WW}} < 100$ GeV). This indicates that the different definitions of the transverse signal and with that the distinct interference contribution has an impact here and could explain the slightly different behavior. It may also explains the slightly different normalization of transverse polarized distributions for this process.
The polsum vs. full ratio is shifted downwards in the SHERPA results compared to the literature predictions according to the positive rather than negative interference already observed in the integrated cross sections. The shapes of the ratios of unpol and the polsums w.r.t. the full as well as relative to each other are largely comparable with the literature result.
ZZjj: Regarding the ZZjj process, the only visible difference is found for the m_{ZZ} distribution shown in Fig. 5.2. At high m_{ZZ}, the difference between the right-handed and the longitudinal predictions seems to be smaller than in the literature, but this could be a statistical effect due to the very small cross section in these bins.
W^+W^-jj: For the W^+W^-jj process (Fig. 5.3), the transverse polarized distributions of the transverse W^- boson momentum $p_{\perp,\mathrm{W}^-}$ at low momenta show a slightly different behavior respective to each other. In addition, the distance between the maxima of the full and polsum distributions for m_{ll} (and η^{W^-}, see Appendix D.1) are slightly larger for the PHANTOM result which could be caused by either slightly larger interference prediction in that region or off-shell effects captured differently in the DPA.

From the ratio plots in Fig. 5.1 for the W^+W^+jj process and the differences between the full and unpol distributions for the other processes, it can be deduced that the unpolarized distribution approximates the full distribution to a good extend. For all three processes, the differences are mostly below 2%. Larger non-resonant effects arise for high transverse momenta of the VB pair and the positron in the W^+W^+jj process reaching differences up to 5% for $p_{\perp,e^+}$ (see Appendix D.1) as well as for the lepton-lepton invariant mass in the W^+W^-jj process below 50 GeV (up to 7-10%).

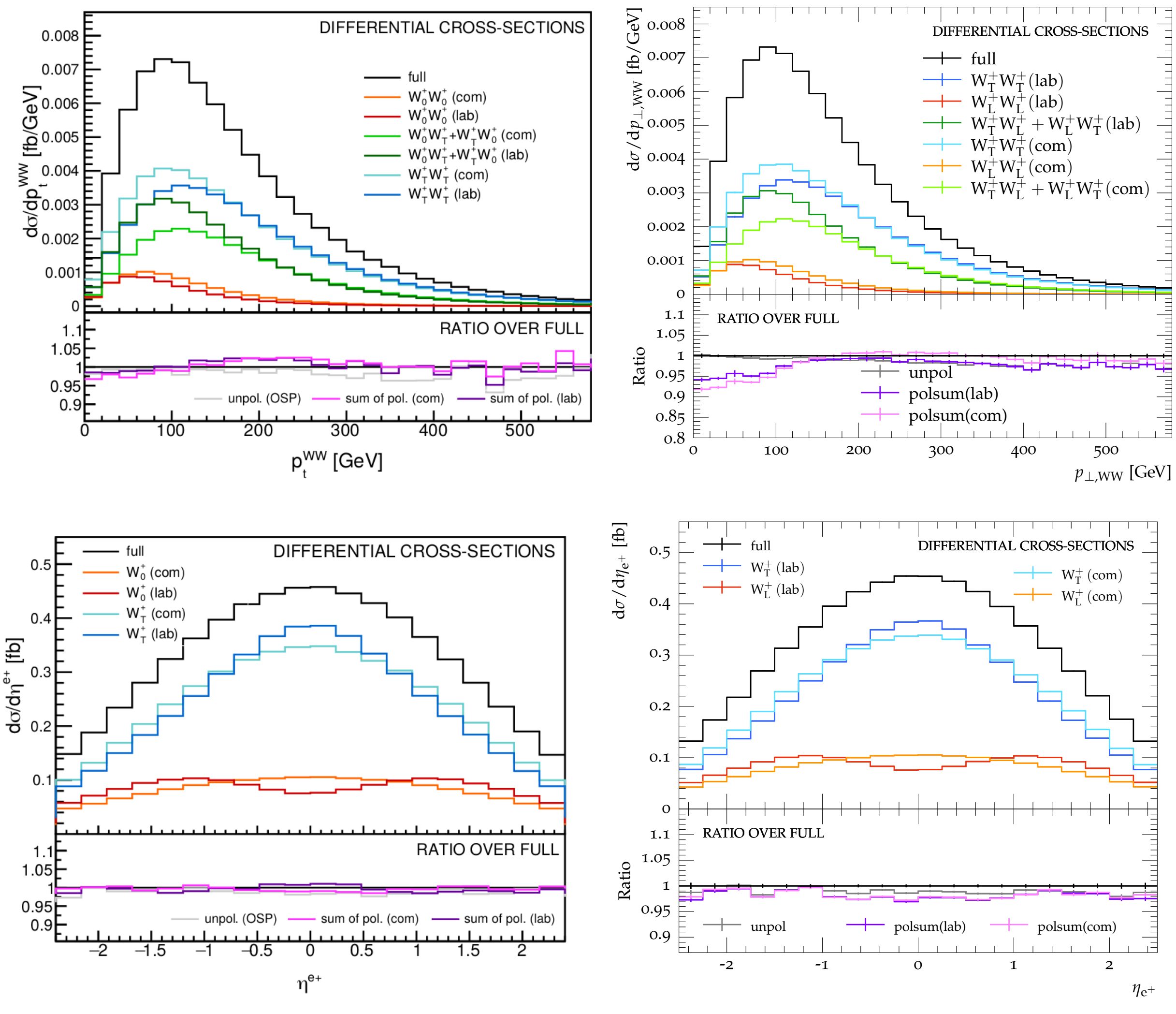

Figure 5.1: Double-polarized distributions of the W^+W^+ transverse momentum $p_{\perp,WW}$ (top) and single-polarized distributions of the positron pseudorapidity η^{e^+} (bottom) for the W^+W^+jj process from the literature [76] (left) and the new SHERPA implementation (right); polarized differential distributions and the ratios over the full off-shell result are shown in the top respectively bottom graph of each subfigure. Distributions are presented with polarization definition in the W^+W^+ center of mass frame (com) and the laboratory frame (lab) in the fiducial phase space according to Sec. 5.2. For the single-polarized distributions, the W^+ boson decaying into an anti-muon-neutrino pair is considered as unpolarized.

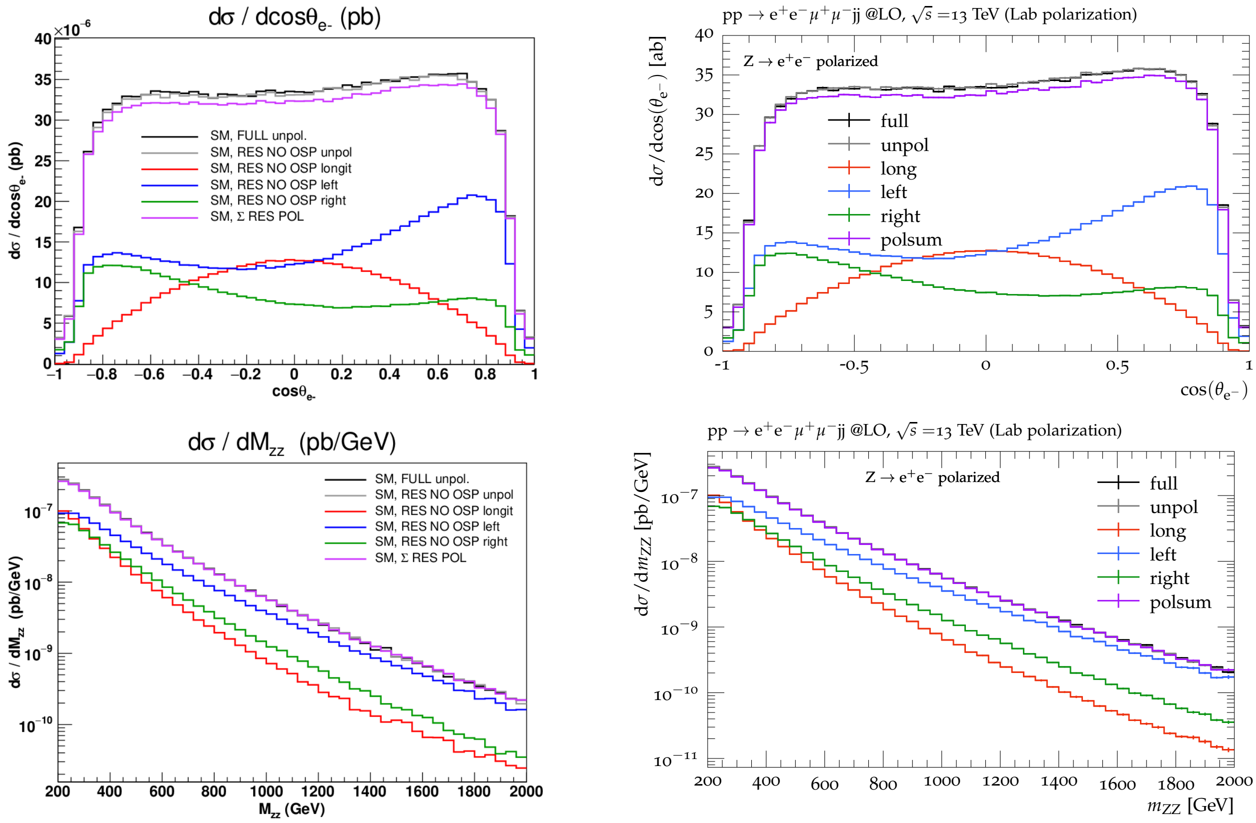

Figure 5.2: Single-polarized distributions of the lepton decay angle $\cos\theta_{e^+}$ (top) and of the ZZ-invariant mass M_{ZZ} (bottom) for the ZZjj process from the literature [58] (left) and the new SHERPA implementation (right); the Z boson decaying into $\mu^+\mu^-$ is considered as unpolarized, the polarization is defined in the laboratory frame (lab), simulations are done in the fiducial phase space according to Sec. 5.2.

In conclusion, a very good agreement between PHANTOM and SHERPA simulations at fixed LO is observed for both integrated and differential cross sections, independent of the VBs involved and the polarization definition used. Observed deviations are small or can be attributed to the different definitions of the transverse polarization in the literature and in SHERPA. Furthermore, it is confirmed that the unpolarized predictions obtained by applying SHERPA's spin-correlated NWA reproduce the full result comparably well as the DPA for the investigated processes and phase spaces. So, all in all, the new SHERPA implementation is able to provide polarized cross section predictions comparable with the literature at fixed LO.

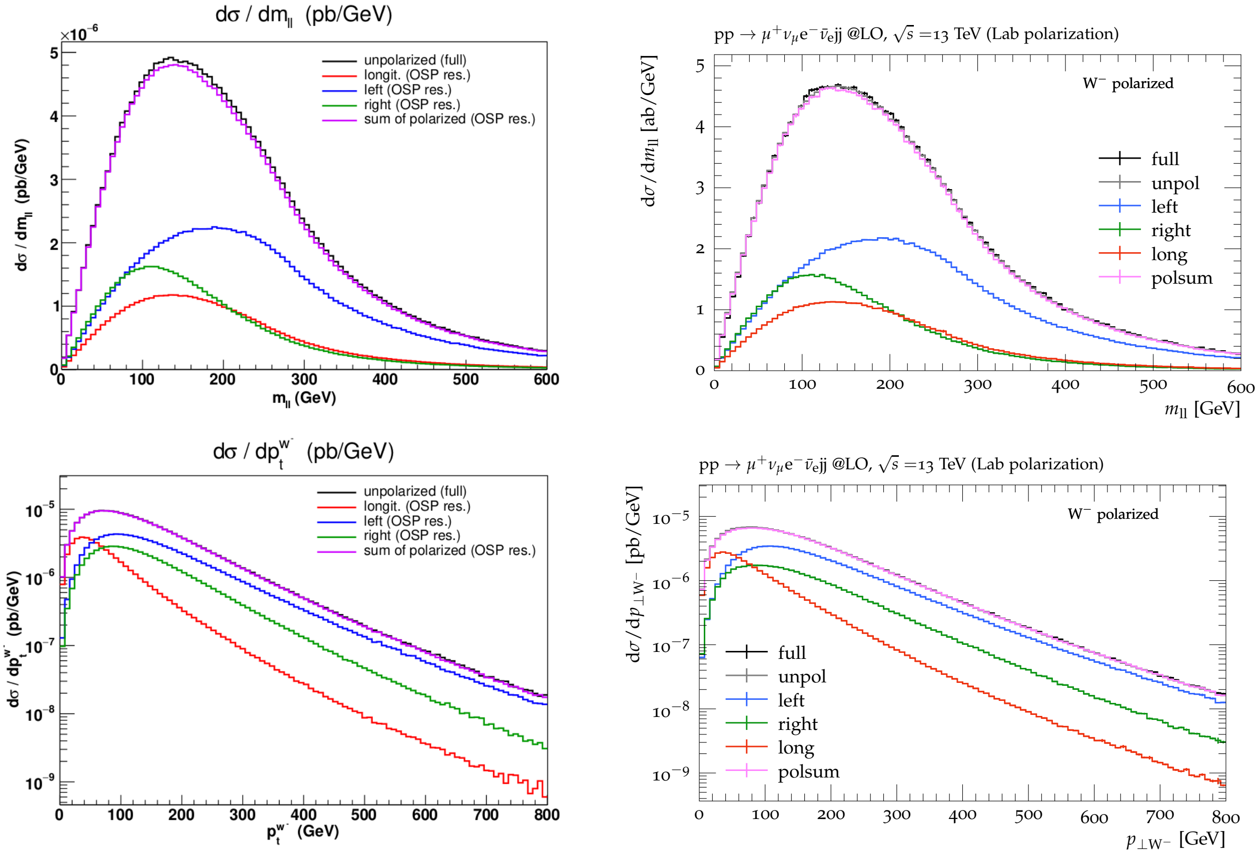

Figure 5.3: Single-polarized distributions of the lepton-lepton-invariant mass m_{ll} (top) and the W$^-$ boson transverse momentum $p_\perp^{W^-}$ (bottom) for the W$^+$W$^-$jj process from the literature [58] (left) and the new SHERPA implementation (right); the W$^+$ boson is considered as unpolarized, the polarization is defined in the laboratory frame(lab), simulations are done in the fiducial phase space according to Sec. 5.2.

5.5 Comparison of coherent and incoherent transverse signal definition for W$^+$j production

As already discussed in Sec. 4.3, the current definition of transverse polarized cross sections in SHERPA does not include any left-right-interference. Within the validation study in this section, deviations between literature and SHERPA predictions are most commonly found for transverse polarized cross sections. In this section, a short comparison of the coherent and incoherent transverse signal definitions from SHERPA with the literature results is presented for the single-W$^+$j production process pp → e$^+\nu_e$j, since for them, the coherent definition can be implemented very easily. The simulation settings and the phase space are chosen according to Ref. [77] to allow for a comparison with literature data. Details about that are given in Appendix C.2.

The literature predictions were computed up to NNLO accuracy with the STRIPPER framework with tree-level amplitudes from the AvH library and one-loop amplitudes from a proprietary

Table 5.9: Integrated cross sections for the W^+j production at fixed LO obtained from the literature [77] and SHERPA; for the SHERPA predictions results for the coherent and the incoherent transverse polarization definition are displayed; the polarization is defined in the laboratory frame, polarization fractions are calculated relative to the unpolarized result.

W^+j	$\sigma^{LO}_{Literature}$ [pb]	fraction [%]	σ^{LO}_{Sherpa} [pb]	fraction [%]	σ^{LO}_{Sherpa} [pb]	fraction [%]
			incoherent definition		coherent definition	
full	408.69(3)		420.97(37)		420.97(37)	
unpol	413.83(3)	100	423.24(9)	100	423.24(9)	100
polsum	413.21(3)	99.850(10)	436.85(10)	103.216(32)	422.62(10)	99.854(32)
int	0.620(31)	0.150(7)	-13.481(37)	-3.185(9)	0.620(36)	0.146(9)
T	319.31(3)	77.160(9)	341.48(8)	80.682(26)	327.24(8)	77.318(25)
L	93.898(5)	22.710(2)	95.371(32)	22.534(9)	95.371(32)	22.534(9)

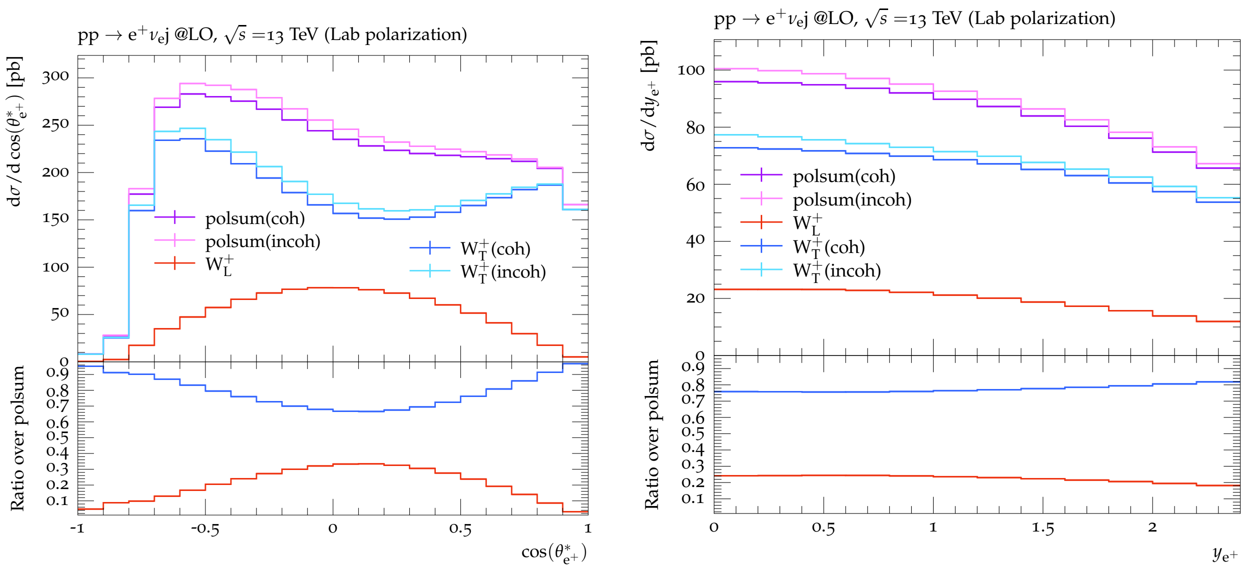

Figure 5.4: Polarized distributions of the positron decay angle $\cos(\theta^*_{e+})$ and the positron rapidity y_{e^+} for the single W^+j production process at fixed LO obtained with SHERPA for incoherent (incoh) and coherent (coh) transverse signal definition (i.e. without and with including left-right interference terms), polarization is defined in the laboratory frame (Lab).

extension of OpenLoops 2. In addition, a spin-correlated narrow-width approximation is applied. A mass smearing procedure is not mentioned. Comparisons with SHERPA simulations with and without mass smearing result in a better agreement between literature and SHERPA predictions if no mass smearing is assumed. Therefore, only these results are summarized in Tab. 5.9 for the two different definitions of the transverse signal in comparison with the literature.

It was not possible to reach full agreement for the full cross section results so differences between SHERPA and literature prediction may occur. Nonetheless, it is evident, that the coherent signal definition corrects cross sections and polarization fractions towards the literature results. While the incoherent transverse fraction differ by 5% compared to the literature the deviation is reduced to <0.5 % for the coherent definition. The interference prediction even agree in cross section and fraction for the coherent definition.

The polarization fractions from SHERPA (coherent definition) and literature possess a good agreement up to the sub-percent level indicating that the implementation also delivers reliable predictions for the single W^+-production case. Remaining differences could be caused to the obviously not completely identical simulation results or result from a potential different handling of spin-correlations.

Fig. 5.4 displays the distribution of the positron decay angle $\cos\left(\theta^*_{e^+}\right)$ and the positron rapidity y_{e^+}. From them, it is evident, that the transverse signal definition can also have an effect on the shapes of the distributions. A comparison with literature distributions in Ref. [77] is more complicated at distribution level since Ref. [77] provides distributions at NNLO accuracy only. Nonetheless, SHERPA can reproduce the principle shapes. Observed deviations can be attributed to higher-order effects, e.g. deviating relative contributions to the polsum result for both shown observables or the decrease of the differential distribution starting at smaller rapidities y_{e^+} than in the literature, especially for the longitudinal contribution.

All in all, this small study demonstrates that deviations observed in the previous section could indeed be explained by the different definitions of the transverse signal used since the distinct definitions can lead to notable differences in polarized integrated and differential cross sections. In addition, no indications could be found that the new SHERPA implementation does not work for the single VB production case.

6 Application in phenomenological studies

In the previous chapter, a very good agreement between the new SHERPA polarization framework and the literature is found for several VB production processes at fixed LO, leading to the conclusion that the new implementation is basically functional. Therefore, it is subsequently applied in some first phenomenological analyses to give an insight into what could be studied in terms of VB polarization utilizing the new features within the powerful capabilities of SHERPA. For all performed simulations, the general simulation remarks given in Sec. 5.1 are valid.

6.1 Influence of the polarization definition on polarized cross sections for VBS processes at fixed LO

The VB pair center-of-mass frame and the parton-parton frame (PPFr) are common reference systems used for VB polarization measurements in experimental analyses of VB production processes [16, 18], but they are not fully studied for all VBS processes in the phenomenological literature yet. With the new polarization feature in SHERPA, it is easy to investigate different polarization definitions; all results for all reference systems of interest can be obtained with a single simulation run. Therefore, as a first application of the new framework, this section investigates four pure electroweak VB production processes in association with two jets with different VB combinations at fixed LO with respect to the differences between Lab, COM and PPFr reference frames. Furthermore, non-resonant and interference contributions are discussed and compared among the processes. The Lab is chosen as the starting point since it represents the measurement frame in SHERPA. Results for other polarization definitions are always compared with the predictions for that reference system within this study.

6.1.1 Simulation setup

In order to study the influence of the polarization definitions on polarized VBS processes, the following VBS processes are considered at fixed LO ($\mathcal{O}(\alpha_{EW}^6)$):

W^+W^+jj: $pp \to e^+ \nu_e \mu^+ \nu_\mu jj$

W^+W^-jj: $pp \to \mu^+ \nu_\mu e^- \bar{\nu}_e jj$

W^+Zjj: $pp \to \mu^+ \nu_\mu e^+ e^- jj$

ZZjj: $pp \to e^+ e^- \mu^+ \mu^- jj$

For each VB combination, only one decay channel is studied and only the ”plus” signatures are considered. Corresponding charge-conjugate processes and other decay channels can be investigated analogously. For comparability, all investigated processes are simulated with the same simulation parameters and phase space. The factorization scale is set to $\mu_F = M_{4l}/\sqrt{2}$. All other simulation parameters are identical to the parameters introduced in Sec. 5.2. The used phase space is defined as follows:

- selection criteria from the fiducial phase space defined in Sec. 5.2
- $M_{4l} > 200$ GeV for a better comparison with DPA results in the literature
- b-veto to suppress top-resonance in W^+Zjj, W^+W^-jj[1]
- $|M_Z - M_{l^+l^-}| < 15$ GeV for reduced γ contribution and finite cross sections

and is referred to as comparison phase space in this study.
Applied RIVET-analyses stay the same as in Sec. 5.2. The set of studied observables is selected from those which were already considered in VB polarization studies for VBS processes in the literature [58, 59, 76] and which possess significantly different shapes for distinct polarizations useful for the extraction of single polarization components from unpolarized distributions. This includes the transverse momentum as well as the pseudorapidity of all VBs $p_{\perp,\mathrm{VB}}$, η_{VB} and final state charged leptons $p_{\perp,l}$, η_l, the charged lepton decay angles of the VBs $\cos\theta^*_l$, the invariant mass of as well as the azimuthal angle difference between two final state, charged leptons from different VBs $m_{ll'}$, $\Delta\Phi_{ll'}$ and the transverse momentum of the VB-pair $p_{\perp,\mathrm{VB1\,VB2}}$.
Single-polarized as well as double-polarized cross sections are studied. For single-polarized distributions of observables that are connected to only one VB, the following statements are referring to only those observables associated with the VB considered as polarized. Observables only connected with the unpolarized VB are found to be nearly unaffected by a change of the polarization definition.

[1]For the W^+W^+jj and the ZZjj process neglecting b quarks in the partonic process reduces the cross section only by 0.5% (ZZjj) [59] or even leads to no differences within the statistical error (W^+W^+jj).

6.1.2 Integrated cross sections and polarization fractions

In this section, the effects of different reference systems on the integrated polarized cross sections are discussed and compared between the considered processes. Fig. 6.1 gives an overview of the polarization fractions for the four investigated VBS-processes obtained for three different reference systems (Lab, COM, PPFr). Fractions for double-polarized (bottom) as well as single-polarized (top) signals are shown. Corresponding cross sections can be found in Appendix D.3. A quick comparison of integrated polarized cross sections with polarization defined in the Lab and COM in the inclusive phase space of Sec. 5.2, also regarding the differences between different VBS processes, was already done in Ref. [76]. Therefore, the following discussion also probes the persistence of their findings in a more realistic setup that also includes basic lepton selection criteria.
In the following discussion, cross section (XS) deviations among the various polarization definitions are quantified as relative differences while absolute differences are stated for fractions. If XS and fraction differences are both specified, a bracket notation is used: XS(fraction).

As noted in the validation study in Chap. 5, SHERPA's NWA provides a good approximation for the full result in the VBS phase space. This is confirmed by the results from this study where the unpol cross section for all processes differs by at max. 1% from the full result. Interestingly, the NWA approximation underestimates the full cross section for the processes including only $W^\pm$ bosons but overestimates it for the W^+Zjj and the ZZjj process.

Regarding double-polarized cross sections/fractions, the TT polarization is the dominant contribution with roughly 55% for all processes, while the LL polarization is the smallest one with 5-9%, beside the interference. It is enhanced in the COM compared to the other two frames for all four processes wherefore this frame might be the best candidate of those for extracting the LL part from the unpolarized result.
In the PPFr, the LL contribution is - for all studied processes - even smaller than in the Lab. If the reference system is changed from the Lab to the PPFr, the polarization contributions of the different processes behave pretty similar. Mixed and LL components are reduced by 4-5(1.4-1.7)% and 7-9(~ 0.5)% (except ZZjj with 12(0.8)% reduction for LL), which is balanced by an increase of the transverse component by 2-4(1.3-1.9)%.
The similarity between the processes found when comparing Lab and PPFr polarization definitions does not appear when evaluating differences between the Lab and the COM definition. The LL component increases similarly for the ZZjj and the W^+Zjj process in the COM w.r.t. the Lab (XS: 22-23%), while it gains significantly more for the W^+W^-jj (XS: 26%) and the W^+W^+jj process (XS: 45%). This leads to a larger LL polarization fraction of 1.3-1.6% for the former three processes and ~ 3% for the W^+W^+jj process. A more detailed analysis of Fig. 6.1 reveals that the W^+W^+jj and the ZZjj processes are influenced the most by the

reference frame change from Lab to COM. Both show a rather large increase of the LL and TT (6(3.3)% (W^+W^+jj), 11(5.3)% (ZZjj)) contributions which is balanced by a reduction of the mixed component by 15%/19%(1.7%). For the W^+W^-jj process, the TT component, however, only shows a moderate increase of ∼2(1)% in the COM w.r.t. the Lab. Consequently, the mixed contributions are less reduced. The W^+Zjj process reveals a fundamentally different behavior when changing the reference system from Lab to COM than the other processes. This has already been observed in Ref. [76] for the inclusive phase space in Sec. 5.2. The enhancement of the LL component is compensated here by a decrease of the TT component. The mixed components basically stay the same for both polarization definitions (LT, <0.5(0.1)%) or even increase slightly (TL, 2(0.4)% w.r.t. the Lab).
In general, the most polarization components in all processes except the W^+Zjj process are more affected by a reference system change from Lab to COM than from Lab to PPFr (exception: TT in the W^+W^-jj process). For the W^+Zjj process, the transverse contributions show larger deviations from the Lab results for the PPFr polarization definition.
Another feature can be identified for all polarization definitions when comparing the two mixed contributions. While the LT and TL components show rather similar proportions (4-6.5(1)% differences) in the W^+W^-jj process, the contribution with transverse W^+ and longitudinal Z boson is preferred in the W^+Zjj process (∼30(6)% difference in each frame).
The interference contribution is very different among the studied processes. The processes involving two $W^\pm$ bosons show a significantly smaller interference fraction (1-3%) than processes with Z boson participation. The largest interference contribution is observed for the ZZjj process with about 6% w.r.t. the unpolarized result. The influence of the chosen polarization definitions on the size of the interference contribution is also strongly process-dependent, spreading from no deviations within MC errors (e.g. ZZjj Lab vs. COM) to differences of 42% (W^+W^+jj Lab vs. PPFr) for XS and 0.7% for fractions (W^+Zjj Lab vs. COM). For all processes, the PPFr polarization definition leads to the largest interference fraction. The COM definition results in the smallest one (except for the ZZjj process with no difference between Lab and COM fraction within the MC errors).

Looking at single-polarized cross sections, it turns out that the VBs are mainly left-handed. The associated fraction is between 44 and 49% for all processes and polarization definitions except for the W^+Zjj process with polarized W^+ boson, where this fraction is much higher, reaching 57-59%. For the majority of processes and polarization definitions, the longitudinal polarization forms the smallest fraction (2-8% smaller than the right-handed fraction). The exception from that is the W^+Zjj process, here the longitudinal fractions are up to 3% larger than the right-handed ones.
Single-polarized cross sections / polarization fractions are less sensitive to varying polarization definitions than their double-polarized associates, as already observed in Ref. [76] in an inclusive phase space and for Lab vs. COM polarization definitions. The largest cross section differences

appear for the longitudinal polarization in the most processes with at max. 8% (ZZjj, Lab vs. COM) (beside the interference).

When going from Lab to PPFr, the longitudinal cross section/fraction is affected the most and is reduced by about the same amount in all processes (4-6($\sim$1-1.5)%). The transverse polarization contributions are slightly increased by 1-3(<1)%.

The deviations between integrated Lab and COM predictions are more process-dependent for single-polarized signals too, compared to the differences observed between Lab and PPFr. The longitudinal components of the W^+W^+jj and the W^+W^-jj process are found to be nearly unaffected by the reference system change (<1(0.4)%)[2]. This is different for the ZZjj and the W^+Zjj process, whose longitudinal components additionally possess different trends when comparing the two polarization definitions: while the longitudinal components for the VBs contributing to the W^+Zjj process show an enhancement of 6(1-1.5)%, the longitudinal contribution for the ZZjj process is reduced by 8(2)%. The contribution of the right-handed single-polarized VBs is enhanced in all processes w.r.t. the Lab, the left-handed contribution is mostly reduced (except for the ZZjj process), if affected at all.

The interference contribution for single-polarized signals is smaller than the interference prediction for double-polarized signals, since some interference terms of the VB considered as unpolarized are already included into the polarized signals. Still, processes involving Z bosons reach interferences contributions of 2-3%. The PPFr polarization definition still leads to the largest interference contributions.

Polarized W^+ bosons reveal a similar interference in both WW-scattering processes- it is the smallest one among all processes. The interference contribution of the (single-)polarized W^- boson in the W^+W^- process is about three times larger than for the polarized W^+ boson. This is not found for the W^+Zjj process, here, simulations with the W^+ or the Z boson being polarized result in about the same interference contribution.

Analogous to double-polarized signals, the influence of the polarization definition on the interference can be large for single-polarized VBs (XS: up to 53% for the W^+W^- process if the W^+ boson being polarized), which - again - depends strongly on the process and, additionally, on the polarized VB within one process (compare e.g. single-polarized W^+ and W^- bosons in the W^+W^-jj process).

[2]This behavior differs from Ref. [76] where the longitudinal components in the W^+W^+jj and the W^+W^-jj process are reduced by 3% in the COM definition w.r.t. the Lab. Therefore, it is concluded in Ref. [76] that the W^+Zjj process is again special among the processes due to the enhancement of this component in the COM w.r.t. the Lab. This cannot be deduced from the results of the present study due to the observed discrepancies for the longitudinal component in the W^+W^+jj and the W^+W^-jj process. They are not caused by the additional lepton selection criteria applied in this study which is concluded from simulations without them (cf. Tab.s D.4, D.5 in the Appendix) revealing similar polarization definition effects as with them. They seem to be due to the different scale choices whose effect is even larger for double-polarized signals: the difference between LL cross sections in Lab and COM is 31[14]% for the W^+W^+jj[W^+W^-jj] process in the literature, while the study within this thesis get a 24%[45%] difference. For the W^+Zjj and the ZZjj process as well as for transverse contributions, such an influence of the scale choice is not observed.

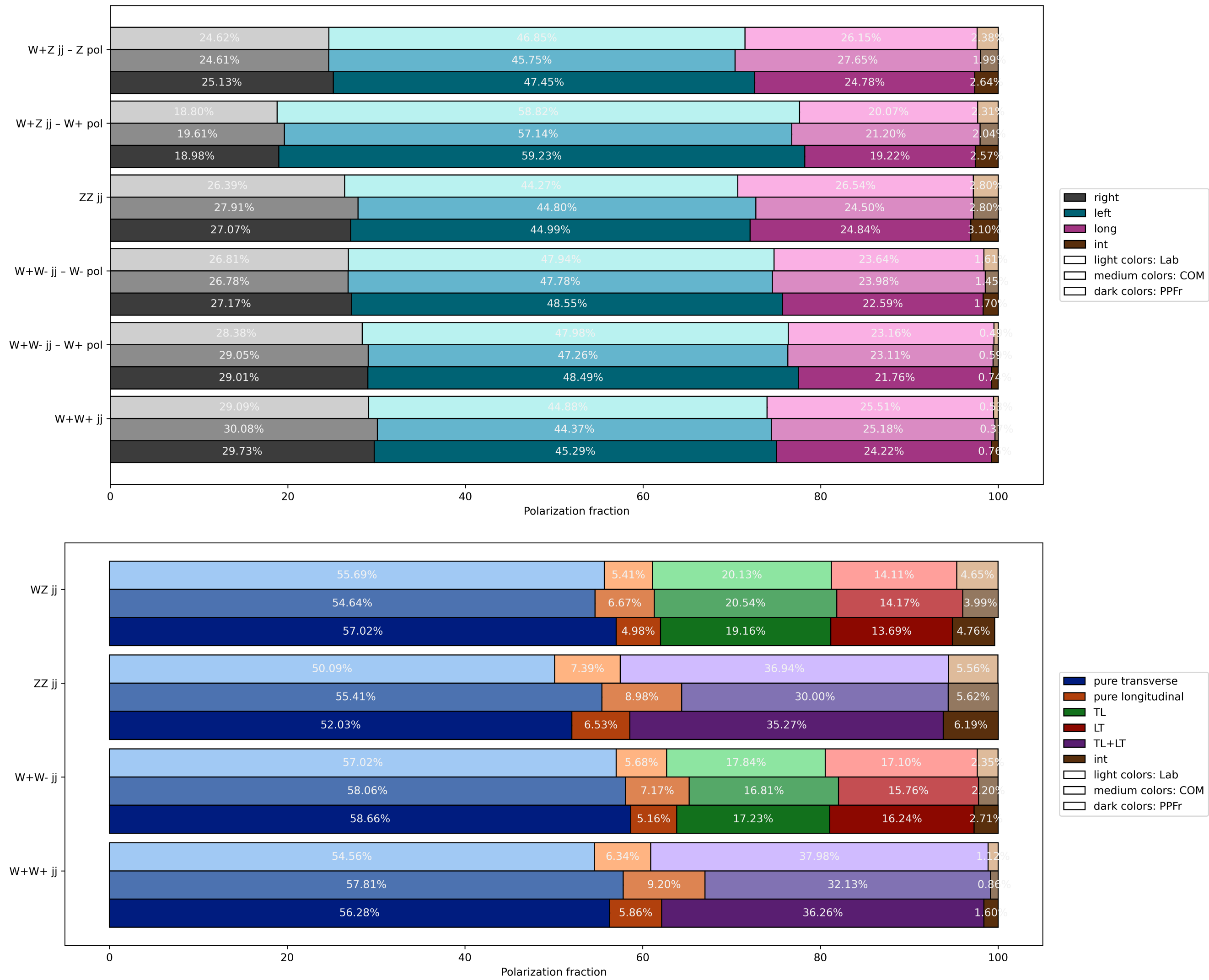

Figure 6.1: Polarization fractions for the pure electroweak W^+W^+jj, W^+W^-jj, W^+Zjj and $ZZjj$ processes at fixed leading order with polarization defined in the laboratory (Lab), the VB pair center-of-mass (COM) and the parton-parton-frame (PPFr); simulations are done in the comparison phase space introduced in Sec. 6.1.1; upper and lower diagrams show single- and double-polarized polarization fractions respectively; polarization fractions are calculated relative to the unpolarized result.

6.1.3 Polarized differential distributions

Besides the integrated cross sections and polarization fractions discussed in the previous section, the polarization definition also has an effect on differential distributions. This largely depends on the chosen observable and the studied configuration (double- or single polarized cross sections with Lab vs. COM or Lab vs. PPFr). The change of the polarization definition is found to have only little influence on the transverse momenta of single leptons or VBs for both single- and double-polarized signals (see Fig. D.12 in the Appendix for an example). $p_{\perp,\mathrm{VB1VB2}}$, m_{ll} and $\Delta\Phi_{\mathrm{ll'}}$ exhibit noticeable shape differences only when changing the reference frame from Lab to COM. For $p_{\perp,\mathrm{VB1VB2}}$, they are much more prominent if double-polarized cross sections are considered; for m_{ll} they are completely local in the region of the peak (see Fig. D.13 for an example). η_{l}, $\cos\theta^{*}_{\mathrm{l}}$ and η_{VB} reveal sizable shape deviations for all configurations. In the following, for each configuration, one observable revealing noticeable shape differences is shown and discussed in more detail to illustrate which deviations can appear on distribution level when changing the reference system. In order to achieve better comparability among the processes, the mixed polarized contributions are combined in this study.

In Fig. 6.2, the polarized VB pair transverse momentum distributions $p_{\perp,\mathrm{VB1VB2}}$ for the four studied VBS processes are displayed as an observable showing significant shape differences for double-polarized signals when changing the reference system from Lab to COM. This observable was already discussed in Ref. [76] for the $\mathrm{W^+W^+jj}$ process also regarding differences between the Lab and COM polarization definition. Comparing this result with the predictions for the other processes, a similar shape is found for all of them.
Considerable differences between the two polarization definitions are visible for all processes. The TT and mixed distributions in the COM and the TT distribution in the Lab exhibit similar shapes among each other in each of the four processes, while the mixed distributions are narrower in the Lab. The LL component has its maximum at lower values than the transverse distributions; it differs between Lab and COM for all processes between $p_{\perp} = 60$ GeV (Lab) and 70 GeV (COM) except for the $\mathrm{W^+Zjj}$ process (both at $p_{\perp} = 60$ GeV). Differences between the two polarization definitions are dominant in the region of the peak. The LL component reveals an enhancement in the COM compared to the Lab for $p_{\perp}$ above the peak to account for the observed larger polarization fraction in that frame. The pure transverse distribution is increased in the COM compared to the Lab for $p_{\perp}$-values below 150-300 GeV, the specific value depends on the process and the associated integrated polarization fraction. For larger $p_{\perp}$ values above 150-300 GeV, the Lab pure transverse component is larger. For the mixed polarization, the sequence is switched to balance the behavior of the pure polarized components. This behavior is found for all studied processes.
However, there are also differences among the processes, so this observable also serves as an example for the observation that changing the polarization definition can lead to process-dependent effects at distribution level, too. The four processes are distinguished mainly by the magnitude of the differences between the polarization definitions in the peak region and in the tail of the distribution. The $\mathrm{W^+W^+jj}$ and the ZZjj process show the largest differences in the peak region, in the tail the differences between the two definitions are small. For the $\mathrm{W^+W^-jj}$ and the $\mathrm{W^+Zjj}$ process, the magnitude of the fraction differences between Lab and COM in peak and tail region is very similar.
Another observable showing process-dependent effects when changing the polarization definition from Lab to COM is the azimuthal angle difference between charged leptons resulting from the decay of two different VBs $\Delta\Phi_{\mathrm{ll'}}$ (cf. Fig. 6.3 and Fig. D.16 in the Appendix). Fig. 6.3

shows single-polarized $\Delta\phi_{\mu^+e^-}$ distributions for the W^+W^-jj process. They indicate that the influence of the polarization definition on the distributions of the same observable can be different for distinct types of (single-)polarized VBs. While the longitudinal fraction reveals the same behavior for (single-)polarized W^+ and W^- bosons being larger in the COM compared to the Lab below angular separations of $\frac{\pi}{2}$ and smaller above, the behavior of the transverse components differs among the two VBs. The left[right]-handed COM-contribution is larger[smaller] compared to the Lab below $\Delta\phi_{\mu^+e^-} = \frac{\pi}{2}$ and vise versa above for the single-polarized W^+ boson but smaller[larger] below and larger[smaller] above $\Delta\phi_{\mu^+e^-} \sim \frac{\pi}{2}$ if the W^- boson is the only polarized VB. Furthermore, it is also evident from this observable that changing the polarization definition can have a significant effect on the shape of distributions even if the integrated cross sections stay nearly unaffected.

Effects of changing the polarization definition are not always process-dependent. As already evident from the polarization fractions, the PPFr polarization definition shows a rather similar effect for all investigated processes w.r.t. the Lab. This also holds at the level of differential distributions.
In Fig. 6.4 (a), the double-polarized Z-boson pseudorapidity distributions η_{Z_e} of the ZZjj process are presented as an observable revealing noticable shape differences when changing the polarization definition from Lab to PPFr. Due to similar effects for all processes and even for all types of VBs, only polarized distributions for one process and VB is shown in Fig. 6.4. Remaining distributions can be found in Fig.s D.14, D.15 (top left) in the Appendix.
The distributions of η_{VB} reveal that the specific polarization definition can influence the discrimination power of observables between different polarizations which is useful for extracting polarization fractions from unpolarized distributions. In the PPFr, the shape of the pseudorapidity distribution for the different polarization combinations become more equalized which reduces the discrimination power among polarizations of that observable in the PPFr w.r.t. the Lab polarization definition. While polarization combinations with at least one longitudinal VB reveal a symmetric shape with two clear maxima at about $\eta_{VB} = \pm 1.5$ and a local minimum at $\eta_{VB} = 0$ in the Lab, in the PPFr, the mixed component has just one maximum at zero pseudorapidity and the two maxima of LL are only barely recognizable. In addition, the pure transverse distribution is broadened around $\eta_{VB} = 0$ for the PPFr definition w.r.t. the Lab, the at least partial longitudinal polarized distributions are narrower than their Lab associates. However, the homogenization of the distributions for different polarization combinations is not a unique property of the PPFr; it can also be observed for the COM definition (cf. Fig. D.15 (top right) in the Appendix). Furthermore, similar shape differences can be identified in the single-polarized case and for the lepton pseudorapidity (cf. Fig. D.15 (c),(d) in the Appendix). Thereby, the effect of the polarization definition on η_{VB} distributions is found to be larger than on η_l distributions where the transverse distributions are already more similar in the Lab frame than for η_{VB} differential cross sections.

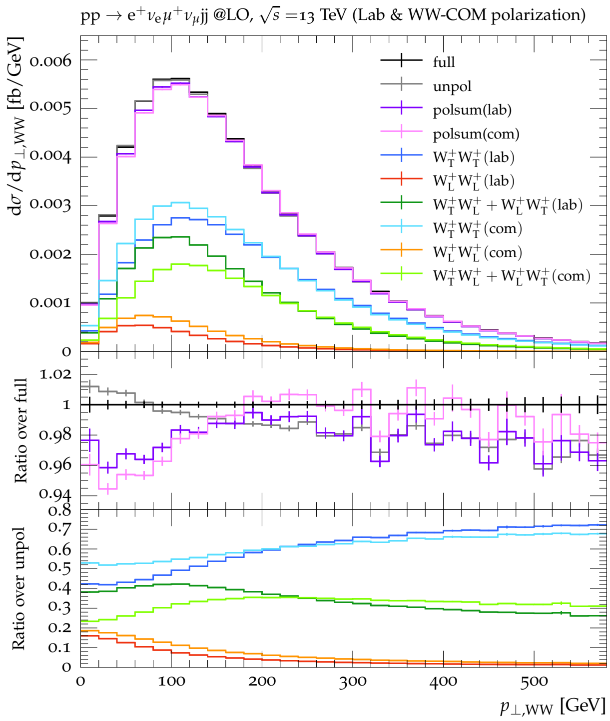

(a) $\mathrm{W^+W^+jj}$

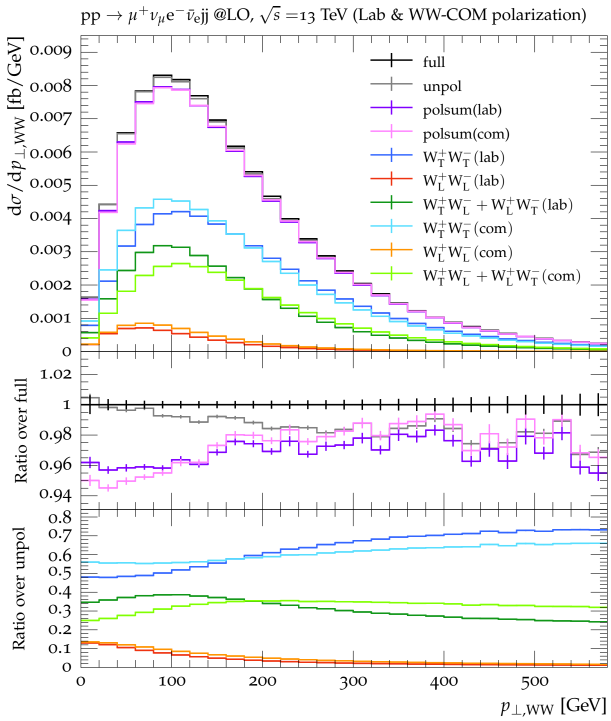

(b) $\mathrm{W^+W^-jj}$

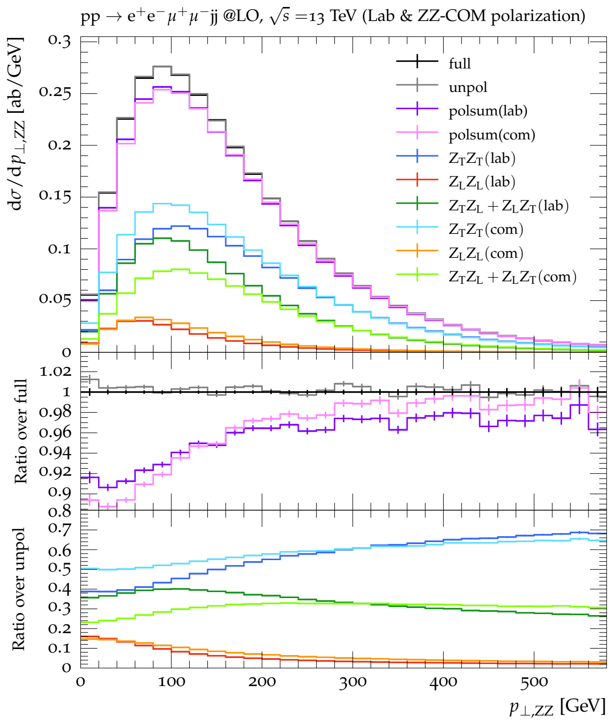

(c) ZZjj

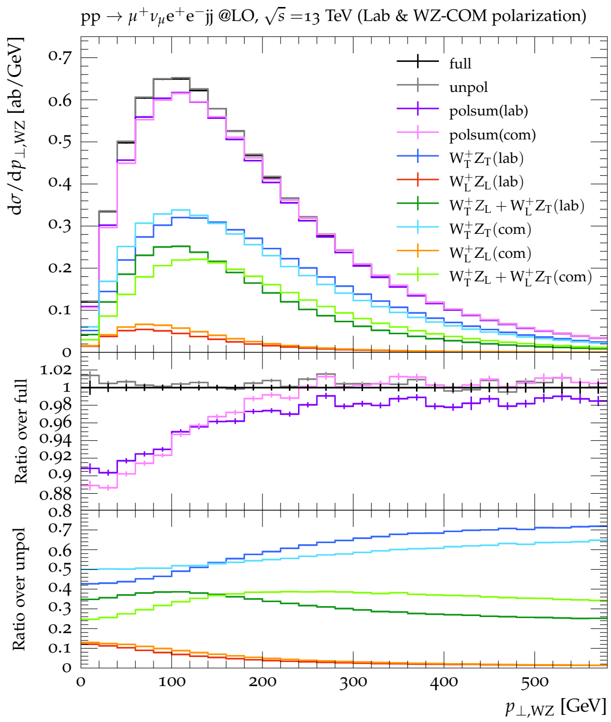

(d) $\mathrm{W^+Zjj}$

Figure 6.2: Double-polarized distributions of the vector boson (VB) pair transverse momentum $p_{\perp,\mathrm{VB1VB2}}$ for the pure electroweak $\mathrm{W^+W^+jj}$, $\mathrm{W^+W^-jj}$, $\mathrm{W^+Zjj}$ and ZZjj processes at fixed leading order with polarization defined in the laboratory (lab) and VB pair center-of-mass frame (com) obtained with SHERPA in the comparison phase space introduced in Sec. 6.1.1.

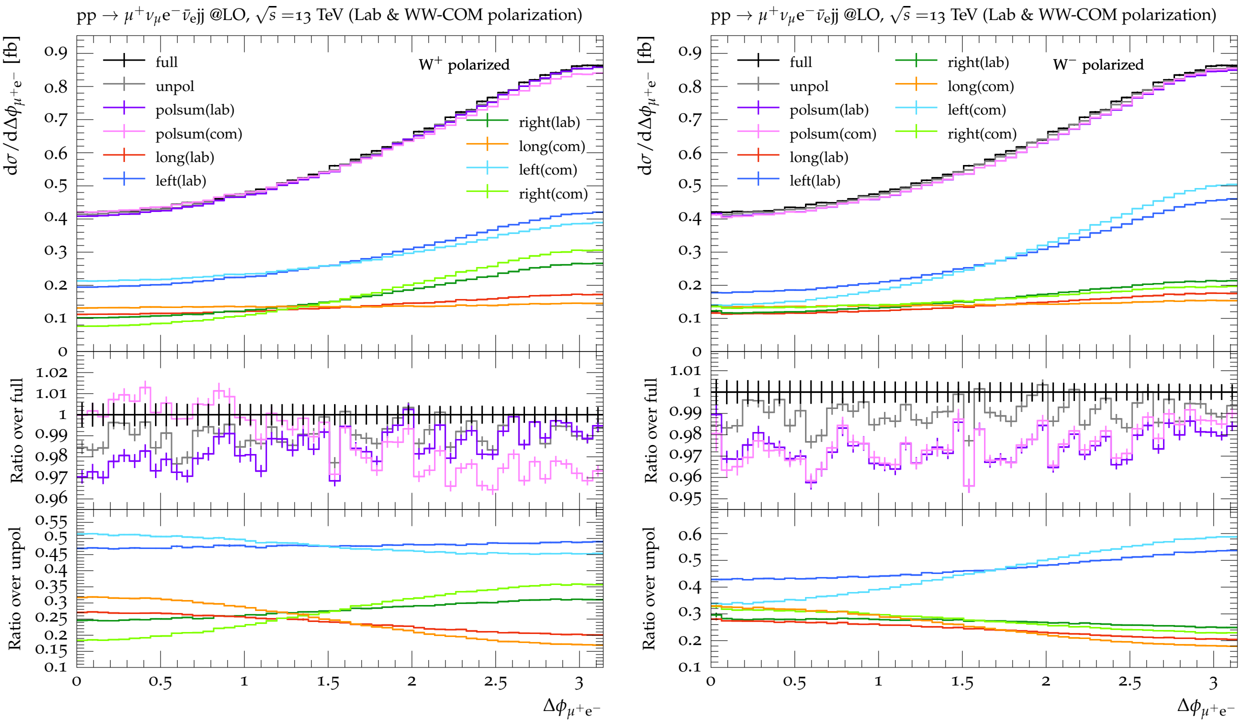

(a) W^+W^-jj - W^+ boson polarized **(b)** W^+W^-jj - W^- boson polarized

Figure 6.3: Single-polarized distributions of the azimuthal angle difference between the electron and the anti-muon $\Delta\Phi_{\mu^+e^-}$ for the W^+W^-jj process at fixed leading order obtained with SHERPA in the comparison phase space introduced in Sec. 6.1.1, the polarization is defined in the laboratory (lab) and the W^+W^--center-of-mass frame (com).

Fig. 6.4 ((b)-(d)) displays the single-polarized distributions of the electron decay angle $\cos^*_{e^-}$ for the Z boson for all investigated polarization definitions. The lepton decay angle is special compared to the other investigated observables since its definition also depends on the choice of a system, namely for the determination of the VB's direction of flight relative to which the lepton decay angle is measured (called observable frame for this discussion). Typically, it is chosen identical to the reference system for polarization definition but in Fig. 6.4 also the other possibilities are shown.

Effects found for the different frame choices are similar among the W^+Zjj and the ZZjj process wherefore only the results for the former are presented here. Corresponding distributions for the ZZjj process can be found in Fig. D.17 in the Appendix.

Independent of the observable and the reference frame, the lepton decay angle distributions exhibit that leptons are preferably emitted orthogonal to the direction of flight of longitudinal polarized Z bosons and approximately (anti-)parallel with respect to the flight direction of (right)left polarized Z bosons.

Only small effects due to the different frame choices are found: if observable and reference system match, the maxima of the distributions are the highest of all distributions with a fixed observable frame. Furthermore, the cross section is reduced between the two maxima of the transverse distributions if the two frames match compared to the non-matching cases.

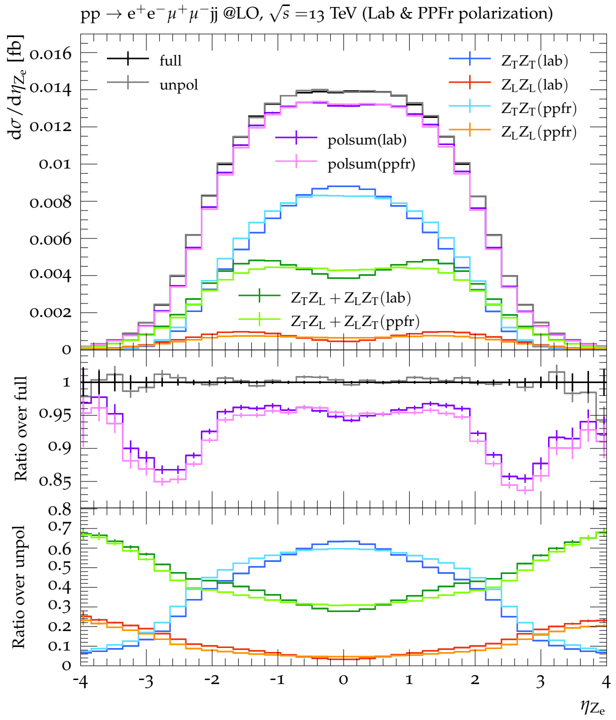

(a) ZZjj - Z boson pseudorapidity

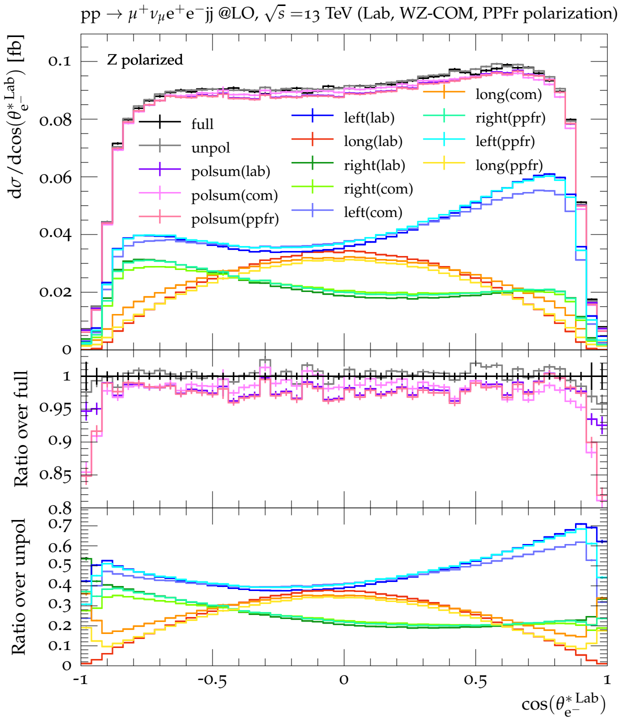

(b) W^+Zjj - Lab observable system

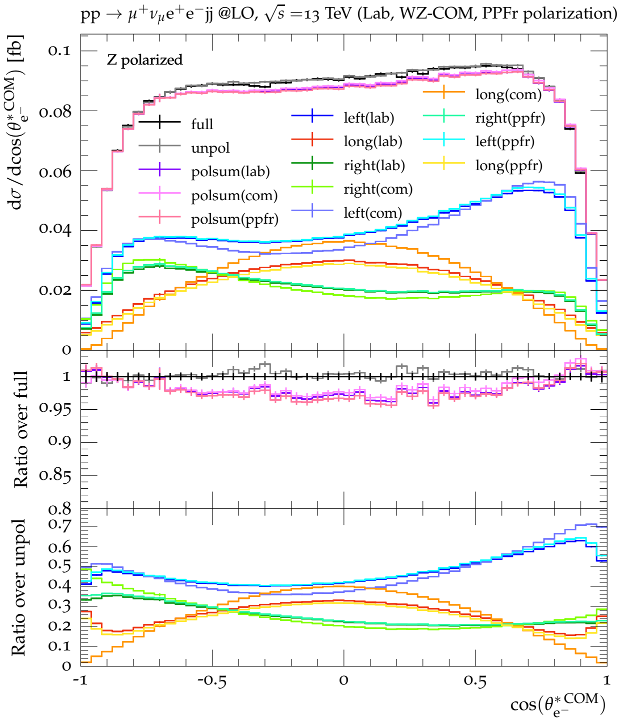

(c) W^+Zjj - W^+Z-COM observable system

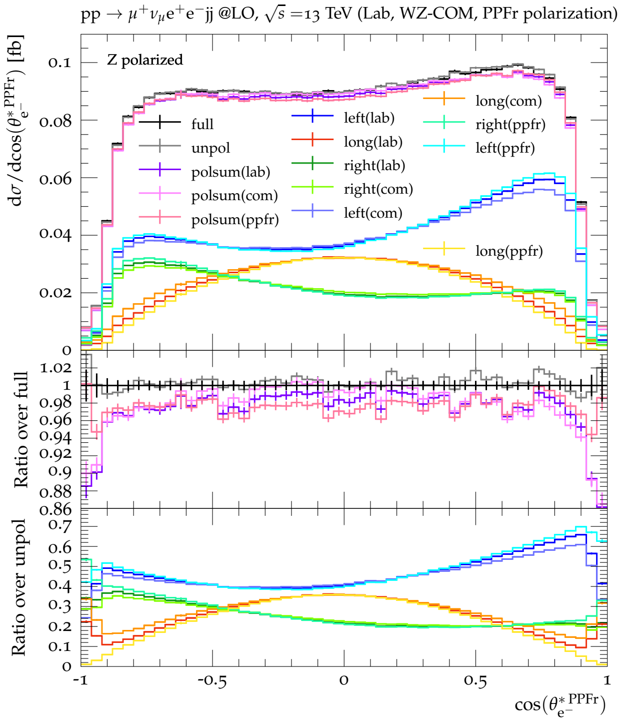

(d) W^+Zjj - PPFr observable system

Figure 6.4: Single-polarized distributions of the electron decay angle $\cos\theta^*_{e^-}$ for the W^+Zjj process with polarization and observable defined in the laboratory (lab), W^+Z-center-of-mass (com) and the parton-parton-frame (ppfr) ((b)-(d)) and double-polarized distributions of the Z boson pseudorapidity η_{Z_e} for the ZZjj process with polarization defined in the laboratory (lab) and the parton-parton-frame (ppfr) ((a)) at fixed leading order obtained with SHERPA in the comparison phase space introduced in Sec. 6.1.1

Likewise, the longitudinal distribution is narrower, if the two frame choice match. These effects are greatest for the COM observable system. Over wide ranges of the distributions differences between Lab and PPFr polarization definition are smaller than differences between Lab and COM for all observable frames. Around $\cos\theta^* = \pm 1$, the longitudinal polarization fraction increases while the transverse fractions decrease (left) or stay constant (right) when observable and polarization frame are different compared to the matched case. The longitudinal contribution reaches zero at $\cos\theta^* = \pm 1$ only for the matched case.

To conclude, in this study the influence of different polarization definitions on VBS processes at fixed LO is studied and compared among the investigated processes. Many aspects regarding the different polarization definitions are found to be similar among them but changing the polarization definition from Lab to COM also leads to process dependent differences in integrated cross sections and some observables for single- as well as double-polarized signals. For integrated double-polarized results, the $\mathrm{W^+Zjj}$ process shows a distinct behavior under reference system change from Lab to COM than the other processes which confirms the observations in Ref. [76] in a more realistic setup. Studies of differential distributions and integrated single-polarized cross sections do not indicate any process which is always special among all the others. Differences in integrated and differential polarized cross sections between the Lab and the PPFr definition, on the other hand, are observed to be similar for all studied processes. This matches the expectations since the COM definition is more directly connected to the specific process than the other two. Furthermore, effects of the polarization definition are found to depend on the specific VB considered as polarized and can influence the discrimination power of observables between different polarizations. Those effects can be present at distribution level even if the integrated XS are basically unaffected by the reference system change.

6.1.4 Interferences between different polarizations, off-shell and non-resonant effects in differential cross sections

Comparing the full and the unpol distributions (see upper ratio plots in Fig. 6.2, 6.3, 6.4), SHERPA's NWA performs well for the discussed observables in all studied processes; non-resonant and not covered off-shell contributions are mostly below 2%. The processes involving at least one Z boson mostly show very flat non-resonant contributions in all discussed observables, being smaller than the non-resonant contributions to the other processes. For the $\mathrm{W^+W^+jj}$ and the $\mathrm{W^+W^-jj}$ process, a considerable increase of the non-resonant contributions is observed in the tails of the $p_{\perp,\mathrm{WW}}$ distribution, reaching nearly 4%.

Interference contributions can be investigated by analyzing the difference between unpol and polsum in the upper ratio plot in the given distributions. Additionally, since polarized cross sections in SHERPA are calculated based on the entire matrix element tensor, the interference between different polarizations can also be computed event-wise as a sum over all off-diagonal terms of the tensor. This allows the direct simulation of interference distributions without relying on any subtraction method. As an example for this feature, Fig. 6.5 (a-j) display the interference distributions of VB pair the transverse momentum $p_{\perp,\mathrm{VB}}$ and of the VB pseudorapidity η_{VB} for different VB types for all four investigated VBS processes.

The shape of interference distributions is found to be process-dependent. Furthermore, different polarization definitions can lead to changes in the interference distributions. The interference distributions of $p_{\perp \mathrm{VB}_1 \mathrm{VB}_2}$ serve as an example for these observations. Although the $p_{\perp \mathrm{VB}_1 \mathrm{VB}_2}$-distributions for all processes show a similar shape peaking at $p_\perp$=70 GeV, the peak widths are different for the different processes. The PPFr distributions are merely shifted upwards compared to the Lab distribution to account for the higher integrated interference and do not show any considerable shape differences. In contrast, the COM distribution has a higher value at the maximum for all processes followed by a faster decrease than the others. The COM interference distribution for the $\mathrm{W^+W^+}$jj process is special among the processes, beside the peak it has a clear minimum at $p_\perp$=210 GeV. This leads to a significant contribution of negative interferences to this process distinct to the other processes, that only show small negative interferences at high $p_\perp$ values or no negative interference at all (ZZjj) for the COM distribution. In contrast to the polarized cross sections, the $\mathrm{W^+}$Zjj process shows the largest overall deviations between COM and the other reference frames for this observable. The interference fraction is the largest for zero $p_\perp$ for all processes and reaches at max. 4-5.5% for $\mathrm{W^+W^+}$jj, $\mathrm{W^+W^-}$jj and 10-12% for $\mathrm{W^+}$Zjj, ZZjj.

The interference distributions for the pseudorapidity (Fig. 6.5(e-i)) show that interference distributions can also largely depend on the concrete VB type under consideration besides a process and polarization definition dependence: the pseudorapidity interference contribution of the $\mathrm{W^-}$ and the Z boson in $\mathrm{W^+W^-}$jj, $\mathrm{W^+}$Zjj and ZZjj processes feature at least two maxima at $\eta \sim \pm 2.5$. For η-distributions of the $\mathrm{W^+}$ boson, they are only faintly visible, if at all. The $\eta_{\mathrm{W^+}}$-distributions tend to have a broad peak centered at zero pseudorapidity for all processes involving $\mathrm{W^+}$ bosons. Furthermore, an influence of the polarization definition is clearly visible especially for the $\mathrm{W^+}$Zjj and the ZZjj process which possess larger integrated interference cross sections: the COM prediction is reduced compared to the other frames around zero pseudorapidity for all VB-η. The Lab-distributions for $\eta_{\mathrm{W^-}}$ and η_{Z} exhibit a third maximum around zero η, for $\eta_{\mathrm{W^+}}$ the broad peak is narrower around zero η than in the distribution for the other frames. Differences for the same VB among the investigated processes are mainly observed for $\eta_{\mathrm{W^+}}$ at the tails of the peak independent of the specific polarization definition. The interference fractions for the η of the $\mathrm{W^+}$ boson are rather small (<4%) compared to the ones for the other VBs reaching at max. (8)16% for the ($\mathrm{W^-}$)Z boson.

A significant influence of the polarization definition on the interference distribution can also be

found for $\Delta\phi_{ll'}$ (cf. upper ratio plots in Fig. 6.3, D.16) where the COM interference distribution can have a completely different shape than the Lab interference (Fig. 6.3 (a)). At max. the interference fraction for this observable reach $\sim$4%.
Regarding the electron decay angle $\cos\theta^*_{e^-}$ (upper ratio plots in Fig. 6.4) the largest impact on the interference distribution is the non-matching reference and observable frame: while the interference cross section is basically flat in the bulk of the distribution with a fraction of about 2-3% it increases rapidly near $\cos\theta^*_{e^-} = \pm 1$ reaching at max. fractions between 10-20%. Interestingly, this increase is not found for the lepton decay angle defined in the COM observable frame (Fig. 6.4 (b)) if the W^+Zjj process is considered. For that case, the distribution is not flat but a symmetrical distribution with a low maximum at $\cos\theta^*_{e^-} = 0$. Such a shape is also found for the corresponding observable in the ZZjj process, but only for the COM reference system. The other polarization definitions for the ZZ-COM-observable system lead to distributions sharing the flat cross section in the bulk and an increase around $\cos\theta^*_{e^-} = \pm 1$.

It is noteworthy that the interference contributions can be reduced by using the coherent transverse signal definition instead of the incoherent definition applied for the shown results. The ability to directly simulate the interference distribution should also ease the inclusion of this contribution in measurements, as there is no need to resort to subtraction methods anymore that can lead to high statistical uncertainties.

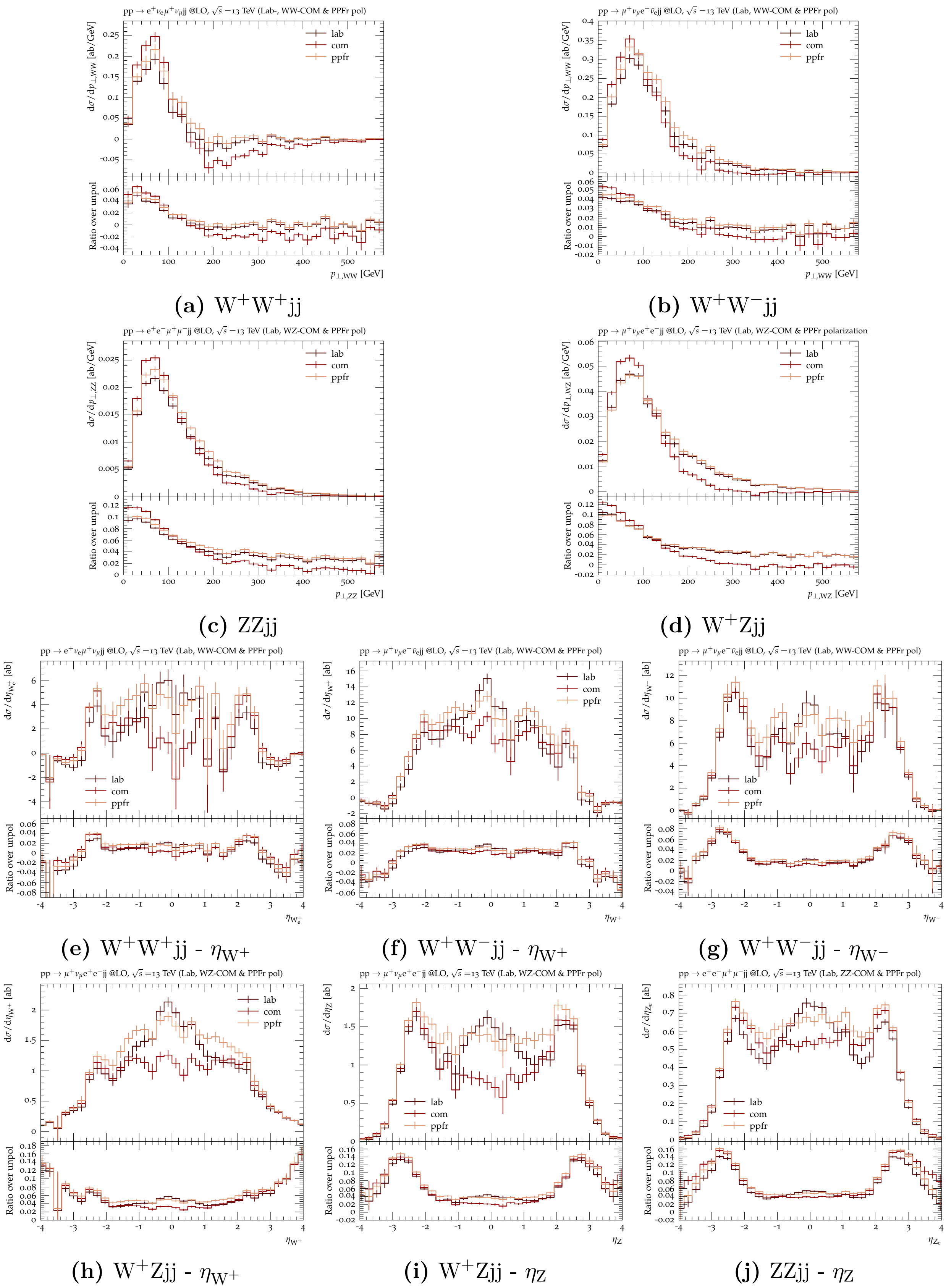

(a) W^+W^+jj **(b)** W^+W^-jj **(c)** $ZZjj$ **(d)** W^+Zjj **(e)** W^+W^+jj - η_{W^+} **(f)** W^+W^-jj - η_{W^+} **(g)** W^+W^-jj - η_{W^-} **(h)** W^+Zjj - η_{W^+} **(i)** W^+Zjj - η_Z **(j)** $ZZjj$ - η_Z

Figure 6.5: Interference distributions of the vector boson (VB) pair transverse momentum $p_{\perp,\mathrm{VB1VB2}}$ (a-d) and of the VB pseudorapidity η_{VB} (e-j) for the pure electroweak W^+W^+jj, W^+W^-jj, W^+Zjj and $ZZjj$ processes at fixed leading order with polarization defined in the laboratory (lab)-, VB pair center-of-mass-frame (com) and the parton-parton-frame (ppfr) obtained with SHERPA in the comparison phase space introduced in Sec. 6.1.1.

6.2 NLO QCD corrections to polarized vector boson production processes

The inclusion of higher perturbative orders in the hard matrix elements and merged calculations provide two ways to obtain higher-order QCD corrections to simulated cross sections. As outlined in Sec. 4.5, it is possible to apply the new polarization framework in SHERPA's NLO QCD calculations. The current implementation leads only to polarized predictions "at nLO QCD accuracy", since the calculation of polarization fractions does not take virtual effects into account. Therefore, the first part of this section focuses on testing, whether SHERPA can nonetheless deliver reliable predictions of the main NLO QCD polarization behavior. This is done by comparing SHERPA results with full fixed-order NLO QCD calculations from the literature. Afterwards, polarized cross sections obtained by combining SHERPA's merging method with the new polarization framework are discussed. In particular, the influence of different merging scales is investigated.
Both studies are done on the example of the inclusive W^+Z production. If deviations between polarization fractions are quantified in this section, relative differences are given in contrast to the previous section since this is the more suitable quantity for the following discussions.

6.2.1 Simulation setup

In order to study higher-order QCD predictions with SHERPA at the example of the inclusive W^+Z production, simulation settings and the phase space are chosen according to Ref. [86]. This allows the comparison with full NLO QCD fixed-order results published there. More specific, the $\mathrm{pp} \to \mathrm{e}^+ \nu_\mathrm{e} \mu^+ \mu^- + X$ process is studied using the simulation settings and phase space definitions given in Tab. 6.1.
Literature predictions in Ref. [86] were obtained with RECOLA [90] and COLLIER [91] for amplitude-generation and MOCANLO for the integration. For polarized calculations, the DPA was used.
SHERPA simulations at nLO accuracy use Born-level matrix elements calculated with AMEGIC, except for the amplitudes employed for the polarization fraction calculations, the VB decays and calculations at LO. Those amplitudes as well as real corrections are computed with COMIX. Loop-virtual corrections are provided by OpenLoops using the SHERPA interface to this program. Since there are still unresolved issues with polarized fixed-order calculations at nLO QCD, the SHERPA simulations presented here are performed on particle-level. The matching of the fixed-order NLO QCD calculation to the resummation of the parton shower is done by SHERPA's internal implementation of the MC@NLO method [57]. The core-scale of the processes is set by SHERPA's METS-scale setter.

Merged calculations with SHERPA in this section investigate the pp $\to e^+ \nu_e \mu^+ \mu^-$ process merged with pp $\to e^+ \nu_e \mu^+ \mu^-$j at LO. All matrix elements are provided by COMIX. The merging algorithm implemented in SHERPA is an extension of the CKKW method as detailed in Ref. [75] (called MEPS@LO). The merging scale is varied between 20 and 1000 GeV. For scale setting, the `MEPS: CORE_SCALE` setting is now used to set the core scale of the process since this provides a consistent scale setting between matrix element calculations and parton shower for additional emissions [92].
All SHERPA simulations performed in this section apply SHERPA's default shower simulation, QED radiation, hadronization, hadron decays and multiple interactions (cf. Ref. [93] for details). QCD jets are identified by the anti-kT algorithm [94] with a jet resolution parameter of $R = 0.4$. Corresponding SHERPA run cards are given in the Appendix Sec. C.3.
The RIVET analysis used for evaluating the simulation results is based on the ATLAS_2017_I1625109 standard analysis. Basically, the same observables as in Ref. [86] are investigated. Selection criteria applied during event generation are set more inclusive than in Tab. 6.1. During the RIVET analysis, the selection criteria in Tab. 6.1 are then applied on the reconstructed final state jets and dressed final state leptons.
The whole study focuses on double-polarized signals.

Table 6.1: Simulation settings and phase space definition used for SHERPA simulations of the inclusive W^+Z production at nLO(QCD)+PS and LO+1j merged with PS.

Setting	
PDF-Set from LHAPDF6 [88]	NNPDF31_nlo_as_0118
Electroweak scheme G_μ	$G_\mu = 1.16638 \cdot 10^{-5}\,\mathrm{GeV}^{-2}$ and complex mass scheme (full), real EW parameters (polarization)
Strong coupling $\alpha_S(M_Z)$	0.118
Core-Scale	$\mu = \frac{1}{2}(M_Z + M_W)$
VB pol masses	$M_W = 80.352$ GeV, $M_Z = 91.153$ GeV
VB pol widths	zero for all VBs in polarization calculations, $\Gamma_W = 2.084$ GeV, $\Gamma_Z = 2.4943$ GeV otherwise
Phase space	$p_{\perp,e^+} > 20$ GeV, $p_{\perp,\mu^\pm} > 15$ GeV, $\lvert y_l \rvert < 2.5$ $\Delta R_{\mu^+\mu^-} > 0.2$, $\Delta R_{\mu^\pm e^+} > 0.3$ [3] 81 GeV $< M_{\mu^+\mu^-} <$ 101 GeV, $M_{T,W}$ [4] $>$30 GeV

[3]The rapidity(y)-azimuthal angle(ϕ) distance is defined according to $\Delta R = \sqrt{(\Delta y)^2 + (\Delta\phi)^2}$
[4]The W^+-boson transverse mass is defined as $M_{T,W} = \sqrt{2p_{\perp,e^+}p_{\perp,\nu_e}(1 - \cos\Delta\phi_{e^+\nu_e})}$.

6.2.2 Comparison of predictions from SHERPA's nLO QCD calculation with full fixed-order NLO QCD literature data

Tab. 6.2 compares the integrated polarized cross sections obtained with SHERPA's nLO (QCD) polarization setup with literature results containing all NLO QCD corrections. Both the laboratory (Lab) as well as the W^+Z-center-of-mass reference frame (COM) are investigated. NLO QCD corrections in W^+Z production can be very large with K-factors around two. This is due to the approximate radiation amplitude of zero, which is present at Born level but not for real corrections at NLO QCD [86]. Compared to LO, the behavior of the LL component at NLO QCD changes respective to the different polarization definitions, its contribution is now larger in the Lab. Its fraction is generally reduced compared to the LO prediction (for SHERPA cf. Appendix D.2.1). The TT component has the largest contribution at both orders and for both reference systems but its relative contribution to the polsum/unpol is also reduced compared to LO. The COM polarization fractions are much more affected by the higher-order corrections than the Lab ones. This qualitative behavior is also predicted by the SHERPA setup.

Comparing the SHERPA and literature results quantitatively, the unpolarized result is 4% smaller than the literature value. Different to the polarization fractions, it also contains all virtual corrections. The observed discrepancy between SHERPA and literature is already present in the full calculations, indicating that it is caused by shower effects. An agreement of the full results at fixed LO was reached, so that different simulation settings can be excluded as a reason for the deviation. The SHERPA unpolarized result approximates the full cross section better than 1.5%, implying that SHERPA's NWA provides a good approximation to the full result also at NLO QCD.

All SHERPA polarized cross sections are reduced by 3-6.5% compared to the literature results, which is about the same as the unpol reduction itself. The largest deviations from the expected 4% reduction are found for the TT polarization (5.5% (Lab) / 6.5% (COM) w.r.t. the literature) which could be due to the different definition of transverse signals used in SHERPA. This could as well, at least partially, explain the more than four (Lab) / three (COM) times larger interference result compared to the literature.

It is noteworthy, that the LL cross section for the COM definition is reduced by 5.5% w.r.t. the literature too, which means that the simulated SHERPA polarization fraction is smaller than the literature prediction (5.586% vs. 5.719% relative to the unpol). This delta cannot be attributed to definition differences and the deviation is not observed for the LL contribution in the Lab definition, where the fractions relative to the unpol agree (5.950% vs. 5.957%). However, this deviation of the LL fractions in the COM of $\sim$2.5% is within the accuracy expected from the different approximations used. That also holds for the polarization fractions

Table 6.2: Integrated double-polarized cross sections for the inclusive W^+Z production at NLO QCD in the phase space defined in Tab. 6.1 obtained with MOCANLO+RECOLA+COLLIER in Ref. [86] and SHERPA for polarizations defined in the laboratory and W^+Z-center-of-mass frame; polarization fractions are calculated relative to the polarization sum, the interference fraction is computed relative to the unpolarized result, K-factors are obtained from dividing NLO QCD by LO cross sections leading to statistical errors of $\mathcal{O}(10^{-3})$ except for the interference ($\mathcal{O}(10^{-1})$), SHERPA results are obtained with an nLO(QCD) setup neglecting virtual corrections on polarization fractions.

W^+Z	$\sigma^{\text{NLO QCD}}_{\text{Paper}}$ [fb]	fraction [%]	K-factor	$\sigma^{\text{nLO+PS}}_{\text{Sherpa}}$ [fb]	fraction [%]	K-factor
full	35.27(1)		1.81	33.80(4)		
unpol	34.63(1)		1.81	33.334(14)		1.80
			Laboratory frame			
polsum	34.544(8)	100	1.80	32.958(16)	100	1.79
int	0.086(13) (diff)	0.248(35)	-2.97	0.376(6)	1.127(19)	3.45
L-L	2.063(1)	5.9721(32)	1.91	1.9835(15)	6.018(6)	1.90
L-T	6.108(2)	17.682(7)	1.93	5.909(5)	17.929(18)	1.94
T-L	7.409(4)	21.448(13)	1.69	7.108(5)	21.568(19)	1.69
T-T	18.964(7)	54.898(24)	1.80	17.957(9)	54.48(4)	1.78
			W^+Z-center-of-mass-frame			
polsum	34.411(9)	100	1.81	32.546(16)	100	1.80
int	0.219(13) (diff)	0.632(38)	1.54	0.787(6)	2.360(18)	1.94
L-L	1.968(1)	5.7191(35)	1.31	1.8622(23)	5.722(8)	1.28
L-T	5.354(1)	15.559(5)	2.65	5.201(4)	15.982(13)	2.69
T-L	5.097(2)	14.812(7)	2.68	4.9024(33)	15.063(13)	2.75
T-T	21.992(9)	63.910(31)	1.62	20.580(11)	63.23(5)	1.59

of the transverse contributions calculated relative to the polsum in Tab. 6.2[5] which reveals an agreement of better than 3%.

This leads to the conclusion that virtual corrections do not seem to have a significant influence on the polarization fractions and SHERPA's nLO (QCD) setup essentially predicts the polarization fractions (and with that the polarized cross sections since the unpol contains full NLO QCD corrections) at NLO QCD. In most cases, the differences between the COM fractions in SHERPA and literature are slightly larger than those for the Lab. This is also true for the K-factors which agree within 1 % for the Lab and 2.6% for the COM.

Fig. 6.6 and 6.7 show the distributions for the decay angle of the anti-muon $\cos\theta^*_{\mu^+}$ and the

[5]As evident from Chap. 5, the influence of the different transverse polarization definitions applied in SHERPA and the literature can be reduced by calculating polarization fractions relative to the polsum instead of relative to the unpolarized result.

positron rapidity y_{e^+} comparing literature and SHERPA predictions for the Lab and COM polarization definition. Results for more observables are given in Appendix D.2.2.
The unpol distributions approximate the full predictions to a comparable extent as the literature, mostly showing deviations of about 2-3% or less. The larger interference contribution due to the different definition of transverse signals in SHERPA is clearly visible in larger differences between the polsum and unpol result, e.g. in the $y_{\mathrm{e}^+} = 0$ region in Fig. 6.7 or between $\cos\theta^*_{\mu^+} = -0.75$ and 0.75 in Fig. 6.6.
Regarding the polarized distributions, it can be deduced that NLO QCD corrections to them can be very non-flat, e.g. for y_{e^+} with polarization defined in the Lab (Fig. 6.7). Furthermore, they can influence distinct VB polarizations very different (e.g. for y_{e^+} in Fig. 6.7, $\Delta\Phi_{\mathrm{e}^+\mu^-}$ in Fig. D.5 in the Appendix). Additionally, shape and size of the NLO QCD corrections for a certain polarization state can largely depend on the polarization definition, as e.g. for distributions of decay angles (Fig. 6.6, Fig. D.5), y_{e^+} (Fig. 6.7), and the considered observable. The SHERPA simulation can reproduce the shapes of the distributions as well as the K factors predicted by the literature for all investigated observables to a very good extent. The normalization of the distributions appears slightly reduced compared to the literature as expected from the integrated cross sections. The SHERPA prediction for the size of the differential K-factors is comparable with the literature.
The shapes of the K-factors exhibit some deviations in some phase space regions in the distributions of the positron rapidity and the lepton decay angles. Remarkably, significant deviations are only present for the Lab polarization definition: for $|y_{\mathrm{e}^+}| > 2$, the differential K-factor for the LL contribution is increased by up to 7% compared to the literature.
A more striking deviation can be seen in the differential K-factors for the lepton decay angle of the Z boson in Fig. 6.6. For $|\cos\theta^*_{\mu^+}| > 0.85$ and LL or TL polarization, the K factor decreases from $K \approx 2$ to values around 1 (LO behavior) in the last bin. In the literature, it remains nearly constant at a value of about 1.8(LL)/1.6(TL). This behavior is also present in the LL and LT decay angle distributions of the W^+ boson (see Fig. D.5(bottom)). This means that merely the longitudinal polarization component of the VB, whose decay angle is considered, is affected. A comparison of results at fixed LO with LO+PS predictions (as done for said decay angle distributions in Appendix D.2.1) reveals, that the shower raises the cross section for the LL, TL (decay angle of the Z boson) or LL and LT (decay angle of the W^+ boson) distributions in the phase space regions near decay angles of 0° and 180° up to 180-190% and 220%, respectively. It seems that the shower in the LO+PS simulation already covers parts of the NLO QCD corrections in that phase space regions which is why the K factor is declining that much in Fig. 6.7.
However, the decay angle distributions for polarizations defined in the COM do not show such a large growth in LO+PS distributions compared to the fixed LO results (see Fig. D.4, right column). This is consistent with the observation that deviations in the K factors only occur for

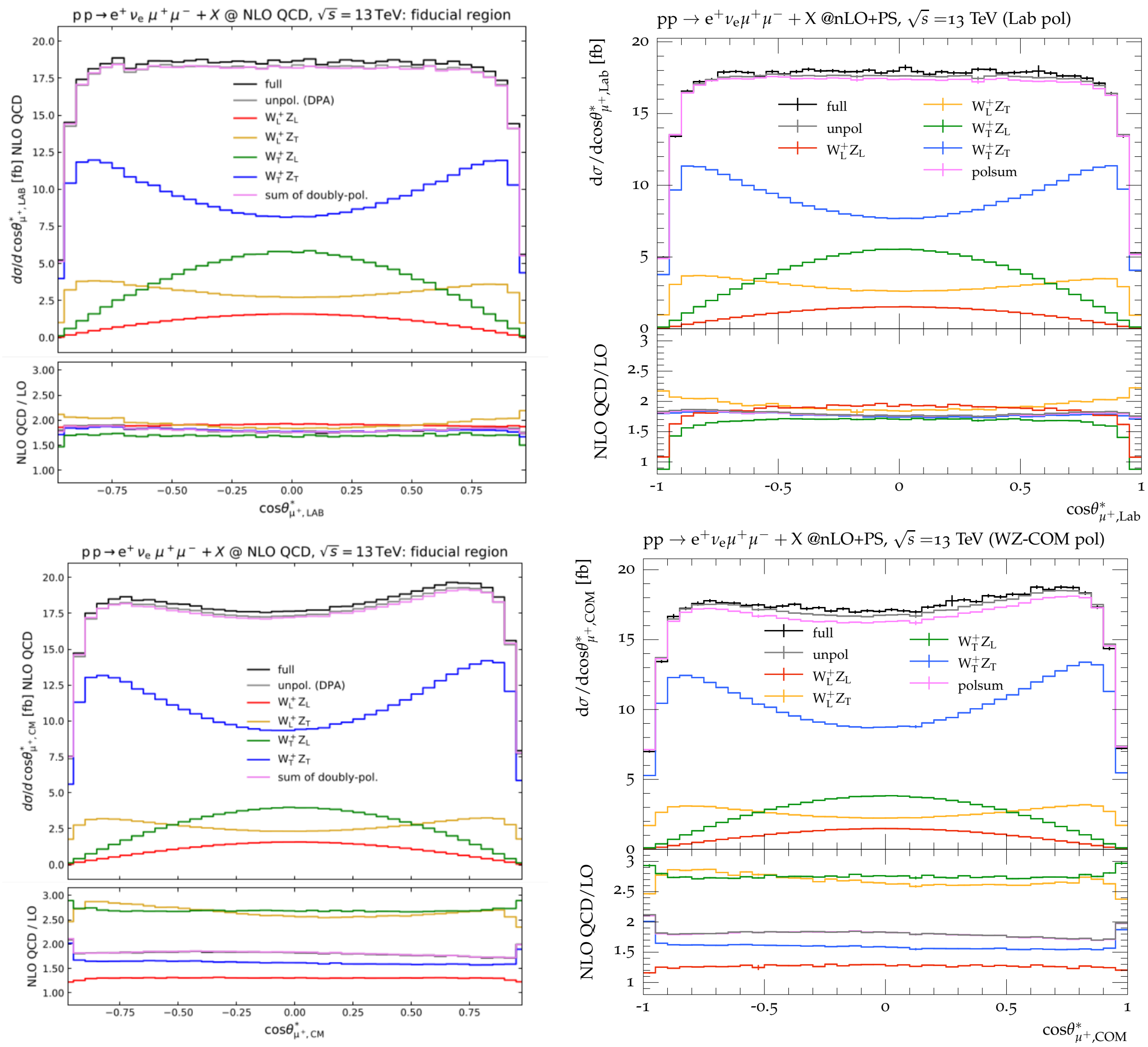

Figure 6.6: Double-polarized distributions of the anti-muon decay angle $\cos\theta^*_{\mu^+}$ in inclusive W^+Z production from literature [86] (left) at full fixed NLO QCD and SHERPA (right) at nLO(QCD)+PS accuracy; polarization is defined in the laboratory (top) and in the W^+Z-center-of-mass frame (bottom), K-factors are the ratio of (n)NLO QCD over LO cross sections.

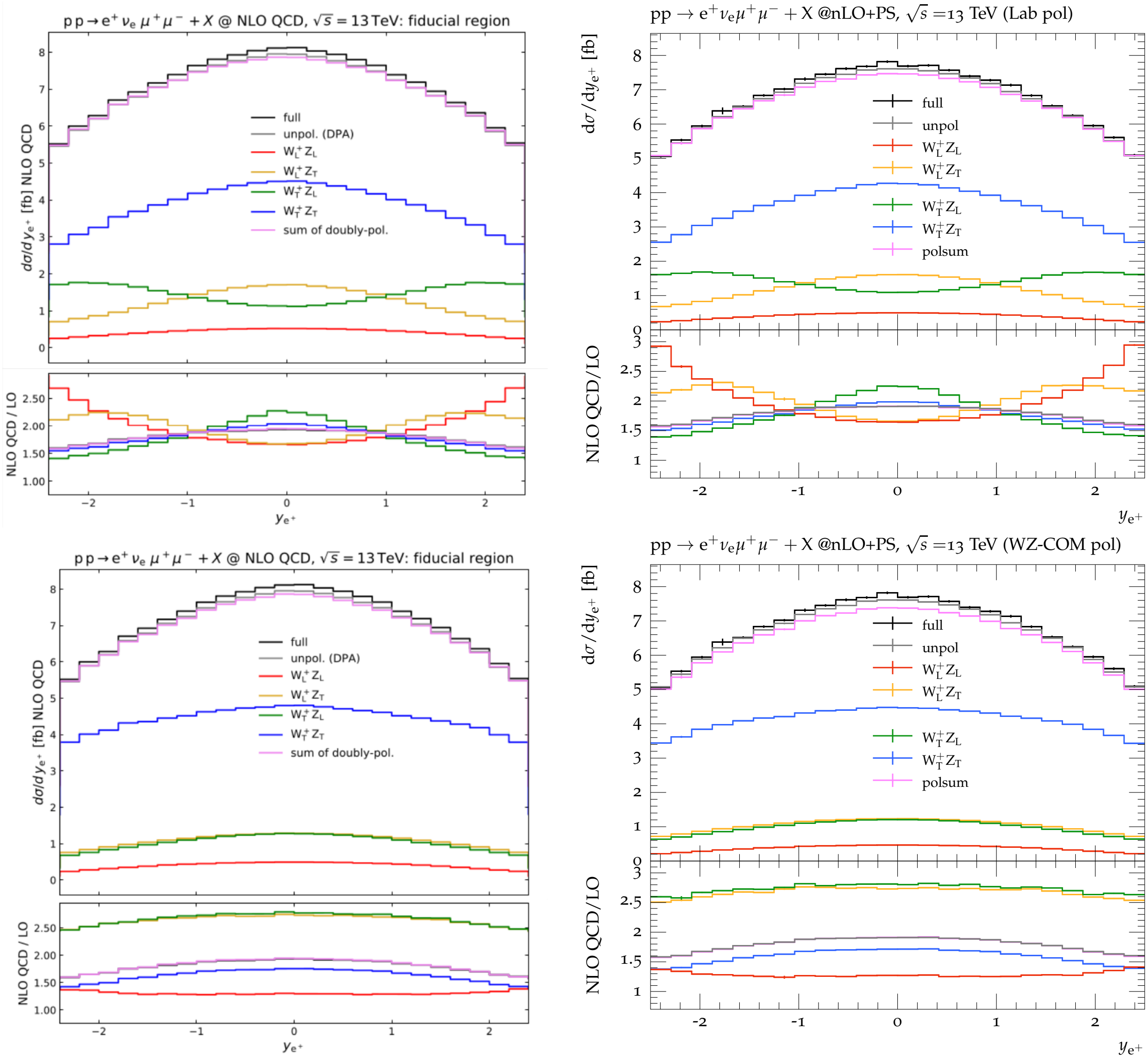

Figure 6.7: Double-polarized distributions of the positron rapidity y_{e^+} in inclusive W^+Z production from literature [86] (left) at full fixed NLO QCD and SHERPA (right) at nLO(QCD)+PS accuracy; polarization is defined in the laboratory (top) and in the W^+Z-center-of-mass frame (bottom), K-factors are the ratio of (n)NLO QCD over LO cross sections.

the Lab decay angles.

Apart from that, no significant deviations in the shapes of the distributions and the K factors can be found. Thus, the effect of virtual corrections on polarization fractions seems to be small at the level of distributions, too. This shows that the nLO(QCD) setup of SHERPA is indeed able to also predict the NLO QCD behavior of polarized cross sections in VB production processes to a very good extend, subject to a small influence of the virtual corrections on polarization fractions also for the other VB production processes.

6.2.3 Study of LO+1jet merging polarization simulation in comparison with nLO (QCD) predictions for the inclusive W^+Z production process

In this section, the combination of merged calculations with the new polarization framework in SHERPA is studied on the example of the inclusive W^+Z production process. It is investigated whether the dependency of the polarized cross sections on the merging scale matches the expectations, i.e.

- at small merging scales: main real NLO QCD corrections are preserved, the results only show a weak dependency on the unphysical merging scale
- larger merging scales: predictions of the NLO QCD corrections get worse and worse, the behavior of the polarization fractions and distributions becomes more and more similar to that at LO

Tab. 6.3, 6.4 and Fig. 6.8, 6.9 summarize the integrated cross sections and polarization fractions obtained from these merged calculations with different merging scales applied. Results for the polarization defined in the Lab (Tab. 6.3, Fig. 6.8) and the W^+Z-COM (Tab. 6.4, Fig. 6.9) are shown. Results for LO+PS and nLO(QCD)+PS simulations are given too for comparison.
Comparing the full and unpol between nLO(QCD)+PS and merged calculation with the smallest merging scale, a deviation of 15% is obvious which is mainly caused by the missing virtual corrections in the merged results. Accordingly, all polarized cross sections and associated K factors appear reduced as well. However, the polarization fractions mostly show deviations of about 1% or less for both polarization definitions, i.e. missing hard matrix element emissions with energies below 20 GeV have no relevant effect on the polarization fractions. Exceptions from that are the pure longitudinal fraction which is enhanced by 2%(COM) and 3%(Lab) in the merged setup and the interference contribution in the Lab (decrease of 2%).
With increasing merging scale, cross sections and K-factors decrease continuously until they reach the LO-results at merging scales between 500 and 1000 GeV depending on the polarization

component (see Appendix D.2.3 for cross sections/K-factors for Q_c=1000 GeV). The only exception from that behavior is the TT component in the COM showing a slight increase (∼0.5%) when scaling up from Q_c=20 GeV to 40 GeV.
A continuous change towards the LO result with increasing merging scale can also be observed for the polarization fractions in the COM (see Fig. 6.9). For Lab polarization fractions (Fig. 6.8), a distinct behavior is observed. While the polarization fractions of the mixed polarized components show a continuous increase (TL) or decrease (LT) towards the LO result, this is not the case for the purely polarized components: the TT component first increases towards the LO results with increasing merging scale, then overshoots it at Q_c=80 GeV and grows even further when scaling up to Q_c=200 GeV. For merging scales above 200 GeV, it decreases again. The LL fraction, in turn, first decreases until Q_c=200 GeV where it undershoots the LO result and starts increasing again with merging scales above 200 GeV.
For the interference fraction, the same unexpected behavior as for the LL contribution is observed for the COM polarization definition. With Q_c=1 TeV, the differences to the LO fractions are at the sub-percent level for both polarization definitions.
A more detailed comparison of the differences between small merging scales of Q_c=20 GeV and 40 GeV reveals only a 1%-effect on the unpol result. Polarized cross sections are differently affected, with deviations ranging from no difference (TT-Lab, LL-COM) to a 4.5%(TL COM) reduction indicating that the missing hard matrix element emissions with energies between 20 and 40 GeV influence different polarization components differently. The interference cross section(fraction) is influenced the most, it is reduced by 13.5(13)%(Lab)/6(5)%(COM) when going from Q_c=20 GeV to 40 GeV. The polarization fractions show a mild trend towards the LO results and differ by 2.3%(LL-Lab) and 3.5% (TL-COM) or less.
Not covered off-shell effects and non-resonant contributions are small (∼1%) for these merged setups but are different between the two merging scales. For Q_c=20 GeV, the unpol result undershoots the full result; for Q_c=40 GeV it is exceeded by about the same amount. This suggests a noticeable influence of hard matrix element emissions between 20 and 40 GeV on the non-resonant contributions.

In Fig. 6.10, the influence of an increasing merging scale on the shape of distributions and K-factors is illustrated on the example of the positron rapidity y_{e^+} for the different polarization combinations with the polarization defined in the Lab.
It can be clearly seen that NLO QCD corrections get more and more lost with increasing merging scale, i.e. the K factors become more and more flat and their normalization is increasingly approaching one. The transition to LO is not identical for all polarization components. Polarization combinations containing a longitudinal W^+ boson display LO behavior not later than $Q_c = 500$ GeV, with K factors being very flat-shaped at $Q_c = 200$ GeV merging scale already. The other polarization combinations, in contrast, even show some differences to the LO behavior at merging scale $Q_c = 500$ GeV. The plots of the normalized shapes at the

Table 6.3: Integrated double-polarized cross sections for the simulation of inclusive W$^+$Z production with up to one jet merged with parton shower at LO; polarized cross sections and K factors (K) for different CKKW-merging scales Q_c are shown in comparison with nLO(QCD)+PS and LO+PS results; all predictions are obtained with SHERPA; polarizations are defined in the laboratory frame (Lab), K factors are obtained from dividing nLO(QCD) by LO cross sections, statistical errors on the K-factors are of the order of $\mathcal{O}(10^{-3})$, except for the interference ($\mathcal{O}(10^{-1})$).

W$^+$Z	$\sigma^{\text{nLO+PS}}_{\text{Sherpa}}$ [fb]	K	$\sigma^{Q_c=20\text{GeV}}_{\text{Sherpa}}$ [fb]	K	$\sigma^{Q_c=40\text{GeV}}_{\text{Sherpa}}$ [fb]	K	$\sigma^{Q_c=80\text{GeV}}_{\text{Sherpa}}$ [fb]	K	$\sigma^{Q_c=200\text{GeV}}_{\text{Sherpa}}$ [fb]	K	$\sigma^{Q_c=500\text{GeV}}_{\text{Sherpa}}$ [fb]	K	$\sigma^{\text{LO+PS}}_{\text{Sherpa}}$ [fb]
full			28.804(27)		27.840(25)								
unpol	33.27(5)	1.79	28.492(17)	1.53	28.206(15)	1.52	26.342(15)	1.42	21.607(12)	1.16	18.910(10)	1.02	18.567(22)
polsum	32.89(5)	1.78	28.175(19)	1.53	27.933(17)	1.51	26.136(16)	1.42	21.456(14)	1.16	18.799(12)	1.02	18.468(24)
int	0.376(18)	3.8	0.316(9)	3.2	0.273(8)	2.77	0.205(8)	2.09	0.152(6)	1.54	0.111(5)	1.13	0.098(10)
L-L	1.983(4)	1.89	1.7511(20)	1.67	1.6946(19)	1.61	1.5078(18)	1.44	1.1763(15)	1.12	1.0496(13)	1.00	1.0493(17)
L-T	5.914(11)	1.93	5.013(5)	1.64	4.914(5)	1.60	4.495(5)	1.47	3.596(4)	1.17	3.108(4)	1.01	3.065(7)
T-L	7.075(13)	1.68	6.063(6)	1.44	6.018(5)	1.43	5.629(5)	1.34	4.724(5)	1.12	4.272(4)	1.01	4.212(9)
T-T	17.92(4)	1.77	15.348(11)	1.51	15.306(10)	1.51	14.504(10)	1.43	11.960(8)	1.18	10.369(7)	1.02	10.141(14)

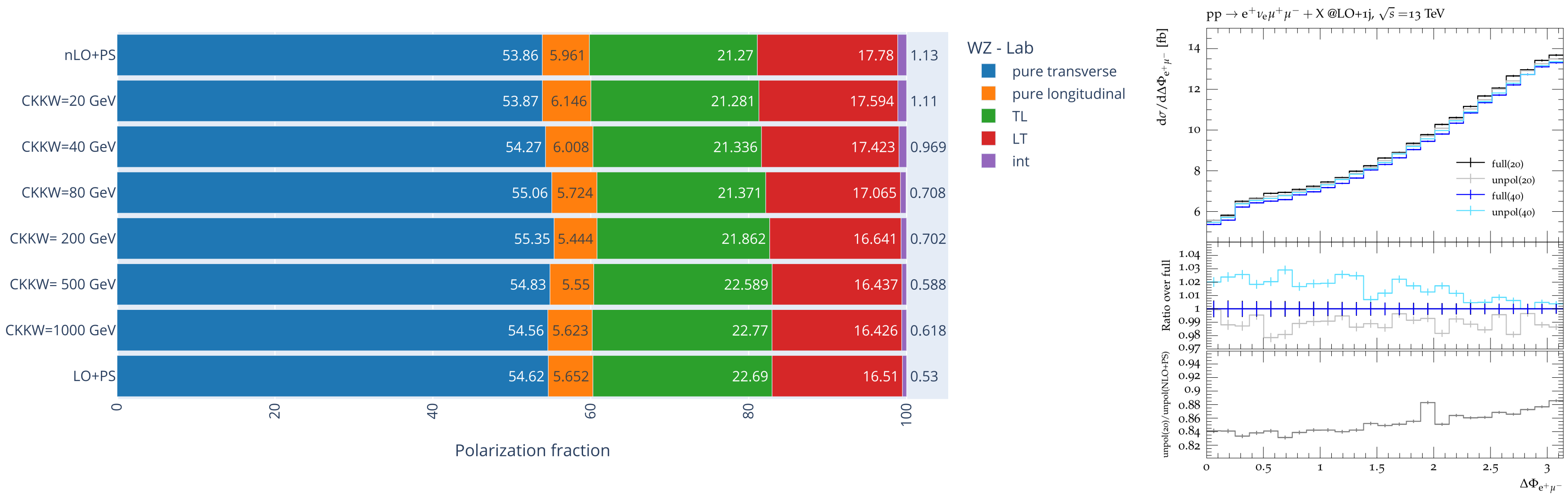

Figure 6.8: Laboratory frame polarization fractions for inclusive W$^+$Z production at nLO(QCD)+PS, LO+PS and LO+1j merged with PS (left) and full, unpolarized distributions from merged calculations (top), corresponding unpol over full (middle) and ratio merged (Q_c = 20 GeV) over NLO QCD+PS unpol for the distribution of the azimuthal angle difference between positron and muon $\Delta\Phi_{e^+\mu^-}$ (right); polarization fractions are calculated relative to the unpol result from data given in table above; all results are obtained with SHERPA.

Table 6.4: Integrated double-polarized cross sections for the simulation of inclusive W$^+$Z production with up to one jet merged to parton shower at LO; polarized cross sections and K factors (K) for different CKKW-merging scales Q_c are shown in comparison with nLO(QCD)+PS and LO+PS results, all predictions are obtained with SHERPA; polarizations are defined in the W$^+$Z-center-of-mass frame (COM), K factors are obtained from dividing nLO(QCD) by LO cross sections, statistical errors on the K-factors are of the order of $\mathcal{O}(10^{-3})$, except for the interference ($\mathcal{O}(10^{-1})$).

W$^+$Z	$\sigma^{\text{nLO+PS}}_{\text{Sherpa}}$ [fb]	K	$\sigma^{Q_c=20\text{GeV}}_{\text{Sherpa}}$ [fb]	K	$\sigma^{Q_c=40\text{GeV}}_{\text{Sherpa}}$ [fb]	K	$\sigma^{Q_c=80\text{GeV}}_{\text{Sherpa}}$ [fb]	K	$\sigma^{Q_c=200\text{GeV}}_{\text{Sherpa}}$ [fb]	K	$\sigma^{Q_c=500\text{GeV}}_{\text{Sherpa}}$ [fb]	K	$\sigma^{\text{LO+PS}}_{\text{Sherpa}}$ [fb]
full			28.804(27)		27.840(25)								
unpol	33.27(5)	1.79	28.492(17)	1.53	28.206(15)	1.52	26.342(15)	1.42	21.607(12)	1.16	18.910(10)	1.02	18.567(22)
polsum	32.47(5)	1.79	27.814(18)	1.53	27.566(16)	1.52	25.787(16)	1.42	21.161(13)	1.16	18.499(11)	1.02	18.175(23)
int	0.796(17)	2.04	0.678(8)	1.73	0.636(7)	1.63	0.553(7)	1.41	0.446(6)	1.14	0.411(5)	1.05	0.391(9)
L-L	1.8649(30)	1.27	1.6272(23)	1.11	1.6288(22)	1.11	1.5679(23)	1.07	1.4684(21)	1.00	1.4511(19)	0.99	1.4668(27)
L-T	5.194(10)	2.68	4.409(5)	2.28	4.255(4)	2.20	3.737(4)	1.93	2.6665(29)	1.38	2.0397(20)	1.05	1.9374(31)
T-L	4.886(9)	2.73	4.143(4)	2.31	3.965(4)	2.21	3.4366(34)	1.92	2.4350(26)	1.36	1.8770(19)	1.05	1.7917(31)
T-T	20.52(4)	1.58	17.635(12)	1.36	17.718(11)	1.37	17.046(11)	1.31	14.591(10)	1.12	13.131(8)	1.01	12.979(18)

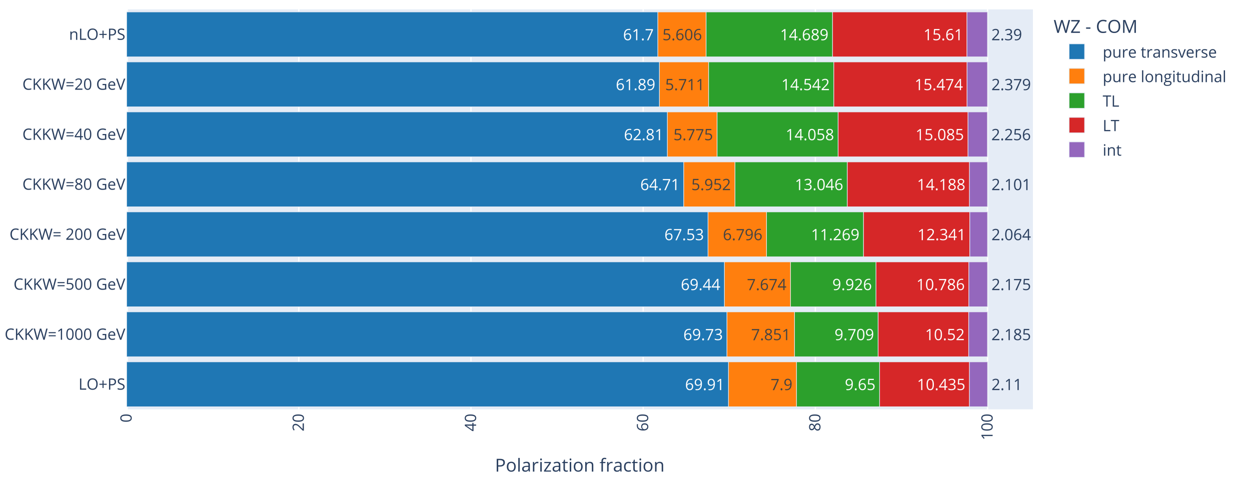

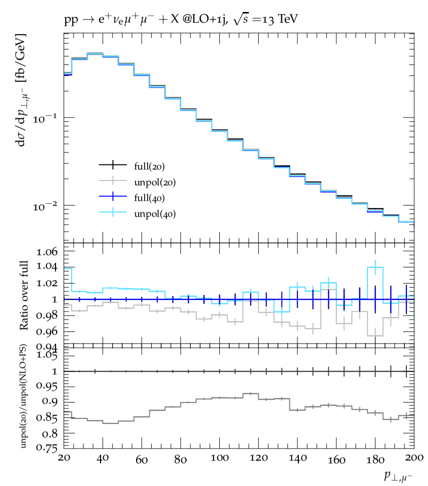

Figure 6.9: W$^+$Z center-of-mass frame (COM) polarization fractions for inclusive W$^+$Z production at nLO(QCD)+PS, LO+PS and LO+1j merged with PS (left) and full, unpolarized distributions from merged calculations (top), corresponding unpol over full ratio (middle) and ratio merged ($Q_c = 20$ GeV) over NLO QCD+PS unpol for the distribution of the muon transverse momentum $p_{\perp\mu^-}$ (right); polarization fractions are calculated relative to the unpol result from data given in table above; all results are obtained with SHERPA.

bottom of each subfigure indicate that choosing a small merging scale is crucial to get a good approximation of the NLO QCD behavior. Significant shape differences compared to the nLO(QCD)+PS predictions can be identified for a merging scale of 80 GeV already.
As can be seen from the normalized shapes and K factors in Fig. 6.10 (and further from the normalized shapes in Fig.s D.7, D.8 in the Appendix), merged calculations with small merging scales predict major parts of the nLO(QCD) polarization behavior - as expected.

Fig. 6.11 displays polarized distributions of the azimuthal angle difference between positron and muon and the muon transverse momentum obtained at nLO(QCD)+PS and from merged calculations with small merging scales (20 and 40 GeV) to illustrate the influence of merged calculations on distributions w.r.t. the nLO(QCD)+PS result (upper ratio plot) and the effect of a merging scale variation (lower ratio plot). Ratios of the polarized contributions are always calculated with respect to their counterparts in the nLO(QCD)+PS/$Q_c = 20$ GeV simulations. Further observables can be found in Appendix D.2.4.
Virtual effects and the missing very soft emission effects from the NLO QCD hard matrix element with energies below 20 GeV reduce all merged distributions by roughly 15% w.r.t. the nLO(QCD)+PS results as already observed for the integrated results. Their influence is not inevitably constant over the entire investigated phase space as can be seen from the ratios $Q_c = 20$ GeV over NLO+PS of the unpolarized result in Fig. 6.8, 6.9.
Merged calculations of the transverse results in Fig. 6.11 roughly show the same reduction as the unpol compared to the nLO(QCD)+PS result.
Nonetheless, it can be noted that the lack of very soft emissions from the hard matrix element below 20 GeV affects some polarization components different than others. For the observables in Fig. 6.11 this is especially true for the pure longitudinal component at high angle separation $\Delta\Phi_{\mathrm{e}^+\mu^-}$ and high $p_{\perp,\mu^-}$ above ~ 150 GeV where the deviations from the nLO(QCD)+PS result are smaller than for the other polarization components or the nLO(QCD)+PS result is even reproduced (Lab-LL $p_{\perp,\mu^-}$).
These specific effects are observed independently of the polarization definitions, but this is not generally true. For low angle separations $\Delta\Phi_{\mathrm{e}^+\mu^-}$ below $\frac{1}{3}\pi$, only the LL component defined in the COM exhibits a larger influence of the missing soft emission, for the Lab definition this is not observed.

When changing the merging scale from 20 to 40 GeV, missing contributions from hard matrix element emissions between 20 and 40 GeV affect the different polarization components differently too (see lower ratio plots in Fig. 6.11): transverse distributions in the Lab and TT distributions in the COM exhibit deviations of less than 2.5% in the most bins for the two different merging scales and the two observables. The LL contribution in the $\Delta\Phi_{\mathrm{e}^+\mu^-}$ distribution at $\Delta\Phi_{\mathrm{e}^+\mu^-}$ below $\frac{2}{3}\pi$ for Lab and $\frac{1}{3}\pi$ for COM is more influenced by these emissions than those other polarization components.

Again a dependence on the polarization definition can be observed: the deviation from the LL result with $Q_c = 20$ GeV is considerably larger for the Lab than for the COM definition, reaching ∼6-8% around $\Delta\Phi_{e^+\mu^-} = 0$ (only 2-4% in COM). The larger LL-deviation in the Lab leads to the conclusion that contributions from hard matrix element emissions between 20 and 40 GeV are one reason for the exceptionally large LL K-factor in the Lab compared to the K-factors for the other polarization components for small $\Delta\Phi_{e^+\mu^-}$ (cf. Fig. D.2.2 (middle)). For the COM polarization definition, the mixed components in the $\Delta\Phi_{e^+\mu^-}$ distribution feature the largest K-factors, presumably caused in parts by the soft emissions between 20 and 40 GeV as indicated from the ∼4% reduction of the $Q_c = 40$ GeV w.r.t. the $Q_c = 20$ GeV result. However, the ratio of the two merged calculations is basically flat and therefore the shape of the differential K-factor must be determined by higher energetic emissions.
Regarding the muon transverse momentum, only the LL(mixed) component is considerably affected by the merging scale variation when the polarization is defined in the Lab(COM) and $p_{\perp,\mu^-} < 60(80)$ GeV. In this phase space region, also the LL(mixed) K-factor(s) (see Fig. D.11) is(are) raised too compared to the others which thus may again (at least partially) be explained by soft emissions between 20 and 40 GeV. In contrast, the giant K factors for the transverse polarization combinations at high transverse momentum observed for both polarization definitions appear to have no real contribution from emissions below 40 GeV.

Patterns recognized in these observables can also be seen for other observables (see Fig. D.2.2) and are consistent with deviations observed for the integrated results. I.e., hard matrix element emissions below 20 GeV (and for the Lab, between 20 and 40 GeV too) have a larger effect on LL compared to the other components. Mixed components in the COM are more affected by emissions between 20 and 40 GeV than the other polarizations in that reference frame. Relations between larger deviations due to the absence of contributions from emissions between 20 and 40 GeV and exceptionally high K-factors in NLO QCD calculations for individual polarization components, that become evident in some phase space regions, can also get noticed for additional observables.

Fig. 6.8 (right) and Fig. 6.9 (right) compare the merged, unpol predictions for the two discussed observables at $Q_c = 20$ GeV and 40 GeV with the corresponding full result indicating that the non-resonant and not-covered off-shell effects amount to 3% or less.

In this study, the combination of SHERPA's merging algorithm with the new polarization feature is tested. Resulting polarization fractions are found to roughly tend to progressively approaching the LO result with increasing merging scale - as expected. However, depending on the polarization definition, the approach to LO results is not necessarily continuous. Distinct polarization fractions show different deviations up to 3.5% and 3%, respectively, when changing the merging scale from 20 to 40 GeV or comparing nLO(QCD)+PS and merged results for a small merging cut. From normalized shapes of observables it is evident that the main nLO QCD polarization behavior is also predicted by merged calculations. Detailed comparisons of both nLO(QCD)+PS and merged distributions as well as results for merging scales of 20 and 40 GeV also reveal deviations that can differ for distinct polarization combinations. These deviations allow for a partial explanation of some (large) K-factors observed in NLO QCD calculations.

In order to evaluate the impact of the observed differences on experimental measurements, scale and PDF variations would still have to be performed, which are not subject of this work. In the most recent $W^{\pm}Z$-production analysis [17], relative uncertainties on polarization fractions amount to 6%(TT), 22%(TL, LL) and 28%(LT) so observed deviations between nLO(QCD)+PS and merged polarization fractions lie within the experimental uncertainties.

However, since measurements of polarization fractions rely on multivariate analyses to determine them from a combination of several differential distributions it is difficult to assess the concrete impact of the observed deviations between the different NLO QCD approximations on experimental results, especially at distribution level.

Influences on distinct polarizations caused by different merging scales can be estimated by merging scale variations. However, it is noteworthy, that similar large deviations for single polarization combinations, relative to the general difference due to missing virtual effects, can also appear compared to full or approximated NLO QCD results which, if only merged predictions are possible, cannot be quantified.

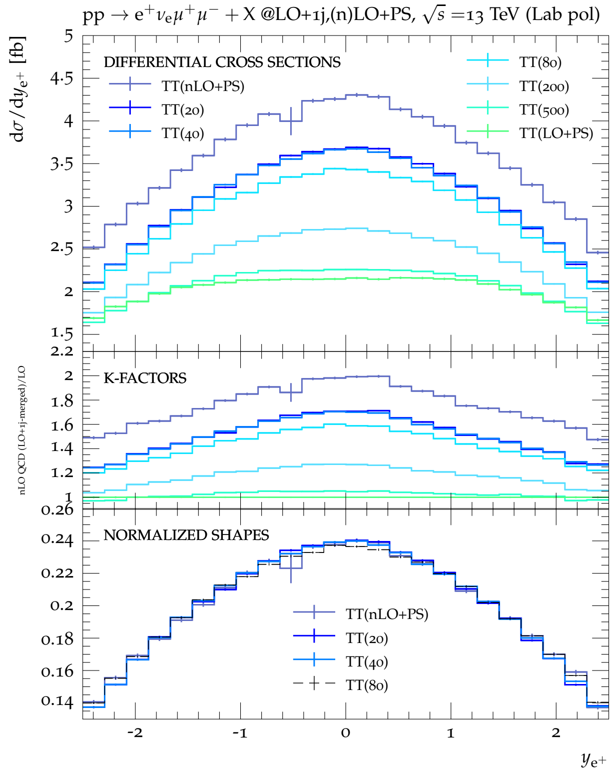

(a) $W^+_T Z_T$

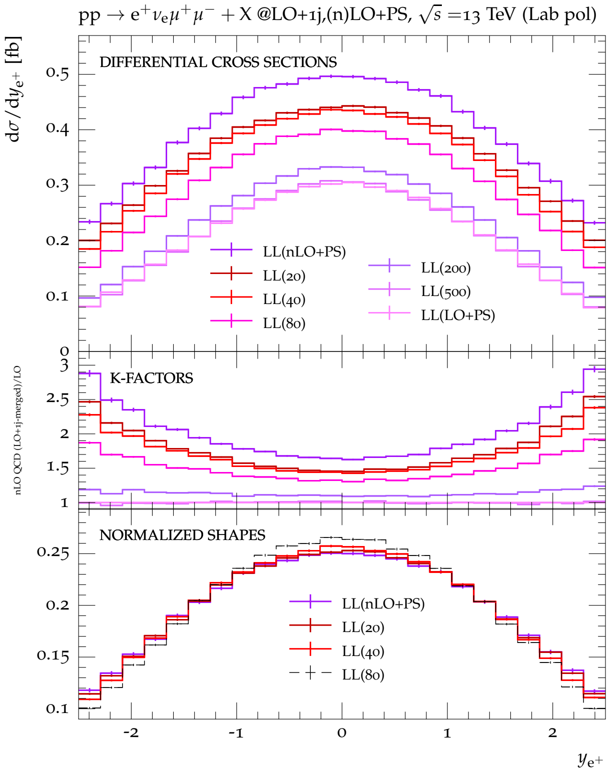

(b) $W^+_L Z_L$

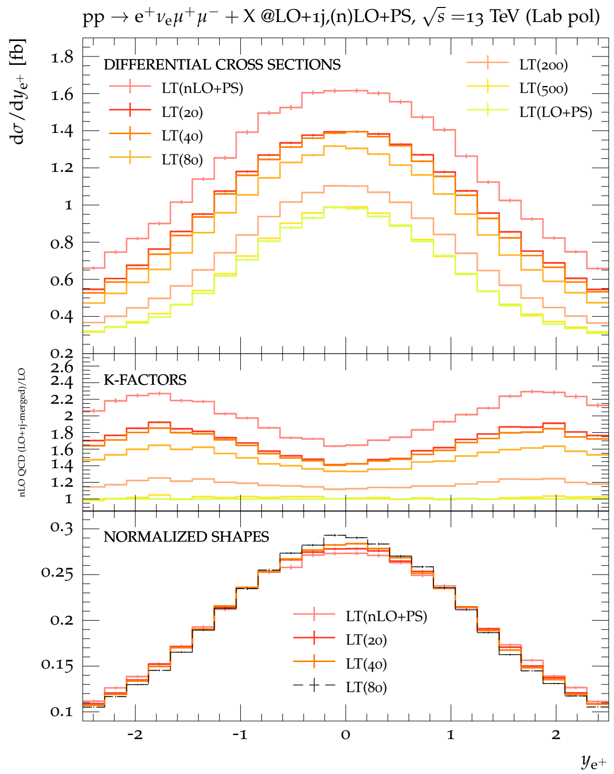

(c) $W^+_L Z_T$

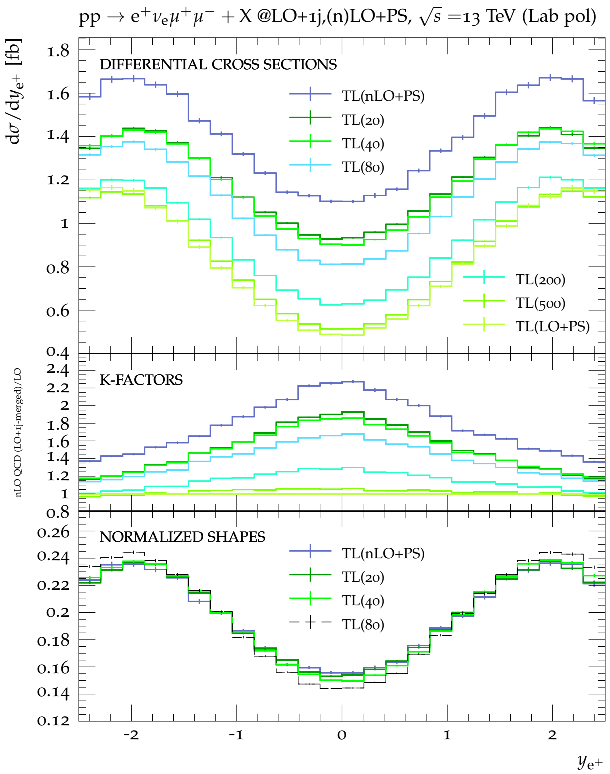

(d) $W^+_T Z_L$

Figure 6.10: Polarized distributions of the positron rapidity for the inclusive W^+Z-production process and several merging scales (numbers in brackets) between 20-500 GeV compared with distributions at nLO(QCD)+PS and LO+PS accuracy; distributions are obtained with SHERPA, K-factors are calculated as nLO(QCD)+PS(LO+1jet merged) over LO+PS, polarization is defined in the laboratory frame, each subfigure shows: nLO(QCD)+PS, LO+1jet merged, LO+PS differential distributions (top), associated K-factors (center) and normalized distributions for merging scales up to 80 GeV (integral equal to 1) (bottom).

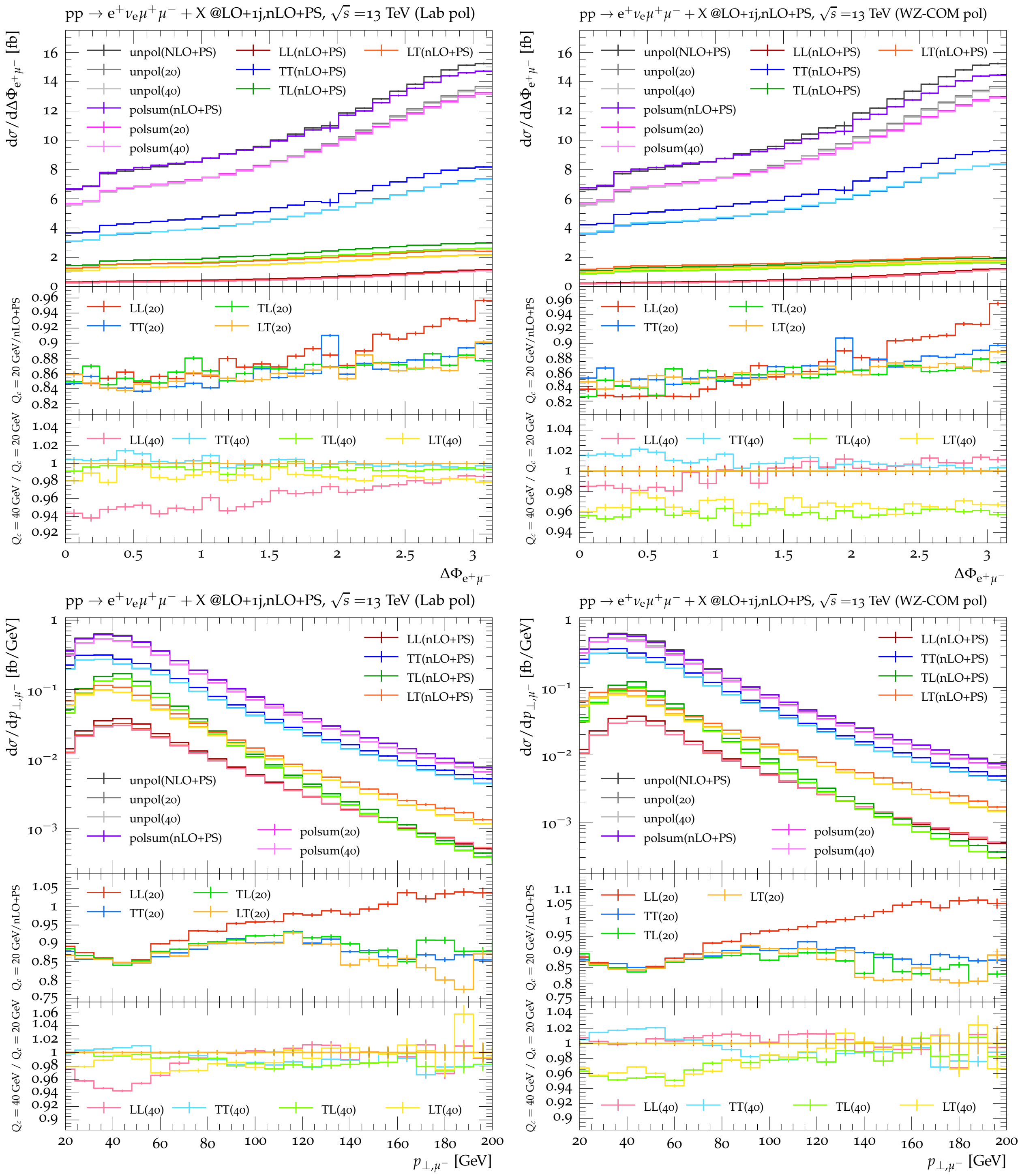

Figure 6.11: Double-polarized distributions of the azimuthal angle difference of positron and muon $\Delta\Phi_{e^+\mu^-}$ and of the muon transverse momentum $p_{\perp,\mu^-}$ for the inclusive W$^+$Z-production process; results obtained with LO+1j merged calculations with CKKW-merging scales of 20 and 40 GeV are shown in comparison with results at nLO(QCD)+PS accuracy; distributions are computed with SHERPA; polarization is defined in the laboratory frame (left) and the W$^+$Z-center-of-mass frame (right), in each subfigure from top to down are shown: differential distributions, ratio Q_c = 20 GeV over nLO(QCD)+PS results, ratio Q_c = 40 GeV / Q_c = 20 GeV.

7 Summary and Outlook

In this thesis, a new implementation in SHERPA is presented that enables the simulation of polarized cross sections for massive unstable VBs. It is based on an already implemented spin-correlated narrow-width approximation to omit not fully resonant diagrams. The calculation is essentially performed unpolarized and polarization fractions are recorded en passant, forming additional weights for each event. Thus, all possible polarization combinations can be obtained by a single simulation run. In addition to that, the interference between different polarizations can be computed event-wise, i.e. without relying on subtraction methods. Several polarization definitions are provided and can be simulated in the same simulation run, if more than one reference system is desired. The use of the new polarization feature in combination with SHERPA's implementation of the MC@NLO method allows to approximately predict NLO QCD polarization behavior. Thereby, effects of virtual corrections on polarization fractions are neglected.

The implementation is validated against literature data at fixed LO for several VBS processes, showing a very good agreement. Noticeable differences are observed only for transverse polarized cross sections and the interference contributions in processes where transverse signals are considered. This could be explained by the different definitions of such signals used in SHERPA and PHANTOM.

Additionally, first applications of the new framework in phenomenological studies are presented in this work. Aspects of VB polarization defined in different reference systems (laboratory (Lab), VB pair center-of-mass (COM) and parton-parton frame (PPFr)) for several VBS processes are discussed at fixed LO. Similarities are identified between the various processes investigated with respect to the influence of different polarization definitions e.g. the larger pure longitudinal cross section in the COM definition or differences between Lab and PPFr polarization definition, but also deviations among the processes get elaborated. Moreover, it is shown that effects of different polarization definitions can depend on the VB considered as polarized and can affect the suitability of observables for extracting polarizations. Observations already made in the literature regarding the influence of the COM relative to the Lab polarization definition on integrated cross sections in an inclusive phase space are confirmed for double-polarized signals in a more realistic fiducial phase space.

Furthermore, NLO QCD polarization effects on the inclusive W^+Z-production are studied in

this work. It is demonstrated that the nLO QCD polarization setup of SHERPA can reproduce the full NLO QCD literature result in good approximation, both at the integrated level as well as for differential distributions. The polarization fractions are found to differ by less than 3% from the full NLO QCD literature result. This is a big step towards NLO QCD polarization samples for LHC analyses from SHERPA.
In addition, it is shown that the main NLO QCD polarization behavior can be predicted in merged calculations too, if a small merging scale is chosen. Deviations, occurring between nLO(QCD)+PS and merged predictions as well as between small merging scales of 20 and 40 GeV are discussed for some observables, partially offering explanations for parts of the NLO QCD K-factors.

So far, the full functionalities of the new features are only applicable to massive VBs. Nonetheless, the majority of the implementation is developed without placing assumptions on the particle spin. Additional new polarization objects and the associated representation of the Lorentz transformations merely need to be added to the framework to enable the polarized simulation of intermediate particles with different spin types. This is planned for the near future for at least massive spin 1/2 particles.
Additionally, the calculation of coherent transverse signals will be added to the polarization framework.
By exploiting the interface to RECOLA [95] for polarized amplitudes of virtual corrections, the current nLO QCD approach could be extended to a full NLO QCD polarization simulation. Fixed order NLO QCD polarization simulations could be enabled too.
Since the functional capability of the new implementation could be demonstrated and successfully validated in this work, it can now be applied in more extensive phenomenological analyses. For example, its application for BSM physics predictions using SHERPA's interface to UFO models is planned. Furthermore, the investigation of shower effects and the NLO QCD polarization behavior in VBS processes is also conceivable, which both have not yet been investigated in the literature.

A Manual

This chapter contains the section of the SHERPA manual [93] which describes the usage of the new feature to simulate polarized cross sections. Compared to [93], the version presented here is extend by some new findings which were made after the merge of the feature into SHERPA's master development branch [79] and will be added to them with the next update of the feature. In addition to that, citations and references within the section are adjusted to this work.

A.1 Simulation of polarized cross sections for intermediate particles

This section documents how Sherpa can be used to simulate polarized cross sections for unstable intermediate state particles. At the moment, only the simulation of polarized cross sections for massive vector bosons is supported. Sherpa can simulate all polarized cross sections in one simulation run. The polarized cross sections are handled during event generation and printed out as additional event weights similar to variation weights. By default, the cross sections for all polarization combinations of the intermediate particles are output. For massive vector bosons also all transverse weights are calculated automatically. Beside this, user-specified weights can be produced as described in section A.1.4. The transverse weights are defined as an incoherent sum of all contributions where all intermediate vector bosons have a definite left- or right-handed polarization, i.e. no left-right-handed interference is included in this definition. Weight names for automatically provided weights have the form `PolWeight_refsystem.particle1.polarization1_particle2.polarization2 ...`, e.g. for a right(+)-handed W^+ and a left(-)-handed W^- the weight name becomes PolWeight_refsystem.W+.+_W+.-. The sequence of the particles in the weight name corresponds to Sherpa's internal particle ordering which can be obtained from the ordering in the process printed out when Sherpa starts running. The `refsystem` denotes the reference system which needs to be specified for an unambitious polarization definition (cf. Sec. A.1.3).
Polarized cross sections in SHERPA can currently be calculated at fixed leading order, LO+PS and in merged calculations. Furthermore, polarized NLO QCD corrections on the vector boson production part (not on the decays) can be simulated approximately by neglecting effects of vir-

tual corrections on polarization fractions. This is currently only possible on particle level using SHERPA's MC@NLO implementation for matching NLO hard matrix elements to the parton shower. Note that the resulting unpolarized prediction which is also used to compute polarized cross sections from the polarization fractions contains all NLO QCD corrections. More details about the definition of polarization for intermediate vector bosons and the implementation in SHERPA can be found in [96].

A.1.1 General procedure

The definition of polarization for particles in intermediate states is only possible for processes which can be factorized into production and decay of them. To neglect possible not-fully-resonant diagrams (i.e. diagrams where not each final state decay product particle line is connected to a single intermediate particle), for which this factorization and the definition of polarization for the intermediate particles is not possible, Sherpa applies an extended narrow-width approximation. All intermediate particles are considered as on-shell but all spin correlations are preserved. The production part of the process is specified in the `PROCESSES` part of the run card whereas the possible decays are characterized in the `HARD_DECAYS` section. Details about `PROCESSES` and `HARD_DECAYS` definition are described in the corresponding chapters of this manual. The following example shows `PROCESSES` and `HARD_DECAYS` definition of the same-sign W^+W^+-scattering with the W decaying into electrons or muons.

```
PARTICLE_DATA:
  24:
    Width: 0
  23:
    Width: 0

WIDTH_SCHEME: Fixed

HARD_DECAYS:
  Enabled: true
  Mass_Smearing: 1
  Channels:
   24,12,-11: {Status: 2}
   24,14,-13: {Status: 2}

PROCESSES:
  - 93 93 -> 24 24 93 93:
      Order: {QCD: 0, EW: 4}
```

Things to notice:

- In PARTICLE_DATA the Width of the intermediate particles must be set to zero since they are handled as stable for the hard process matrix element calculation. The particles are then decayed by the internal (hard) decay module. If VBs are considered as intermediate particles, the width of all VBs must be set to zero to preserve SU(2) Ward-Identities. This also holds true for processes where only one VB type participates as intermediate particle (e.g. same-sign WW-scattering process).
- For the calculation of polarized cross sections, spin-correlations between production and decay of the intermediate particles must be enabled (which is the default)
- Enabling the smearing of the mass of the intermediate VBs according to a Breit-Wigner distribution improves the applied spin-correlated narrow-width approximation by also retaining some of the off-shell effects, details cf. HARD_DECAYS section.
- WIDTH_SCHEME is set to Fixed (real couplings) to be consistent with setting all VB widths to zero.

The central setting to enable the calculation of polarized cross sections is:

```
HARD_DECAYS:
  Pol_Cross_Section:
    Enabled: true
```

The polarization vectors of massive vector bosons are implemented according to [35], equation (3.19). Specifically, the polarization vectors are expressed in terms of Weyl spinors. For that, an arbitrary light-like vector needs to be chosen. The definition of vector boson polarization is not unambiguous. It can be specified by the options described in the following sections: Pol_Cross_Section:Spin_Basis and Pol_Cross_Section:Reference_System.

A.1.2 Spin basis

For massive vector bosons, the choice of a light-like vector for their description in the Weyl spinor formalism is not really arbitrary since it characterizes the spin axis chosen to define the polarization. By default, the reference vector is selected such that polarization vectors are expressed in the helicity basis since this is the common choice for vector boson polarization. The polarization vectors are then eigenvectors of the helicity operator and have the same form as in (3.15) in [35] after transformation from spinor to vector representation. Sherpa provides several gauge choices for the Weyl spinors. To really get the polarization vectors in this form, the following spinor gauge choice must be chosen:

```
COMIX_DEFAULT_GAUGE: 0
```

```
HARD_DECAYS:
  Pol_Cross_Section:
    Enabled: true
        Spin_Basis: Helicity
```

If `Spin_Basis: ComixDefault` is selected, the COMIX default reference vector specified by `COMIX_DEFAULT_GAUGE` (default 1 which corresponds to $(1.0, 0.0, 1/\sqrt{2}, 1/\sqrt{2})$) is used. Furthermore, it is possible to hand over any constant reference vector:

```
HARD_DECAYS:
  Pol_Cross_Section:
        Enabled: true
        Spin_Basis: 1.0, 0.0, 1.0, 0.0
```

A.1.3 Reference system

The helicity of a massive particle is not Lorentz invariant. Therefore a reference system needs to be chosen to define vector boson polarization unambiguously. Sherpa supports the following options:

`Reference_System: Lab` (default)
Vector boson polarization is defined in the laboratory frame.

`Reference_System: COM`
Vector boson polarization is defined in the center of mass system of all hard-decaying particles.

`Reference_System: PPFr`
Vector boson polarization is defined in the center of mass system of the two interacting partons.

Sherpa allows the calculation of polarized cross sections for different polarization definitions specified by different reference systems in one simulation run:

```
HARD_DECAYS:
  Pol_Cross_Section:
    Enabled: true
    Reference_System: [Lab, COM]
```

In addition to the options explained above, any reference system defined by one or several hard process initial or final state particles can be used. This can be specified by the particle numbers of the desired particles according to the Sherpa numbering scheme. Distinct particle numbers should only be separated by a single white space, at least if more than one reference system is specified. The second reference frame in the following example is the parton-parton rest frame.

```
HARD_DECAYS:
  Pol_Cross_Section:
    Enabled: true
    Reference_System: [Lab, 0 1]
```

In the Sherpa event output, polarized cross sections of vector bosons defined in different frames are distinguished by adding the reference frame keyword to the weight names, e.g. PolWeight_Lab.W+.+_W+.-. For reference systems defined by particle numbers, `refsystemn` is added to avoid commas in weight names. n is the place in the reference system list specified in the YAML-File starting at 0. For the example above this means e.g. PolWeight_refsystem1.W+.+_W+.-.

A.1.4 Custom polarized cross sections

Sherpa provides the calculation of two different types of custom polarized cross sections. On the one hand, it is possible to specify a comma separated list of weight names from the automatically calculated cross sections. These cross sections are then added by Sherpa and printed out as additional event weights. On the other hand, partially unpolarized cross sections can be calculated. These can be specified by the numbers of the particles which should be considered as unpolarized. Again, the numbering of the particles follows the Sherpa numbering scheme. Noteworthy, the partially unpolarized weights also contain interference contributions from the unpolarized intermediate particles. Therefore an additional interference weight is added to the output describing the sum of the remaining interference contributions. Custom weights are generally specified by `Weight` in the run card. By adding numbers to `Weight` e.g. `Weight1`, `Weight2` ... more than one custom cross section can be calculated. The number is limited to `Weight10` by default but can be increased by using `Number_of_custom_weights`. In the following example the W^- is considered as unpolarized:

```
HARD_DECAYS:
  Enabled: true
  Mass_Smearing: 1
  Channels:
    24,12,-11: {Status: 2}
```

```
    -24,-14,13: {Status: 2}
  Pol_Cross_Section:
   Enabled: true
   Weight1: W+.+_W-.+, W+.-_W-.+
   Weight2: 3

PROCESSES:
  - 93 93 -> 24 -24 93 93:
      Order: {QCD: 0, EW: 4}
```

For partially unpolarized cross sections, the weight naming pattern is adjusted. The polarization of the unpolarized particle in the weight names is set to "U" and their spin labels are moved to the beginning of the weight name. If more than one intermediate particle is considered as unpolarized, the particle ordering among the unpolarized particles is preserved. The weight name is then prefixed by the name of the custom weight as specified in the run card. Thus, for the single-polarized cross section of a right-handed W^+ boson in opposite sign W^+W^- production with polarization defined in the laboratory frame (named Weight2 in the example run card above), the final weight name becomes `PolWeight_Lab.Weight1_W-.u_W+.+`.
For custom cross sections specified by weight names (e.g. `Weight1` in the example above), `PolWeight_refsystem.Weightn` is used instead to avoid long weight names. Hereby, `Weightn` corresponds to the corresponding setting in the run card.

B Theoretical remarks

B.1 Completeness relation for off-shell vector bosons

In Sec. 2.2.1, the completeness relation and a representation of polarization vectors for on-shell massive VBs is given. Since massive VBs appear as unstable particles within observable processes they are off-shell. Off-shell polarization vectors can be obtained from their on-shell associations by replacing the VB rest mass by the invariant mass of the off-shell VB momentum $\sqrt{q^2}$. This effectively changes the longitudinal polarization only:

$$\varepsilon_0^\mu(p) = \frac{p^0}{\sqrt{q^2}}\Big(\frac{|\vec{p}|}{p^0}, \cos\phi\sin\theta, \sin\phi\sin\theta, \cos\theta\Big)\,. \tag{B.1}$$

An off-shell VB can have four spin degrees of freedoms, the fourth auxiliary polarization can be chosen as [59]:

$$\varepsilon_A^\mu = \sqrt{\frac{q^2 - m_{\mathrm{V}}^2}{q^2 m_{\mathrm{V}}^2}}\left(E, |\vec{q}|\sin\theta\cos\phi, |\vec{q}|\sin\theta\sin\phi, |\vec{q}|\cos\theta\right). \tag{B.2}$$

It vanishes for on-shell particles as expected. The completeness relation for off-shell particles can be obtained by the same replacement as for the polarization vectors:

$$-g^{\mu\nu} + \frac{q^\mu q^\nu}{q^2} = \sum_{i=1}^{3} \varepsilon_\lambda^\mu(q)\varepsilon_\lambda^{\nu *}(q)\,. \tag{B.3}$$

Adding

$$\varepsilon_A^\mu(q)\varepsilon_A^{\nu *}(q) = \frac{q^2 - m_{\mathrm{V}}^2}{q^2 m_{\mathrm{V}}^2} q^\mu q^\nu \tag{B.4}$$

on both sides of Eq. B.3 leads to the completeness relation in Eq. 3.10 used in Sec. 3.3.

B.2 Remarks on the matrix element transformation in Eq. 4.7

In this section, some remarks to the derivation of Eq. 4.7 are given. Only matrix elements of intermediate VBs are considered since intermediate fermions are not part of this thesis. For simplicity, the production tensor of a process with two intermediate VBs is considered and momentum dependencies of polarization vectors and matrix elements are suppressed. The reduction to decay matrices always involving only one single VB or the extension to production processes with more than two VBs are straightforward.
May $\tilde{\varepsilon}^{\text{parti}\,\mu}_{\lambda_i}$ and $\varepsilon^{\text{parti}\,\mu}_{\kappa_i}$ be the (outgoing [1]) polarization vectors of polarization λ_i and κ_i in the desired (new) and the matrix element calculation's default (old) polarization definition, respectively. Both are connected by a linear combination (basis transformation):

$$\tilde{\varepsilon}^{\text{parti}\,\mu}_{\lambda_i} = a^{\text{parti}}_{\lambda_i,+}\varepsilon^{\text{parti}\,\mu}_{+} + a^{\text{parti}}_{\lambda_i,-}\varepsilon^{\text{parti}\,\mu}_{-} + a^{\text{parti}}_{\lambda_i,0}\,\varepsilon^{\text{parti}\,\mu}_{0}\,. \tag{B.5}$$

The squared matrix elements in the new polarization definition can be written in the form:

$$|\mathcal{M}^{\text{new}}|^2_{\lambda_1\lambda_2,\lambda_1'\lambda_2'} = \mathcal{M}^{\text{prod}}_{\mu_1,\mu_2}\tilde{\varepsilon}^{\text{part1}\,\mu_1}_{\lambda_1}\tilde{\varepsilon}^{\text{part2}\,\mu_2}_{\lambda_2}\mathcal{M}^{*\text{prod}}_{\nu_1,\nu_2}\tilde{\varepsilon}^{*\text{part1}\,\nu_1}_{\lambda_1'}\tilde{\varepsilon}^{*\text{part2}\,\nu_2}_{\lambda_2'}\,. \tag{B.6}$$

Substituting Eq. B.5 into Eq. B.6 yields:

$$\begin{aligned}
|\mathcal{M}^{\text{new}}|^2_{\lambda_1\lambda_2,\lambda_1'\lambda_2'} &= \mathcal{M}^{\text{prod}}_{\mu_1,\mu_2}\Big[a^{\text{part1}}_{\lambda_1,+}\varepsilon^{\text{part1}\mu_1}_{+} + a^{\text{part1}}_{\lambda_1,-}\varepsilon^{\text{part1}\mu_1}_{-} + a^{\text{part1}}_{\lambda_1,0}\,\varepsilon^{\text{part1}\mu_1}_{0}\Big] \\
&\cdot\Big[a^{\text{part2}}_{\lambda_2,+}\varepsilon^{\text{part2}\,\mu_2}_{+} + a^{\text{part2}}_{\lambda_2,-}\varepsilon^{\text{part2}\,\mu_2}_{-} + a^{\text{part2}}_{\lambda_2,0}\,\varepsilon^{\text{part2}\,\mu_2}_{0}\Big] \\
&\cdot\mathcal{M}^{*\text{prod}}_{\nu_1,\nu_2}\Big[a^{*\text{part1}}_{\lambda_1',+}\,\varepsilon^{*\text{part1}\nu_1}_{+} + a^{*\text{part1}}_{\lambda_1',-}\,\varepsilon^{*\text{part1}\nu_1}_{-} + a^{*\text{part1}}_{\lambda_1',0}\,\varepsilon^{*\text{part1}\nu_1}_{0}\Big] \\
&\cdot\Big[a^{*\text{part2}}_{\lambda_2',+}\,\varepsilon^{*\text{part2}\,\nu_2}_{+} + a^{*\text{part2}}_{\lambda_2',-}\,\varepsilon^{*\text{part2}\,\nu_2}_{-} + a^{*\text{part2}}_{\lambda_2',0}\,\varepsilon^{*\text{part2}\,\nu_2}_{0}\Big] \\
&= a^{\text{part1}}_{\lambda_1,+}a^{\text{part2}}_{\lambda_2,+}a^{*\text{part1}}_{\lambda_1',+}\,a^{*\text{part2}}_{\lambda_2',+}\,\underbrace{\mathcal{M}^{\text{prod}}_{\mu_1,\mu_2}\varepsilon^{\text{part1}\mu_1}_{+}\,\varepsilon^{\text{part2}\,\mu_2}_{+}}_{\mathcal{M}^{\text{old}}_{++}}\underbrace{\mathcal{M}^{*\text{prod}}_{\nu_1,\nu_2}\varepsilon^{*\text{part1}\nu_1}_{+}\,\varepsilon^{*\text{part2}\,\nu_2}_{+}}_{\mathcal{M}^{*\text{old}}_{++}} \\
&+ a^{\text{part1}}_{\lambda_1,-}a^{\text{part2}}_{\lambda_2,+}a^{*\text{part1}}_{\lambda_1',+}\,a^{*\text{part2}}_{\lambda_2',+}\,\underbrace{\mathcal{M}^{\text{prod}}_{\mu_1,\mu_2}\varepsilon^{\text{part1}\mu_1}_{-}\,\varepsilon^{\text{part2}\,\mu_2}_{+}}_{\mathcal{M}^{\text{old}}_{-+}}\underbrace{\mathcal{M}^{*\text{prod}}_{\nu_1,\nu_2}\varepsilon^{*\text{part1}\nu_1}_{+}\,\varepsilon^{*\text{part2}\,\nu_2}_{+}}_{\mathcal{M}^{*\text{old}}_{++}} \\
&+ \ldots\,.
\end{aligned} \tag{B.7}$$

The last expression corresponds to the sum in Eq. 4.7 for two particles and follows from the fact that only the polarization vector changes in the matrix element, i.e. $\mathcal{M}^{\text{prod}}_{\mu_1,\mu_2}$ is the same in the old and new matrix element. All in all, it contains $m^2_{nhel1}\cdot m^2_{nhel2}$ (equals to 81 for two VB) terms with m_{nheli} denoting the spin degrees of freedom of particle i, i.e. all matrix elements of the old production tensor take part to each of the matrix elements in the new polarization basis.

[1]For decay matrices incoming polarization vectors need to be considered instead

C Runcards

C.1 SHERPA-Simulation of VVjj processes

The following run cards got compiled for the same-sign W^+W^+ scattering process and utilized for the validation against Ref. [76]. They configure the polarization simulation and the full calculation, respectively. For the other VVjj production simulations, only minor adjustments are necessary: For all W^+W^+jj, the vector bosons in the `PROCESSES` description and the allowed decays in the `HARD_DECAYS` section are changed accordingly (cf. Tab. C.1). Additionally, the

Table C.1: SHERPA `PROCESSES` and `HARD_DECAYS` syntax for the SHERPA simulation of VVjj processes.

Process	full	polarized calculation	
	`PROCESSES`	`PROCESSES`	`HARD_DECAYS`
Validation against Ref. [76], [59] (only ZZjj) and phenomenological simulations (only ZZjj)			
W^+W^-jj	93 93 -> -11 12 13 -14 93 93	93 93 -> 24 -24 93 93	24,12,-11: Status:2
			-24,-14,13: Status:2
W^+Zjj	93 93 -> -11 12 13 -13 93 93	93 93 -> 24 23 93 93	24,12,-11: Status:2
			23,13,-13:: Status:2
ZZjj	93 93 -> 11 -11 13 -13	93 93 -> 23 23 93 93	23,13,-13: Status:2
			23,11,-11: Status:2
Validation against Ref. [58] and phenomenological simulations			
W^+W^-jj	93 93 -> 11 -12 -13 14 93 93	93 93 -> 24 -24 93 93	24,14,-13: Status:2
			-24,-12,11: Status:2
$W^{(+)}$Zjj	93 93 -> -13 14 11 -11 93 93	93 93 -> 24 23 93 93	24,14,-13: Status:2
			23,11,-11:: Status:2

mass selection criteria on the VB pair invariant mass are added to the `SELECTORS` for the full simulation by the help of the `Variable_Selector`, e.g. for the $W^{(+)}$Zjj:

```
- VariableSelector:
Variable: m
```

```
Flavs: [-11, 12, 13, -13]
Ranges:
- [200, E_CMS]
```

The required mass cut on the Z mass is given by
[Mass, 13, -13, <MINZMASS>, <MAXZMASS>] or
[Mass, 11, -11, <MINZMASS>, <MAXZMASS>] within the SELECTORS scoped setting.
Except for the W^+W^+jj validation simulation, the scale was set to:
SCALES: {VAR{0.5*Abs2(p[2]+p[3]+p[4]+p[5])}} (full) or
SCALES: {VAR{0.5*Abs2(p[2]+p[3])}} (polarized).
For the validation against Ref. [58] the jet selection criteria were adjusted. A perfect b-veto on initial and final states is realized by setting the b-quark massive:

```
PARTICLE_DATA:
5:
Massive: true
```

The Single_Polarized_Channel setting was only used for processes involving two identical VBs to provide single-polarized cross sections where the polarized VB decaying due to a certain decay channel. This setting specifies the decay channel whose parent VB should be polarized (for ZZjj simulation: Single_Polarized_Channel: {Weight1: Z.T_Z.0, Z.0_Z.T}). Corresponding weights are calculated by a private method in PolWeights_Map and therefore is not documented in the manual. To investigate VB polarization defined in the parton-parton frame, PPFr has to be added to the Reference_System list.

```
# Sherpa configuration for same sign WW-production from jj and W-
   decay to e-nu, my-nu

# set up beams for LHC run 2
BEAMS: 2212
BEAM_ENERGIES: 6500

# Switch off multiparton interactions
MI_HANDLER: None  # Amisic
# Switch off Shower generator
SHOWER_GENERATOR: None
# no hadronisation
FRAGMENTATION: None
# switch off QED corrections
ME_QED: {ENABLED: false}
# matrix element calculation
ME_GENERATORS:
```

```
- Comix
BEAM_REMNANTS: false

# PDF settings
PDF_LIBRARY: LHAPDFSherpa
PDF_SET: NNPDF30_lo_as_0130
ALPHAS: {USE_PDF: 1}

# Coupling constants
EW_SCHEME: Gmu
GF: 0.0000116637
WIDTH_SCHEME: Fixed

EVENT_GENERATION_MODE: Weighted
SCALES: VAR{PPerp(p[4])*PPerp(p[5])}

# Specify certain spinor gauge to receive expected helicity states
COMIX_DEFAULT_GAUGE: 0

# Modified particle data
PARTICLE_DATA:
  24:
    Width: 0
    Mass: 80.358
  23:
    Mass: 91.153
    Width: 0

# Disable QED correction module
YFS:
   MODE: None

# Allowed W-decays after calculating their production matrix
   element
HARD_DECAYS:
  Enabled: true
  Mass_Smearing: 1
  Channels:
```

```
    24,12,-11: {Status: 2}
    24,14,-13: {Status: 2}
  QED_Corrections: 0
# Settings for polarized cross sections
  Pol_Cross_Section:
    Enabled: true
    Spin_Basis: Helicity
    Reference_System: [Lab, COM]
    Weight1: W+.0_W+.T, W+.T_W+.0
    Single_Polarized_Channel: 24,12,-11

# production process: (jj -> W W j j)
PROCESSES:
- 93 93 -> 24 24 93 93:
    Order: {QCD: 0, EW: 4}

# Jet cuts
SELECTORS:
- FastjetSelector:
    Expression: Mass(p[4]+p[5])>500
    Algorithm: antikt
    N: 2
    PTMin: 20.0
    EtaMax: 5.0
- FastjetSelector:
    Expression: abs(Eta(p[4])-Eta(p[5]))>2.5
    Algorithm: antikt
    N: 2
    PTMin: 20.0
    EtaMax: 5.0

ANALYSIS: Rivet
RIVET:
  --analyses:
     - MC_polssWW_Analysis
     - MC_polssWW_Analysis:PHASESPACE=FIDUCIAL
  --ignore-beams: 1
```

```
# Sherpa configuration for the simulation of the full same-sign W-
    pair production process in association with two jets (mixed
    flavor decay channel only)
BEAMS: 2212
BEAM_ENERGIES: 6500

MI_HANDLER: None
SHOWER_GENERATOR: None
FRAGMENTATION: None
ME_QED: {ENABLED: false}
ME_GENERATORS:
- Comix
BEAM_REMNANTS: false

PDF_LIBRARY: LHAPDFSherpa
PDF_SET: NNPDF30_lo_as_0130
ALPHAS: {USE_PDF: 1}

YFS:
    MODE: None

EW_SCHEME: Gmu
GF: 0.0000116637
# Constructing real complings from complex EW parameters
# in CMS is ambigious
GMU_CMS_AQED_CONVENTION: 4

PARTICLE_DATA:
  24:
    Mass: 80.358
    Width: 2.084
  23:
    Mass: 91.153
    Width: 2.494

EVENT_GENERATION_MODE: Weighted
SCALES: VAR{PPerp(p[6])*PPerp(p[7])}
```

```
PROCESSES:
- 93 93 -> -11 12 -13 14 93 93:
    Order: {QCD: 0, EW: 6}

SELECTORS:
- FastjetSelector:
    Expression: abs(Eta(p[6])-Eta(p[7]))>2.5
    Algorithm: antikt
    N: 2
    PTMin: 20.0
    EtaMax: 5.0
- FastjetSelector:
    Expression: Mass(p[6]+p[7])>500
    Algorithm: antikt
    N: 2
    PTMin: 20.0
    EtaMax: 5.0

ANALYSIS: Rivet
RIVET:
  --analyses:
      - MC_polssWW_Analysis
      - MC_polssWW_Analysis:PHASESPACE=FIDUCIAL
  --ignore-beams: 1
```

C.2 SHERPA-Simulation of W^+j production

In this section, some details are presented about the short study of the single W^+j production process regarding the different definitions of the transverse signal recently used in SHERPA (incoherent definition) and in the literature (coherent definition including left-right interference). Tab. C.2 summarizes the simulation settings and the phase space selection chosen according to Ref. [77].
To calculate the coherent transverse signal, the labeling method described in Fig. 4.4 is extended such that the interference terms in the amplitude tensor get labeled with two indices per particle too and get stored in a temporary C++ map containing all labeled entries of the amplitude

[1]For the definition of $M_{T,\mathrm{W}}$ see Sec. 6.2.1

Table C.2: Simulation settings and phase space definition used for SHERPA simulations of the single W^+j production process at fixed LO.

Setting	
PDF-Set from LHAPDF6 [88]	NNPDF31_lo_as_0118
Electroweak scheme G_μ	$G_\mu = 1.16638 \cdot 10^{-5}\,\mathrm{GeV}^{-2}$ and complex mass scheme (full), real EW parameters (polarization)
Strong coupling $\alpha_S(M_Z)$	0.118
Factorization scale	$\mu_F = \frac{1}{2}\left(\sqrt{M_W^2 + p_{\perp,W}^2} + \sum_{i=\mathrm{jets}} p_{\perp,j}\right)$
VB pol masses	$M_W = 80.352$ GeV, $M_Z = 91.1535$ GeV
VB pol widths	zero for all VB in polarization calculations, $\Gamma_W = 2.084$ GeV, $\Gamma_Z = 2.4943$ GeV otherwise
Phase space	$p_{\perp,j} > 30$ GeV, $\lvert y_j \rvert < 2.4$
	$p_{\perp,e^+} > 25$ GeV, $\lvert \eta_{e^+} \rvert < 2.5$
	$\Delta R_{e^+,j} > 0.4$, $M_{T,W}$ [1] $>$50 GeV

tensor. Furthermore, the method for allowing the addition of polarization weights specified in the run card is adjusted such that interference terms can be added too.

```
# Sherpa configuration for single W+jet-production and W-decay to
  e-nu
BEAMS: 2212
BEAM_ENERGIES: 6500

MI_HANDLER: None
SHOWER_GENERATOR: None
FRAGMENTATION: None
ME_QED: {ENABLED: false}
ME_GENERATORS:
- Comix
BEAM_REMNANTS: false

PDF_LIBRARY: LHAPDFSherpa
PDF_SET: NNPDF31_lo_as_0118
ALPHAS: {USE_PDF: 1}

YFS:
  MODE: None
```

```yaml
SCALES: VAR{0.25*(sqrt(PPerp2(p[2])+Abs2(p[2]))+PPerp(p[3]))*(sqrt(
    PPerp2(p[2])+Abs2(p[2]))+PPerp(p[3]))}

EW_SCHEME: Gmu
GF: 0.0000116638
WIDTH_SCHEME: Fixed

COMIX_DEFAULT_GAUGE: 0

PARTICLE_DATA:
  24:
    Mass: 80.3520
    Width: 0
  23:
    Mass: 91.1535
    Width: 0

HARD_DECAYS:
  Enabled: true
  # disable mass smearing
  Mass_Smearing: 0
  Channels:
    24,12,-11: {Status: 2}
  QED_Corrections: 0
  Pol_Cross_Section:
    Enabled: true
    # coherent transverse signal definition
    Weight1: W+.T, W+.+-, W+.-+
    # new interference contribution without left-right
       interference
    Weight2: W+.0+, W+.+0, W+.0-, W+.-0
    # new polsum including left-right interference
    Weight3: W+.T, W+.0, W+.+-, W+.-+

# (jj -> W j)
PROCESSES:
- 93 93 -> 24 93:
```

```
    Order: {QCD: 1, EW: 1}

SELECTORS:
- FastjetFinder:
    Algorithm: antikt
    N: 1
    PTMin: 30.0
    YMax: 2.4

ANALYSIS: Rivet
RIVET:
  --analyses:
      - MC_singleW_Analysis
      - MC_singleW_Analysis:PHASESPACE=FIDUCIAL
  --ignore-beams: 1
```

C.3 Inclusive W^+Z production at nLO QCD+PS and LO+1j merged with PS with SHERPA

The first run card printed below is used for the polarized simulation of the inclusive W^+Z production at LO with up to one jet merged with parton shower, the second one to compute polarized predictions within SHERPA's nLO QCD setup for polarization calculation (cf. Sec. 4.5). The third run card is utilized for the performed full calculations. The `METS` scale setter in the nLO QCD run setup is used for the comparison with NLO QCD fixed-order calculations. For the comparison with merged calculations, the core scale is set with `MEPS:CORE_SCALE` for a scale setting consistent with the parton shower for additional emissions [92]. To perform the simulations at fixed LO and LO+PS displayed in Appendix D.2.1, the run cards for the nLO+PS calculation to validate with fixed-order results need to be slightly adjusted by:

LO+PS The `PROCESSES` setting in the nLO+PS and merged calculations is replaced by
```
PROCESSES:
- 93 93 -> 24 23:
Order: QCD: 0, EW: 2
```
The scale is set analogously to the polarized calculations. Furthermore, the PDF set is changed to `NNPDF31_lo_as_0118`.

LO parton shower, hadronization, QED corrections, beam remnants and multi-parton interactions are disabled as in the run cards in Appendix C.1, the `PROCESSES` section is chosen as given for the LO+PS setup, for scale-setting the `MEPS` scale setter is replaced by the `VAR` scale setter

```
# Sherpa-configuration for inclusive WZ-production at LO
# with up to one jet merged to parton shower
BEAMS: 2212
BEAM_ENERGIES: 6500

ME_GENERATORS:
   - Comix

PDF_LIBRARY: LHAPDFSherpa
PDF_SET: NNPDF31_nlo_as_0118
ALPHAS: {USE_PDF: 1}

MEPS:
 CORE_SCALE: VAR{0.25*sqr(80.352+91.153)}

EVENT_GENERATION_MODE: Weighted

EW_SCHEME: Gmu
GF: 0.0000116638
WIDTH_SCHEME: Fixed

PARTICLE_DATA:
   24:
      Mass: 80.352
      Width: 0
   23:
      Mass: 91.153
      Width: 0

COMIX_DEFAULT_GAUGE: 0

HARD_DECAYS:
   Enabled: true
   Mass_Smearing: 1
   Channels:
```

```
      24,12,-11: {Status: 2}
      23,13,-13: {Status: 2}
   Pol_Cross_Section:
      Enabled: true
      Spin_Basis: Helicity
      Reference_System: [Lab, COM]
      Weight1: 2
      Weight2: 3

PROCESSES:
- 93 93 -> 24 23 93{1}:
      Order: {QCD: 0, EW: 2}
      CKKW: 20 #40, 80, 200, 500, 1000

ANALYSIS: Rivet
RIVET:
  --analyses:
      - MC_WZ_NLOQCD
      - MC_WZ_NLOQCD:PHASESPACE=FIDUCIAL
  --ignore-beams: 1
  USE_HEPMC_SHORT: 1
```

```
# Sherpa configuration for inclusive W+Z production @nLO QCD with
    shower
BEAMS: 2212
BEAM_ENERGIES: 6500

ME_GENERATORS:
  - Comix
  - Amegic
  - OpenLoops

PDF_LIBRARY: LHAPDFSherpa
PDF_SET: NNPDF31_nlo_as_0118
ALPHAS: {USE_PDF: 1}

# for nLO+PS simulations performed to compare with merged
    calculations
#MEPS:
```

```yaml
#  CORE_SCALE: VAR{0.25*sqr(80.352+91.153)}

# Scale setting for comparison with fixed order calculations
SCALES: METS{0.25*sqr(80.352+91.153)}

EVENT_GENERATION_MODE: Weighted

EW_SCHEME: Gmu
GF: 0.0000116638
WIDTH_SCHEME: Fixed

PARTICLE_DATA:
  24:
    Mass: 80.352
    Width: 0
  23:
    Mass: 91.153
    Width: 0

# speed and neg weight fraction improvements
NLO_CSS_PSMODE: 2

COMIX_DEFAULT_GAUGE: 0

HARD_DECAYS:
  Enabled: true
  Mass_Smearing: 1
  Channels:
    24,12,-11: {Status: 2}
    23,13,-13: {Status: 2}
  Pol_Cross_Section:
    Enabled: true
    Spin_Basis: Helicity
    Reference_System: [Lab, COM]
    Weight1: 2
    Weight2: 3

# pp -> WZ @NLO, matching to shower with MC@NLO
```

```
PROCESSES:
- 93 93 -> 24 23:
     Order: {QCD: 0, EW: 2}
     NLO_Mode: MC@NLO
     NLO_Order: {QCD: 1, EW: 0}
     ME_Generator: Amegic
     RS_ME_Generator: Comix
     Loop_Generator: OpenLoops

ANALYSIS: Rivet
RIVET:
  --analyses:
       - MC_WZ_NLOQCD
       - MC_WZ_NLOQCD:PHASESPACE=FIDUCIAL
  --ignore-beams: 1
  USE_HEPMC_SHORT: 1
```

```
# Sherpa configuration for the full inclusive WZ production at NLO
   +PS accuracy and for up to one jet merged with PS calculations

BEAMS: 2212
BEAM_ENERGIES: 6500

ME_GENERATORS:
  - Comix
  - Amegic
  - OpenLoops

PDF_LIBRARY: LHAPDFSherpa
PDF_SET: NNPDF31_nlo_as_0118
ALPHAS: {USE_PDF: 1}

# for merged setups and nLO+PS simulations performed to compare
   with merged calculations
#MEPS:
#  CORE_SCALE: VAR{0.25*sqr(80.352+91.153)}

# Scale setting for comparison with fixed order calculations
SCALES: METS{0.25*sqr(80.352+91.153)}
```

```
EVENT_GENERATION_MODE: Weighted

EW_SCHEME: Gmu
G_MU: 0.0000116638
GMU_CMS_AQED_CONVENTION: 4

PARTICLE_DATA:
  24:
    Width: 2.084
    Mass: 80.352
  23:
    Width: 2.4943
    Mass: 91.153

NLO_CSS_PSMODE: 2

COMIX_DEFAULT_GAUGE: 0

# PROCESSES section for full NLO+PS calculation
PROCESSES:
- 93 93 -> -11 12 13 -13:
    Order: {QCD: 0, EW: 4}
    NLO_Mode: MC@NLO
    NLO_Order: {QCD: 1, EW: 0}
    ME_Generator: Amegic
    RS_ME_Generator: Comix
    Loop_Generator: OpenLoops

# PROCESSES section for merged setups
#PROCESSES:
#- 93 93 -> -11 12 13 -13 93{1}:
#    Order: {QCD: 0, EW: 4}
#    CKKW: 20 # 40 80 200 500 1000

SELECTORS:
- [PT, -11, 10, E_CMS]
- [PT, 13, 5, E_CMS]
```

```
- [PT, -13, 5, E_CMS]
- [Y, 90, -5.0, 5.0]
- [Mass, 13, -13, 71, 111]

ANALYSIS: Rivet
RIVET:
  --analyses:
      - MC_WZ_NLOQCD
      - MC_WZ_NLOQCD:PHASESPACE=FIDUCIAL
  --ignore-beams: 1
  USE_HEPMC_SHORT: 1
```

D Supplementary data

D.1 Further observables studied for the validation of the new polarization feature at fixed LO

In this section, distributions for further observables are given which are compared with literature predictions to validate the new polarization feature at fixed LO. They come from the same simulations as the distributions shown in Chap. 5 which should be consulted for information about simulation parameters and phase space definition. Fig. D.1 displays further observables for the W^+W^-jj process, Fig. D.2 for the W^+W^-jj process and Fig. D.3 those for the ZZjj process. Corresponding literature predictions can be found in Ref. [58] for the W^+W^-jj process, in Ref. [76] for the W^+W^+jj process and in Ref. [59] for the ZZjj process.

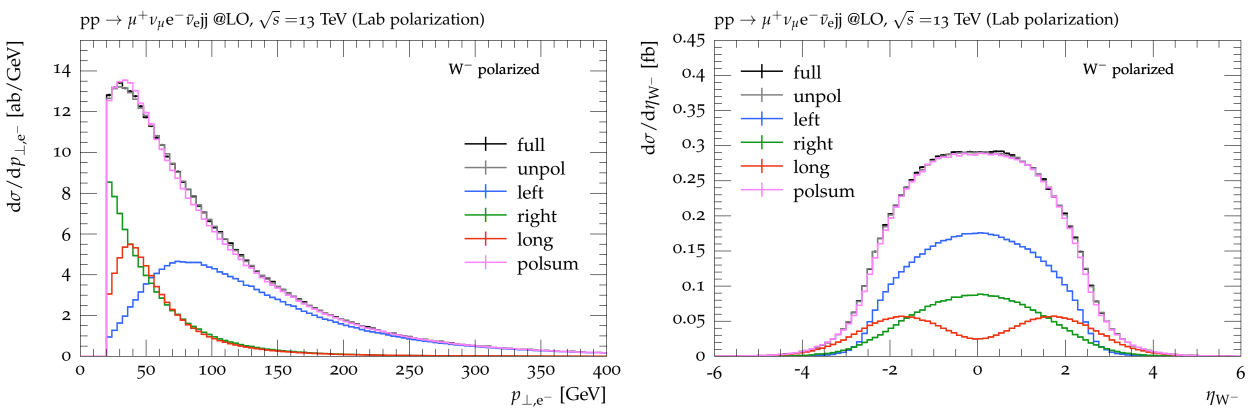

Figure D.1: Single-polarized distributions of the transverse momentum of the electron $p_{\perp,\mathrm{e}^-}$ (top) and of the W^- boson pseudorapidity η^{W^-} (bottom) for the W^+W^-jj process obtained with the new SHERPA implementation at fixed leading order; the W^+ boson is considered as unpolarized, the polarization is defined in the laboratory frame (lab), simulations are done in the fiducial phase space according to Sec. 5.2.

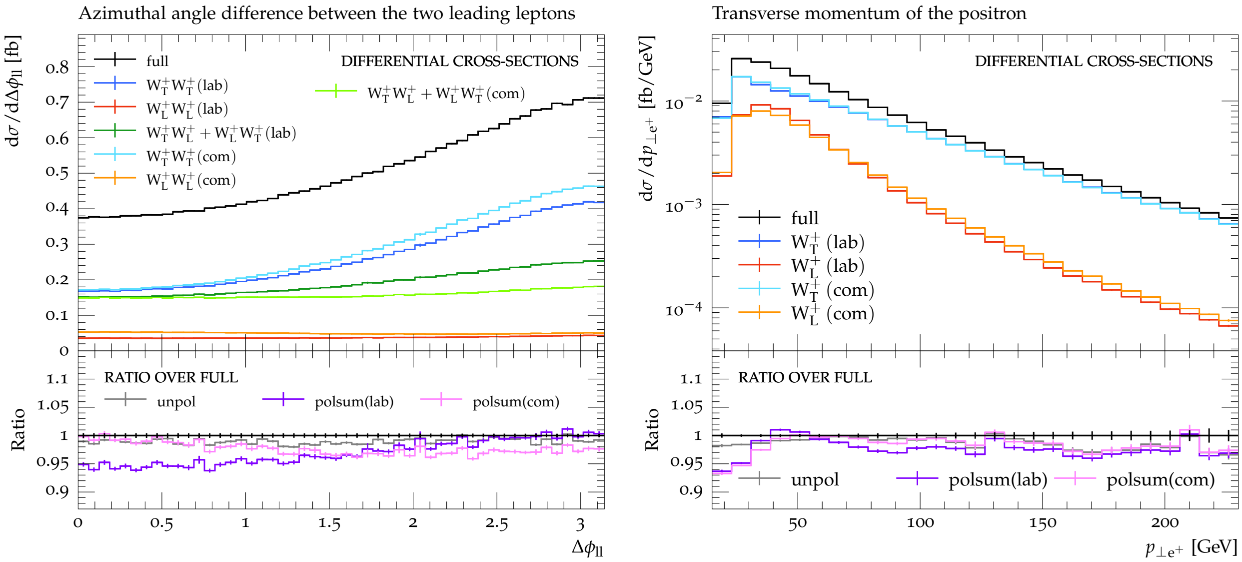

Figure D.2: Double-polarized distributions of the azimuthal angle difference between the two charged leptons $\Delta\phi_{\rm ll}$(left) and single-polarized distributions of the transverse momentum of the positron $p_{\perp,e^+}$(right) for the $\mathrm{W^+W^+}$jj process obtained with the new SHERPA implementation at fixed leading order; for the single-polarized distribution the $\mathrm{W^+}$ boson decaying into $\mathrm{e^+}\nu_\mathrm{e}$ has a definite polarization state, the other $\mathrm{W^+}$ boson decaying into $\mu^+\nu_\mu$ is kept unpolarized. Distributions are computed with polarization defined in the $\mathrm{W^+W^+}$-center of mass frame (com) and the laboratory frame (lab) assuming the fiducial phase space described in Sec. 5.2. In each sub-plot, the polarized differential distributions are shown at the top and the ratios over the full off-shell result are presented at the bottom.

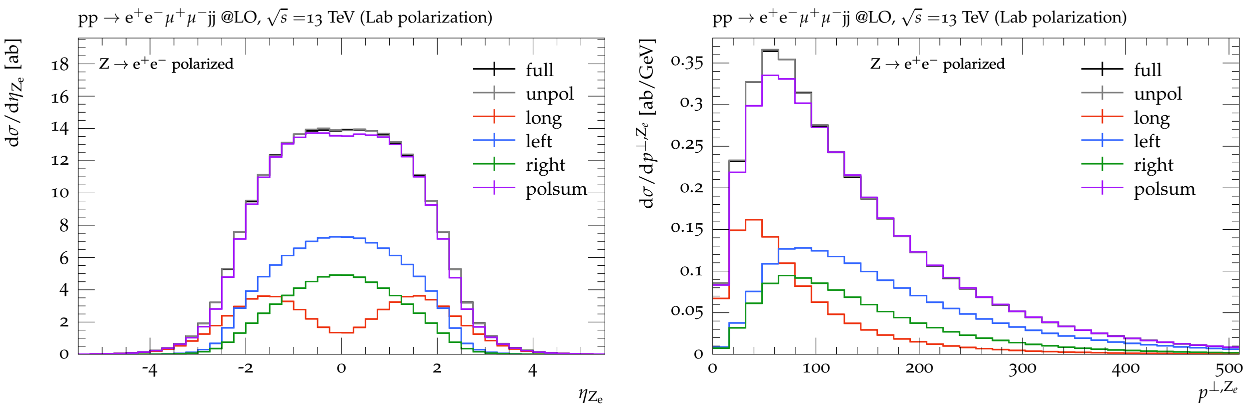

Figure D.3: Single-polarized distributions of the pseudorapidity (left) and in the transverse momentum (right) of the Z decaying into $\mathrm{e^+e^-}$ $\eta^{\rm Ze}$ and $p_\perp^{\rm Ze}$ for the ZZjj process obtained with the new SHERPA implementation at fixed leading order; the Z boson decaying into $\mu^+\mu^-$ is considered as unpolarized, the polarization is defined in the laboratory frame (lab), simulations are done in the fiducial phase space according to Sec. 5.2.

D.2 Supplementary data to the study of NLO QCD corrections for inclusive W^+Z production from SHERPA

D.2.1 Integrated cross sections and decay angle distributions for the inclusive W^+Z-production process at LO+PS from SHERPA

In this section, SHERPA integrated cross sections for the inclusive W^+Z production process at LO+PS accuracy are given in Tab. D.1. They are used to calculate the K factors in Sec. 6.2.2. Furthermore, lepton decay angle distributions for the W^+- and the Z-boson are displayed obtained, from SHERPA calculations at fixed LO and LO+PS to show the influence of the shower on these distributions (Fig. D.4). The applied simulation setups are very similar to those used for the nLO QCD+PS and merged calculations, see Appendix C.3 for details.

Table D.1: Integrated cross sections for the inclusive W^+Z production process at LO+PS with polarization defined in the laboratory frame (Lab) and the W^+Z-center-of-mass frame (COM); results are computed in the fiducial phase space from Sec. 6.2.2; polarization fractions are calculated relative to the polsum result, interference fractions relative to the unpol.

W^+Z	σ_{Lab} [fb]	fraction [%]	σ_{COM} [fb]	fraction [%]
unpol	18.527(9)		18.527(9)	
polsum	18.418(11)	100	18.121(10)	100
int	0.109(5)	0.587(26)	0.407(4)	2.194(23)
L-L	1.0461(12)	5.680(7)	1.4593(17)	8.053(11)
L-T	3.0529(31)	16.575(19)	1.9358(17)	10.683(11)
T-L	4.2046(35)	22.829(23)	1.7845(16)	9.848(10)
T-T	10.114(6)	54.92(5)	12.941(8)	71.42(6)

D.2.2 Further observables for the comparison of SHERPA's nLO QCD+PS polarization setup with NLO QCD fixed-order literature calculations

Fig. D.5 presents polarized distributions of observables for the inclusive W^+Z production process which has been studied to compare SHERPA's nLO QCD+PS polarization setup with NLO QCD fixed-order calculations in addition to the distributions already shown in Sec. 6.2.2. Only the SHERPA results are displayed here, the corresponding literature distributions can be found in Ref. [86].

D.2.3 Cross sections and K-factors for merging scale at 1 TeV

Table D.2: Integrated cross sections for the simulation of inclusive W^+Z production with up to one jet merged to parton shower at leading order; polarized cross sections, polarization fractions and K factors (K) for CKKW-merging scales Q_c=1000 GeV are shown, all predictions are obtained with SHERPA; polarizations are defined in the laboratory and the W^+Z-center-of-mass frame, K factors are obtained from dividing merged by LO cross sections, statistical errors on the K-factors are of the order of $\mathcal{O}(10^{-3})$, except for the interference ($\mathcal{O}(10^{-1})$).

W^+Z	$\sigma_{\text{Sherpa}}^{Q_c=1\text{TeV}}$ [fb]	fraction [%]	K	$\sigma_{\text{Sherpa}}^{Q_c=1\text{TeV}}$ [fb]	fraction [%]	K
	Laboratory frame			W^+Z-center-of-mass frame		
unpol	18.453(10)	100	0.99	18.453(10)	100	0.99
polsum	18.339(11)	99.38(8)	0.99	18.049(11)	97.81(8)	0.99
int	0.114(5)	0.618(28)	1.16(16)	0.403(5)	2.185(25)	1.030(31)
L-L	1.0376(12)	5.623(7)	0.99	1.4488(19)	7.851(11)	0.99
L-T	3.0311(34)	16.426(20)	0.99	1.9413(18)	10.520(11)	1.00
T-L	4.202(4)	22.770(24)	0.99	1.7916(18)	9.709(11)	1.00
T-T	10.068(7)	54.56(5)	0.99	12.867(8)	69.73(6)	0.99

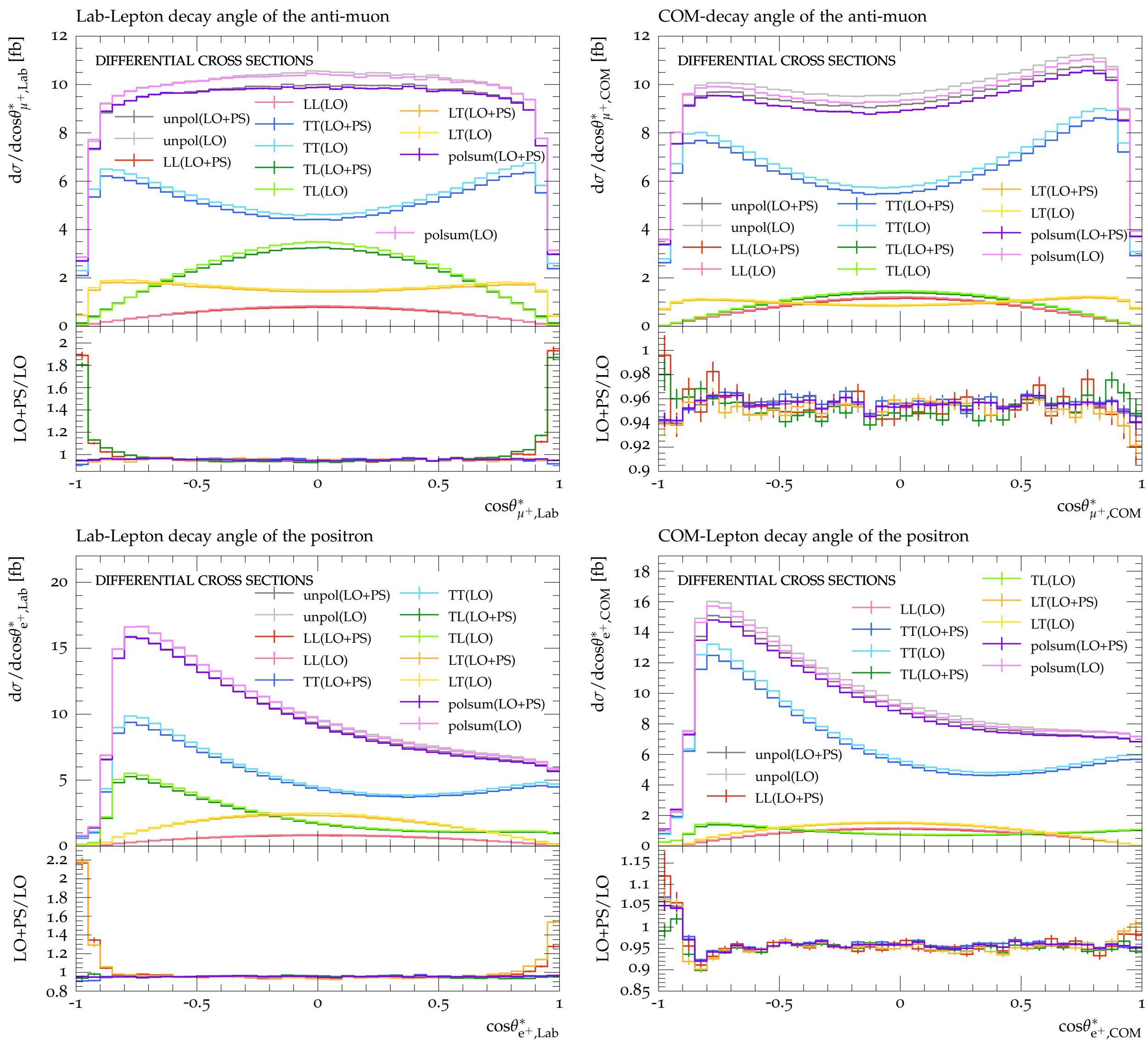

Figure D.4: Double-polarized distributions of the lepton decay angles $\cos\theta^*$ in inclusive W^+Z production from fixed LO and LO+PS calculations with SHERPA, top: anti-muon decay angle (decay product of the Z boson), bottom: decay angle of the positron (decay product of the W^+ boson) with polarization defined in the Lab, top of each subfigure displays the polarized distributions for fixed LO and LO+PS calculations, bottom of each subfigure contains the ratio LO+PS/LO to show potential shower effects; vector boson polarization is defined in the laboratory frame (Lab) (left) and in the W^+Z-center-of-mass frame (COM) (right).

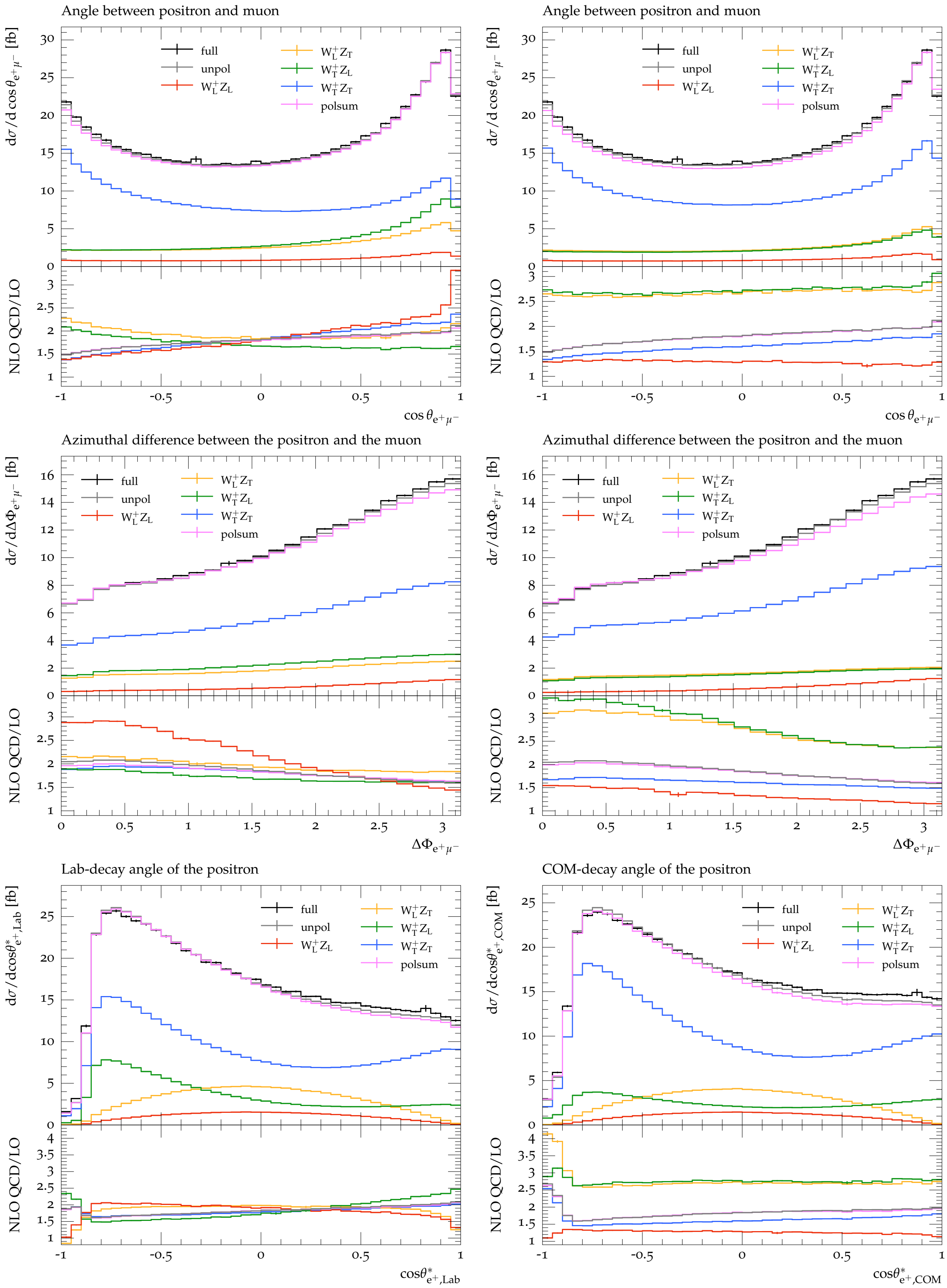

Figure D.5: Double-polarized distributions of the positron decay angle $\cos\theta_{e^+}$ (bottom), the cosine of the angle and the azimuthal angle difference between positron and muon $\cos\theta_{e^+\mu^-}$ (top) and $\Delta\Phi_{e^+\mu^-}$ (middle) in inclusive W^+Z production obtained with SHERPA at nLO(QCD)+PS accuracy; polarization is defined in the laboratory (left) or W^+Z-center-of-mass-frame (right); simulation parameter and phase space are chosen identical to Ref. [86].

D.2.4 Merged calculation approximation to nLO+PS result and dependency on small merging scales for additional observables

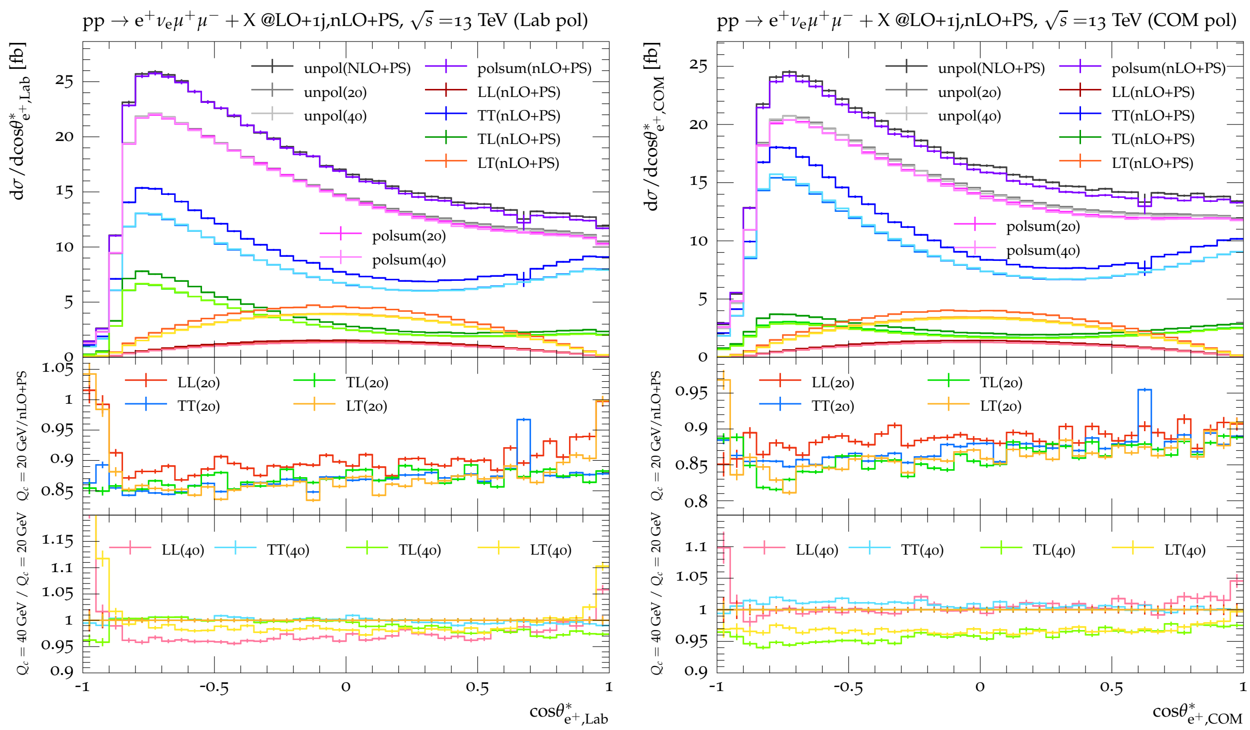

Figure D.6: Double-polarized distributions of the charged lepton decay angle of the W^+ boson $\cos\theta^*_{e+}$ for the inclusive W^+Z-production process; results obtained with LO+1j merged calculations with CKKW-merging scales of 20 and 40 GeV are shown in comparison with results at nLO(QCD)+PS accuracy; distributions are computed with SHERPA, vector boson polarization is defined in the laboratory frame (left) and the W^+Z-center-of-mass frame (right), in each subfigure from top to down are shown: differential distributions, ratio $Q_c = 20$ GeV over nLO(QCD)+PS results, ratio $Q_c = 40$ GeV / $Q_c = 20$ GeV.

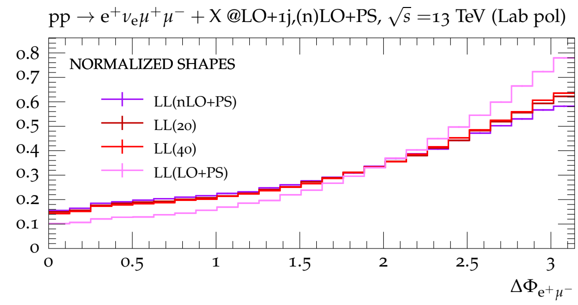

(a) $W^+_L Z_L$ - Lab

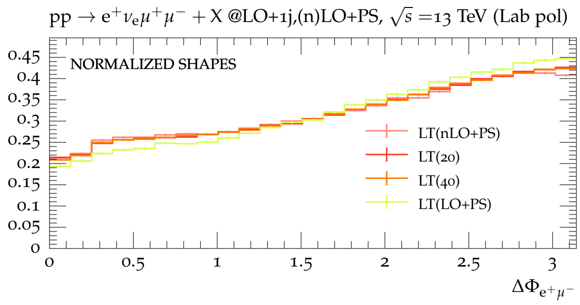

(b) $W^+_L Z_T$ - Lab

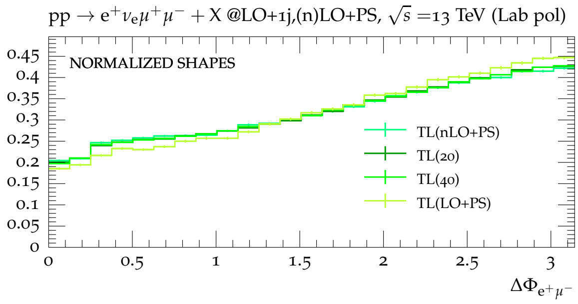

(c) $W^+_T Z_L$ - Lab

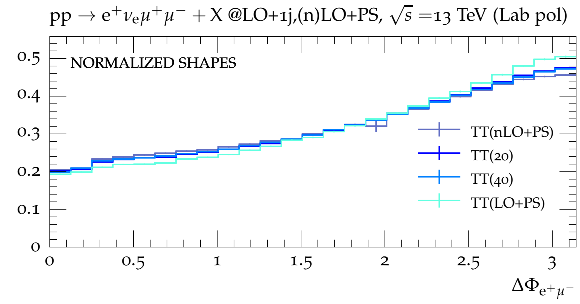

(d) $W^+_T Z_T$ - Lab

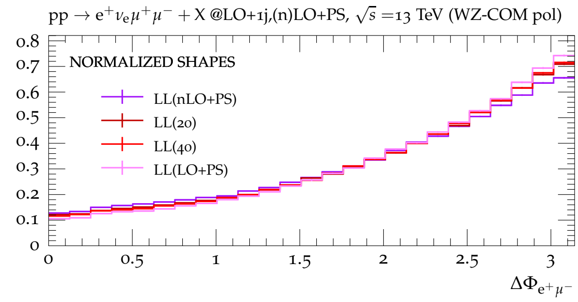

(e) $W^+_L Z_L$ - COM

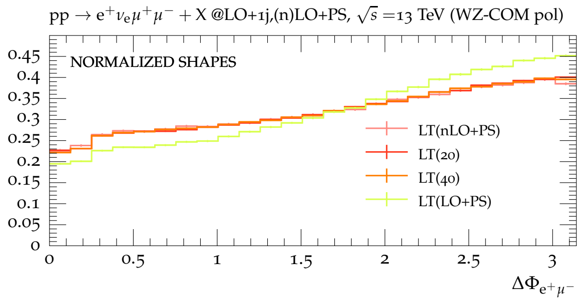

(f) $W^+_L Z_T$ - COM

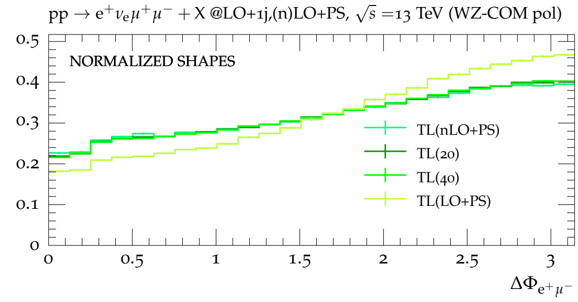

(g) $W^+_T Z_L$ - COM

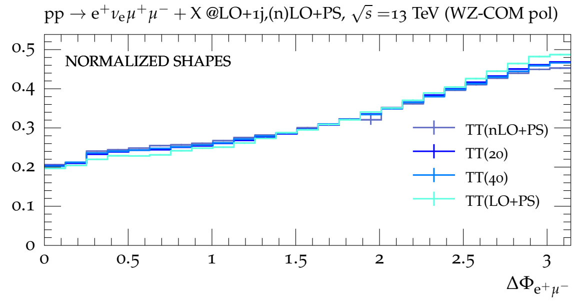

(h) $W^+_T Z_T$ - COM

Figure D.7: Normalized double-polarized distributions of the azimuthal angle difference between positron and muon $\Delta\Phi_{e^+\mu^-}$ for inclusive W^+Z-production for different polarization combinations from nLO(QCD)+PS, LO+PS and LO+1j merged with PS simulations with SHERPA; polarization is defined in the laboratory (Lab) ((a)-(d)) and in the W^+Z-center-of-mass frame (COM) ((e)-(h)).

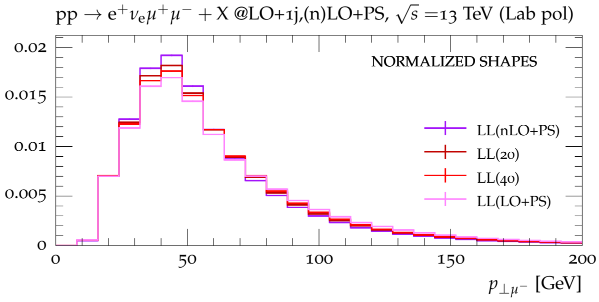

(a) $\mathrm{W}^+_\mathrm{L}\mathrm{Z}_\mathrm{L}$ - Lab

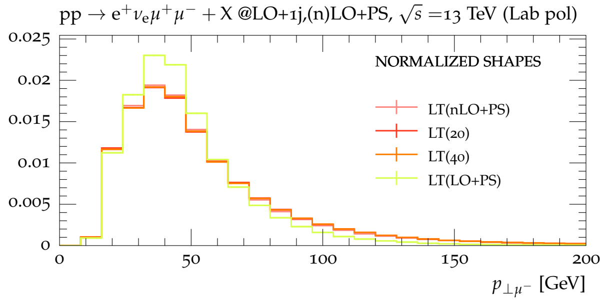

(b) $\mathrm{W}^+_\mathrm{L}\mathrm{Z}_\mathrm{T}$ - Lab

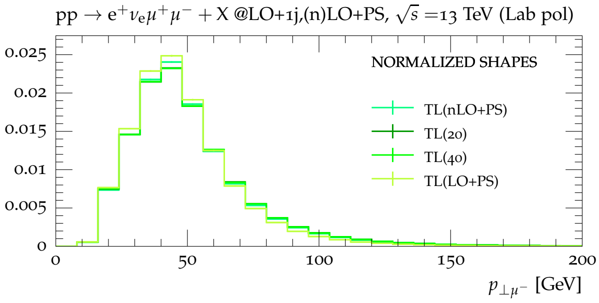

(c) $\mathrm{W}^+_\mathrm{T}\mathrm{Z}_\mathrm{L}$ - Lab

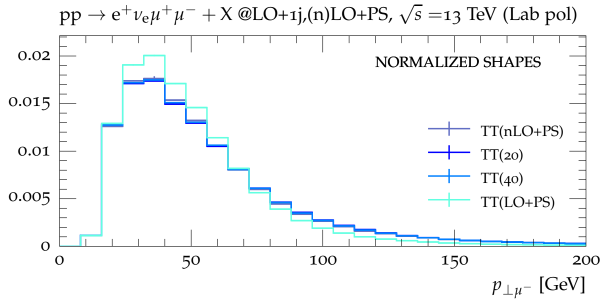

(d) $\mathrm{W}^+_\mathrm{T}\mathrm{Z}_\mathrm{T}$ - Lab

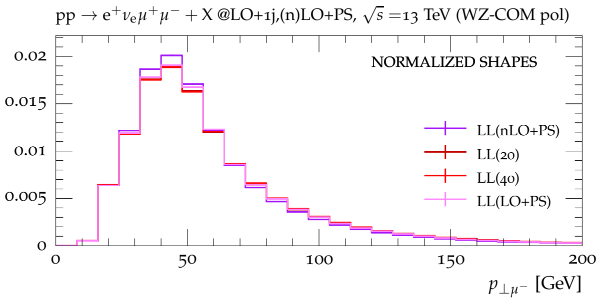

(e) $\mathrm{W}^+_\mathrm{L}\mathrm{Z}_\mathrm{L}$ - COM

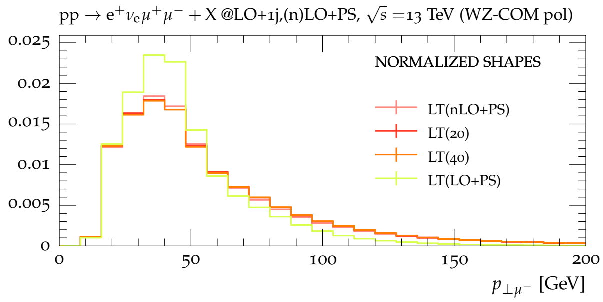

(f) $\mathrm{W}^+_\mathrm{T}\mathrm{Z}_\mathrm{L}$ - COM

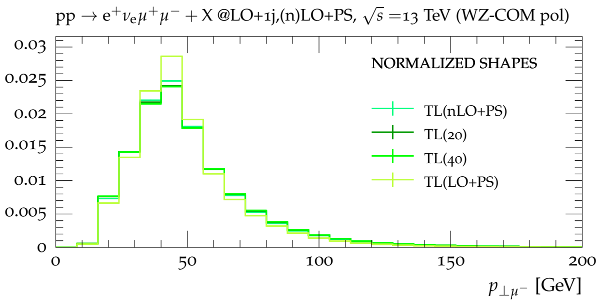

(g) $\mathrm{W}^+_\mathrm{L}\mathrm{Z}_\mathrm{T}$ - COM

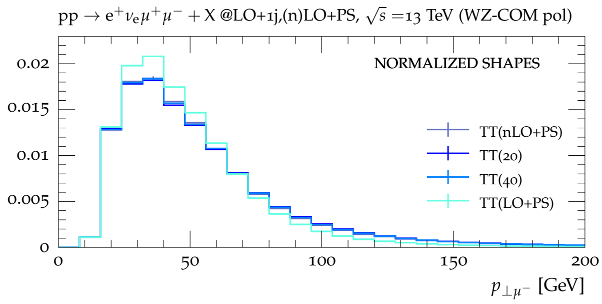

(h) $\mathrm{W}^+_\mathrm{T}\mathrm{Z}_\mathrm{T}$ - COM

Figure D.8: Normalized double-polarized distributions of the muon transverse momentum $p_{\perp,\mu^-}$ for inclusive $\mathrm{W}^+\mathrm{Z}$-production for different polarization combinations from nLO(QCD)+PS, LO+PS and LO+1j merged with PS simulations with SHERPA; polarization is defined in the laboratory (Lab) ((a)-(d)) and in the $\mathrm{W}^+\mathrm{Z}$-center-of-mass frame (COM) ((e)-(h)).

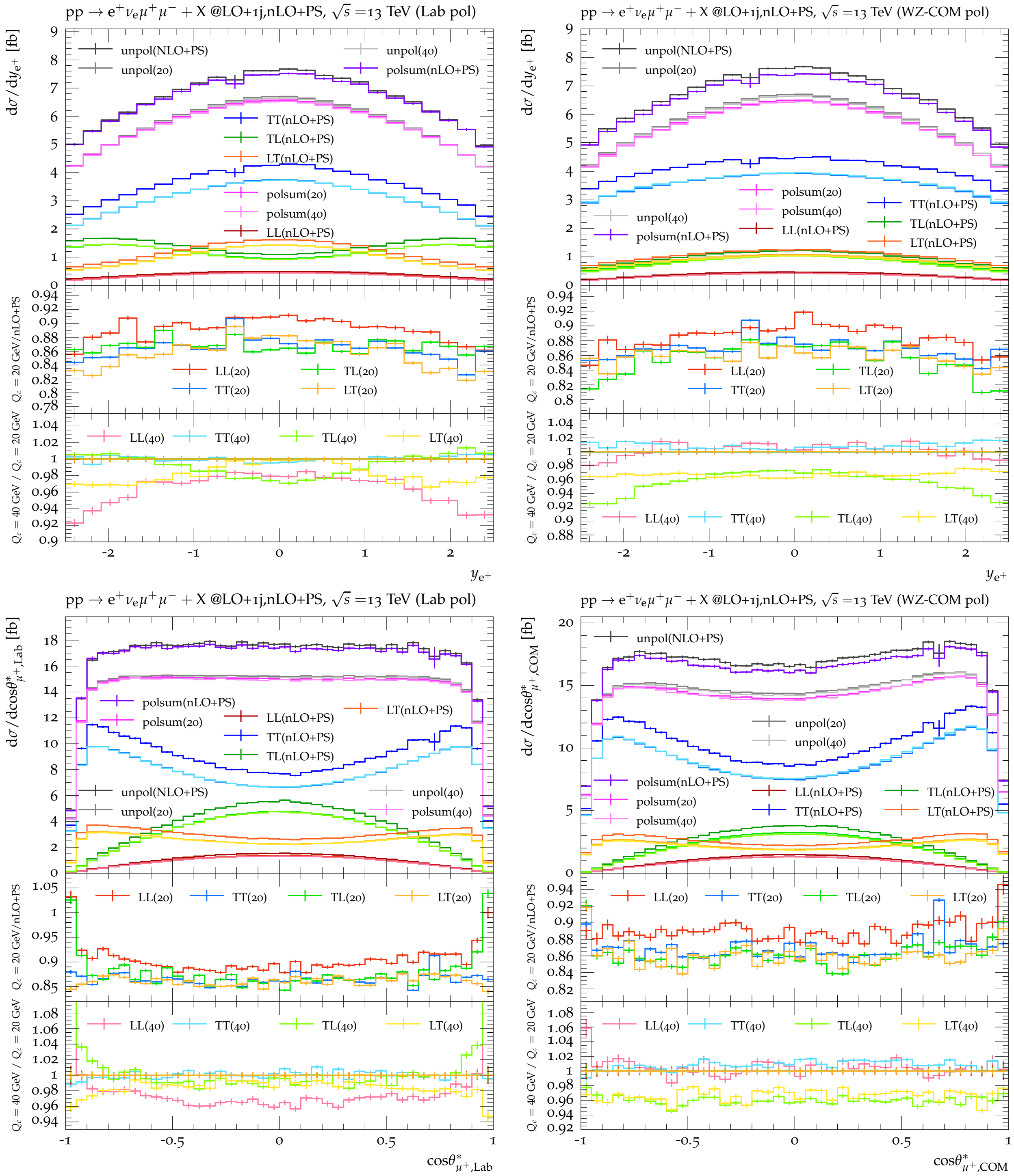

Figure D.9: Double-polarized distributions of the positron rapidity y_{e^+} and the anti-muon decay angle $\cos\theta^*_{\mu^+}$ for the inclusive W^+Z-production process; results obtained with LO+1j merged calculations with CKKW-merging scales of 20 and 40 GeV are shown in comparison with results at nLO(QCD)+PS accuracy; distributions are computed with SHERPA, vector boson polarization is defined in the laboratory frame (left) and the W^+Z-center-of-mass frame (right), in each subfigure from top to down are shown: differential distributions, ratio $Q_c = 20$ GeV over nLO(QCD)+PS results, ratio $Q_c = 40$ GeV / $Q_c = 20$ GeV.

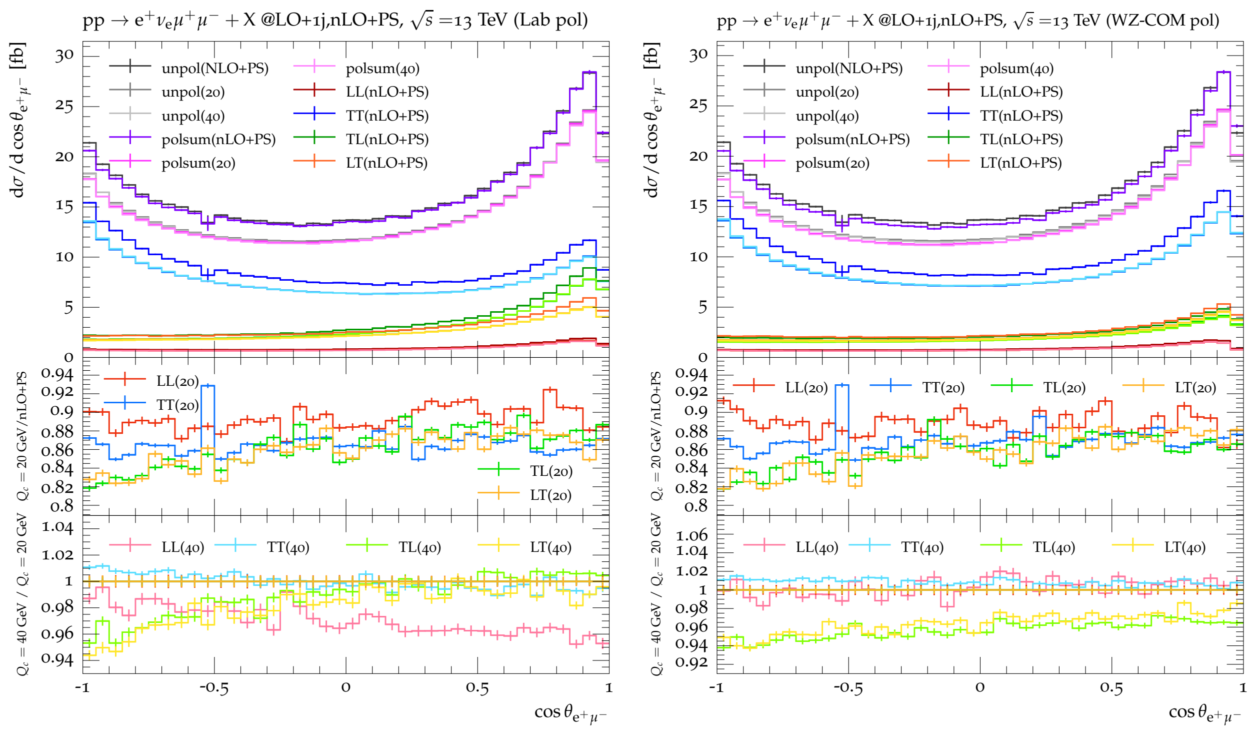

Figure D.10: Double-polarized distributions of the angle between differently charged leptons $\cos\theta_{e^+\mu^-}$ for the inclusive W^+Z-production process; results obtained with LO+1j merged calculations with CKKW-merging scales of 20 and 40 GeV are shown in comparison with results at nLO(QCD)+PS accuracy; distributions are computed with SHERPA, vector boson polarization is defined in the laboratory frame (left) and the W^+Z-center-of-mass frame (right), in each subfigure from top to down are shown: differential distributions, ratio $Q_c = 20$ GeV over nLO(QCD)+PS results, ratio $Q_c = 40$ GeV / $Q_c = 20$ GeV.

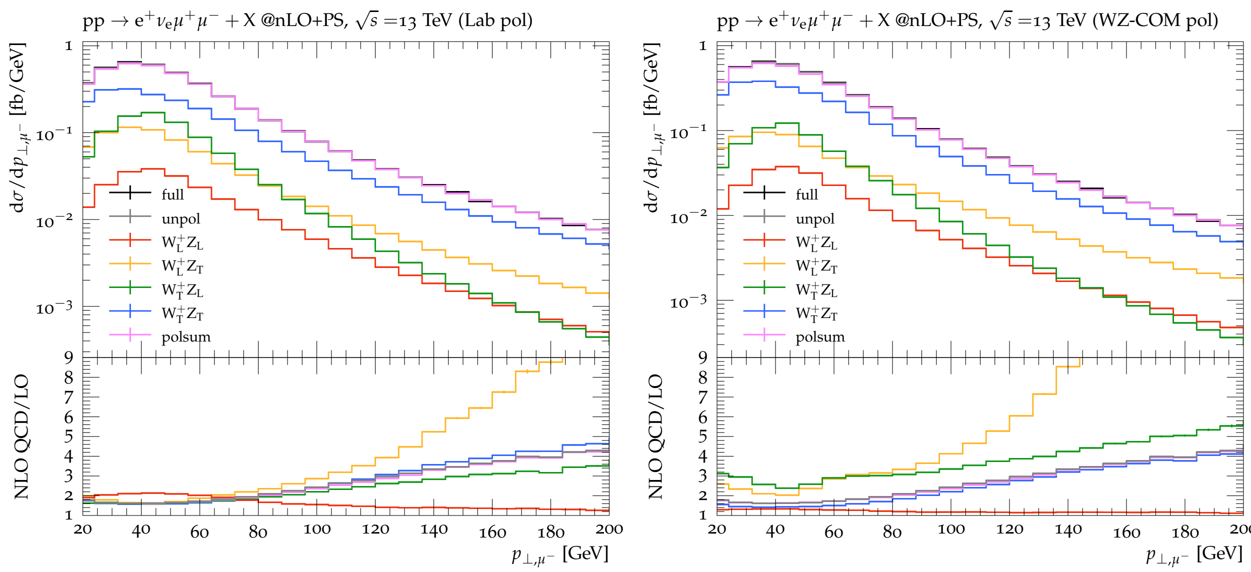

Figure D.11: Double-polarized muon transverse momentum distribution $p_{\perp,\mu^-}$ at nLO+PS accuracy for the inclusive W^+Z-production process obtained with SHERPA; K-factors (bottom) are calculated as nLO(QCD)+PS over LO+PS; polarization is defined in laboratory (left, Lab) and the W^+Z-center-of-mass frame (right, COM).

D.3 Supplementary data to the study of the influence of the polarization definition on polarized cross sections for VBS processes at fixed LO

D.3.1 Integrated cross sections for the four investigated VBS-processes at fixed LO

In this section, the cross sections associated to Fig. 6.1 are given obtained with SHERPA in the comparison phase space from Sec. 6.1.1. For each process, two unpol results are displayed for results in the fiducial phase space since single- and double-polarized cross sections are obtained from two different simulations runs. It is not actually necessary to run two simulations for the two different types of signals. This was only necessary here because the definition of partially unpolarized signals has been changed in the meantime.

Table D.3: Integrated cross sections for the ZZjj process at fixed leading order with polarization defined in the laboratory (Lab), the ZZ-center-of-mass frame (COM) and the parton-parton frame (PPFr); results are computed with SHERPA in the comparison phase space from Sec. 6.1.1; polarization fractions are calculated relative to the unpolarized result, for single-polarized distributions, the Z boson decaying into an electron-positron pair is considered as polarized; R denotes the ratio of the cross section in the COM, PPFr polarization definition relative to the cross section in the Lab.

ZZ	σ_{Lab} [fb]	fraction [%]	σ_{COM} [fb]	fraction [%]	R	σ_{PPFr} [fb]	fraction [%]	R
full				0.060987(27)				
				Single-polarized cross sections				
unpol				0.06116(4)				
int	0.001712(24)	2.80(4)	0.001712(23)	2.80(4)	1.0	0.001895(24)	3.10(4)	1.11
Z_{right}	0.016143(14)	26.394(28)	0.017068(15)	27.906(29)	1.06	0.016558(15)	27.071(29)	1.03
Z_{left}	0.027079(21)	44.27(4)	0.027401(21)	44.80(4)	1.01	0.027516(21)	44.99(4)	1.02
Z_{long}	0.016230(15)	26.536(29)	0.014984(14)	24.498(27)	0.92	0.015195(14)	24.843(28)	0.94
				Double-polarized cross sections				
unpol				0.061143(33)				
polsum	0.05773(4)	94.42(9)	0.05771(4)	94.39(9)	1.00	0.05737(4)	93.82(9)	0.99
int	0.003399(31)	5.56(5)	0.003434(31)	5.62(5)	1.01	0.003782(31)	6.19(5)	1.11
L-L	0.004518(7)	7.388(12)	0.005492(8)	8.982(14)	1.22	0.003992(6)	6.528(11)	0.88
T-L+L-T	0.022584(20)	36.94(4)	0.018340(17)	29.996(32)	0.81	0.021562(19)	35.27(4)	0.95
T-T	0.030629(26)	50.09(5)	0.033880(29)	55.41(6)	1.11	0.031812(27)	52.03(5)	1.04

Table D.4: Integrated cross sections for the W^+W^+jj process at fixed leading order with polarization defined in the laboratory (Lab), the W^+W^+jj-center-of-mass frame (COM) and the parton-parton frame (PPFr); results are computed with SHERPA in the comparison phase space from Sec. 6.1.1 with (fiducial) and without (inclusive) lepton selection criteria; polarization fractions are calculated relative to the unpolarized result; for single-polarized distributions, the W^+ boson decaying into an positron-neutrino pair is considered as polarized; R denotes the ratio of the cross section in the COM, PPFr polarization definition relative to the cross section in the Lab.

W^+W^+	σ_{Lab} [fb]	fraction [%]	σ_{COM} [fb]	fraction [%]	R	σ_{PPFr} [fb]	fraction [%]	R
				Inclusive phase space				
unpol				2.5594(12)				
				Single-polarized cross sections				
W^+_{right}	0.6875(7)	26.863(30)	0.7022(7)	27.438(31)	1.02	0.7047(7)	27.533(31)	1.03
W^+_{left}	1.1973(9)	46.78(4)	1.1906(9)	46.52(4)	0.99	1.2156(9)	47.49(4)	1.02
W^+_{long}	0.6712(6)	26.226(26)	0.6633(6)	25.918(25)	0.99	0.6359(5)	24.844(24)	0.95
				Double-polarized cross sections				
L-L	0.17491(28)	6.834(11)	0.24718(34)	9.658(14)	1.41	0.16099(25)	6.290(10)	0.92
T-L+L-T	0.9920(10)	38.76(4)	0.8313(8)	32.481(34)	0.84	0.9491(9)	37.08(4)	0.96
T-T	1.3889(13)	54.27(6)	1.4767(14)	57.70(6)	1.06	1.4457(14)	56.49(6)	1.04
				Fiducial phase space				
full				1.2961(7)				
				Single-polarized cross sections				
unpol				1.2829(8)				
int	0.0067(8)	0.53(6)	0.0047(8)	0.37(6)	0.7	0.0097(8)	0.76(6)	1.45
W^+_{right}	0.3731(5)	29.09(4)	0.3859(5)	30.08(4)	1.03	0.3814(5)	29.73(4)	1.02
W^+_{left}	0.5758(6)	44.88(6)	0.5692(6)	44.37(6)	0.99	0.5810(6)	45.29(6)	1.01
W^+_{long}	0.3272(4)	25.506(34)	0.3231(4)	25.182(32)	0.99	0.3107(4)	24.221(31)	0.95
				Double-polarized cross sections				
unpol				1.2843(6)				
polsum	1.2698(11)	98.88(10)	1.2733(11)	99.14(10)	1.00	1.2638(11)	98.40(10)	1.00
int	0.0144(9)	1.12(7)	0.0110(9)	0.86(7)	0.76	0.0205(9)	1.60(7)	1.42
L-L	0.08139(13)	6.338(10)	0.11817(17)	9.202(14)	1.45	0.07531(12)	5.864(10)	0.93
T-L+L-T	0.4877(5)	37.98(4)	0.4126(4)	32.13(4)	0.85	0.4657(5)	36.26(4)	0.95
T-T	0.7007(7)	54.56(6)	0.7424(7)	57.81(6)	1.06	0.7228(7)	56.28(6)	1.03

Table D.5: Integrated cross sections for the W^+W^-jj process at fixed leading order with polarization defined in the laboratory (Lab), the W^+W^-jj-center-of-mass frame (COM) and the parton-parton frame (PPFr); results are computed with SHERPA in the comparison phase space from Sec. 6.1.1 with (fiducial) and without (inclusive) lepton selection criteria; polarization fractions are calculated relative to the unpolarized result, R denotes the ratio of the cross section in the COM, PPFr polarization definition relative to the cross section in the Lab.

W^+W^-	σ_{Lab} [fb]	fraction [%]	σ_{COM} [fb]	fraction [%]	R	σ_{PPFr} [fb]	fraction [%]	R
				Inclusive phase space				
unpol				3.7267(11)				
				Single-polarized cross sections				
W^+_{right}	1.0202(6)	27.376(19)	1.0372(7)	27.832(19)	1.02	1.0454(6)	28.052(19)	1.02
W^+_{left}	1.7956(8)	48.181(26)	1.7856(8)	47.913(26)	0.99	1.8244(8)	48.953(26)	1.02
W^+_{long}	0.9115(6)	24.458(17)	0.9045(6)	24.271(17)	0.99	0.8576(5)	23.013(16)	0.94
W^-_{right}	1.0517(7)	28.220(20)	1.0633(7)	28.532(19)	1.01	1.0738(7)	28.815(20)	1.02
W^-_{left}	1.7396(8)	46.678(25)	1.7195(8)	46.139(26)	0.99	1.7637(8)	47.325(26)	1.01
W^-_{long}	0.9346(5)	25.077(16)	0.9429(5)	25.301(16)	1.01	0.8880(5)	23.828(15)	0.95
				Double-polarized cross sections				
L-L	0.23313(29)	6.256(8)	0.28843(31)	7.739(9)	1.24	0.21084(28)	5.658(8)	0.90
L-T	0.6783(6)	18.200(17)	0.6162(6)	16.535(16)	0.91	0.6471(6)	17.363(16)	0.95
T-L	0.7015(5)	18.823(15)	0.6544(5)	17.561(14)	0.93	0.6774(5)	18.177(15)	0.97
T-T	2.1136(13)	56.72(4)	2.1674(12)	58.16(4)	1.03	2.1911(13)	58.80(4)	1.04
				Fiducial phase space				
full				1.8850(12)				
				Single-polarized cross sections				
unpol				1.8642(7)				
int	0.0091(7)	0.49(4)	0.0109(7)	0.59(4)	1.20	0.0139(7)	0.74(4)	1.53
W^+_{right}	0.5290(4)	28.377(24)	0.5415(4)	29.047(24)	1.02	0.5408(4)	29.009(25)	1.02
W^+_{left}	0.8944(6)	47.98(4)	0.8810(5)	47.258(34)	0.99	0.9039(6)	48.488(35)	1.01
W^+_{long}	0.43170(35)	23.158(21)	0.43075(35)	23.107(20)	1.00	0.40561(33)	21.758(19)	0.94
int	0.0301(8)	1.61(4)	0.0270(7)	1.45(4)	0.9	0.0316(7)	1.70(4)	1.05
W^-_{right}	0.4998(5)	26.808(28)	0.4993(5)	26.783(27)	1.00	0.5065(5)	27.170(27)	1.01
W^-_{left}	0.8937(5)	47.943(33)	0.8908(5)	47.785(33)	1.00	0.9050(5)	48.545(33)	1.01
W^-_{long}	0.44061(34)	23.636(20)	0.44707(34)	23.982(20)	1.01	0.42111(31)	22.590(19)	0.96
				Double-polarized cross sections				
unpol				1.8657(6)				
polsum	1.8219(11)	97.65(6)	1.8246(11)	97.80(6)	1.00	1.8151(10)	97.29(6)	1.00
int	0.0438(9)	2.35(5)	0.0411(9)	2.20(5)	0.94	0.0506(9)	2.71(5)	1.16
L-L	0.10594(12)	5.678(7)	0.13378(15)	7.171(9)	1.26	0.09632(12)	5.163(6)	0.91
L-T	0.31912(29)	17.104(17)	0.29396(29)	15.756(16)	0.92	0.30293(28)	16.237(16)	0.95
T-L	0.33294(30)	17.845(17)	0.31356(30)	16.806(17)	0.94	0.32144(29)	17.229(17)	0.97
T-T	1.0639(7)	57.02(4)	1.0833(7)	58.06(4)	1.02	1.0944(7)	58.66(4)	1.03

Table D.6: Integrated cross sections for the W^+Zjj process at fixed leading order with polarization defined in the laboratory (Lab), the W^+Zjj-center-of-mass frame (COM) and the parton-parton frame (PPFr); results are computed with SHERPA in the comparison phase space from Sec. 6.1.1; polarization fractions are calculated relative to the unpolarized result, R denotes the ratio of the cross section in the COM, PPFr polarization definition relative to the cross section in the Lab.

W^+Z	σ_{Lab} [fb]	fraction [%]	σ_{COM} [fb]	fraction [%]	R	σ_{PPFr} [fb]	fraction [%]	R
full				0.16604(13)				
				Single-polarized cross sections				
unpol				0.16645(10)				
int	0.00385(8)	2.31(5)	0.00340(8)	2.04(5)	0.88	0.00428(8)	2.57(5)	1.11
W^+_{right}	0.03129(4)	18.799(29)	0.03263(5)	19.607(31)	1.04	0.03158(4)	18.975(29)	1.01
W^+_{left}	0.09790(8)	58.82(6)	0.09511(8)	57.14(6)	0.97	0.09858(8)	59.23(6)	1.01
W^+_{long}	0.03340(4)	20.069(28)	0.03529(4)	21.205(29)	1.06	0.03199(4)	19.217(26)	0.96
int	0.00396(9)	2.38(5)	0.00332(8)	1.99(5)	0.84	0.00439(9)	2.64(5)	1.11
Z_{right}	0.04098(5)	24.624(33)	0.04095(5)	24.605(32)	1	0.04182(5)	25.126(33)	1.02
Z_{left}	0.07798(6)	46.85(5)	0.07615(6)	45.75(5)	0.98	0.07898(6)	47.45(5)	1.01
Z_{long}	0.04352(5)	26.150(32)	0.04602(5)	27.65(4)	1.06	0.04125(5)	24.782(31)	0.95
				Double-polarized cross sections				
unpol				0.16675(8)				
polsum	0.15899(11)	95.35(8)	0.16009(11)	96.01(8)	1.01	0.15816(11)	94.85(8)	0.99
int	0.00776(8)	4.65(5)	0.00665(8)	3.99(5)	0.86	0.00794(8)	4.76(5)	1.02
L-L	0.009019(15)	5.409(9)	0.011114(18)	6.665(11)	1.23	0.008309(13)	4.983(8)	0.92
L-T	0.023529(29)	14.111(19)	0.023624(28)	14.168(18)	1.00	0.022824(28)	13.688(18)	0.97
T-L	0.033568(35)	20.131(23)	0.034248(35)	20.539(23)	1.02	0.031953(32)	19.163(21)	0.95
T-T	0.09287(7)	55.69(5)	0.09110(7)	54.64(5)	0.98	0.09507(7)	57.02(5)	1.02

D.3.2 Further observables

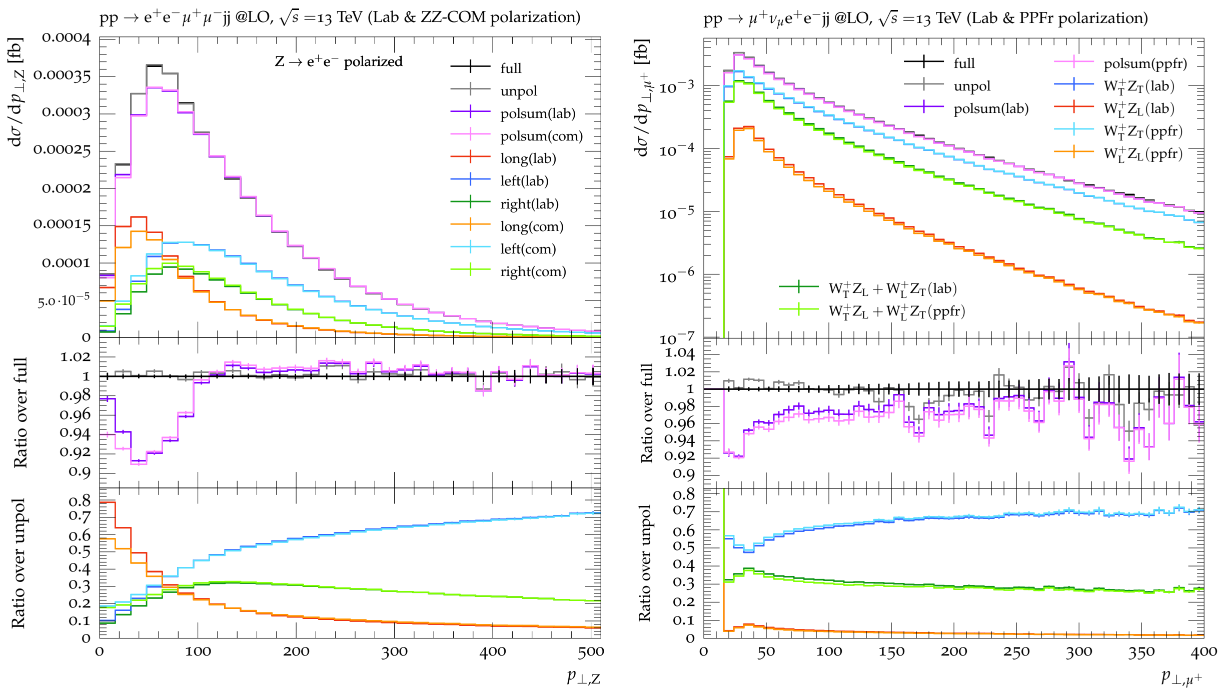

Figure D.12: Examples for transverse momenta distributions for different reference frames, the left figure displays the single-polarized distributions of the Z boson transverse momentum $p_{\perp,\mathrm{Z}}$ in the ZZjj process for polarization defined in the laboratory (lab) and the ZZ-center-of-mass frame (com), the Z boson decaying into an electron-positron pair is assumed to be polarized; in the right figure, the double-polarized distributions of the transverse momentum of the anti-muon $p_{\perp,\mu^+}$ for the W^+Zjj process are shown for polarization defined in the laboratory (lab) and the parton-parton frame (ppfr); distributions are obtained with SHERPA in the comparison phase space introduced in Sec. 6.1.1 at fixed leading order.

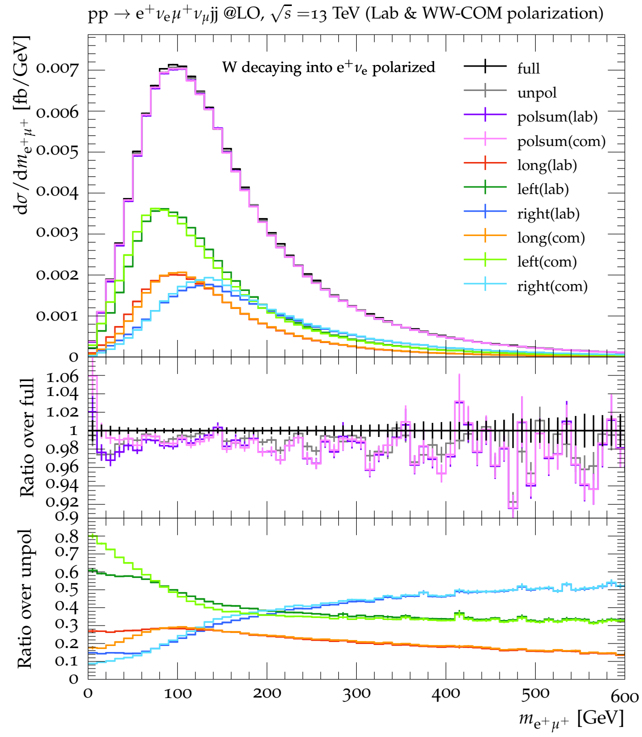

Figure D.13: Example distributions for the $m_{ll'}$ distributions: Single-polarized distributions of the positron anti-muon invariant mass $m_{e^+\mu^+}$ for the W^+W^+jj process for polarization defined in the laboratory (lab) and the W^+W^+-center-of-mass frame (com), the W^+ boson decaying into a positron-neutrino pair is assumed to be polarized; distributions are obtained with SHERPA in the comparison phase space introduced in Sec. 6.1.1 at fixed leading order.

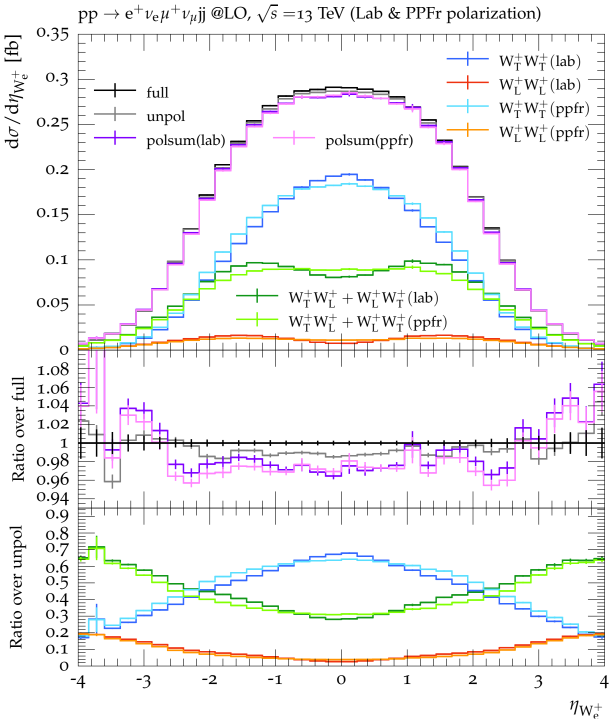

(a) W^+W^+jj - W^+ boson pseudorapidity

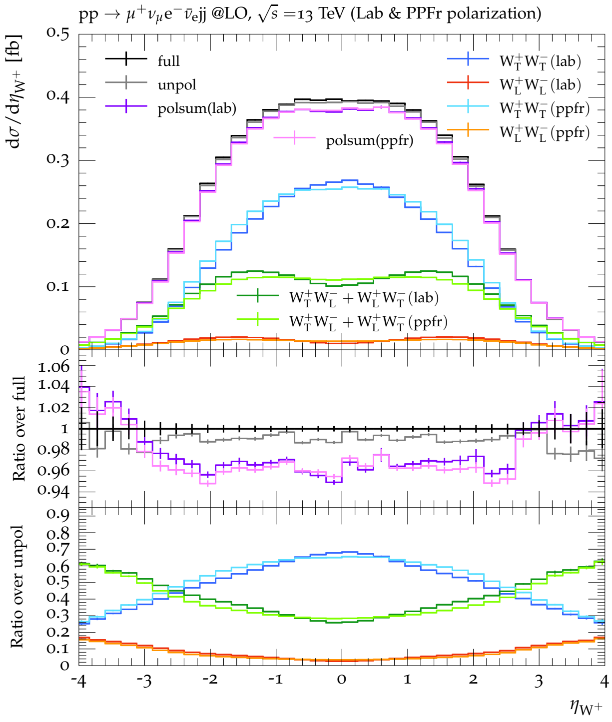

(b) W^+W^-jj - W^+ boson pseudorapidity

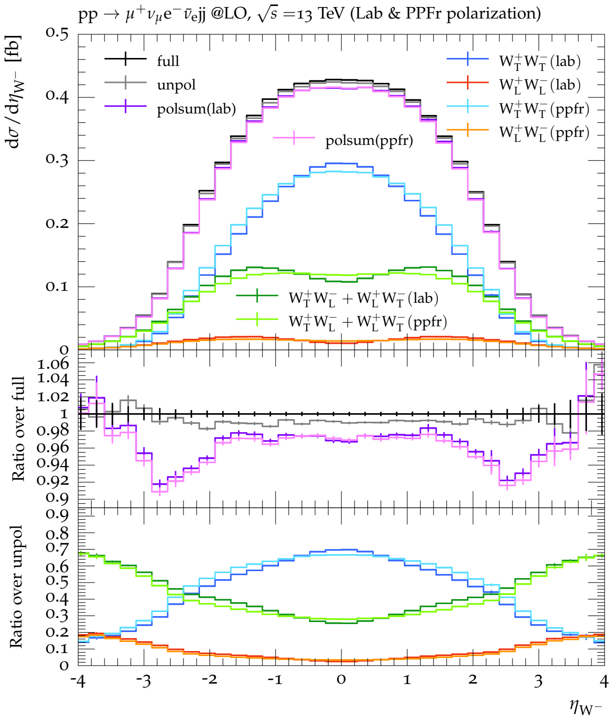

(c) W^+W^-jj - W^- boson pseudorapidity

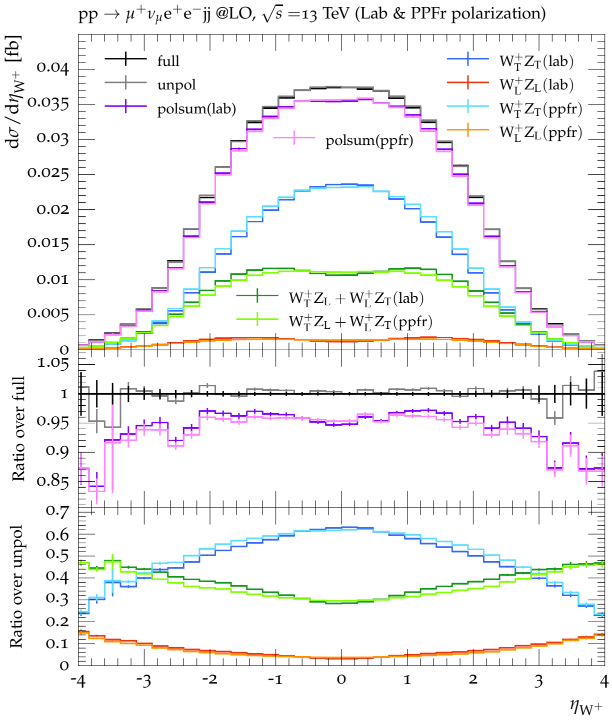

(d) W^+Zjj - W^+ boson pseudorapidity

Figure D.14: Double-polarized pseudorapidity distributions of the W bosons η_W in the W^+W^+jj, the W^+W^-jj and the W^+Zjj process obtained with SHERPA in the comparison phase space introduced in Sec. 6.1.1 at fixed leading order, the polarization is defined in the laboratory (lab) and the parton-parton frame (ppfr)

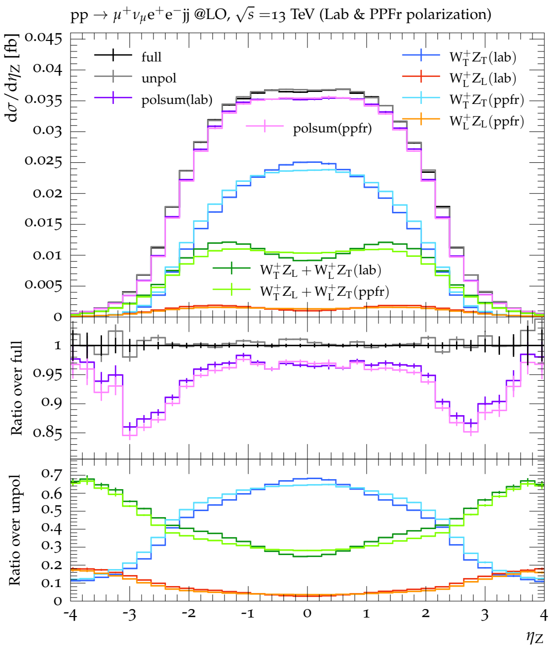

(a) W^+Zjj - Z boson pseudorapidity, Lab vs. PPFr, double-polarized

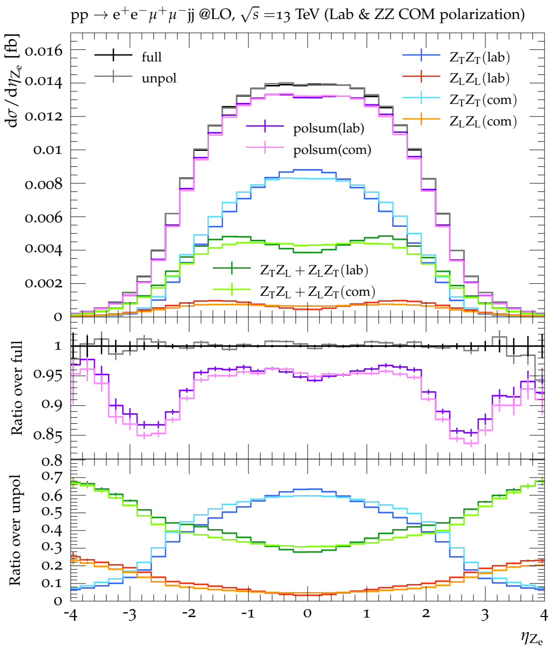

(b) ZZjj - Z boson pseudorapidity, Lab vs. COM, double-polarized

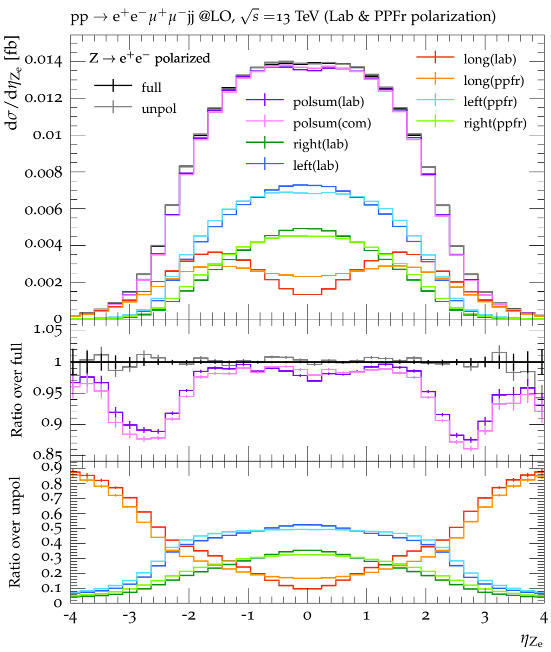

(c) ZZjj - Z boson pseudorapidity, Lab vs. PPFr, single-polarized

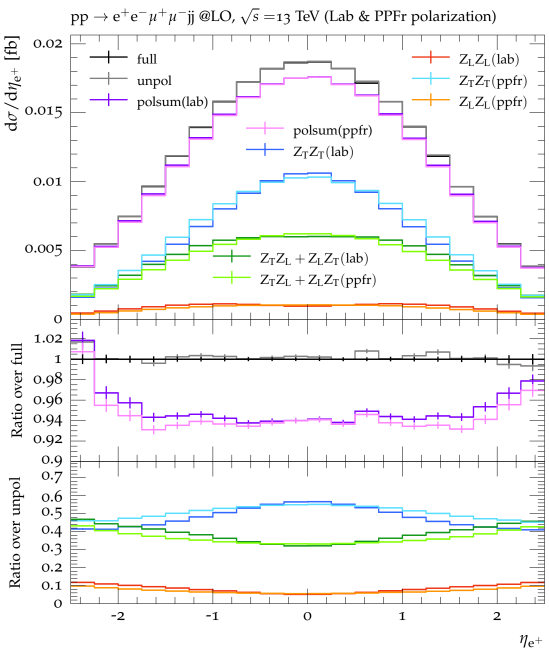

(d) ZZjj - positron pseudorapidity, Lab vs. PPFr, double-polarized

Figure D.15: Polarized Z boson pseudorapidity distributions η_Z for the W^+Zjj (a) and the ZZjj ((b), (c)) process as well as polarized positron pseudorapidity distributions η_{e^+} (d) for the ZZjj process; all distributions are obtained with SHERPA at fixed leading order in the comparison phase space introduced in Sec. 6.1.1; for the single-polarized distributions (c), the Z boson decaying into an electron-positron pair is considered as polarized.

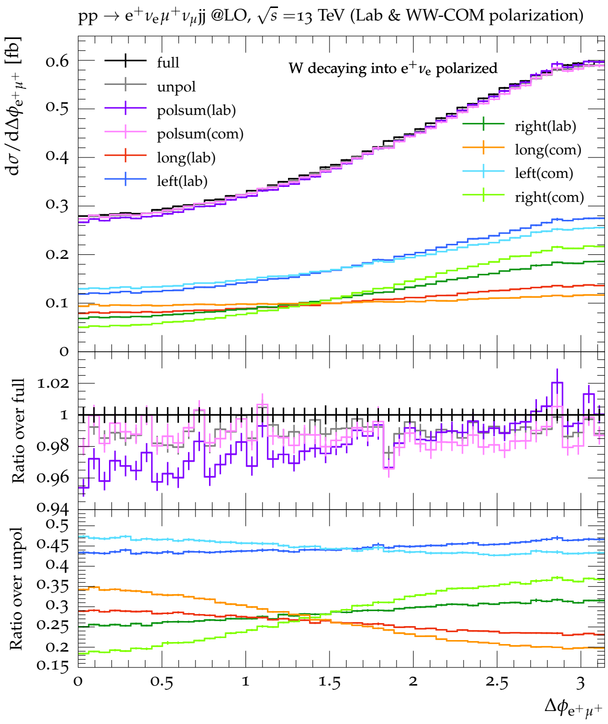

(a) W^+W^+jj - W^+ polarized

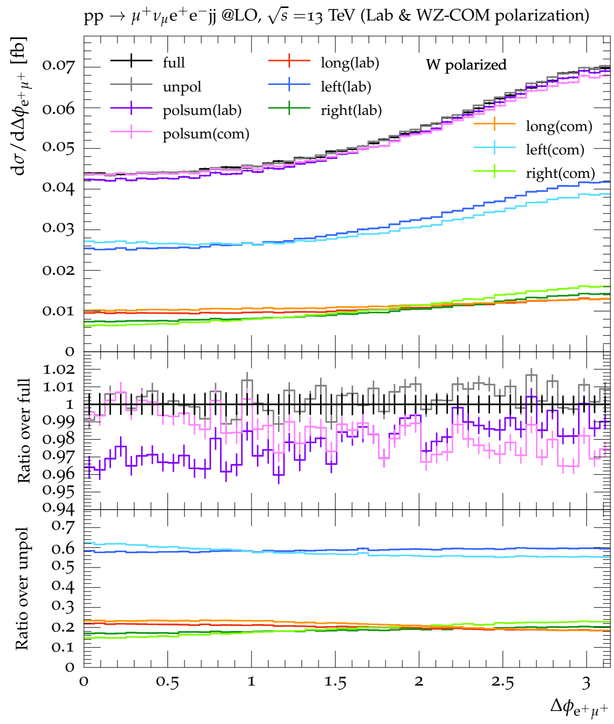

(b) W^+Zjj - W^+ polarized

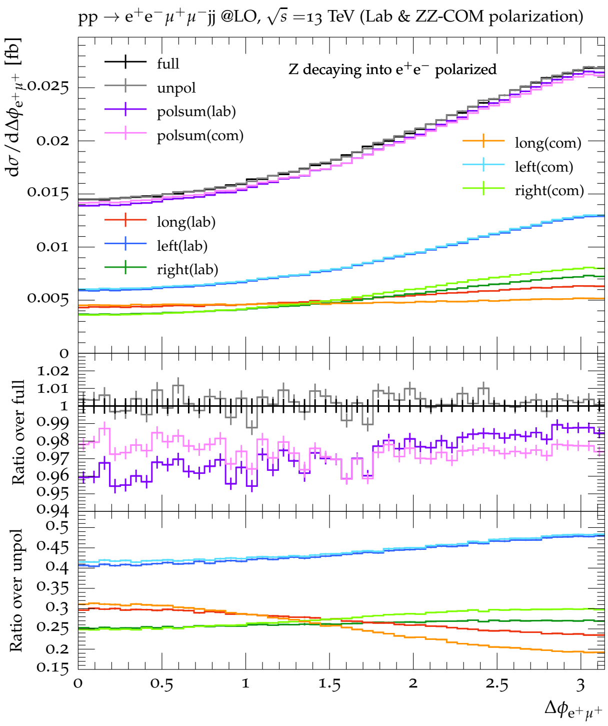

(c) $ZZjj$ - Z polarized

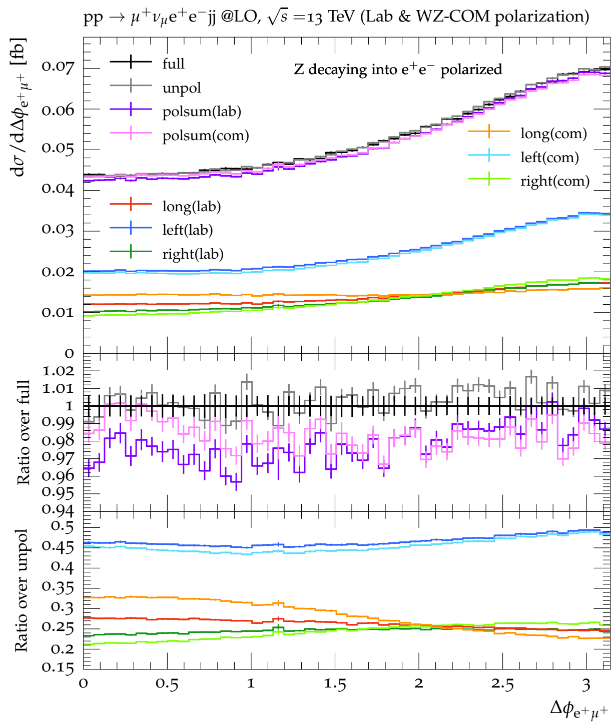

(d) W^+Zjj - Z polarized

Figure D.16: Single-polarized azimuthal angle difference between charged leptons from different vector bosons $\Delta\Phi_{e^+\mu^+}$ in the W^+W^+jj, the $ZZjj$ and the W^+Zjj process obtained with SHERPA in the comparison phase space introduced in Sec. 6.1.1 at fixed leading order, the polarization is defined in the laboratory (lab) and the vector boson pair center-of-mass frame (com); for the results of the W^+W^+jj and the $ZZjj$ processes the vectors bosons decaying into the electron flavor decay channel are considered as polarized.

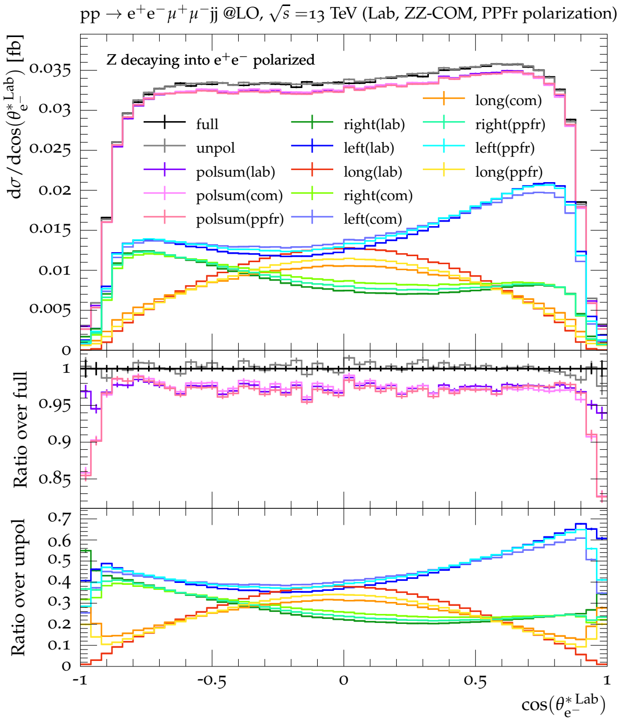

(a) ZZjj - Lab observable system

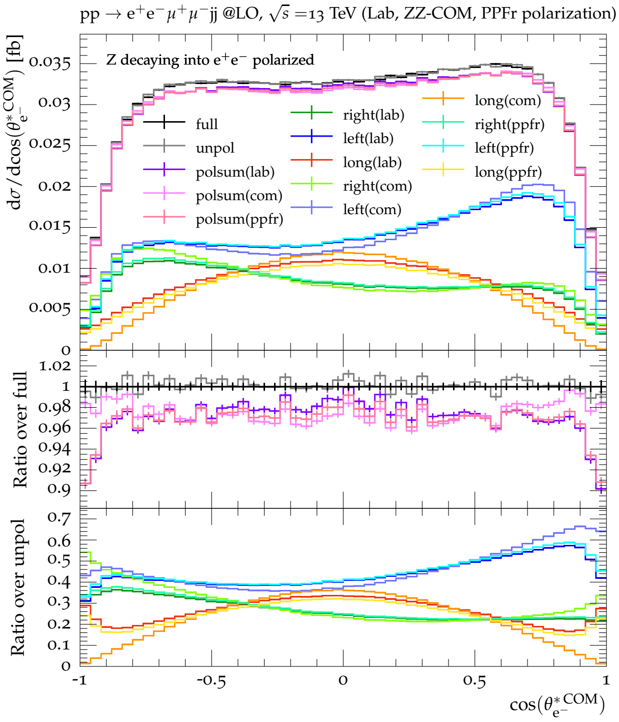

(b) ZZjj - COM observable system

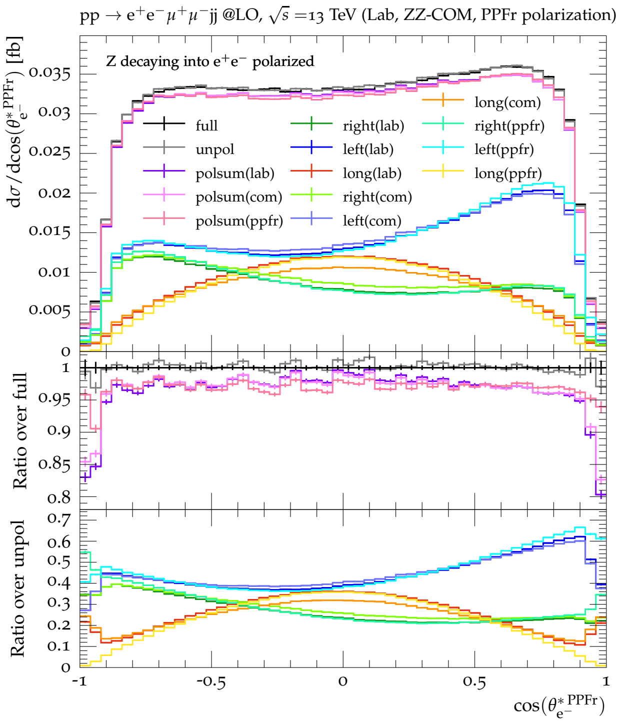

(c) ZZjj - PPFr observable system

Figure D.17: Single-polarized distributions of the electron decay angle $\cos\theta^*_{e^-}$ for the ZZjj process at fixed leading order with polarization defined in the laboratory (lab), ZZ-center-of-mass (com) and the parton-parton-frame (ppfr); results are obtained with SHERPA in the comparison phase space introduced in Sec. 6.1.1, the Z boson decaying into an electron-positron-pair is considered to be polarized.

List of Figures

List of Tables

Bibliography

[1] ATLAS Collaboration, “Observation of a new particle in the search for the Standard Model Higgs boson with the ATLAS detector at the LHC,” Phys. Lett. B 716 (2012) 1-29, doi:10.1016/j.physletb.2012.08.020, arXiv:1207.7214v2 [hep-ex].

[2] CMS Collaboration, “Observation of a new boson at a mass of 125 GeV with the CMS experiment at the LHC,” Phys. Lett. B 716 (2012) 30, doi:10.1016/j.physletb.2012.08.021, arXiv:1207.7235v2 [hep-ex].

[3] C. Bittrich, “Evidence for Scattering of Electroweak Gauge Bosons in the $W^{\pm}Z$ Channel with the ATLAS Detector at the Large Hadron Collider,” PhD thesis (Technische Universität Dresden, 2020), https://cds.cern.ch/record/2719126/files/CERN-THESIS-2020-039.pdf.

[4] G. Bertone et al., “Particle Dark Matter: Evidence, Candidates and Constraints,” Phys.Rept.405:279-390,2005, doi:10.1016/j.physrep.2004.08.031 (2004), arXiv:hep-ph/0404175v2 [hep-ph].

[5] M. Schmaltz, “Physics beyond the standard model (Theory): Introducing the Little Higgs,” Nuclear Physics B - Proceedings Supplements **117**, 40 (2003), https://doi.org/10.1016%2Fs0920-5632%2803%2901409-9.

[6] L. Canetti et al., “Matter and Antimatter in the Universe,” New J. Phys. 14 (2012) 095012, doi:10.1088/1367-2630/14/9/095012 (2012), arXiv:1204.4186v2 [hep-ph].

[7] D. Espriu and B. Yencho, “Longitudinal WW scattering in light of the ”Higgs” discovery,” Phys. Rev. D 87, 055017 (2013), doi:10.1103/PhysRevD.87.055017 (2012), arXiv:1212.4158v2 [hep-ph].

[8] J. Chang et al., “WW Scattering in the Era of Post Higgs Discovery,” doi:10.1103/PhysRevD.87.093005 (2013), arXiv:1303.6335v1 [hep-ph].

[9] S. Braß et al., “Transversal Modes and Higgs Bosons in Electroweak Vector-Boson Scattering at the LHC,” Eur. Phys. J. C (2018) 78: 931, doi:10.1140/epjc/s10052-018-6398-4 (2018), arXiv:1807.02512v1 [hep-ph].

[10] CMS Collaboration, "Measurement of the Polarization of W Bosons with Large Transverse Momenta in W+Jets Events at the LHC," Phys.Rev.Lett.107 (2011) 021802, doi:10.1103/PhysRevLett.107.021802, arXiv:1104.3829v1 [hep-ex].

[11] ATLAS Collaboration, "Measurement of the polarisation of W bosons produced with large transverse momentum in pp collisions at $\sqrt{s} = 7$ TeV with the ATLAS experiment," Eur. Phys. J. C72 (2012) 2001, doi:10.1140/epjc/s10052-012-2001-6, arXiv:1203.2165v2 [hep-ex].

[12] ATLAS Collaboration, "Measurement of the W boson polarisation in $t\bar{t}$ events from pp collisions at $\sqrt{s} = 8$ TeV in the lepton+jets channel with ATLAS," Eur. Phys. J. C 77 (2017) 264, doi:10.1140/epjc/s10052-017-4819-4 (2016), arXiv:1612.02577v3 [hep-ex].

[13] CMS Collaboration, "Measurement of the W boson helicity fractions in the decays of top quark pairs to lepton + jets final states produced in pp collisions at $\sqrt{s} = 8$ TeV," Phys. Lett. B 762 (2016) 512, doi:10.1016/j.physletb.2016.10.007, arXiv:1605.09047v2 [hep-ex].

[14] CMS and ATLAS Collaborations, "Combination of the W boson polarization measurements in top quark decays using ATLAS and CMS data at $\sqrt{s} = 8$ TeV," JHEP 08 (2020) 051, doi:10.1007/JHEP08(2020)051, arXiv:2005.03799v2 [hep-ex].

[15] CMS Collaboration, "Angular coefficients of Z bosons produced in pp collisions at $\sqrt{s} = 8$ TeV and decaying to $\mu^+\mu^-$ as a function of transverse momentum and rapidity," Phys. Lett. B 750 (2015) 154, doi:10.1016/j.physletb.2015.08.061, arXiv:1504.03512v2 [hep-ex].

[16] ATLAS Collaboration, "Measurement of $W^\pm Z$ production cross sections and gauge boson polarisation in pp collisions at $\sqrt{s} = 13$ TeV with the ATLAS detector," Eur. Phys. J. C 79 (2019) 535, doi:10.1140/epjc/s10052-019-7027-6, arXiv:1902.05759v2 [hep-ex].

[17] ATLAS Collaboration, "Observation of gauge boson joint-polarisation states in $W^\pm Z$ production from pp collisions at $\sqrt{s} = 13$ TeV with the ATLAS detector," (2022), arXiv:2211.09435v1 [hep-ex].

[18] CMS Collaboration, "Measurements of production cross sections of polarized same-sign W boson pairs in association with two jets in proton-proton collisions at $\sqrt{s} = 13$ TeV," Phys. Lett. B 812 (2020) 136018, doi:10.1016/j.physletb.2020.136018 (2020), arXiv:2009.09429v2 [hep-ex].

[19] P. Azzi et al., "Report from Working Group 1: Standard Model Physics at the HL-LHC and HE-LHC," (2019), arXiv:1902.04070v3 [hep-ph].

[20] CMS Collaboration (CMS), *Vector Boson Scattering prospective studies in the ZZ fully leptonic decay channel for the High-Luminosity and High-Energy LHC upgrades*, tech. rep. (CERN, Geneva, 2018), https://cds.cern.ch/record/2650915.

[21] J. Alwall et al., “The automated computation of tree-level and next-to-leading order differential cross sections, and their matching to parton shower simulations,” J. High Energy Phys. 07 (2014) 079, doi:10.1007/JHEP07(2014)079, arXiv:`1405.0301v2 [hep-ph]`.

[22] D. B. Franzosi et al., “Automated Predictions from Polarized Matrix Elements,” J. High Energ. Phys. 2020, 82 (2020), doi:10.1007/JHEP04(2020)082 (2019), arXiv:`1912.01725v2 [hep-ph]`.

[23] A. Ballestrero et al., “PHANTOM: a Monte Carlo event generator for six parton final states at high energy colliders,” Comput. Phys. Commun. 180 (2014) 401-417, doi:10.1016/j.cpc.2008.10.005, arXiv:`0801.3359v2 [hep-ph]`.

[24] E. Bothmann et al., “Event Generation with Sherpa 2.2,” SciPost Phys. 7 (2019) 034, doi:10.21468/SciPostPhys.7.3.034, arXiv:`1905.09127v2 [hep-ph]`.

[25] M. D. Schwartz, *Quantum Field Theory and the Standard Model* (Cambridge University Press, New York, 2014).

[26] S. Raby, *Introduction to the Standard Model and beyond* (Cambrige Universiy Press Cambrige, 2021).

[27] M. Thomson, *Modern Particle Physics* (Cambridge University Press, 2013).

[28] J. Iliopoulos and T. N. Tomaras, *Elementary Particle Physics - The Standard Theory* (Oxford University Press Oxford, 2021).

[29] F. Jegerlehner, *Electroweak Theory and LEP physics*, Lectures given in the ”Troisième Cycle de la Physique en Suisse Romande” at the Ecole Polytechnique Fédérale Lausanne, Accessed on 1st Feb 2023 9:46 pm, `http://www-com.physik.hu-berlin.de/~fjeger/ll.pdf`.

[30] G. Eichmann, *Appendix B: Poincaré group*, Lecture notes to QCD and hadron physics lecture at Técnico Lisboa and universities of Graz and Gießen, Accessed on: 17 January 2023 12:30 am, 2020, `http://cftp.ist.utl.pt/%7Egernot.eichmann/2020-QCDHP/App-Poincare.pdf`.

[31] A. Pelster, *Chapter 6: Poincaré group*, Lecture notes to Quantum Field Theory lecture at TU Kaiserslautern, winter term 2020/21, Accessed on: 17 January 2023 12:30 am, 2021, `https://www-user.rhrk.uni-kl.de/~apelster/Vorlesungen/WS2021/v6.pdf`.

[32] G. Costa and G. Fogli, *Symmetries and Group Theory in Particle Physics*, Vol. 823, Lecture Notes in Physics (Springer Verlag Berlin Heidelberg, 2012).

[33] M. Robinson, *Symmetry and the Standard Model* (Springer Science+Business Media New York, 2011).

[34] M. Maggiore, *A Modern Introduction to Quantum Field Theory* (Oxford University Press, 2005), https://ebookcentral.proquest.com/lib/slub/detail.action?docID=422922.

[35] S. Dittmaier, "Weyl–van der Waerden formalism for helicity amplitudes of massive particles," Phys. Rev. D **59**, 016007 (1998), arXiv:9805445v1 [hep-ph], https://link.aps.org/doi/10.1103/PhysRevD.59.016007.

[36] E. Leader, *Spin in Particle Physics*, Cambridge Monographs on Particle Physics, Nuclear Physics and Cosmology (Cambridge University Press, 2001), pp. 1–17.

[37] W. N. Polyzou et al., "Spin in relativistic quantum theory," doi:10.1007/s00601-012-0526-8 (2012), arXiv:1208.5840v1 [nucl-th].

[38] B. van der Waerden, "Spinoranalyse," Nachrichten Akad. Wiss. Göttingen, Math.-Physik. Kl. **100** (1929).

[39] E. Wigner, "On Unitary Representations of the Inhomogeneous Lorentz Group," Annals of Mathematics **40**, 149 (1939), http://www.jstor.org/stable/1968551 (visited on 01/22/2023).

[40] S. Weinberg, *The Quantum Theory of Fields Volume I* (Cambridge University Press New York, 2005).

[41] S. Todt, "The $W^{\pm}W^{\pm}$ Scattering Process – Theoretical Studies, Observation, Cross-section Measurement, and EFT Reinterpretation at $\sqrt{s} = 13$ TeV with the ATLAS Detector," PhD thesis (Technische Universität Dresden, Sept. 2022), https://cds.cern.ch/record/2845282.

[42] F. Mandl and G. Shaw, *Quantum Field Theory*, Revised Edition (John Wiley and Sons Ltd, 1995).

[43] H. Haber, *Polarization sum for massless spin-one particles*, Part of Lecture Physics 218 (Advanced Quantum Field Theory) winter quarter 2016, Accessed on: 30 Jan 2023 8:48 pm, http://scipp.ucsc.edu/~haber/ph218/polsum.pdf.

[44] S. L. Glashow, "Partial-Symmetries of Weak Interactions," Nuclear Physics **22**, 579 (1961).

[45] A. Salam, "Elementary Particle Theory," Almqvist and Wiksell (1968).

[46] S. Weinberg, "A Model of Leptons," Phys. Rev. Lett. **19**, 1264 (1967), https://link.aps.org/doi/10.1103/PhysRevLett.19.1264.

[47] F. Englert and R. Brout, "Broken Symmetry and the Mass of Gauge Vector Mesons," Phys. Rev. Lett. **13**, 321 (1964), https://link.aps.org/doi/10.1103/PhysRevLett.13.321.

[48] P. W. Higgs, "Broken Symmetries and the Masses of Gauge Bosons," Phys. Rev. Lett. **13**, 508 (1964), https://link.aps.org/doi/10.1103/PhysRevLett.13.508.

[49] G. S. Guralnik, C. R. Hagen, and T. W. B. Kibble, "Global Conservation Laws and Massless Particles," Phys. Rev. Lett. **13**, 585 (1964), https://link.aps.org/doi/10.1103/PhysRevLett.13.585.

[50] C. Bierlich et al., "A comprehensive guide to the physics and usage of PYTHIA 8.3," (2022), arXiv:2203.11601v1 [hep-ph].

[51] M. Bahr et al., "Herwig++ Physics and Manual," Eur.Phys.J.C58:639-707,2008 (2008), arXiv:0803.0883v3 [hep-ph].

[52] J. Bellm et al., "Herwig 7.0/Herwig++ 3.0 release note," Eur. Phys. J. C **76**, 196 (2016), arXiv:1512.01178 [hep-ph].

[53] S. Höche, "Introduction to parton-shower event generators," (2014), arXiv:1411.4085v2 [hep-ph].

[54] J. Krause, "Simulation of Particle Collisions for the Large Hadron Collider at the Intersection of Theory and Experiment," PhD thesis (TU Dresden, 2019), https://iktp.tu-dresden.de/IKTP/pub/19/thesis-2019-07-johannes-krause.pdf.

[55] A. Buckley et al., "General-purpose event generators for LHC physics," doi:10.1016/j.physrep.2011.03.005 (2011), arXiv:1101.2599v1 [hep-ph].

[56] J. Campbell, J. Huston, and F. Krauss, *The Black Book of Quantum Chromodynamics* (Oxford University Press, 2018).

[57] S. Hoeche et al., "A critical appraisal of NLO+PS matching methods," JHEP09(2012)049, doi:10.1007/JHEP09(2012)049 (2011), arXiv:1111.1220v2 [hep-ph].

[58] A. Ballestrero et al., "W boson polarization in vector boson scattering at the LHC," JHEP 03 (2018) 170, doi:10.1007/JHEP03(2018)170, arXiv:1710.09339v3 [hep-ph].

[59] A. Ballestrero et al., "Polarized vector boson scattering in the fully leptonic WZ and ZZ channels at the LHC," JHEP 09 (2019) 087, doi:10.1007/JHEP09(2019)087, arXiv:1907.04722v2 [hep-ph].

[60] T. Gleisberg et al., "Event generation with SHERPA 1.1," JHEP 0902:007,2009 (2008), arXiv:0811.4622v1 [hep-ph].

[61] J. Ohnemus, "An Order $\alpha^{-}s$ calculation of hadronic $W^{\pm}Z$ production," Phys. Rev. D **44**, 3477 (1991).

[62] Bloch, F. and Nordsieck, A., "Note on the Radiation Field of the Electron," Phys. Rev. **52**, 54 (1937), https://link.aps.org/doi/10.1103/PhysRev.52.54.

[63] T. Kinoshita, "Mass singularities of feynman amplitudes," Journal of Mathematical Physics **3**, 650 (1962), eprint: https://doi.org/10.1063/1.1724268, https://doi.org/10.1063/1.1724268.

[64] Lee, T. D. and Nauenberg, M., “Degenerate systems and mass singularities,” Phys. Rev. **133**, B1549 (1964), https://link.aps.org/doi/10.1103/PhysRev.133.B1549.

[65] S. Catani and M. Seymour, “A general algorithm for calculating jet cross sections in NLO QCD,” Nuclear Physics B **485**, 291 (1997).

[66] S. Catani et al., “The dipole formalism for next-to-leading order QCD calculations with massive partons,” Nuclear Physics B **627**, 189 (2002).

[67] F. Buccioni et al., “OpenLoops 2,” Eur.Phys.J. C79 (2019) no.10, 866 (2019), arXiv:1907.13071v2 [hep-ph].

[68] F. Krauss et al., “AMEGIC++ 1.0: A Matrix element generator in C++,” JHEP **02**, 044 (2002), arXiv:hep-ph/0109036.

[69] T. Gleisberg and S. Hoeche, “Comix, a new matrix element generator,” JHEP 0812:039,2008, doi:10.1088/1126-6708/2008/12/039 (2008), arXiv:0808.3674v2 [hep-ph].

[70] M. Moretti et al., “O’Mega: An Optimizing Matrix Element Generator,” AIP Conference Proceedings 583 (2001) 173, doi:10.1063/1.1405295, arXiv:hep-ph/0102195v1 [hep-ph].

[71] F. A. Berends and W. T. Giele, “Recursive Calculations for Processes with n Gluons,” Nucl. Phys. B **306**, 759 (1988).

[72] P. Nason, “A New Method for Combining NLO QCD with Shower Monte Carlo Algorithms,” Journal of High Energy Physics **2004**, 040 (2004).

[73] S. Frixione and B. R. Webber, “Matching NLO QCD computations and parton shower simulations,” Journal of High Energy Physics **2002**, 029 (2002).

[74] S. Catani et al., “QCD Matrix Elements + Parton Showers,” Journal of High Energy Physics **2001**, 063 (2001).

[75] S. Höche et al., “QCD matrix elements and truncated showers,” Journal of High Energy Physics **2009**, 053 (2009).

[76] A. Ballestrero et al., “Different polarization definitions in same-sign WW scattering at the LHC,” Phys. Lett. B 811 (2020) 135856, doi:10.1016/j.physletb.2020.135856, arXiv:2007.07133v2 [hep-ph].

[77] M. Pellen et al., “Polarised W+j production at the LHC: a study at NNLO QCD accuracy,” JHEP 02 (2022) 160, doi:10.1007/JHEP02(2022)160, arXiv:2109.14336v3 [hep-ph].

[78] Sherpa-Team, *Sherpa release 2.2.15*, ”https://gitlab.com/sherpa-team/sherpa/tree/v2.2.15”, Acessed on 4 April 2023 5:46 pm, https://gitlab.com/sherpa-team/sherpa/tree/v2.2.14.

[79] Sherpa-Team, *Sherpa - current development version*, ”https://gitlab.com/sherpa-team/sherpa”, https://gitlab.com/sherpa-team/sherpa.

[80] S. Höche et al., "Beyond Standard Model calculations with Sherpa," Eur.Phys.J. C75 (2015) 135, doi:10.1140/epjc/s10052-015-3338-4 (2014), arXiv:`1412.6478v2 [hep-ph]`.

[81] P. Richardson, "Spin Correlations in Monte Carlo Simulations," JHEP 0111 (2001) 029, doi:10.1088/1126-6708/2001/11/029, arXiv:`hep-ph/0110108v1 [hep-ph]`.

[82] J. Alnefjord et al., "The chirality-flow formalism for the standard model," Eur. Phys. J. C (2021) 81: 371, 24pp, doi:10.1140/epjc/s10052-021-09055-2 (2020), arXiv:`2011.10075v2 [hep-ph]`.

[83] *Private conversation with Giovanni Pelliccioli.*

[84] J. Liersch, "Phenomenology of polarized Cross-Sections for $W^{\pm}Z$ in Sherpa," Bachelor thesis (TU Dresden, 2022), `https://cds.cern.ch/record/2851268`.

[85] T. Burghardt, "Validation of polarized simulations for WZjj production in Sherpa," Bachelor thesis (TU Dresden, 2022), `https://cds.cern.ch/record/2849363`.

[86] A. Denner and G. Pelliccioli, "NLO QCD predictions for doubly-polarized WZ production at the LHC," Phys. Let. B (2021) 136107, doi:10.1016/j.physletb.2021.136107, arXiv:`2010.07149v2 [hep-ph]`.

[87] C. Bierlich et al., "Robust Independent Validation of Experiment and Theory: Rivet version 3," SciPost Phys. 8, 026 (2020), doi:10.21468/SciPostPhys.8.2.026, arXiv:`1912.05451v3 [hep-ph]`.

[88] A. Buckley et al., "LHAPDF6: parton density access in the LHC precision era," Eur.Phys.J. C, 132 (2014), arXiv:`1412.7420v2 [hep-ph]`.

[89] C. Bittrich and M. Buhring, *Rivet-Analyse for polarized same-sign WW scattering process*, Accessed on: 24 Oct 2022 3:47 pm, `https://gitlab.cern.ch/atlas-germany-dresden-vbs-group/rivet_analyses/-/tree/master/WWss/VBSCost`.

[90] S. Actis et al., "RECOLA: REcursive Computation of One-Loop Amplitudes," (2016), arXiv:`1605.01090v1 [hep-ph]`.

[91] A. Denner et al., "Collier: a fortran-based Complex One-Loop LIbrary in Extended Regularizations," doi:10.1016/j.cpc.2016.10.013 (2016), arXiv:`1604.06792v2 [hep-ph]`.

[92] *Private conversation with Frank Siegert.*

[93] Sherpa Team, *Sherpa version 3.0.0 manual*, Accessed on 25 feb 2023 11:48 am, `https://sherpa-team.gitlab.io/sherpa/master/index.html#`.

[94] Matteo Cacciari and others, "The anti-kT-jet clustering algorithm," Journal of High Energy Physics **2008**, 063 (2008).

[95] A. Denner et al., "Recola2: REcursive Computation of One-Loop Amplitudes 2," (2017), arXiv:`1711.07388v2 [hep-ph]`.

[96] M. Hoppe, M. Schönherr, and F. Siegert, "In preparation, topic: polarized cross sections for vector boson production with Sherpa," (2023).

Danksagung

An dieser Stelle möchte ich all jenen danken, ohne die diese Arbeit niemals möglich gewesen wäre, sei es aufgrund der Unterstützung bei dieser Arbeit oder bei dem Studium zuvor.
Zunächst möchte ich meinem Betreuer Dr. Frank Siegert danken für die Möglichkeit, meine Masterarbeit in seiner Gruppe an so einem interessanten Thema schreiben zu dürfen und für die vielen Diskussionen über Polarisation von Vektorbosonen und Monte-Carlo-Eventgeneratoren. Außerdem bin ich sehr dankbar für die Möglichkeit, meine Arbeit beim MCnet Meeting in Graz, bei QCD@LHC in Orsay und bei der DPG-Frühjahrstagung in Dresden vorstellen zu dürfen. Ein weiterer großer Dank gilt auch meinem zweiten Betreuer Dr. Marek Schönherr, der immer für Diskussionen zu zweit oder zu dritt bereit war, viele hilfreiche Erklärungen lieferte und schließlich auch die Zweitkorrektur meiner Arbeit übernahm.
Furthermore, I am very happy to have ended up in such a nice and familiar working group. Thank you very much for the nice barbecue-, fire- and beer garden evenings and the many interesting, motivating and funny conversations also outside of physics. Ein weiterer Dank geht an Dirk Bachmann, Jan-Eric Nitschke, Max Stange, Stefanie Todt and Daniel Zablizki für das Korrekturlesen meiner Arbeit und die vielen guten Verbesserungsvorschläge.
Den wohl größten Dank haben die folgenden Personen verdient, ohne ihre fortwährende Motivation ich niemals bis ans Ende meine Studiums gekommen wäre. Einen unglaublich großen Dank an

- meiner Mutter Diana Hoppe: dafür, dass Du unablässlich dabei bist, uns den Rücken freizuhalten und ständig dafür Sorge trägst, dass es uns allen gut geht
- meine Familie Diana, Andreas, Damaris & Leonard Hoppe, Daniel Zablizki: dafür, dass Ihr immer für mich da wart und mich in schwierigen Zeiten so häufig motiviert habt
- Christopher Grüner: dafür, dass wir die schwierigen Anfänge unseres Studiums gemeinsam durchgestanden haben in den vielen tollen Nachmittagen und Abenden, in denen wir zusammen über Übungsaufgaben verzweifelten und trotzdem immer noch Gelegenheit zum Lachen fanden
- Dirk Bachmann: für die Hilfe bei kniffligen Computerproblemen jeglicher Art und motivierende Gespräche
- Erik Bachmann: dafür, dass Du immer für mich da warst, mir über viele, nicht ausschließlich englische und computertechnische, Hürden geholfen hast, mich beständig motiviert und an mich geglaubt hast und immer für physikalische Diskussionen zur Verfügung standest, die so häufig zu meinem tieferen Verständnis beigetragen haben.

Erklärung

Hiermit erkläre ich, dass ich diese Arbeit im Rahmen der Betreuung am Institut für Kern- und Teilchenphysik ohne unzulässige Hilfe Dritter verfasst und alle Quellen als solche gekennzeichnet habe.

Mareen Hoppe

Dresden, April 2023